1993

Frequency conversion analysis of noise in heterojunction bipolar transistor oscillators including periodically modulated noise sources

Bradley Allen Kramer
Iowa State University

Order Number 9321184

Frequency conversion analysis of noise in heterojunction bipolar transistor oscillators including periodically modulated noise sources

Kramer, Bradley Allen, Ph.D.

Iowa State University, 1993

U·M·I
300 N. Zeeb Rd.
Ann Arbor, MI 48106

Frequency conversion analysis of noise in heterojunction bipolar transistor oscillators including periodically modulated noise sources

by

Bradley Allen Kramer

A Dissertation Submitted to the

Graduate Faculty in Partial Fulfillment of the

Requirements for the Degree of

DOCTOR OF PHILOSOPHY

Department: Electrical Engineering and Computer Engineering
Major: Electrical Engineering (Microelectronics)

Approved:

Signature was redacted for privacy.

In Charge of Major Work

Signature was redacted for privacy.

For the Major Department

Signature was redacted for privacy.

For the Graduate College

Iowa Sate University
Ames, Iowa

1993

TABLE OF CONTENTS

ACRONYMS AND ABBREVIATIONS

AM: Amplitude Modulation
dB: Decibel
dBV: Decibels Referenced to 1 Volt
dBW: Decibels Referenced to 1 Watt
BJT: Bipolar Junction Transistors
dc: Direct Current
fF: Femtofarads
FM: Frequency Modulation
GaAs: Gallium Arsenide
GHz: Gigahertz
HEMT: High Electron Mobility Transistor
HBT: Heterojunction Bipolar Transistor
Hz: Hertz
IEEE: Institute of Electrical and Electronic Engineers
kHz: Kilohertz
LNA: Low Noise Amplifier
mA: Milliampere
MBE: Molecular Beam Epitaxy
MESFET: Metal Semiconductor Field Effect Transistor
MHz: Megahertz
MMIC: Monolithic Microwave Integrated Circuit
MOCVD: Metal Organic Chemical Vapor Deposition
MOSFET: Metallic Oxide Semiconductor Field Effect Transistor
mS: Millisiemans
mS: Millisecond
nH: Nanohenery
nsec: Nanosecond
pF: Picofarad
PLL: Phase Locked Loop
PM: Phase Modulation
psec: Picosecond
Q: Quality Factor
rms: Root Mean Square
SSB: Single Sideband
VCO: Voltage Controlled Oscillator

1. INTRODUCTION

Oscillators can be found in a wide variety of electronic equipment. They perform a number of different functions spanning from highly stable frequency standards to voltage controlled oscillators, which may be used to achieve frequency modulation. The noise characteristics of these oscillators often limit the capabilities of many electronic systems, including radar systems, electronic location systems, radio communication equipment, and electronic test equipment. The need for more accurate radar systems and improved performance in other electronic equipment has generated considerable interest in analyzing the noise performance of oscillators. However, many of the current oscillator noise analyses are based on greatly simplified assumptions such as treating the oscillator as a linear circuit [1, 2]. Even the more in depth oscillator analyses ignore other significant effects such as the modulation of the noise sources within the oscillator [3,4]. Accordingly, these analyses are often inaccurate in predicting the noise performance of microwave oscillators [5]. Thus, a better understanding of the mechanisms which affect the noise characteristics of oscillators is needed to improve the design of many microwave oscillators.

1.1. Statement of Purpose

The primary purpose of this paper is to present an analysis procedure which accurately models the noise characteristics of microwave oscillators. This procedure accounts for the significant mechanisms which determine oscillator noise performance including the frequency conversion of noise through both circuit nonlinearities and noise source modulation. It can also be used to determine the significance of each of the individual noise sources on the overall oscillator noise characteristics. In addition, the proposed approach is suitable for possible integration into modern microwave computer aided design applications such as LIBRA™, HARMONICA™, or MDS™ and could potentially allow the output noise spectrum of an oscillator circuit to be optimized numerically.

While the vast majority of the work contained in this paper applies to a wide variety of oscillator circuits, the main emphasis is on oscillators which contain heterojunction

bipolar transistors (HBTs). Recently considerable interest has been given to HBTs in the development of high quality microwave oscillators due to the excellent flicker noise performance of these devices [6]. They are also expected to gain wide spread use in future MMIC applications. Since bipolar transistors are basically a simplified form of HBTs, this research is also applicable to bipolar transistor oscillators. Many of the characteristics of MESFET oscillators have previously been analyzed by the author [7]. The most significant limitation of this previous analysis is associated with ignoring the effects of noise source modulation. Much of the analysis presented in this research may also be used to analyze noise source modulation in MESFET oscillators, when applied in conjunction with Rizzoli's analysis of MESFET mixers [8]. Finally, it should be noted that the research presented in this paper has limited application for oscillators which incorporate transferred electron devices. This is due to the quasi-static modelling technique which is implemented in the analysis and is likely to be the most significant limitation of the analysis presented in this paper.

In order to demonstrate specific details of the procedure, the analysis of a particular HBT oscillator is discussed. It should be noted, however, that the procedure which is presented in this paper may be used to analyze nearly any oscillator topology and is not limited to the particular topology discussed in the paper. In addition, it should be noted that the research presented in this paper can be applied to nearly any nonlinear periodically driven circuit, including mixers, frequency multipliers, frequency dividers, and limiters.

1.2. General Overview

A review of the literature which is relevant to the research presented in this paper is given in Section 1.3. This review covers topics related to the analysis of noise in oscillators and microwave mixers. The review of noise modulation in microwave mixers is shown to be particularly significant for this paper since the modulation of noise in oscillators has not previously been discussed in literature.

A review of numerous topics which are related to the the noise characteristics of HBT oscillators is given in Section 2. This section is intended to provide a review of basic

background information. Any reader who has no understanding of the basic operation of oscillators may find it useful to read Section 2 before reading Section 1.3 of this paper.

Section 3 contains a discussion of the analysis approach which has been developed in this research. This approach is contrasted with other possible approaches and it is justified in terms of its numerical efficiency and compatibility with existing CAD programs.

Large-signal models, which are required for the analysis procedure, are developed in Section 4. In Section 4.1, a large signal HBT model is developed based primarily on the popular Gummel-Poon transistor model. However, it is shown that some modifications to the Gummel-Poon model are required in order to accurately describe the characteristics of HBTs. The HBT model is then implemented in a large signal oscillator model in Section 4.2. This large signal model is used to establish the nonlinear characteristics of the oscillator.

In Section 5, a linear model of the oscillator is developed. This linear model is generated from the large signal oscillator modeled which is developed in Section 4. It accurately accounts for the conversion of noise between the various harmonics of the oscillator due to device nonlinearities.

Noise models of the HBT device are developed in Section 6. In Section 6.1, a microwave frequency noise model is generated. It is found that a standard transistor noise model can be used to model the noise characteristics of an HBT at microwave frequencies. A low frequency HBT flicker noise model is developed in Section 6.2. Both the microwave frequency noise model and low frequency flicker noise model are expressed as a function of the bias conditions within the HBT and thus can be used to describe the large signal noise characteristics of the HBT.

In Section 7, the modulation of the noise sources within the oscillator are discussed. The analysis of noise source modulation in oscillators has not previously been reported in literature. The results of the analyses in Sections 4 through 7 are then combined, and the overall noise characteristics of the oscillator are modelled. Both the amplitude and phase spectrums are generated, and the significance of the individual noise sources in determining the overall spectrum of the oscillator is discussed.

1.3. Review of Relevant Literature

A number of oscillator phase noise models have been reported in literature. Most are based on very specific oscillator topologies and make drastic simplifying assumptions. Several of the more popular oscillator analyses are reviewed in this section. A review is also given of several mixer noise analyses which may be applied to the analysis of noise source modulation in oscillators.

One of the most popular models which is commonly used to explain the qualitative characteristics of oscillator noise was first developed by Leeson [4]. He analyzed oscillator phase noise using the feedback topology shown in Figure 1.1. The oscillator in this figure is modelled as an amplifier with a frequency independent voltage gain, A_V, and a feedback circuit with a bandpass frequency response. Using heuristic arguments in conjunction with this model, Lesson found that the output spectrum of an oscillator will be effected by low frequency flicker noise, which is upconverted to the oscillator sidebands through circuit nonlinearities. Leeson's model has also been used as a basis for several other oscillator analyses [9, 10, 11]. Several qualitative conclusions were reached as a result of these other oscillator analyses: (1) Oscillations will occur at any frequency where the open loop gain, $A_V H_0$, is equal to one and the open loop phase shift is an integer multiple of 360°. (2) Any practical oscillator will be a nonlinear circuit where the nonlinearities are required to limit the amplitude of oscillation such that the open loop gain is one. (3) The nonlinearities in the circuit will cause any flicker noise which is present in the oscillator to be upconverted to the oscillator sidebands. (4) The phase noise

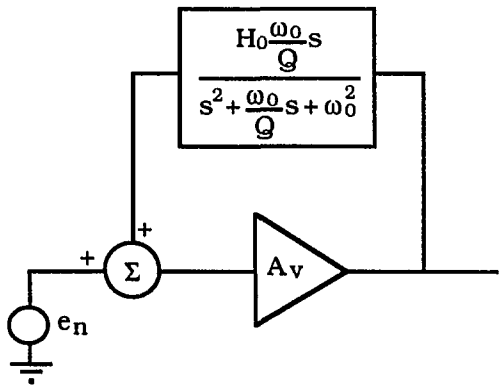

Figure 1.1. Leeson's Oscillator Model

performance of the oscillator can be improved by increasing the loaded Q of the feedback circuit, maximizing the power which is available from the oscillator, minimizing the amplifier noise figure, reducing the flicker noise sources in the oscillator, and minimizing the losses in the feedback circuit.

While the analyses which are based on Leeson's model are useful for qualitatively explaining many of the noise characteristics of feedback oscillators, several significant simplifications are required. Impedance mismatch effects which tend to degrade oscillator noise characteristics are ignored. In addition, it is assumed that the oscillator operates at the center frequency of the resonator. In nearly all microwave oscillators, this condition will not be met and this simplification tends to make the model overly optimistic. Probably the most significant simplification is in modeling the effects of the noise conversion between the various sidebands of the oscillator. An "effective upconverted flicker noise figure" is typically defined to account for these noise conversion effects. There is no practical method to determine a value for this parameter or how much flicker noise is upconverted due to nonlinearities. In addition, the microwave frequency noise figure of the active devices in the oscillator will also be degraded under large-signal conditions. This is not accounted for in these analyses.

Many of the more recent oscillator analyses have concentrated on circuits containing MESFETs. Siweris and Schiek [3] studied the flicker noise upconversion mechanisms which determine the phase noise levels in oscillators. The analysis was applied to oscillator topologies which contain a single MESFET. The nonlinearities in the gate-to-source capacitance, transconductance, and output conductance of the MESFET were considered. All other elements in the oscillator were assumed to be linear. The impact of the low frequency flicker noise on the oscillator phase noise was then evaluated. In order to simplify the analysis it was assumed that (1) the linear network provides a low input impedance at all of the harmonic frequencies of the oscillator, (2) the frequency response of the linear network is symmetrical with respect to the frequency of oscillation, (3) the impedance loading the drain of the MESFET is real at the frequency of oscillation, and (4) the nonlinear components can be described by polynomials of second order or less. From this analysis, Siweris and Schiek concluded that amplitude fluctuations in MESFET oscillators depend only on nonlinearities in the transconductance and drain-to-source resistance of the MESFET and that the

nonlinearities in the gate-to-source capacitance have no effect on the amplitude fluctuations. While the phase noise level was found to be dependent on all three nonlinear components, it was a null level only when the gate-to-source capacitance was linear. As a result, is was concluded that the phase noise performance was primarily determined by the gate-to-source capacitance nonlinearities.

As previously discussed by the author [7], it appears that the conclusions obtained by Siweris and Schiek were a result of the simplifying assumptions which were made during the analysis. Specifically, it was shown that if the second and third assumptions which are mentioned above are not satisfied, then the amplitude and phase fluctuations in the oscillator will depend on all of the nonlinear components. These assumptions will not be valid in most microwave oscillators. In addition, the gate-to-drain capacitance is usually considered to be a nonlinear component in most MESFET models and should be considered in any general MESFET oscillator analysis. However, despite these shortcomings, the general approach which was implemented by Siweris and Schiek was one of the first reported attempts to model noise conversion due to circuit nonlinearities in a detailed manner.

Debney and Joshi [12] also analyzed the relationship between the oscillator phase noise performance and the nonlinear behavior of GaAs MESFETs. By using the results of a general oscillator analysis performed by Kurokawa [13], Debney and Joshi were able to derive an expression for the power spectral density of phase noise in terms of the oscillator circuit parameters and flicker noise levels. Kurokawa's analysis gives an expression for the phase noise of an oscillator in terms of the noise generated at the frequency of oscillation. Debney and Joshi extended this theory to include the effect of flicker noise upconversion due to mixing in the circuit nonlinearities. From this analysis, Debney and Joshi concluded that the amplitude and phase fluctuations in MESFET oscillators are dependent on all of the nonlinear MESFET elements, and that no single nonlinear element plays a dominant role in the flicker noise upconversion process.

While the simplifying assumptions required for the analysis presented by Siweris and Schiek were not used by Debney and Joshi, the nonlinearities in the gate-to-source capacitance of the MESFET were ignored. This capacitance is typically considered to be

one of the dominant MESFET nonlinearities in the generation of oscillator phase noise. Siweris and Schiek also determined that Kurokawa's oscillator theory was improperly applied by Debney and Joshi. As pointed out by Siweris and Schiek [3], the flicker noise which is upconverted to both sidebands will be correlated while Kurokawa's oscillator analysis is based on the assumption that the noise at both sidebands is uncorrelated. This effect was not accounted for by Debney and Joshi.

Several authors have analyzed various circuit topologies in an attempt to minimize the flicker noise upconversion process. Riddle and Trew [5] proposed that a source coupled differential pair, as shown in Figure 1.2a, could be used to reduce the amount of flicker noise which is upconverted. The upconversion process was analyzed by modeling the flicker noise as a voltage source in series with each MESFET gate and then modelling the MESFET differential pair using the equivalent circuit shown in Figure 1.2b. It was postulated that any small variation in either flicker noise source, V_{n1} or V_{n2}, would result in half of this voltage increasing the gate-to-source voltage in one MESFET, and the other half reducing the gate-to-source voltage of the other MESFET. The gate-to-source capacitance of one MESFET would then increase and the gate-to-source capacitance of the other MESFET would decrease by the same amount. Accordingly, no net change in the input impedance of the differential pair would result and the flicker noise upconversion process would be defeated. However, the experimental results, which were reported by Riddle and Trew, did not show the expected improvement in oscillator phase noise. This discrepancy was attributed to the phase delay associated with the physical separation of the MESFETs which were in discrete packages.

Several other factors could also be responsible for degrading the phase noise of the

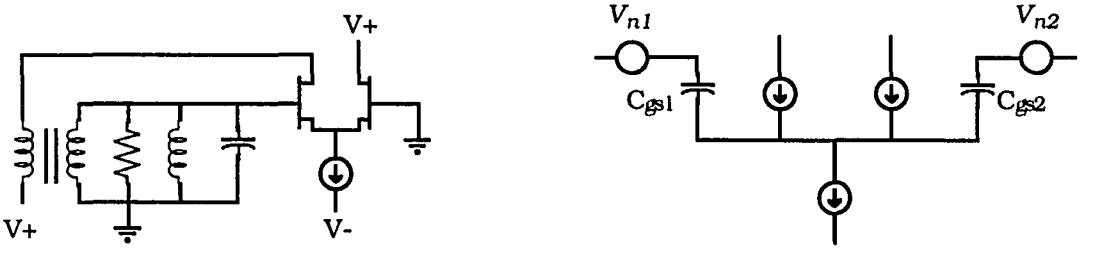

(a) Oscillator Topology (b) Differential MESFET Pair Model

Figure 1.2. Oscillator Topology Proposed by Riddle and Trew

oscillator. The simplified analysis, which was presented by the authors, did not account for the nonlinearities in the drain-to-source conductance, transconductance, or the gate-to-drain capacitance in the MESFETs. A more detailed analysis of the oscillator indicates that the drain-to-source conductance will have a significant impact on the upconversion of flicker noise [7]. In addition, if any flicker noise is present in the current source which biases the differential pair, it will modulate the gate-to-source capacitance of both MESFETs. As a result, this flicker noise will be upconverted and degrade the phase noise performance of the oscillator.

Chen et al. [14] have also analyzed the circuit requirements for reducing the upconversion of flicker noise. By studying a general oscillator model, Chen et al. determined that the upconversion of flicker noise would be eliminated if all of the nonlinear devices could be described by polynomials which contained only odd ordered terms. This type of nonlinear device is referred to in literature as an odd-symmetrical device. The result of Chen's analysis was verified experimentally by realizing an odd-symmetrical oscillator which operated in the 10 kHz frequency range. By injecting a 50 Hz signal into the oscillator and observing the output spectrum, Chen was able to tune the biasing of the oscillator until it was odd symmetrical. When the oscillator was tuned to this point, the 50 Hz sidebands were eliminated from the oscillator output. However, no reduction in the oscillator phase noise was achieved since the level of flicker noise in the oscillator was insignificant regardless of the oscillator tuning.

A paper published by Hearn [15] includes a discussion of the experimental procedure and conclusions of Chen's analysis. Hearn contended that an odd symmetrical oscillator will only defeat the flicker noise upconversion process if the flicker noise and carrier signal are combined prior to odd symmetrical limiting. In many odd symmetrical circuits, such as back-to-back limiter diodes, the flicker noise associated with the internal circuit components will still be upconverted. It was also noted that the experimental technique used by Chen et al. did not ascertain whether the sidebands of the oscillator output were due to amplitude or phase fluctuations. A more complete measurement technique is required in order to verify Chen's et al. theory for both amplitude and phase fluctuations.

Takaoka and Ura [16] have developed a method for analyzing the process by which amplitude fluctuations may be converted to phase fluctuations. While this work is not capable of analyzing the upconversion of flicker noise, it is useful for determining the level of AM-to-PM conversion at the frequency of oscillation. This analysis may be used to calculate the output spectrum of an oscillator from the characteristics of the feedback circuit, the noise figure, the describing function of the amplifier, and the AM-to-PM conversion coefficient of the amplifier. Due to the complexity of the calculations required for this analysis, it is probably most useful in a computer program format. In addition, many of the parameters required for this analysis must be determined experimentally, such as the AM-to-PM conversion coefficient and the noise figure of the amplifier. These parameters are very difficult to measure under large signal conditions.

While many oscillator analyses have been completed, no widely accepted procedure exists for analyzing the noise characteristics of oscillators. The analyses discussed in this section indicate that the simplified approaches to analyzing the noise characteristics of oscillators are inadequate. The reported conclusions are often in conflict. (Such as the conclusions reported by Siweris and Schiek versus those reported by Debney and Joshi.) In addition, most of these analyses, contain empirical parameters which cannot be determined by analysis or measurement and apply only to specific topologies. More significantly, these analyses neglect the effects of the modulation of noise sources on the oscillator characteristics. Any noise source which varies as a function of bias will be modulated by the large-signal characteristics of the oscillator. This effect is ignored in all of these oscillator analyses even though it has been found to have a significant impact on the noise performance of other nonlinear periodically driven circuits [17]. One of the major purposes of the research presented in this paper is to demonstrate a procedure for analyzing the effects of noise source modulation. In addition, the effects of noise source modulation are shown in this research to invalidate many of the models which have been discussed previously in this chapter. For example, it is shown that an odd symmetrical oscillator will not defeat the upconversion of flicker noise since it is upconverted through noise source modulation.

Noise modulation effects were perhaps best summed up by Maas [18] in a discussion regarding diode mixers:

> The history of mixer noise analysis is remarkable in that the properties of noise in mixers were well understood early in their history, but a workable, accurate noise model was not generated until the mid-1970s. . . .
>
> The key to understanding mixer noise is not simply to understand the shot and thermal noise processes, which are relatively simple, but to appreciate the more subtle correlation properties of the noise, and the effect of the time-varying elements, particularly the junction capacitance, upon them. For the dc-biased diode, the correlation properties are simply those of any white noise process: components at different frequencies are not correlated. For the pumped diode, however, the components down-converted to the IF from different mixing frequencies - including unwanted mixing products - are partially correlated, and their correlation raises the noise level. . . .

These same comments also apply to any nonlinear periodically excited circuit including oscillators. Consider, for example, any oscillator which contains an arbitrary number of nonlinear devices. Any noise which is present in the oscillator components will be converted to all of the oscillator sidebands through the circuit nonlinearities. A second mechanism by which the noise can be frequency converted is through noise source modulation. If any noise source is a function of a voltage or current within the oscillator, it will be modulated in a periodic manner. This modulation will also cause the noise to be frequency converted to all of the oscillator sidebands. Thus, the noise at any oscillator sideband will be partially correlated with the noise at all of the other sidebands. It is the analysis of these frequency conversion and noise correlation effects which is crucial to achieving an accurate analysis of oscillator noise properties.

Conversion matrix techniques, which may be used to analyze frequency conversion effects due to circuit nonlinearities, are well established [13] in the analysis of microwave mixers. These techniques may also be applied to oscillator analyses [11, 19]. However, the analysis of noise source modulation in microwave oscillators has all but been ignored in reported literature. (See, for example, the references cited in Rizzoli's review paper on microwave CAD [20].) One analysis which considers noise modulation in microwave oscillators, in a very simplified manner, has been reported by Siweris and Schiek [21].

Siweris and Schiek analyzed a MESFET oscillator. The large-signal operation of the oscillator was simulated using a harmonic balance algorithm and conversion matrix techniques were used to represent the oscillator as a linear circuit. (Harmonic balance algorithms and conversion matrices are discussed in Appendix A and Section 5 of this

paper.) Only the baseband frequency and the sideband frequencies at the first harmonic of the oscillator were considered in the conversion matrix analysis. All other harmonics were ignored. A linear flicker noise source was inserted into the model, and the output phase noise was modelled. It was found to be in poor agreement with the measured results. The flicker noise source was then scaled in magnitude in an attempt to account for noise source modulation. The magnitude of scaling was selected as an empirical factor to make the modeled results match the measured values. This scaling factor will be different for different oscillator designs. No attempt was made in the analysis to model the frequency conversion of the flicker noise due to noise source modulation or to represent the noise source modulation as a set of partially correlated noise sources at each of the oscillator sidebands.

While little information has been reported regarding noise source modulation effects in oscillators, these effects have been analyzed in diode and MESFET mixers and many of the results of these mixer analyses may also be applied to oscillators. An analysis which has been performed by Held and Kerr [17] is usually referenced as the most advanced treatment of noise source modulation.

Held and Kerr made use of the results reported by Dragone [22] to correctly model the noise modulation and correlation effects in diode mixers. The dominant sources of noise in diode mixers were found to be shot and thermal noise. Thermal noise sources are not functions of bias and thus were modeled as simple linear noise sources. The shot noise levels are dependent on the diffusion current in the diodes, and as a result, these noise sources are modulated. This modulation results in a partial correlation of the noise at the various sidebands of the LO signal. Dragone had previously analyzed the modulation of shot noise and determined that the correlation between these sidebands is given by,

$$\left\langle I_{S_j}\, I^{*}_{S_k} \right\rangle = 2\, q\, I_{j-k}\, \Delta f \tag{1.1}$$

where I_{j-k} is a Fourier coefficient of the diffusion current which generates the shot noise and i_{S_j} is the amount of shot noise current present at the upper sideband of harmonic j. Thus, the average value of the diffusion current through a diode determines the magnitude of the shot noise while the harmonics of this current determine the amount of correlation

between the sidebands. It should be noted that modulation of flicker noise in diode mixers was not analyzed by Held and Kerr.

An analysis of noise source modulation in MESFET mixers has been performed by Rizzoli [6, 20]. Rizzoli used the results of a FET noise analysis, which was performed by Statz et al. [23], to establish the correlation matrix of the noise sources within MESFETs. A quasi-static assumption was used to convert this noise correlation matrix into a time varying matrix. This time varying matrix was then used to model the noise modulation within the MESFET. However, the use of this correlation matrix under large-signal conditions is of questionable validity since it was derived under the assumption of linear operation. Statz's FET noise model has also been found to be in poor agreement with noise measurements on modern microwave MESFETs [24]. In addition, it is implicitly implied in Rizzoli's analysis that all of the noise sources within MESFETs are amplitude modulated and that no phase modulation occurs. A more in-depth analysis is required to verify this assumption. The modulation of flicker noise was not considered in Rizzoli's analysis.

It appears that no analysis of noise source modulation in homojunction bipolar transistors or HBTs has ever been reported. This is not really surprising since it is well known that MESFETs may be used to achieve superior mixer performance by virtue of their square law properties. A general approach which may be used to analyze noise source modulation in transistors and HBTs is developed in Section 7 of this paper.

2. REVIEW OF RELATED TOPICS

2.1. Statistical Properties of Noise

Every current or voltage within a given electrical circuit can be viewed as consisting of a deterministic signal and of noise. Electrical noise is a random process, and as such cannot be described in a deterministic sense. Thus, a mathematical expression cannot be written which gives an exact future value of a noisy electrical signal even if all of the properties of the signal are known. However, a given noisy signal can be described in terms of statistical parameters. These statistical parameters have physical significance and can be used to describe the electrical properties of noise. In this section, some of the more significant statistical parameters of noise are reviewed. The parameters are discussed in terms of a noisy current signal. However, this discussion is also valid for voltage signals. The three most common types of electronic noise are thermal noise, shot noise, and flicker noise. Each of these types of noise is discussed in subsequent sections.

One of the most significant expressions which can be used to describe a noisy current, i, is the probability density function, p(i). This function gives the probability that the current will lie in an interval between i and i+di. From its definition, it is obvious, that the probability density function must be nonnegative and, since a given current must have some real value, its integral over all values of current must equal unity.

$$\int_{-\infty}^{\infty} p(i)\, di = 1. \tag{2.1}$$

In simple terms, the probability density function is greatest for values which the current, i, is most likely to have.

The most common sources of electrical noise have a probability density function which is Gaussian. This means that the probability density function of nearly all electrical currents can be described by Equation 2.2 [25].

$$p(i) = \frac{1}{\sqrt{2\pi\sigma^2}} \exp\left[-\frac{(i - \bar{i})^2}{2\sigma^2}\right]. \tag{2.2}$$

In Equation 2.2, $\bar{i}$ is the average current, and σ is the standard deviation at which the actual current varies from this nominal value. When a current or voltage in an electronic circuit is being described, what is usually being referred to is its nominal value. The standard deviation, σ, gives a measure of how noisy a given signal is and is equal to the rms value of the noise. Therefore, the current described by Equation 2.2 has a nominal value of $\bar{i}$ and the noise associated with this current, i_n, has an rms value of σ.

Several other parameters associated with a given noisy signal can also be determined from the probability density function. For example, the expectation value of a given function, f(i), can be calculated from the probability density function. The expectation value of a function gives the average value of that function and can be calculated from Equation 2.3 [25].

$$E[f(i)] = \int_{-\infty}^{\infty} f(i)\, p(i)\, di \tag{2.3}$$

From Equations 2.2 and 2.3, the expectation values given below can be derived.

$$E[i] = \bar{i} \tag{2.4a}$$

$$E[i^2] = \bar{i}^2 + \sigma^2 \tag{2.4b}$$

$$E[(i - \bar{i})^2] = \sigma^2 \tag{2.4c}$$

The above results all have physical interpretations. For example, Equation 2.4b indicates that the total power dissipated in a 1 Ω resistor is equal to the power dissipated by the average current through the resistor plus the power dissipated due to the noise current through the resistor.

Probably the most significant expectation value for circuit analysis is the autocorrelation function, $R_i(\tau)$, of a signal. The autocorrelation function of a given current noise is defined as [26]:

$$R_i(\tau) = E[i(t)\, i(t + \tau)]. \tag{2.5}$$

The autocorrelation function gives an indication of how closely related a random signal is to its value at some future point in time. For example, if a noise source has an

autocorrelation function which is nearly equal to σ^2 for values of τ less than 1 second, then the noise will typically not vary significantly over a period of 1 second. Thus, the probability density function of a random signal determines the probability that the signal will have given value, while the autocorrelation function indicates how quickly the signal can vary from this value.

Since the autocorrelation function indicates how quickly a random signal can vary, it seems likely that it should also contain information about the frequency spectrum of the signal. (Any signal which varies quickly with time must contain high frequency components while those signals which vary slowly consist primarily of low frequency components.) This is indeed the case. The autocorrelation function of a current, i, and its power spectral density, $S_i(f)$, are related by the Fourier transform [26].

$$S_i(f) = \mathcal{F}\{R_i(\tau)\} \tag{2.6}$$

The power spectral density of a given current noise is defined as the expectation value of the square of the current noise per unit frequency and has units of A^2/Hz. Thus, this parameter represents a measure of how much power would be supplied by a given noise source per unit frequency to a 1 Ω resistor. While there are many other statistical parameters associated with a given noise source, the power spectral density and rms value of the noise source are the parameters which are most often of use in circuit analysis.

2.2. Thermal Noise

Thermal noise can be visualized as free electrons interacting with thermally agitated molecules in a resistive material. (Thermal noise is also referred to in literature as Johnson or Brownian noise.) As an electron interacts with thermally agitated molecules it will accelerate and generate time varying electric and magnetic fields. The time varying fields affect the motion of the other electrons resulting in a chaotic motion of all of the electrons in the material. This random motion of electrons results in a random time varying potential at the terminals of the conductor.

The effect of thermal noise in electronic circuits was first observed in a vacuum tube amplifier by J. B. Johnson at Bell Telephone Laboratories in 1927. One year later, H.

Nyquist published a quantitative theoretical treatment of thermal noise [27]. This theoretical work of Nyquist may be combined with Plank's expression for black body radiation to give the rms value of the thermal noise current appearing across an open circuit resistor as [25],

$$\sqrt{\overline{i_n^2}} = \sqrt{4\,g\,\Delta f \frac{h\,f}{e^{h\,f/k\,T} - 1}}\,. \tag{2.7}$$

In the above expression, h is Plank's constant, k is Boltzman's constant, T is the absolute temperature, g is the conductance of the resistor, f is the frequency, and Δf is the bandwidth. By applying a infinite series expansion to the exponential term in the above equation, it can be shown that if f/T is less that 1 GHz/°K then Equation 2.7 may be approximated as,

$$\sqrt{\overline{i_n^2}} = \sqrt{4\,k\,T\,g\,\Delta f}\,. \tag{2.8}$$

Since for most practical circuits, f/T will be less than 1 GHz/°K, Equation 2.8 will be used throughout the rest of this paper. Equation 2.7 is of important theoretical significance, however, since Equation 2.8 would indicate that the total thermal noise power which is available from a resistor is infinite. This result is obviously invalid and Equation 2.7 may be used to prove that that the total thermal noise power which is available from a resistor is finite [25]. Equation 2.8 indicates that the power spectral density of a thermal current noise source may be expressed as,

$$S_I(f) = 4\,k\,T\,g. \tag{2.9}$$

For an arbitrary linear n-port network, all of the noise sources within the network may be modeled as a current source in parallel with each port as shown in Figure 2.1. In general, these noise sources will be partially correlated. If the linear network is passive, and all of the noise sources are due to thermal noise, then the correlation between any two noise sources at the external ports is given by [28]

$$\langle i_j\, i_k \rangle = 4\,k\,T\,\mathrm{Re}(y_{jk}) \tag{2.10}$$

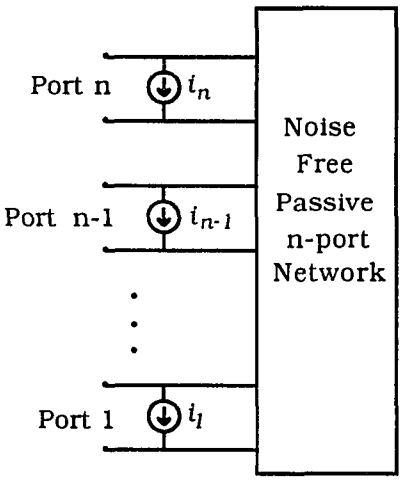

Figure 2.1. Equivalent circuit for a Passive Linear One-Port Network

where i_k is the current noise across port k, and y_{jk} is a y-parameter of the passive n-port network. Using this representation, the thermal noise within any passive linear network can be modelled.

2.3. Shot Noise

Shot noise is generated when current flows across a potential barrier such as a space charge region in a semiconductor. Current flow is created by a sequence of electrons or holes traveling across a region at random points in time. Each electron or hole generates a pulse of current as it travels across the potential barrier. This may be described mathematically by the expression

$$i(t) = \sum_m a_m f(t-t_m) \tag{2.11}$$

where a_m is the amplitude of the mth pulse, t_m is the point in time when the mth pulse occurs, and f is a function which describes the shape of the current pulse due to the transition of a single carrier. The power spectral density of this random sequence of current pulses may be determined by applying Carson's theorem [29] to Equation 2.11.

Carson's theorem applies to any pulse train where each pulse occurs at a random point in time and is independent of when any other pulse occurs. Carson's theorem is given by Equation 2.12.

$$S_i(\omega) = 2\,\nu\,\overline{a^2}\,\left|\mathcal{F}(j\omega)\right|^2 \tag{2.12}$$

In Equation 2.12, $S_i(\omega)$ is the power spectral density of the current, ν is the average rate of the pulses, $\overline{a^2}$ is the mean square of the pulse amplitudes, and $\mathcal{F}(j\omega)$ is the Fourier transform of the pulse waveshape. For the case of current across a space charge region, the average rate of the current pulses is given by,

$$\nu = \frac{I}{q} \tag{2.13}$$

and the mean square of the pulse amplitudes is given by,

$$\overline{a^2} = q^2 \tag{2.14}$$

where q is the charge of an electron and I is the dc current flowing across the potential barrier. If the current pulses are short, then the shape of the pulses can be approximated by an impulse function. The Fourier transform of an impulse function is given by,

$$\mathcal{F}(j\omega) = 1. \tag{2.15}$$

Combining Equations 2.12 through 2.15, the power spectral density of shot noise may be expressed as,

$$S_i(f) = 2\,I\,q. \tag{2.16}$$

Integrating the above equation across all frequencies indicates that an infinite amount of noise power is available from any device exhibiting shot noise. This is obviously nonphysical. Equation 2.16 was derived by using an impulse function to describe the shape of a current pulse. In an actual device, such as a diode, the width of the current pulse is limited by the transit time of an electron across the junction. As a result, Equation 2.16 is only valid for frequencies whose period is significantly greater than the transit time. The power spectral density of the shot noise will roll off for frequencies whose period is much less than the transit time.

2.4. Flicker Noise

At low frequencies, flicker noise is the dominant type of noise generated in many devices. This type of noise is also referred to in literature by various other names including 1/f noise (pronounced "one-over-f noise"), excess noise, current noise, semiconductor noise, or contact noise. van der Ziel [30] found that in many devices, the power spectral density of flicker noise may be expressed as,

$$S(f) = C \frac{i_d^m}{f^n}. \tag{2.17}$$

In the above equation C is a constant which depends on the characteristics of the conductor, i_d is the current through the device, f is the frequency, m is a constant which is usually very close to 2, and n is a constant which can range from .6 to 1.5 for various devices. In general, it is found that the constant C will vary inversely with the size of the device. Field effect devices tend to exhibit some of the the highest levels of flicker noise [29]. Bipolar transistors also exhibit moderate levels of flicker noise with typical corner frequencies around 10 kHz. Flicker noise can also be found in most conductors and resistors, but at much lower levels than in active devices.

The physical origin of flicker noise is poorly understood. Both Buckingham [29] and van der Ziel [31] have provided detailed reviews of the theories associated with flicker noise. However, it is found that no single theory explains the cause of flicker noise in every device. As noted by Buckingham [29]:

> 1/f noise is an enigmatic phenomenon. In electronic devices it is almost invariably present, as has been known for many years, and yet its physical origin remains as obscure today as it has ever been. Numerous experimental and theoretical studies of 1/f noise have revealed its many-faceted and intractable character; and after all the effort that has been expended, there are few categorical statements that may be said about it.

Despite the large controversy surrounding flicker noise, it is generally accepted that flicker noise may be viewed as the modulation of current through a given device [31]. For example, consider a resistor which is driven by a dc current source as shown in Figure 2.2. The voltage across the resistor will vary as a function of time due to flicker noise. Since the current through the resistor is a constant, the only way in which the voltage across

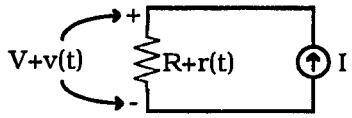

Figure 2.2. Resistor Connected to a Constant Current Source

the device can be time varying is if the resistance itself is time varying. This can be expressed mathematically from ohms law,

$$V + v(t) = I\,[R + r(t)]. \tag{2.18}$$

Since the time varying components of Equation 2.18 must be equal,

$$v(t) = I\,r(t). \tag{2.19}$$

Equation 2.19 requires that the power spectral density of the voltage and resistance fluctuations must be related by,

$$S_V(f) = I^2\,S_r(f). \tag{2.20}$$

From the above equation, since the voltage across the resistor has a flicker noise spectrum, the resistance fluctuations must also have a spectrum which is inversely proportional to frequency. This observation is supported by several experimental analyses [29]. One of the most novel and convincing analyses was performed by Voss and Clark [32]. In their analysis, the thermal noise voltage across a resistor was measured for a long period of time. It was found that the square of the thermal noise voltage varied with a flicker noise spectrum. Since the square of the thermal noise voltage is equal to a constant times the resistance, R, the only way it can vary with a flicker noise type of spectrum is if the resistance itself varies with a spectrum which is inversely proportional to frequency.

Equation 2.20 also leads to another interesting observation. If the power spectral density of the voltage across the resistor is proportional to the square of the current as indicated by Equation 2.17, the power spectral density of the resistance fluctuations must be independent of current. In other words, the fluctuations in the resistance modulate the voltage and the mechanism which causes these fluctuations is not a function of bias.

While the above approach is generally accepted as a valid analysis of flicker noise, there is a large amount of controversy regarding the mechanism which modulates the resistance. Two areas which are often debated are whether flicker noise is due to mechanisms associated with the surface or bulk of the semiconductor device, and whether it is a result of the modulation in the number of carriers, or in the mobility of the carriers in a given material. Flicker noise has been attributed to a wide range of mechanisms including thermal modulation effects, diffusivity fluctuations, trapping mechanisms with distributed time constants, and variations in surface recombination velocity [29]. In many devices, flicker noise is attributed to a combination of these mechanisms.

2.5. Basic Oscillator Theory

An ideal oscillator can be defined as an electronic circuit which produces a periodic output signal with no input or driving signal. Thus, when designing an oscillator, the goal is to produce an unstable circuit such that the poles of the circuit are in the right hand plane. For such a circuit, the output voltage will be an exponentially increasing oscillatory function. After the oscillations have built up to a sufficient level, the nonlinearities in the oscillator components will limit the amplitude and cause the oscillations to stabilize at a given level. Ideally, at this point the output of the oscillator would be perfectly periodic. However, a number of noise sources will exist in the components of the oscillator, and these noise sources will modulate both the amplitude and frequency of the output signal. A simplified analysis of these modulation effects is given in this section.

A block diagram of a feedback oscillator is shown in Figure 2.3. This type of oscillator consists of a forward gain stage with voltage gain $G(\omega)$ and a feedback circuit whose frequency response is given by $\beta(\omega)$. The voltage source, e_n, accounts for the noise sources which exist in the oscillator. In most feedback oscillators, the forward gain stage will be an amplifier with approximately constant gain near the frequency of oscillation and the feedback circuit will have a bandpass response. If the parameters of the amplifier and feedback circuit are chosen correctly, oscillations will build up in the circuit. Ideally, the signal out of the oscillator would be periodic. However, every real oscillator will be

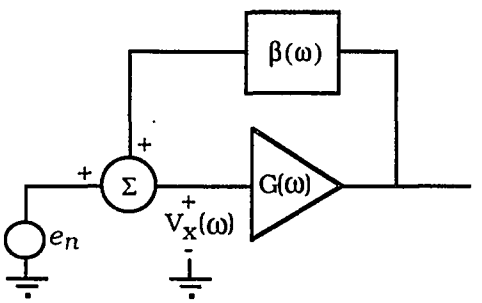

Figure 2.3. Feedback Oscillator Block Diagram

amplitude modulated and phase modulated by the noise sources which exist in the oscillator. The goal in most oscillator designs is to minimize this modulation.

In order to simplify the analysis of the oscillator in Figure 2.3, the circuitry is approximated as being linear and it is assumed that no impedance mismatches exist between the amplifier and feedback circuit. The voltage out of the oscillator is then equal to the voltage at the input of the amplifier stage times the gain of this stage,

$$V_{out}(\omega) = G(\omega)\, V_x(\omega) = G(\omega)\, [e_n + V_{out}(\omega)\, \beta(\omega)]. \tag{2.21}$$

Equation 2.21 can be simplified to

$$\frac{V_{out}(\omega)}{e_n} = \frac{G(\omega)}{1 - G(\omega)\, \beta(\omega)}. \tag{2.22}$$

When oscillations occur, the output voltage will be many orders of magnitude greater than the noise source, e_n. Therefore, the ratio on the right hand side of Equation 2.22 must be extremely large at the frequency of oscillation, and the denominator of this ratio must be approximately zero. As a result,

$$\left| G(\omega)\, \beta(\omega) \right| = 1 \tag{2.23}$$

$$\underline{/G(\omega)\, \beta(\omega)} = 2\, \pi\, n \tag{2.24}$$

Equations 2.23 and 2.24 are known as the Barkhausen or Nyquist criteria of oscillation [33]. Oscillations will occur at any frequency where the Barkhausen criteria are satisfied. In practice, the product of G(s) and β(s) is set to be greater than one under

small signal conditions in order to guarantee that oscillations will occur. Under this condition, oscillations will continually increase in magnitude until the nonlinearities of the oscillator limit the amplitude of the output signal. The amplitude of the oscillations will stabilize at the point where the large signal gain of the oscillator is equal to one.

If the amplifier stage is assumed to have a constant gain and the feedback circuit has a bandpass response then,

$$G(\omega) = A_v \tag{2.25}$$

$$\beta(\omega) = \frac{H_0 \frac{\omega_0}{Q} j\omega}{\omega_0^2 + \frac{\omega_0}{Q} j\omega - \omega^2} \tag{2.26}$$

From the above two Equations, it can be seen that in order to satisfy the Barkhausen criteria for oscillation, the frequency of oscillation must be ω_0 and

$$A_v H_0 = 1. \tag{2.27}$$

Combining Equations 2.22, 2.25, and 2.26, the ratio of the output voltage to the input noise voltage is given by

$$\frac{V_{out}(\omega)}{e_n} = \frac{A_v}{1 - A_v \frac{H_0 \frac{\omega_0}{Q} j\omega}{\omega_0^2 + \frac{\omega_0}{Q} j\omega - \omega^2}} = \frac{A_v \{\omega_0^2 + \frac{\omega_0}{Q} j\omega - \omega^2\}}{\omega_0^2 - \omega^2 + \frac{\omega_0}{Q}(1 - A_v H_0) j\omega} \tag{2.28}$$

Since ω_0 is the frequency of oscillation, if ω_m is the offset frequency from the carrier then,

$$\omega = \omega_0 + \omega_m \tag{2.29}$$

Combining Equations 2.27 through 2.29,

$$\frac{V_{out}(\omega)}{e_n} = \frac{A_v \{-2\omega_0 \omega_m - \omega_m^2 + j \frac{\omega_0}{Q}(\omega_0 + \omega_m)\}}{-2\omega_o \omega_m - \omega_m^2} \tag{2.30}$$

For frequencies near the carrier such that ω_m is much less than ω_0,

$$V_{out}(\omega) = e_n A_v \left(1 - j \frac{\omega_0}{2 Q \omega_m}\right) = e_n A_v \left(1 - j \frac{f_0}{2 Q f_m}\right) \tag{2.31}$$

Equation 2.31 gives the noise voltage at the output of the oscillator as a function of offset frequency. Note that this voltage will have a random phase angle with respect to the carrier. As a result, half of the sideband noise power will result in amplitude fluctuations and half will result in phase fluctuations. (See Figure 2.4.) The phase noise of a oscillator is often described quantitatively as single sideband phase noise, $\mathcal{L}(f_m)$. This quantity is defined as the ratio of the power spectral density in one phase modulated sideband to the power in the carrier [9]. From the above definition and Equation 2.31,

$$\mathcal{L}(f_m) = \frac{1}{C} \frac{|V_{out}(f_m)|^2}{2 R_{out}} = \frac{e_n^2 A_v^2}{2 R_{out} C} \left[1 + \left(\frac{f_0}{2 Q f_m}\right)^2\right] \tag{2.32}$$

where R_{out} is the output impedance of the amplifier stage, and C is the carrier power.

The value of e_n can be expressed in terms of the noise figure, F, of the amplifier stage. From the definition of noise figure, the equivalent noise voltage at the input of the amplifier is equal to the thermal noise of the source impedance times the square root of the noise figure. Since the impedance of the amplifier and the feedback circuit are matched, half of this noise voltage will appear across the amplifier. As a result,

$$e_n^2 = (.5)^2 F (4 k T R_{in}) = k T F R_{in} \tag{2.33}$$

$$\mathcal{L}(f_m) = \left\{A_v^2 \frac{R_{in}}{R_{out}}\right\} \frac{k T F}{2 C} \left[1 + \left(\frac{f_0}{2 Q f_m}\right)^2\right]. \tag{2.34}$$

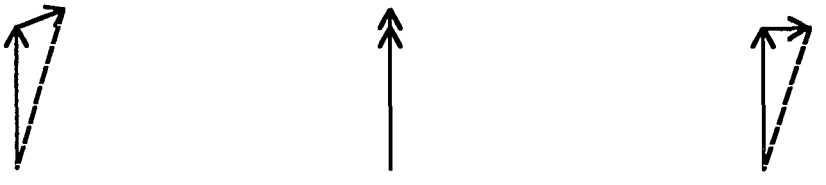

(a) Both AM and PM (b) AM (c) PM

Figure 2.4. Modulation of a Carrier Signal by an Uncorrelated Noise Source

Note that the first quantity on the right hand side of Equation 2.34 is simply the power gain, G, of the amplifier. Accordingly,

$$\mathcal{L}(f_m) = \frac{k\,T\,F\,G}{2\,C}\left[1 + \left(\frac{f0}{2\,Q\,fm}\right)2\right]. \tag{2.35}$$

Equation 2.35 gives the single sideband phase noise of the oscillator as a function of offset frequency. This equation will only be accurate if the parameters are valid under large signal conditions. The noise figure, F, is one of these parameters which must be valid under large signal conditions. The amplitude of the oscillations will affect the noise figure of the amplifier at the carrier frequency. In addition, any flicker noise which is present in the oscillator will tend to be converted to the frequency of oscillation due to circuit nonlinearities. The total noise figure is the sum of these two components as given by Equation 2.36.

$$F = F_c + \frac{F_L'}{f_m} \tag{2.36}$$

F_C is defined as the noise figure of the amplifier at the frequency of oscillation, and the second term accounts for the effects of flicker noise. The prime is used on the second term to indicate that it refers to the upconverted flicker noise at the frequency of oscillation rather than the low frequency flicker noise.

Combining Equations 2.35 and 2.36,

$$\mathcal{L}(f_m) = \frac{k\,T\,G}{2\,C}\left[\frac{F_L'\,f_0^2}{4\,Q^2\,f_m^3} + \frac{F_c\,f_o^2}{4\,Q^2\,f_m^2} + \frac{F_L'}{f_m} + F_c\right]. \tag{2.37}$$

Equation 2.37 shows the various effects which create oscillator phase noise and is essentially identical to the results given by Gerber and Ballato [9]. The last term in the quantity on the right side of Equation 2.37 refers to the phase noise which is generated by the addition of the amplifier noise to the carrier power. The feedback circuit has no effect on this term. Since the spectrum generated by this term is equivalent to the output spectrum of an oscillator phase modulated by white noise, this portion of the spectrum is referred to as white PM as shown in Figure 2.5. The second-to-last term is generated in an identical manner to white PM noise except that the added noise originates from the upconverted flicker noise. As a result, this portion of the spectrum is referred to as flicker

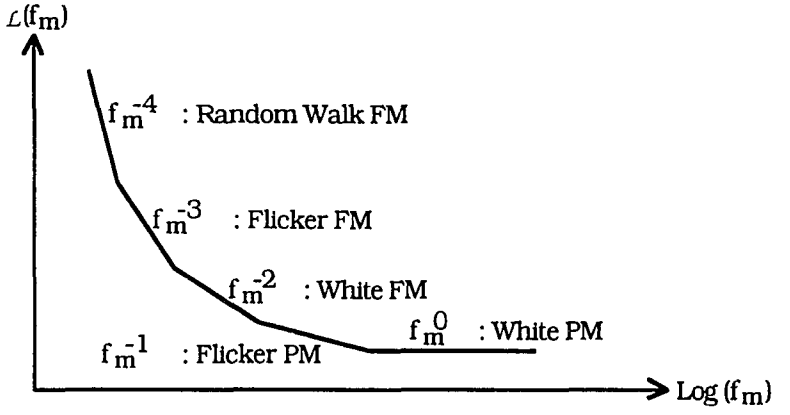

Figure 2.5. Oscillator Single Sideband Phase Noise Spectrum

PM and has a 3 dB-per-octave slope. The first two terms on the right side of Equation 2.37 refer to the portions of the output spectrum which are increased in power by the feedback effects of the oscillator. The first term originates from upconverted flicker noise which is within the bandwidth of the feedback network. Since the output spectrum associated with this term is identical to an oscillator output which is frequency modulated by flicker noise, this portion of the spectrum is referred to as flicker FM. The second term accounts for the effect of noise generated near the frequency of oscillation which is within the feedback bandwidth of the oscillator. This component is referred to as white FM. Many oscillators also contain a phase noise spectral component which exhibits a 12 dB-per-octave slope at frequencies very close to the frequency of oscillation. This spectral component is referred to as random walk FM. The physical cause of this type of noise is poorly understood.

Equation 2.37 indicates several methods for reducing the phase noise of an oscillator. The saturation level of the amplifier should be kept at the highest possible level thus maximizing the carrier power, C. The power gain of the amplifier, G, can be reduced by keeping the losses in the feedback circuit to a minimum. These two effect will reduce all of the spectral components shown in Figure 2.5. The white FM and flicker FM components may also be reduced by increasing the loaded Q of the oscillator. A more general expression of this quantity for any feedback oscillator is given by Equation 2.38 [34]. The spectral components associated with the flicker noise may also be reduced by minimizing the amount of flicker noise which is upconverted. This may be accomplished

by using dc biasing techniques which keep the amplitude of the low frequency flicker noise to a minimum. Selecting large active devices generally tends to reduce the level of flicker noise present. The flicker noise upconversion process should also be minimized. (Details on how to analyze the upconversion process are also given in Sections 5 and 7.)

$$Q = \frac{f_0}{2} \left. \frac{\delta / G(s)\, \beta(s)}{\delta f} \right|_{f = f_0} \tag{2.38}$$

2.6. Heterojunction Bipolar Transistors

Significant interest in heterojunction bipolar transistors has been shown in recent years. They have achieved cutoff frequencies as high as 165 GHz [35] and show a significant improvement in high frequency noise performance over conventional bipolar transistors. In addition, these devices show much lower levels of flicker noise than field effect transistor devices. As a result of their high cutoff frequencies and low flicker noise levels, HBTs have found increasing applications in oscillator design. Accordingly, the basic operation of a conventional GaAs/AlGaAs single heterojunction HBT is discussed in this section. (This device is based on the the results reported by Asbeck [36].) Double heterojunction HBTs have been produced, but they typically show no improvement in performance levels, and are more costly to fabricate. HBTs on InP and Si substrates are also of current interest, but are not considered here.

A cross sectional view of a GaAs/AlGaAs HBT is shown in Figure 2.6. The device in this figure is representative of a typical HBT. It consists of several semiconductor layers which are normally grown using MBE or MOCVD. Typical doping levels and layer thicknesses for this structure are given in Table 2.1. The first layer which is grown on a semi-insulating GaAs substrate is the collector contact layer. This GaAs layer is heavily doped n-type and is used to minimize the collector contact resistance and spreading resistance. The ohmic contacts for the collector are formed directly on this layer. On top of the collector contact layer is the collector layer. This GaAs layer is more lightly doped than the collector contact layer. A very thin base layer is then grown on the collector layer and is very heavily doped. In most HBTs, this base layer is doped more heavily than the emitter which is in sharp contrast to a conventional transistor. The base layer also consists of GaAs material and the ohmic contacts for the base are fabricated directly on

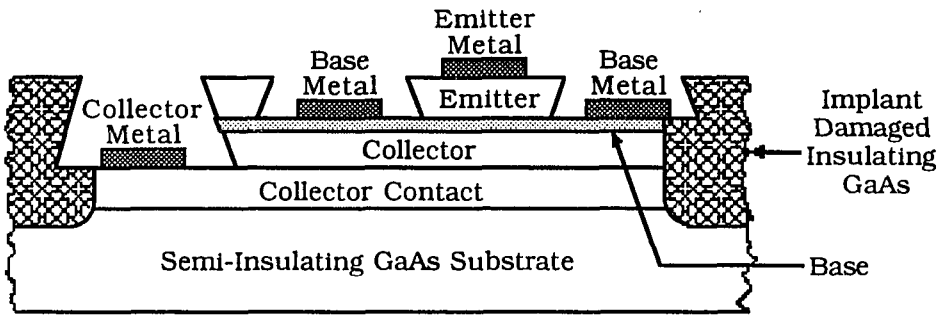

Figure 2.6. Cross Sectional View of a GaAlAs/GaAs HBT [36]

this layer. An AlGaAs emitter layer is then grown on top of the base layer to form a heterojunction at the base-emitter interface. It is this heterojunction which is used to produce the increased performance of the HBT device. The mechanisms which allow for this increased performance are discussed in the latter portion of this section. Finally, an n^+ contact layer is formed on top of the emitter layer. As the name implies, this layer is used to allow the formation of a low resistance ohmic contact to the emitter region.

The cause of the increased performance of HBTs as compared to conventional BJTs can be understood by considering the energy band diagram in Figure 2.7. This energy band diagram is valid for HBTs with graded base-emitter junctions. As shown in the figure, the bandgap of AlGaAs is wider than that of GaAs. For a typical Al mole fraction of 0.3, the bandgap of the emitter is 0.374 eV greater than the bandgap of the base [36]. Thus, the potential barrier which the electrons have to overcome to diffuse into the base is 0.374 eV less than the potential barrier which the holes must overcome to diffuse from the base

Table 2.1. Layer structure and doping levels for a AlGaAs/GaAs HBT

Layer	Composition	Thickness (Å)	Doping (cm^{-3})
Contact	n^+ GaAs	750	1×10^{19}
Emitter	n^- $Al_{.3}Ga_{.7}As$	2500	5×10^{17}
Base	p^+ GaAs	500 - 1000	5×10^{18} - 1×10^{20}
Collector	n^- GaAs	5000	3×10^{16}
Contact	n^+ GaAs	6000	4×10^{18}

into the emitter. As a result, the diffusion of holes from the base into the emitter is negligible. For GaAs/AlGaAs HBTs the ratio of electron diffusion current to hole diffusion current, which is defined as the diffusion current gain, is given approximately by Equation 2.39 [37].

$$\beta_d \cong 5\frac{N_E}{N_B}\exp\left[\frac{\Delta E_g}{k\,T}\right] \tag{2.39}$$

In the above equation, N_E is the dopant level in the emitter, and N_B is the dopant level in the base. Thus, for a bandgap difference of .374 eV, the heterojunction enhances the diffusion current gain by roughly 10^6. This dramatic increase is due to the fact that the diffusion of holes from the base is blocked by the heterojunction. Since the diffusion current is blocked, various forms of recombination current dominate the base current.

The various components of the currents in transistors and HBTs are shown in Figure 2.8 [37]. The base current is a result of holes injected from the base towards the emitter region. As the holes leave the base region, some recombine with the electrons in the base-emitter depletion region giving rise to the recombination current I_{rd}. The remaining holes diffuse into the emitter resulting in the current I_{pe}. In a conventional transistor diffusion current is the dominant portion of the base current for most bias conditions in the active region. However, in HBTs, the diffusion current is blocked and the recombination current is the dominant component of the base current. As a result, the overall current gain of a HBT is usually limited by the recombination current in the base-emitter depletion region and the current gain will normally not improve by more

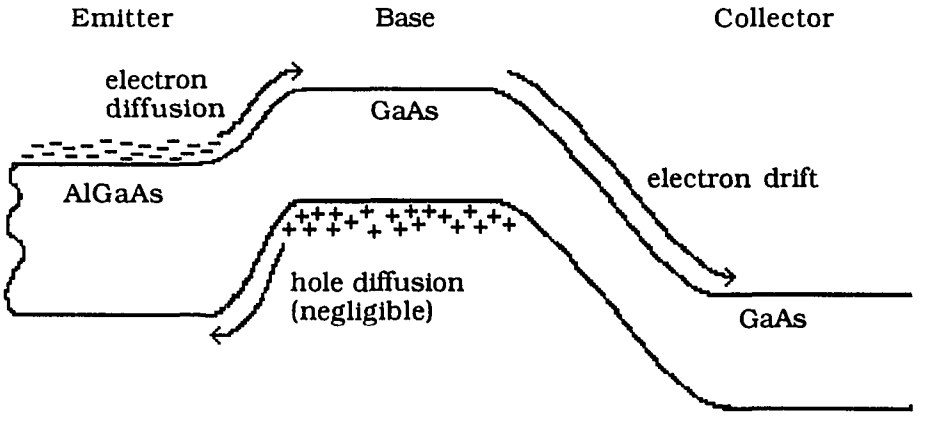

Figure 2.7. Energy Band Diagram of a AlGaAs/GaAs HBT

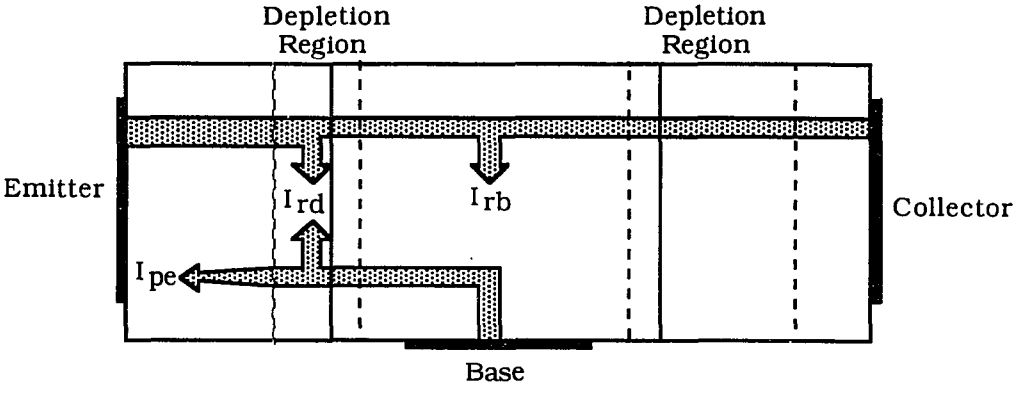

Figure 2.8. Components of Current flow in a GaAlAs/GaAs HBT

than a factor of 10 over a conventional BJT. However, by making some design tradeoffs, the high frequency performance of HBTs can be dramatically improved.

As indicated by Equation 2.39, a tradeoff can be made between the doping levels of the base and emitter regions and the bandgap of the HBT. Due to the effects of the exponential term in this equation, the base can actually be doped more heavily than the emitter region while maintaining a high diffusion current gain. Heavy doping of the base region has several advantages. The base resistance is minimized which increases the cutoff frequency and reduces the noise figure of the device. In addition, current crowding effects in the base region are normally reduced to a negligible level. Since the base resistance is greatly reduced, the thickness of the base region can also be reduced. Reducing the thickness of this layer greatly reduces the forward transit time in the base region. This reduction in the forward transit time is the most significant factor in increasing the cutoff frequency of HBTs as compared to conventional BJTs. Thus by increasing the doping in the base region and reducing the thickness of this region, the high frequency performance and noise characteristics of HBTs can be greatly improved over those of BJTs.

3. DISCUSSION OF ANALYSIS APPROACH

In Section 2.5, a simplified oscillator analysis was given. In this analysis, some of the mechanisms which effect the noise characteristics of oscillators were discussed. It was shown that the nonlinearities of the circuit effect the upconversion of flicker noise. Several other phenomenon should also be modelled in an accurate oscillator analysis. The mechanisms which create AM-to-PM and PM-to-AM effects in oscillators should be considered. Any general analysis approach should not require assumptions regarding the topology of the circuit, or the sinusoidal nature of the waveforms within the circuit. In addition, a general approach should allow for more elaborate oscillator designs such as the incorporation of automatic gain control or limiters in the circuit as well as nonlinear load impedances. Perhaps one of the most significant considerations in an oscillator model is the analysis of noise source modulation. This has been found to be a very significant effect in microwave mixers [17]. However, to the authors knowledge, no in-depth analysis of this phenomenon in oscillators has previously been reported. In this paper, an oscillator analysis is given which can be used to model all of the mechanisms discussed above. An overview of this analysis is given in this section, and a discussion of the advantages of this approach as compared to more straight forward techniques is also provided.

The analysis approach selected for this research has significant advantages over those discussed in Section 1.3. Many of the analyses reviewed in this section require assumptions regarding the topology of the circuit. Only a few of these implement an in-depth analysis of the frequency conversion effects which are due to circuit nonlinearities. Most of these analyses are not compatible with numerical optimization techniques. Even more significantly, the modulation of noise sources is ignored in all of these analyses. The approach considered in this paper overcomes these disadvantages.

Another approach to analyzing the noise characteristics of oscillators, which has been suggested to the author on numerous occasion, is to use a time domain simulator, such as a transient analysis in SPICE. The noise sources within the oscillator could be included in the simulation and the time domain waveform out of the oscillator generated. By applying a Fourier transform to the output waveform the noise spectrum of the oscillator could be observed. This analysis approach was actually attempted by Bunting

et al. [38]. However, this approach has several limitations which render it impractical. For example, consider a 1 GHz oscillator which has flicker noise sources present. In order to observe the oscillator output spectrum at offset frequencies of 1 kHz or greater, the oscillator must be simulated for roughly 1 ms which corresponds to a simulation over 1,000,000 cycles of oscillation. This obviously requires very long simulation times. Bunting et al. also found that several difficulties were also associated with performing a discrete Fourier transform on the simulated data. Finally, it should be noted that an optimization of the noise performance of the oscillator is not possible with this approach since the long transient analysis and discrete Fourier transform would have to be performed for each optimization step.

An overview of the analysis approach discussed in this paper is shown in Figure 3.1. This approach could potentially be used to perform a numerical optimization of the noise performance of oscillators. It can be viewed as two interrelated analyses. One of these analyses is associated with the nonlinear circuit characteristics of the oscillator and is shown in the left column of Figure 3.1. The other accounts for noise source modulation effects and is shown in the right column of Figure 3.1. The results of these two analyses may be combined to determine the overall noise characteristics of the oscillator.

The first step in analyzing the nonlinear circuit characteristics is to generate a large signal model for each of the components in the oscillator. In this research, the only nonlinear component which is considered is a HBT. The HBT model which is developed is based largely on the Gummel-Poon transistor model. However, it is shown that the Gummel-Poon model does not accurately characterize the base-emitter diffusion capacitance in HBTs. A new model for the base-emitter diffusion capacitance has been developed by the author [39] and is discussed in Section 4.1.

Once a large signal model for each component has been generated, a large signal oscillator simulation can be performed. This simulation is used to model the voltage and current waveforms that would occur in the oscillator in the absence of any noise sources. Thus, it models the nominal (average) waveforms which exist in the actual oscillator circuit. This simulation can be implemented using a time domain simulator such as SPICE or a harmonic balance simulator such as LIBRA. However, the use of a harmonic balance simulator would be required if the noise characteristics of the oscillator were to

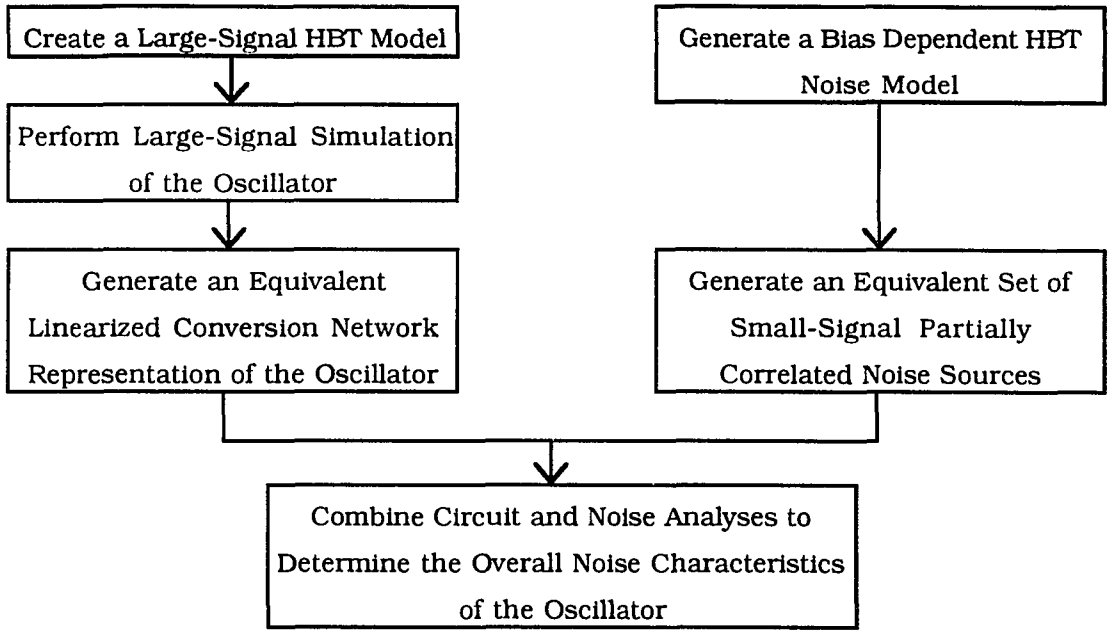

Figure 3.1. Block Diagram of the Proposed Approach

be optimized. The basic operation of harmonic balance simulators is discussed in Appendix A.

The results of the large signal simulation can be used to generate an equivalent linear circuit representation of the oscillator. This equivalent circuit is based on conversion network theory and is discussed in Section 5. It models the frequency conversion of all of the noise within the oscillator which results from circuit nonlinearities. Basically, the large signal simulation models the noise-free characteristics of the oscillator, and the conversion matrix representation models how the noise sources perturb the oscillations from this ideal noise free condition.

In addition to analyzing the circuit nonlinearities, the noise characteristics of each of the components within the oscillator must be considered. This is represented by the box in the upper right-hand corner of Figure 3.1. In this research, the noise sources within HBT's and those due to losses in the resonator circuit are considered. These noise sources are due to shot noise, thermal noise, and flicker noise. The models for these noise sources, which must be valid under large signal conditions, are developed in Section 6.

Once the noise source models have been developed, the modulation of these noise sources can be analyzed. This analysis is performed in Section 7. The noise sources within a given oscillator, which are functions of currents or voltages, will vary as a periodic function of time. This periodic variation contributes to the frequency conversion of noise between the various oscillator sidebands. No rigorous analysis of frequency conversion due to noise source modulation in an oscillator has been reported. Some work has been completed in regard to noise source modulation in diode and MESFET mixers [17, 23]. However, these analyses do not include the effects of 1/f noise source modulation. The theory required to analyze the modulation of 1/f noise sources is also developed in Section 7.1.

The results of the noise source modulation analysis are then combined with results of the conversion matrix analysis and the overall noise characteristics of the oscillator can determined. Both the amplitude and phase noise spectrums can be modelled from this analysis. In addition, the significance of the individual noise sources in the oscillator can be determined. These results are presented in Sections 7.2 and 7.3.

There are numerous advantages to the analysis approach discussed above. It accounts for all of the dominant mechanisms which effect the noise characteristics of oscillators. No assumptions are required in terms of the circuit topology, and any number of nonlinear devices can be included in the circuit. Thus, more complex topologies which incorporate automatic gain control or limiters in the circuit can be analyzed. No assumptions are required in regard to the sinusiodal nature of the waveforms or the termination of the signals at higher frequencies. The modulation of noise sources within the oscillator are also considered in this approach. No previously reported oscillator analysis accounts for these complex modulation effects. Finally, the analysis discussed here is compatible with current harmonic balance algorithms. As a result, this approach could potentially be used to numerically optimize the noise characteristics of oscillators.

One approach which could be used to optimize the noise characteristics of an oscillator is shown in Figure 3.2. The large signal characteristics of the oscillator are first established by using an harmonic balance algorithm. The conversion matrix representation of the oscillator is established from the large signal results. Noise source

modulation effects can then be analyzed and the overall noise characteristics of the oscillator can be modelled. If the noise characteristics meet the required performance levels, the the optimization is complete. Otherwise, various circuit parameters in the oscillator can be adjusted and the optimization process repeated.

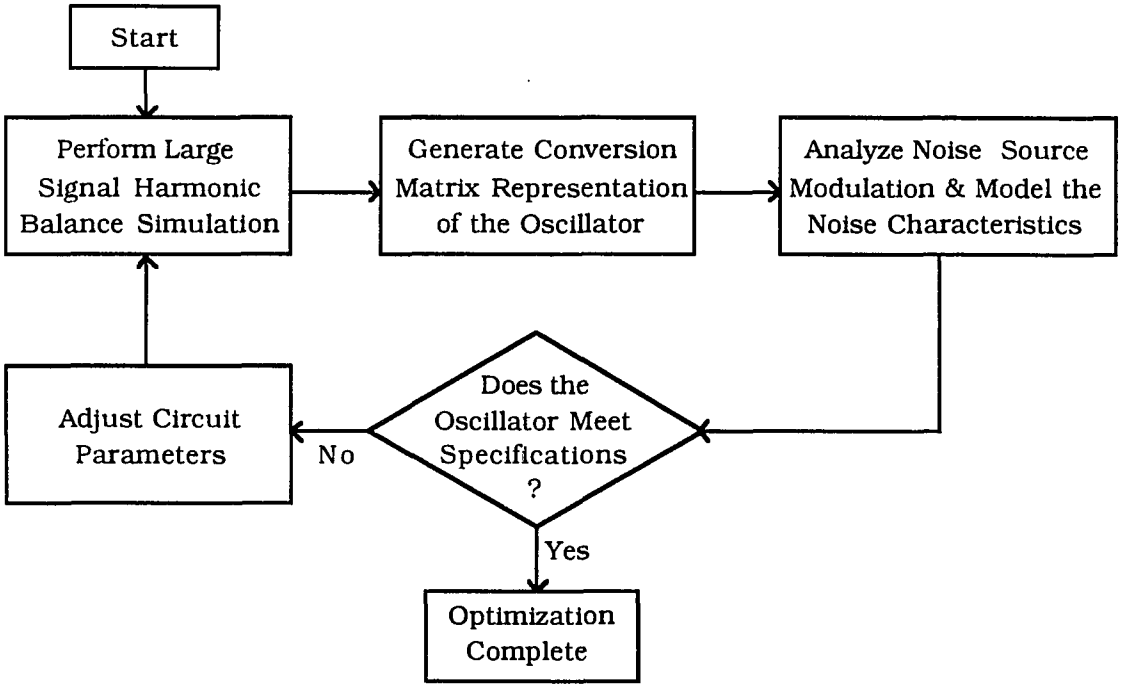

Figure 3.2. Block Diagram for Optimization of Oscillator Noise Characteristics

4. LARGE SIGNAL MODELS

4.1. Large Signal HBT Model

In this research the noise characteristics of HBT oscillators are considered. In order to accurately analyze the frequency conversion of noise due to circuit nonlinearities, a large signal HBT model must be generated. The HBT model which has been generated for this research is based on the Gummel-Poon transistor model [40]. This model was originally derived by analyzing homojunction transistors. However, the use of the Gummel-Poon model for HBTs is supported by both theoretical analyses [41, 42] and experimental results [43, 44, 45]. Accordingly, the Gummel-Poon model as implemented in SPICE [46] and other circuit simulators, is used in this research with one significant exception. As a result of the variation in forward transit time with respect to collector current in HBTs, the base-emitter diffusion capacitance cannot be accurately modeled by the Gummel-Poon model as implemented in SPICE. A new model for this diffusion capacitance was developed in this research. Details of this new base-emitter diffusion capacitance model have previously been documented by the author [39] and are also discussed in a latter portion of this section.

The theoretical derivation of the Gummel-Poon model has previously been reported in detail [40, 47] and accordingly, is not discussed in this paper. Rather, the extraction of the various Gummel-Poon model parameter values from experimental measurements is discussed. The relationships between these parameter values and the physical mechanisms which determine current flow in HBTs are also discussed. In order to demonstrate the parameter extraction process, a single HBT device which has been fabricated on a 25 mil thick GaAs substrate is characterized. The HBT device is connected to bondpads such that cascade probes can be used to make electrical connection in a 50 Ω system.

The generation of the large-signal HBT model was initiated by measuring the thermal resistance of the GaAs substrate based on a procedure developed by Adlerstein [48]. The steps which were used to measure the thermal impedance are summarized as follows: (1) The HBT MMIC was mounted on a Cascade-Microtech Model 42 probe station. This probe station was modified such that the backside temperature of the MMIC could be

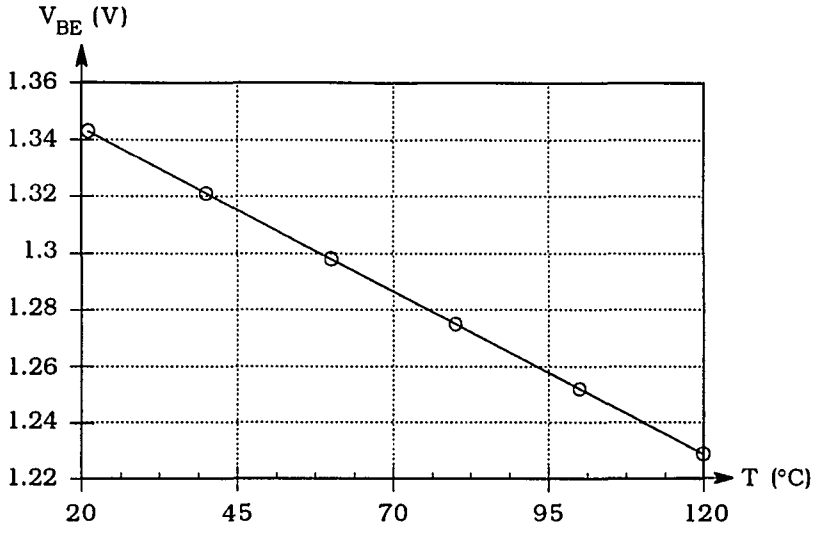

Figure 4.1. Measured Base-Emitter Voltage as a Function of Back-Plate Temperature

adjusted. (2) The values of V_{BE} required to maintain I_C at 3 mA with V_{CE} set to 4.85 V were recorded for various back-plate temperatures. These data are plotted in Figure 4.1. (3) A function generator, 50 Ω load resistor, and oscilloscope were connected to the HBT as shown in Figure 4.2a. Ferrite beads were placed at the ends of the scope probes in order to keep the HBT from oscillating at higher frequencies. (4) The back-plate temperature was then held at 20 °C and a pulsed voltage was applied across the base-emitter junction as indicated by Figure 4.2b. The width of the pulsed signal was kept much shorter than the thermal time constant of the MMIC substrate. For a typical HBT device, the thermal time

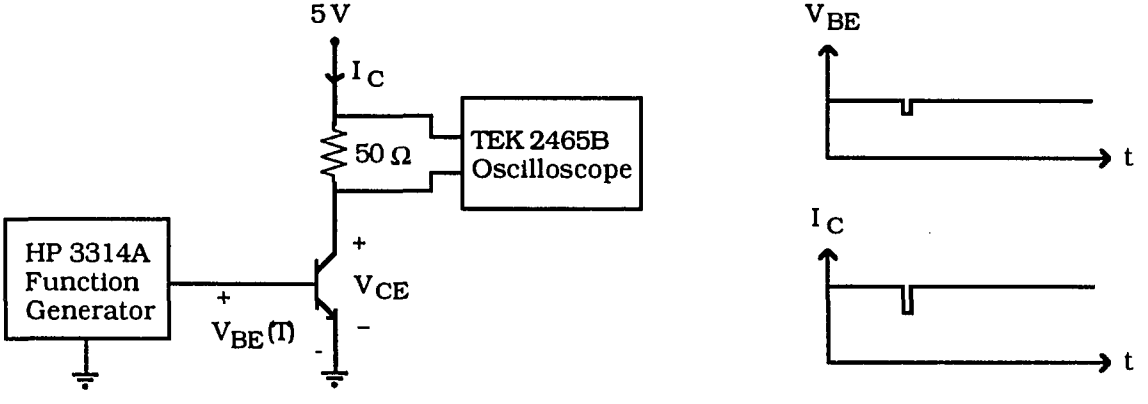

(a) Measurement Schematic (b) Signal Waveforms

Figure 4.2. Circuit Topology and Signal Waveforms for Thermal Impedance Measurement

constant of the GaAs substrate is on the order of 1 μs [48]. Accordingly, the pulse width was set to 20 ns for this research. (5) The collector current for the test setup in Figure 4.2 was monitored by measuring the voltage across the 50 Ω load resistor and the base-emitter voltage was adjusted to achieve a collector current of 3 mA during the narrow portion of the pulse. (6) The HBT terminal voltages and currents were then measured during both the narrow and wide portions of the pulsed signal. This data set was then used to determine the thermal impedance of the MMIC substrate as discussed below.

Note that the values of I_C and V_{CE} during the narrow portion of the pulse are identical to those which were used when Figure 4.1 was generated. Thus the value of V_{BE} during the narrow portion of the pulse can be used in conjunction with Figure 4.1 to determine the average temperature of the HBT. Since the average power dissipated in the HBT can be calculated from the measured currents and voltages, the thermal impedance of the MMIC substrate can be determined from this data set [48].

The procedure described above was used to generate a plot of the device to back-plate temperature as a function of power dissipation as shown in Figure 4.3. The open circle symbols in this figure represent measured data points and the curve represents a second order polynomial curve fit of these data which is given by Equation 4.1.

$$\Delta T = 507.9\, P_{diss} + 2130\, P_{diss}^2 \qquad (4.1)$$

In the above equation, ΔT is given in °K and P_{diss} is given in watts. Equation 4.1 demonstrates that the temperature change across the substrate is not a linear function of power dissipation. This occurs because the thermal impedance of GaAs increases with temperature. It is also significant to note that the general characteristics of the curves in Figures 4.1 and 4.3 are in good agreement with those obtained by Adlerstein [48]. Equation 4.1 was used throughout this research to estimate the temperature change across the MMIC substrate. All of the subsequent measurements reported in this section were taken with the back-plate temperature adjusted such that the HBT device temperature was maintained at 40 °C. By maintaining a constant HBT device temperature, the accuracy of the Gummel-Poon parameter extraction process is improved.

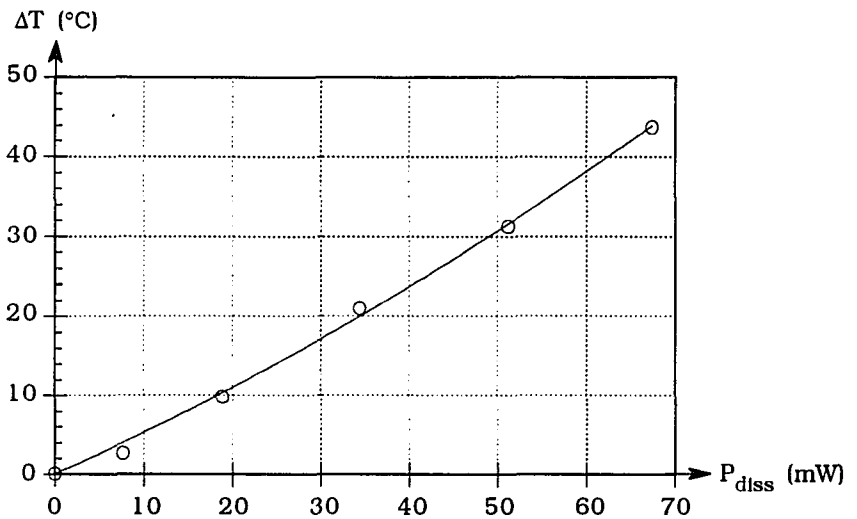

Figure 4.3. HBT-to-Back-Plate Temperature Change Versus Device Power Dissipation

Once the thermal impedance of the HBT substrate is measured, the Gummel-Poon model parameters may be extracted. A schematic diagram of the Gummel-Poon model is shown in Figure 4.4. This diagram also includes elements which model the interconnect parasitics associated with the metalization on the top surface of the MMIC. The standard Gummel-Poon model consists of the elements which are inside of the dashed box. The remaining parasitic element values were extracted based on layout geometries using the the microwave simulation program LIBRA™ [49].

Equations 4.2 through 4.13 are the nonlinear expressions which constitute the Gummel-Poon model for an NPN transistor as implemented in SPICE [46]. It should be noted that the bias dependence of the base resistance and forward transit time are not modelled by these equations. The base resistance in HBTs may be accurately modelled as a constant resistance. The current crowding effects which cause the base resistance of conventional transistors to be bias dependant, are negligible in HBTs due to the heavy base doping [44]. It is also shown in this research, that the Gummel-Poon model as implemented in SPICE does not accurately characterize the forward transit time in HBTs. Accordingly, a new model is described in the latter portions of this section which accurately characterizes the forward transit time in HBTs. Equations 4.2 through 4.12 may be used to accurately model the characteristics of HBTs and will be used in the remainder of this paper. (Equation 4.13 does not accurately describe the base-emitter

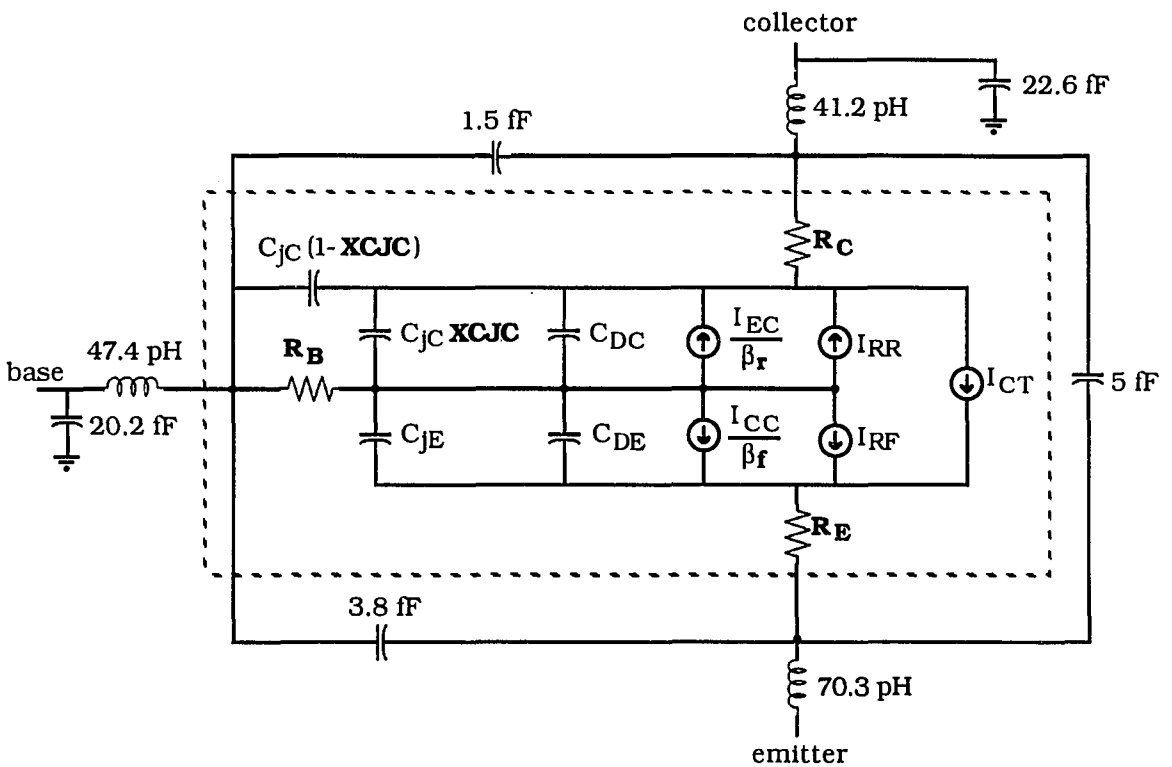

Figure 4.4. Gummel-Poon Transistor Model Including Interconnect Parasitics

diffusion capacitance in HBTs. A new base-emitter diffusion capacitance model which is valid for HBTs is developed in this section.) The physical mechanisms which Equations 4.2 through 4.13 describe are summarized in the following paragraphs. The model parameters given in these equations are summarized in Table 4.1.

At this point, a few comments regarding the notation which has been used in Figure 4.4 and Equations 4.2 through 4.13 is in order. Any variable which is a SPICE model parameter is given in bold font for easy identification. The variables V_{BE} and V_{BC} refer to the voltages across the intrinsic HBT device, while the variables V_{BE} and V_{BC} refer to the terminal voltages. (i. e. V_{BE} refers to the voltage across C_{DE} and V_{BC} refers to the voltage across C_{DC}.) This notation for the HBT junction voltages is used throughout this paper. With this notation in mind, the physical mechanisms associated with each equation is described below.

Equations 4.3 and 4.4 describe the current which flows from the collector to the emitter due to the diffusion of electrons across the base-emitter and base-collector

junctions respectively. These equations are related to the current source I_{CT} shown in Figure 4.4 through Equation 4.2. The current sources I_{EC}/β_r and I_{CC}/β_f model the

$$I_{CT} = I_{CC} - I_{EC} \tag{4.2}$$

$$I_{CC} = \frac{\mathbf{I_S}}{q_b}\left(e^{(q\,V_{BE}/\mathbf{N_F}\,k\,T)} - 1\right) \tag{4.3}$$

$$I_{EC} = \frac{\mathbf{I_S}}{q_b}\left(e^{(q\,V_{BC}/\mathbf{N_R}\,k\,T)} - 1\right) \tag{4.4}$$

$$I_{RF} = \mathbf{I_{SE}}\left(e^{(q\,V_{BE}/\mathbf{N_E}\,k\,T)} - 1\right) \tag{4.5}$$

$$I_{RR} = \mathbf{I_{SC}}\left(e^{(q\,V_{BC}/\mathbf{N_C}\,k\,T)} - 1\right) \tag{4.6}$$

$$q_b = \frac{q_1}{2}\left[1 + \sqrt{1 + 4\,q_2}\right] \tag{4.7}$$

$$q_1 = \left(1 - \frac{V_{BC}}{\mathbf{V_A}} - \frac{V_{BE}}{\mathbf{V_B}}\right)^{-1} \tag{4.8}$$

$$q_2 = \frac{\mathbf{I_S}}{\mathbf{I_{KF}}}\left(e^{(q\,V_{BE}/\mathbf{N_F}\,k\,T)} - 1\right) + \frac{\mathbf{I_S}}{\mathbf{I_{KR}}}\left(e^{(q\,V_{BC}/\mathbf{N_R}\,k\,T)} - 1\right) \tag{4.9}$$

$$C_{jC} = \mathbf{C_{JCO}}\left(1 - \frac{V_{BC}}{\mathbf{V_{JC}}}\right)^{-\mathbf{MJC}} \tag{4.10}$$

$$C_{jE} = \mathbf{C_{JEO}}\left(1 - \frac{V_{BE}}{\mathbf{V_{JE}}}\right)^{-\mathbf{MJE}} \tag{4.11}$$

$$C_{DC} = \mathbf{T_R}\frac{d\,I_{EC}}{d\,V_{BC}} \tag{4.12}$$

$$C_{DE} = \mathbf{T_F}\frac{d\,I_{CC}}{d\,V_{BE}} \tag{4.13}$$

Table 4.1. Gummel-Poon Model Parameters

Symbol	SPICE 2G Keyword	Parameter Name	Value (A, V, Ω, F)
I_S	IS	Saturation current	5.45202×10^{-23}
I_{SE}	ISE	Base-emitter leakage saturation current	5.82688×10^{-19}
I_{SC}	ISC	Base-collector leakage saturation current	6.9094×10^{-12}
I_{KF}	IKF	High injection forward current	12.74578×10^{-3}
I_{KR}	IKR	High injection reverse current	∞
N_F	NF	Forward emission coefficient	1.093442
N_R	NR	Reverse emission coefficient	1
N_E	NE	Base-emitter leakage emission coefficient	1.57668
N_C	NC	Base-collector leakage emission coefficient	1.88121
β_f	BF	Ideal forward current gain	10^5
β_r	BR	Ideal reverse current gain	1
V_A	VAF	Forward Early voltage	480
V_B	VAR	Reverse Early voltage	∞
R_B	RB	Base resistance	8.2
R_E	RE	Emitter resistance	3.9
R_C	RC	Collector resistance	10.8
T_F	TF	Forward transit time	0
T_R	TR	Reverse transit time	0
C_{JE0}	CJE	Zero bias base-emitter depletion capacitance	19.03×10^{-15}
C_{JC0}	CJC	Zero bias base-collector depletion capacitance	89.09×10^{-15}
V_{JE}	VJE	Base-emitter built in potential	1.55262
V_{JC}	VJC	Base-collector built in potential	0.87401
MJE	MJE	Base-emitter grading coefficient	0.56467
MJC	MJC	Base-collector grading coefficient	0.18321
XCJC	XCJC	Fraction of C_{JC} connected to the internal nodes	0.24096
FC	FC	Depletion capacitance parameter [46]	.99
T	T	Temperature at which parameters are measured	40 °C

Table 4.2. Gummel-Poon Model Parameters Set at Default Values

Symbol	SPICE 2G Keyword	Parameter Name	Default Value (A, V, Ω, F, eV)
R_{BM}	RBM	Minimum base resistance at high current	RB
I_{RB}	ISE	Base resistance high current level	∞
$X_{\tau F}$	XTF	Coefficient for bias dependence of τ_F	0
$V_{\tau F}$	VTF	Voltage describing V_{BC} dependence of τ_F	∞
$I_{\tau F}$	ITF	High current parameter for effect on τ_f	0
$P_{\tau F}$	PTF	Excess phase at $f=1/(2\pi\tau_f)$	0
C_{JS}	CJS	Zero bias collector-substrate capacitance	0
V_{JS}	VJS	Substrate junction built in potential	.75
MJS	MJS	Substrate junction grading coefficient	0
$X_{T\beta}$	XTB	Forward and reverse β temperature coefficient	0
X_{TI}	XTI	Saturation current temperature exponent	3
E_G	EG	Energy gap for temperature effect on I_S	1.11
k_f	KF	Flicker noise coefficient	0
a_f	AF	Flicker noise exponent	1

current flowing from the base to emitter and base to collector due to the diffusion of holes from the base region. In typical HBTs, the base-emitter heterojunction will block the diffusion of holes from the base to emitter and will normally make the I_{CC}/β_f current source negligible. Equations 4.5 and 4.6 are used to model the current flowing from the base to the emitter and from the base to the collector due to the recombination of carriers in the respective depletion regions, and at the surface of these regions. Equations 4.7 through 4.9 describe the impact of the Early voltages and high level injection effects on the current flow through the transistor. Equation 4.8 is used to model Early voltage effects, while Equation 4.9 models high level injection effects, such as the Kirk effect. These effects are combined in Equation 4.7. This equation also indicates that high level injection effects become significant when q_2 is on the order of 0.25. Equations 4.10

through 4.13 are used to model the nonlinear capacitances within the transistor model. Equations 4.10 and 4.11 model the junction capacitances while Equations 4.12 and 4.13 model the diffusion capacitances within BJTs.

The first step in extracting the HBT model parameters is to determine the values of the parasitic terminal resistances R_E, and R_B. Surprisingly, these parameters are some of the most difficult to extract and a number of methods have been proposed for the measurement of each of these resistances. One of the most popular methods which has been used to measure the emitter resistance in BJTs is the open collector method [47, 50]. This method is implemented by plotting the variation in the collector-to-emitter voltage as a function of base current with the collector current set to zero. As indicated by Getrue, the slope of this curve may be used to extract R_E in bipolar transistors. However, when this method was applied to the HBT, negative emitter resistance values were obtained. The accuracy of the open collector method for the measurement of R_E has also been called into question by other authors [44, 51]. Thus the open collector method was considered invalid for the measurement of R_E in HBTs.

An alternative method of extracting information about R_E and R_B is based on the I-V characteristics of HBTs. Equations 4.3 through 4.6 indicate that if V_{BC} is maintained at zero volts, the base current is a result of the diffusion of holes over the base-emitter junction (I_{CC}/β_f), and due to recombination in the base-emitter depletion region (I_{RF}). As discussed in Section 2.5, the heterojunction in a HBT effectively blocks the diffusion of holes from the base region, and accordingly the I_{CC}/β_f term may be neglected. Thus in HBTs, the base current is given by I_{RF} when V_{BC} is less than or equal to zero volts. From Equation 4.5, when V_{BE} is significantly greater than $q/N_R K T$ (this quantity is typically on the order of 25 mV) then the exponential term will be much greater than 1 and the base current can be expressed as,

$$I_B = I_{SE} e^{(q V_{BE}/N_E k T)} \Big|_{V_{BC}=0,\ V_{BE}>.2\,V} \cdot \qquad (4.14)$$

Thus, a plot of I_B on a logarithmic scale as a function of V_{BE} will yield a straight line plot. If I_b is plotted on a logarithmic scale as a function of the *extrinsic* base to emitter voltage, V_{BE}, then any deviation of this curve from a straight line is a result of voltage drops across the base and emitter resistance. A plot of I_B as a function of V_{BE} is shown in Figure

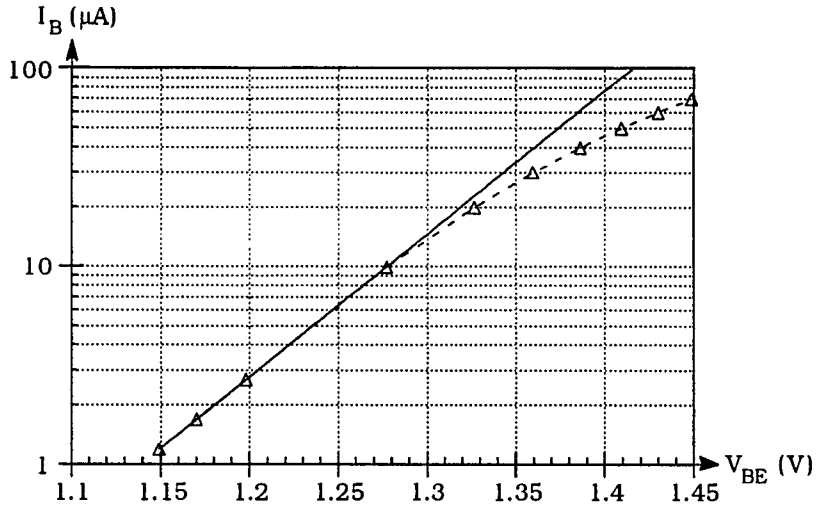

Figure 4.5. Gummel Plot of the HBT Base Current

4.5 along with a straight-line projection of I_B as a function of V_{BE}. The plot shown in this figure is referred to in literature as a Gummel plot. Using the schematic in Figure 4.4, it can be seen that the difference in voltage between the two curves in Figure 4.5 is given by,

$$V_{BE} - V_{BE} = R_E I_E + R_B I_B . \tag{4.15}$$

Theoretically, Equation 4.15 could be used at two different bias conditions to determine the values of R_E and R_B. However, In order to obtain an appreciable difference between V_{BE} and V_{BE} the base and emitter currents must be relatively large. Measurements of the HBT indicated that if V_{BE} is greater than 1.35 V, the emitter current is more than 100 times larger than the base current. Accordingly, under these high bias conditions, the voltage drop across the emitter resistance is dominant. (It will be shown shortly that the base resistance is about twice the emitter resistance.) Thus, the base resistance cannot be measured effectively by using Equation 4.15. Equation 4.15 was used at a base current of 70 μA and an emitter current of 12.926 mA to establish a relationship between R_E and R_B.

A second method which which may be used to extract information about the R_B and R_E is known as the circle method [47]. This measurement technique is based on a small-signal measurement of an HBT over a broad frequency range. The input impedance of the transistor is determined over this frequency range with the collector and emitter

grounded. The input impedance of the HBT is then plotted over this frequency range with the real part of the impedance plotted as the abscissa and the imaginary part plotted as the ordinate. In theory, this locus of points should form a circle [52]. In addition, at high frequencies, the input impedance will approach $R_E + R_B$. This can be seen from the simplified schematic in Figure 4.6. This schematic is a small-signal equivalent circuit of the Gummel-Poon model shown in Figure 4.5, with the interconnect parasitics removed and the collector shorted to ground. At high frequencies, the base-emitter capacitance will tend to short out the base emitter junction. This will cause the base resistance, R_B, to essentially be shorted to the emitter resistance, R_E. When the transistor is biased in the normal active region, the value of the base-emitter capacitance will be several orders of magnitude greater than the base-collector capacitance. As a result, at moderately high frequencies, the base-emitter capacitance will be a relatively low impedance while the base-collector capacitance will have a impedance much greater than R_E and R_B. Accordingly, at these moderately high frequencies, the input impedance of the circuit approaches $R_E + R_B$. As noted by Sansen, as the frequency increases such that the impedance of the base-collector capacitance approaches R_B, a second circle locus is generated and at infinite frequency, the input impedance approaches R_E.

In order to perform this measurement, the S-parameters of the HBT were measured over a frequency range of .14 to 14 GHz. The S-parameter data set was then loaded into the

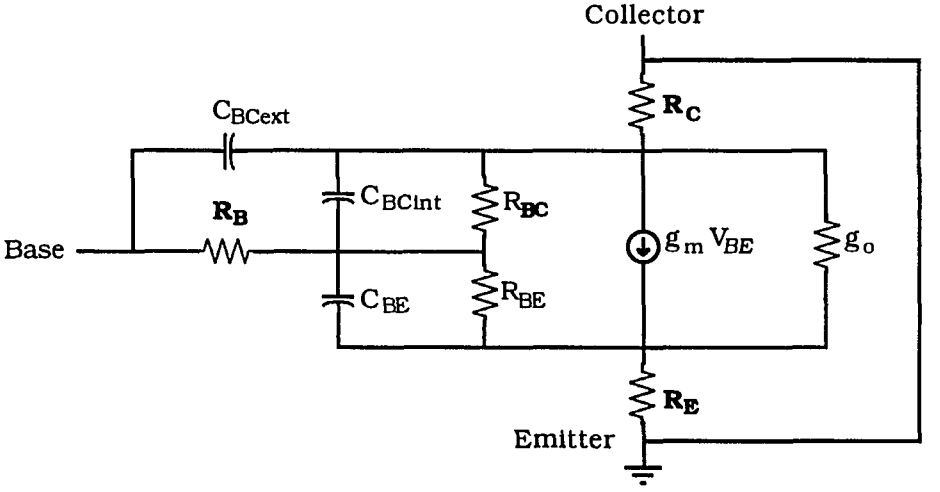

Figure 4.6. Simplified Small-Signal Gummel-Poon Model

software program LIBRA™ and the parasitic interconnect components shown in Figure 4.5 were deembedded from the measurements. Libra was then used to determine the input impedance of the transistor with the output shorted. A circle plot of the resulting data is shown in Figure 4.7. The data was then curve fit to a circle using the software program Kaliedagraph [53] and the result is shown as the solid curve in this figure. (Nearly all of the curve fits discussed in this section were performed using the program Kaliedagraph.) From this curve fit, the high frequency intersection was found to be 12.44 Ω. Thus,

$$R_E + R_B = 12.44\ \Omega. \tag{4.16}$$

From Equation 4.15 at the bias condition mentioned previously, and Equation 4.16, the values of R_E and R_B were determined simultaneously. The value of R_E was found to be 4.24 Ω and R_B was found to be 8.2 Ω.

It should be noted that the circle method can be prone to a number of inaccuracies. If the parasitic emitter lead inductance has an error of ΔL_E then the value of $R_E + R_B$ will be in error by $(\omega_T \Delta L_E)$, where ω_T is the cutoff frequency of the transistor in radians [54]. In addition, if the values of the parasitic capacitances across the HBT terminals are in error, then this can also effect the results of the circle technique [52]. However, the relative amount of error is proportional to the ratio of the error in the parasitic capacitances to

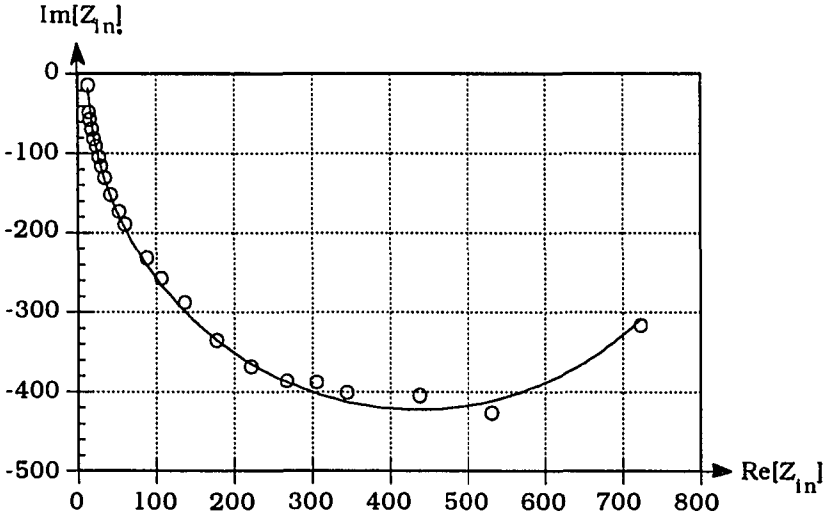

Figure 4.7. Circle Plot of HBT Input Impedance

C_{BE}. Since C_{BE} will be shown to be about two orders of magnitudes greater than the parasitic capacitances, it is likely that any error due to this effect is minimal. Finally, if the value of C_{BCext} is very large with respect to C_{BE} this will also effect the circle measurement. This error increases with increasing value of R_C and g_m [52]. Thus, to minimize the error associated with the circle method, it is best to select a bias condition where ω_T is minimized, C_{BC} is minimized, g_m is minimized, R_C is minimized, and C_{BE} is maximized. Obviously some of these goals are in conflict. For the purposes of this research, a bias condition was selected where V_{CE} was .5 V, and the collector current was 1 mA. The bias condition was selected to be in the saturated region which has the advantage of reducing ω_T, g_m, and R_C, but has the disadvantage of increasing C_{BC}.

Unwin and Knott [55] have also analyzed several methods of extracting parasitic transistor resistances. They suggest using noise figure measurements to determine the parasitic resistance values. Accordingly, noise figure measurements were used to verify the above resistance measurements. The noise parameters of the HBT were measured at a bias current of .5 mA and a collector voltage of 5 V. (Noise parameters and measurements are discussed in detail in Section 6.) The modelled and measured noise parameters of the HBT were then compared. It was found that the value of R_B was in good agreement with the results given above. However, the value of R_E which was obtained was slightly less at 3.6 Ω. Thus an average value of 3.9 Ω was used for R_E.

$$R_E = 3.9\ \Omega \tag{4.17}$$

$$R_B = 8.2\ \Omega \tag{4.18}$$

More recently, Park and Neugroschel have proposed a method for extracting the values of R_E and R_B [51]. The method which they propose is similar to the circle method discussed above, except that the transistor is measured in the common base configuration. While the method does appear to be valid, a number of simplifying assumptions are required in its derivation. It appears that the method proposed by Park and Neugroschel can achieve roughly the same level of accuracy as the circle method, and that there is no real advantage of disadvantage of using their method over the circle method.

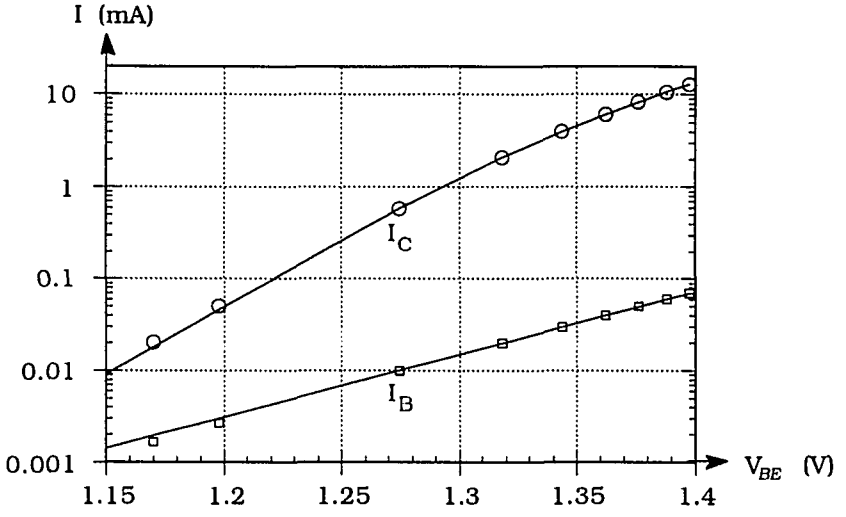

Figure 4.8. HBT Gummel Plots of I_B and I_C

Once the values of R_B and R_E have been extracted, a number of other SPICE parameters can easily be extracted using Gummel plots [47]. Gummel plots of I_B and I_C are shown in Figure 4.8. This figure gives the base and collector currents of the HBT as a function of the *intrinsic* base-emitter voltage, V_{BE}, while holding V_{BC} at zero volts. V_{BE} was calculated from V_{BE} at each bias condition using Equations 4.15, 4.17, and 4.18. Since V_{BE} is related to V_{BE} through the values of R_E and R_B, it is important that these values are extracted accurately, or the Gummel plots will be in error.

The measured Gummel data points are given by the symbols in Figure 4.8. By curve fitting these data points to the appropriate Gummel-Poon model expressions, a number of parameter values can be extracted. Consider, for example, the Gummel plot of the base current. As discussed previously in this section, when V_{BC} is set to zero the base current is dominated by the forward recombination current, I_{RF}, and may be modelled by Equation 4.5. By curve fitting the measured data to Equation 4.5, the Gummel-Poon parameters I_{SE} and N_E were extracted. The resulting curve is given by the solid line in Figure 4.8. The extracted values for I_{SE} and N_E were 20.251 fA and 2.3587 respectively. Note that the plot of the base current is essentially a straight line. This is characteristic of HBTs since the base current is dominated by recombination. In homojunction BJTs, this curve would consist of two distinct slopes. At lower currents, the slope would be a

result of recombination while at higher currents, the slope would be a associated with the diffusion current.

The collector current data points shown in Figure 4.8 can be used to extract other Gummel-Poon parameters in a similar manner. If V_{BC} is set to zero, Equations 4.2 through 4.4 show that I_C is equal to I_{CC}. Thus, the Gummel data given in Figure 4.8 can be curve fit to Equations 4.3, 4.7, 4.8, and 4.9. As discussed below, the reverse Early voltage, V_B, was set to a default value of infinity, and thus for the Gummel data curve fit, q_1 was set equal to unity. Using the afore mentioned equations, the parameters I_S, N_F, and I_{KF} were curve fit to the measured data. The values obtained for the parameters were 7.3467×10^{-23} A, 1.0825, and 5.2631 mA respectively. Note in this case, that the Gummel plot of the collector current is not a straight-line plot, but has a curvature associated with it. This curvature is a result of high level injection effects such as the Kirk effect [56]. At low collector current levels, such that I_C is much less than I_{KF}, the value of q_2 in Equation 4.9 will be much less than unity, and the value of q_b will be very close to unity. As a result, at low current levels, the collector current is set by the parameters I_S and N_F. Accordingly, at low collector current levels, the curve in Figure 8.6 is nearly a straight line. At higher current levels, high level injection effects take place which reduce the current gain of the transistor. The parameter I_{KF} models the current level where these high level injection effects take place. Thus, at collector currents approaching 5.3 mA, the slope of the collector current curve starts to roll off.

A Gummel plot, which is similar to those shown previously is given in Figure 4.9. However, this Gummel plot applies to the HBT biased in the inverted region. In this case, V_{BE} was set to zero, and the base current was measured as a function of V_{BC}. Since the current flowing out of the collector terminal was essentially equal to the base current and very small, the value of V_{BC} was approximated as being equal to V_{BC}. For base currents of less than 80 μA, as shown in Figure 4.9, this approximation is valid to within 1 mV. From the schematic in Figure 4.4 and Equations 4.3 through 4.6, with V_{BE} set to zero, the base current is made up of two components, I_{EC}/β and I_{RR}. In this research, this current was modelled as being entirely a result of recombination current, I_{RR}, for reasons which are explained below. Accordingly, the data in the figure below was fit to Equation 4.6 and the parameters I_{SC} and N_C were extracted as 6.9094 pA and 1.8812 respectively. The resulting fit is shown as the solid curve.

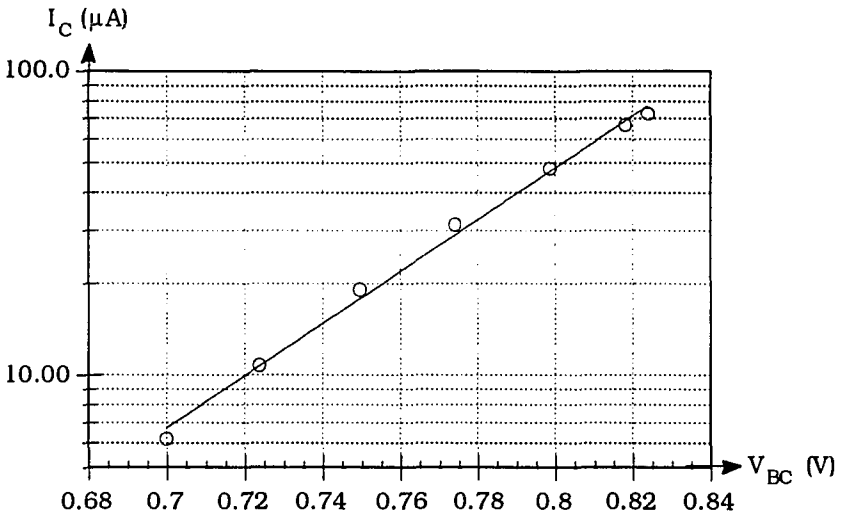

Figure 4.9. Gummel Plot of I_B with the HBT Biased in the Inverted Region

Note, that the data plotted in this figure tends to roll off slightly at higher currents. If this current were made up of a combination of recombination current and diffusion current, then the data should curve *upward* at higher currents rather than roll off [47]. Thus, the data in the figure is either a result of I_{EC}/β_r or I_{RR}. If the fitted data discussed above were a result of diffusion current, then the resulting reverse current gain, β_r, would be 1.1e-7. However, Asbeck [37] indicated that for a GaAs junction the diffusion current gain should roughly be given by,

$$\beta_d = \frac{v(n)}{v(p)}\frac{N_B}{N_C} \cong 5\frac{N_B}{N_C} \cong .05. \tag{4.19}$$

This large discrepancy indicates that the data is due primarily to recombination current. In addition, the base-collector ideality factor, N_C, was found to be fairly close to 2 which is characteristic of recombination current. Whereas, if the current was due to diffusion current, this factor should be closer to 1. Thus, the base current is most likely a result of recombination.

As noted previously, when the reverse Gummel data was taken, with V_{BE} set to zero, the current flowing from the collector terminal was essentially equal to the base current. This indicates that the current due to the diffusion of the electrons from the collector to

the base, I_{EC}, is essentially negligible. This is expected since the base is much more heavily doped than the collector. Accordingly, the parameters associated with I_{EC} in Equation 4.4, may be set such that this current is negligible. It was found that by setting I_{KR} and N_R to the SPICE default values, that I_{EC} was negligible for any reasonable base-collector voltage. Thus I_{KR} was set of infinity, and N_R was set to unity.

Also, as discussed above, the currents due to the diffusion of holes from the base to emitter, I_{CC}/β_f, and due to diffusion from the base to collector, I_{EC}/β_r are negligible for any reasonable bias condition. Thus, the values of β_f and β_r must be selected to satisfy this condition. By setting β_r to the SPICE default value of unity, the reverse diffusion current was found to be negligible. The value of β_f was estimated using Equation 2.39 to be on the rough order of 10^5. The use of this value of β_f results in a negligible level of forward base diffusion current. It should be emphasized the the selection of the parameter values for I_{KR}, N_R, β_f, and β_r are not necessarily accurate values for these parameters; but rather are values which are sufficient to make the corresponding components of current negligible in the Gummel-Poon model. Since the components of currents which these parameters represent are negligible in the actual HBT, extracting these parameters is not necessary or practical.

Two other Gummel-Poon model parameters which are required to describe the dc characteristics of the HBT are the Early voltages V_A and V_B. Since the current due to the diffusion of electrons from the collector to the base, I_{EC}, was found to be negligible, the Early voltage in the reverse direction will not have a significant impact on the characteristics of the HBT. Accordingly, it was set to the SPICE default value of infinity. The Early voltage in the forward direction, V_A, is more difficult to determine. Theoretically, the Early voltage could be extracted from the dc I-V curve in the active region. However, due to thermal effects, this technique yields a negative Early voltage. Rather, the Early voltage was extracted by fitting measured HBT S-parameters to the equivalent circuit model shown in Figure 4.10 at a relatively high bias current of 8.5 mA at several values of V_{CE}. The Early voltage can then be extracted from the output conductance of the equivalent circuit model using the equation,

$$V_A = \frac{I_C}{g_o} - V_{CE}. \tag{4.20}$$

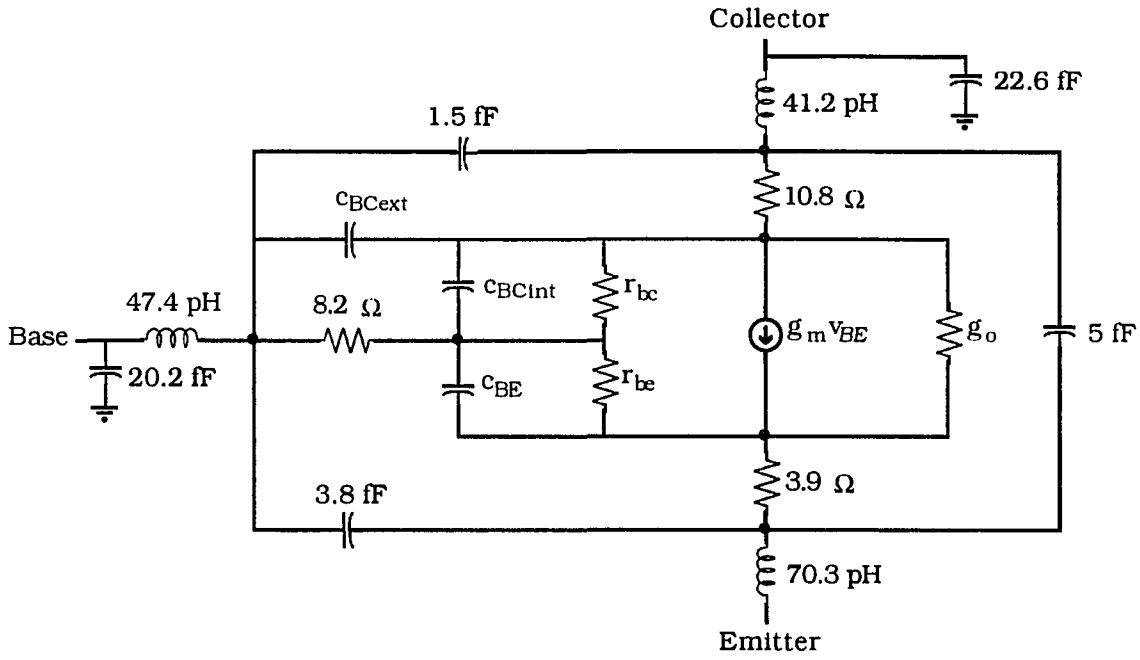

Figure 4.10. Small-Signal HBT Model Including Interconnect Parasitics

Using this method, V_A was found to be 480 V. It should be noted that this measurement technique is only moderately accurate since the value of the output conductance was 18.3 μmhos which is a difficult level to measure in a 50 Ω S-parameter system. However, the value of the Early voltage does not have a significant impact on the characteristics of the HBT since it is so large. In addition, the value obtained is within the range of typical values for Early voltages in HBTs. (The Early voltage of HBTs usually range from 150 V to 1200 V [45].) This extraordinarily high early voltage is a direct result of the heavy base doping in HBT devices. As a result of this heavy base doping, the variation in the base width with respect to base-collector voltage is minimal, and thus the Early voltage is very large.

The one remaining Gummel-Poon parameter which must be extracted to define the dc characteristics of the HBT is the parasitic collector resistance, R_C. This can be quite difficult since the value of R_C actually varies with collector current, even though it is modelled in SPICE as a constant [47]. The value of R_C will be smallest when the device is biased in the saturated region, and increases as the devices is biased in the active region.

As noted by Getreu, the use of the open emitter method may not be used to accurately extract the value of R_C due to changes in the effective junction areas [47]. (The open emitter method is analogous to the open collector method of measuring R_E discussed on page 43.) One approach which was selected to extract the value of R_C for this research is an extension of an approach suggested by Getrue to determine the limiting values of the collector resistance. Since all of the dc Gummel-Poon parameter values other than R_C have been extracted, the value of R_C can be selected to match the Gummel-Poon model to the measured dc I-V curves. It should be noted that this approach will tend to model R_C at its value in the saturated region, but will partially take into account its value in the active region.

The dc I-V curves of the HBT are shown in Figure 4.11. The symbols represent measured data points, while the solid curves represent the Gummel-Poon model results. To extract R_C, its value was simply varied until the modeled data matched the measured data. For example, if the value of R_C were increased by 5 Ω, then the dc I-V curves would shift to the right by 30 mV at a collector current of 6 mA. This effect would be noticeable in the saturated region of the I-V curves. Based on this approach, the collector resistance was extracted as, 10.8 Ω.

A second approach which was used to determined the value of R_C was to fit the small-signal Gummel-Poon model to a set of measured S-parameters at several bias conditions. The accuracy of the fit was not heavily dependent on the value of R_C. However, a good fit was obtained with a collector resistance of 10.8 Ω.

The dc I-V curves shown in Figure 4.11 demonstrate the accuracy of the extracted dc Gummel-Poon parameters. In general, the measured and modelled data points match quite well. However, note that the measured I-V data points do decrease slightly with increasing V_{CE} in the active region of operation. This indicates that the measurement on the thermal impedance of the substrate are slightly too low. The downward slope of the I-V curves is a thermal effect that is common in HBTs. As the device is heated, the collector current will drop for a given base current. The drop in I_C is a direct result in the difference in ideality factors for the base and collector currents. The ideality factor for the base current is given by N_E and is equal to 2.3587 while the ideality factor for the collector current is N_F and is given by 1.0825. As a result, for an increase in temperature the ratio

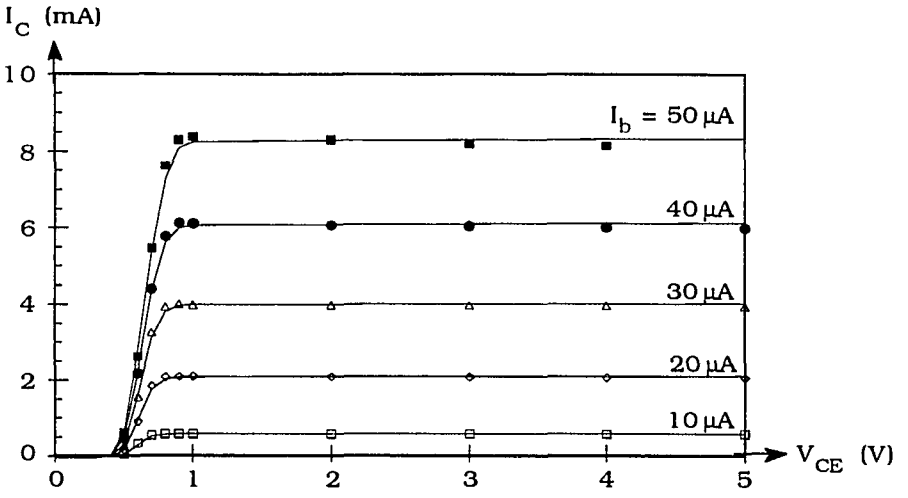

Figure 4.11. Modeled and Measured HBT I-V Curves

of I_{CC} to I_{RF} will decrease. This indicates that an increase in temperature of the HBT device will cause a decrease in collector current for a given base current. As discussed at the beginning of this section, the back-plate temperature of the HBT was adjusted to maintain the device at 40 °C. The data in Figure 4.11 indicate that the amount that the temperature was adjusted was not quite enough, and the downward slope in the data resulted. However, the adjustment of the back-plate temperature was useful since the downward slope is about 5 times more pronounced when the back-plate temperature is held constant.

The remaining Gummel-Poon parameters, which have not yet been extracted are all associated with the ac characteristics of the device. These parameters are used to describe the capacitors shown in the Gummel-Poon model. Each of these ac parameters was extracted by fitting the equivalent small-signal HBT model shown in Figure 4.10 to measured S-parameter data over a wide frequency range. This fitting procedure was performed using the software program LIBRA [49] and was repeated over a wide range of HBT bias conditions. By modelling the bias dependence of each of the capacitors in the Gummel-Poon model, the parameter values were extracted.

The parameter XCJC, which is associated with the base-collector capacitance, was extracted by fitting the measured data to the small-signal model at four different bias

conditions simultaneously. This parameter determines the percentage of the total base-collector depletion capacitance which is modelled as being across the intrinsic base-collector junction. (See Figure 4.4.) By fitting the HBT at four bias conditions in the active and cutoff regions simultaneously, the capacitance across the base-collector junction was limited to depletion capacitance. The extracted value for XCJC was .24096. Thus, the majority of the base-collector depletion capacitance was modelled as being connected to the external base node. This indicates that a significant portion of the area associated with base collector junction is not in the active region of the device but is associated with the regions covered by the base ohmic contacts. (See Figure 2.6.) Accordingly, the base-collector capacitance could potentially be reduced by reducing the surface area of this region.

The S-parameters of the HBT were measured at all of the bias conditions shown in Figure 4.11 and 30 additional bias conditions in the cutoff and inverted regions of operation. The measured S-parameters were fit to the equivalent circuit model shown in Figure 4.10 using the software program LIBRA [49]. The circuit file which was used to perform this curve-fit is given in Appendix B. It was found that a good fit could be obtained at all of the bias conditions by allowing the value of C_{BCext} to be 3.15 C_{BCint}. Thus, the base-collector capacitance was modelled as depletion capacitance. This capacitance is plotted as a function of bias in Figure 4.12. The base-collector capacitance was found to be essentially independent of V_{BE} as expected and could be accurately modelled by the depletion capacitance equation. By fitting Equation 4.10 to the data points in Figure 4.12 the extracted parameter values of 89.09 fF, .87401 V, and 0.18321 for C_{JC0}, V_{JC}, and MJC respectively were obtained. The resulting fit is shown by the solid curve in Figure 4.12.

When the base-collector junction is forward biased, it is possible that some of C_{BCint} actually comes from diffusion capacitance. However, estimating the amount of diffusion capacitance is very difficult without specific information regarding the GaAs material in the collector region. Since the base is much more heavily doped than the collector, the diffusion capacitance for this junction is similar to that for a p^+-n diode and is given by [57],

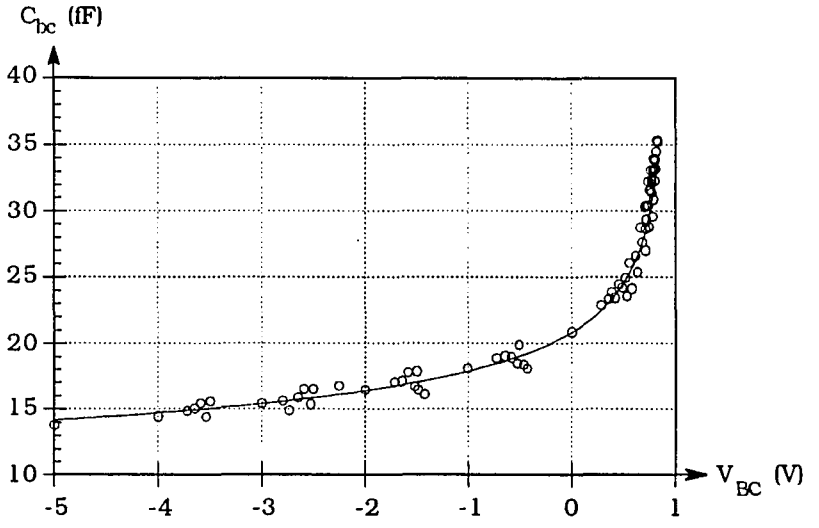

Figure 4.12. C_{BCint} as a Function of Base-Collector Voltage

$$C_{DC} = \frac{q\, I_{RR}}{k\, T}\frac{\tau_p}{2}. \tag{4.21}$$

In the above equation, τ_p is the minority carrier lifetime of holes in the collector region and the above equation is only valid for frequencies less than $1/\tau_p$. For intrinsic GaAs, τ_p is on the order of 10 ns [58]. For GaAs which is doped, this value will decrease by several orders of magnitude. In addition, the dominant component of current across the base-collector junction is due to recombination. This indicates that the minority carrier lifetime is very small. If τ_p is assumed to be 1 ps, then the diffusion capacitance for base currents less than 80 μA will be less than 1.5 fF. Thus, the data in Figure 4.12 indicates that the diffusion capacitance is negligible for any bias condition of interest. Thus, T_R was set to zero in Equation 4.12.

The parameters associated with the base-emitter capacitance were also extracted from measured S-parameters. This capacitance is a result of both depletion capacitance, and diffusion capacitance. The depletion capacitance is the dominate capacitance when the base emitter junction in reverse biased, or only slightly forward biased. However, under large forward bias conditions, the diffusion capacitance is the dominant form of capacitance. The diffusion capacitance, as modelled in SPICE, is given by Equation 4.13.

However, this expression is found to be invalid for the diffusion capacitance in HBTs. The values of C_{BE} which were extracted from the small signal HBT model are shown in Figure 4.13. The data points were extracted from the measurements where the HBT was biased in the normal active region or saturation region. Note from the figure that the base-emitter capacitance is not only a function of the collector current, but is also a heavy function of the base-collector voltage. This is not in agreement with Equations 4.11 and 4.13 which indicate that C_{BE} should be nearly independent of V_{BC} when the HBT is biased in the normal active region. This error is a direct result of a simplifying assumption which was made during the implementation of the Gummel-Poon model in SPICE.

Based on the charge control theory used to derive the Gummel-Poon model, the base-emitter diffusion capacitance may be expressed as [47],

$$C_{DE} = g_m \tau_F = g_m (\tau_E + \tau_{EBD} + \tau_B + \tau_{CBD}) \tag{4.22}$$

where τ_F is the forward transit time, τ_E is the emitter delay, τ_{EBD} is the emitter-base depletion region transit time, τ_B is the base transit time, and τ_{CBD} is the base-collector depletion region transit time. In most conventional transistors, τ_{CBD} is relatively small because the electrons are swept through the base-collector depletion region by the electric field which is present. In the base region, the electrons are transported as a result of

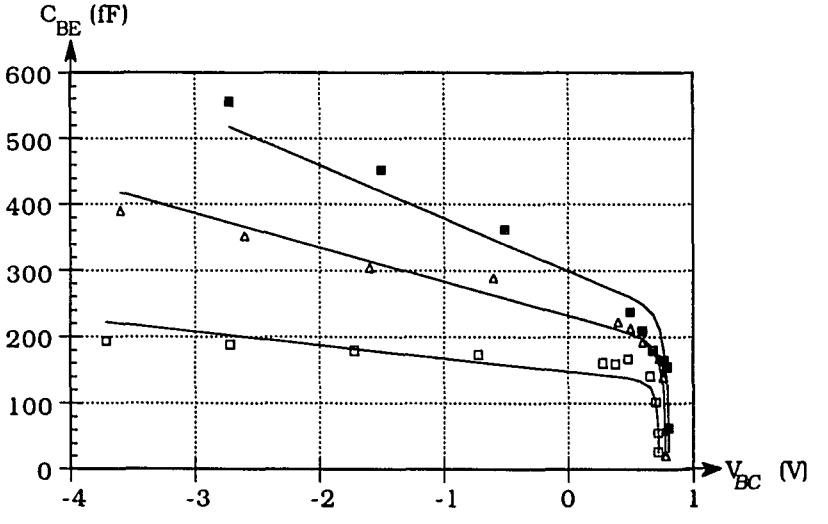

Fig. 4.13 Modelled Values of C_{BE} (Symbols and bias conditions correspond to Fig. 4.11.)

diffusion and move much more slowly. Accordingly, the base transit time is usually the dominate transit time. The other transit times τ_E and τ_{EBD} are associated with holes stored in the emitter and in the emitter-base depletion region. These components are typically much smaller than the base transit time. As a result, the forward transit time in most transistors can be modelled as the base transit time. This transit time is nearly independent of bias and is effected primarily by base width modulation effects. Accordingly, the base-emitter diffusion capacitance model as implemented in SPICE models the forward transit time primarily as a constant, but based on empirical measurements, does allow the forward transit time to be varied when the collector current is greater than I_{KF}. This allows the forward transit time to increase as a result of the Kirk effect. However, as discussed below, this base-emitter diffusion capacitance model is not valid for HBTs.

In HBTs, the base width is very narrow, and the time required for an electron to diffuse across the base is relatively small. As a result, to accurately model the forward transit time in HBTs, all of the components of τ_F given in Equation 4.22 must be considered.

In HBT devices, the diffusion capacitance which results from τ_E is small and may be neglected [36]. This is due to the fact that the heterojunction blocks the diffusion of holes and thus very few holes are stored in the emitter region.

The diffusion capacitance which is associated with τ_{EBD} is given by [36]

$$C_{EBD} = g_m \tau_{EBD} = \frac{g_m C_{jE}}{\frac{\delta(I_{CC}+I_{RF})}{\delta V_{BE}}}. \tag{4.23}$$

Combining Equations 4.3, 4.5, and 4.23 under low forward bias conditions where $q_b \cong 1$ and $g_m = \delta I_{CC}/\delta V_{BE}$,

$$C_{EBD} = \frac{C_{jE}}{1 + \frac{I_{SE}}{I_S}\frac{N_F}{N_E}\exp\left[\frac{q V_{BE}}{k T}\left(\frac{1}{N_E} - \frac{1}{N_F}\right)\right]} \tag{4.24}$$

Since the above equation involves depletion capacitance, it was used in conjunction with Equation 4.11 to extract the parameters associated with C_{jE}. The resulting curve fit and measured data points are shown in Figure 4.14.

The remaining components of diffusion capacitance are associated with the transit times τ_B and τ_{CBD}. These transit times are difficult to separate without detailed knowledge of the HBT device structure. However, the strong base-to-collector voltage dependence of C_{BE} in Figure 4.13, suggests that τ_{CBD} is the dominant component. This is in agreement with reported numerical analyses of the current flow in HBTs [59, 60]. For GaAlAs/GaAs HBTs, τ_B is on the order of .6 ps [36], which at a collector current of 4 mA, corresponds to a diffusion capacitance of 54 fF. Thus, the data in Fig. 4.13 indicates that τ_B is dominated by τ_{CBD}.

For a given carrier velocity in the base-collector depletion region, v(x), τ_{CBD} can be calculated from the expression [36]

$$\tau_{CBD} = \frac{1}{2}\int_0^{W_c} \frac{dx}{v(x)} \tag{4.25}$$

where W_c is the width of the base-collector depletion region. The carrier velocity in the base-collector depletion region is determined by several physical phenomenon and is a

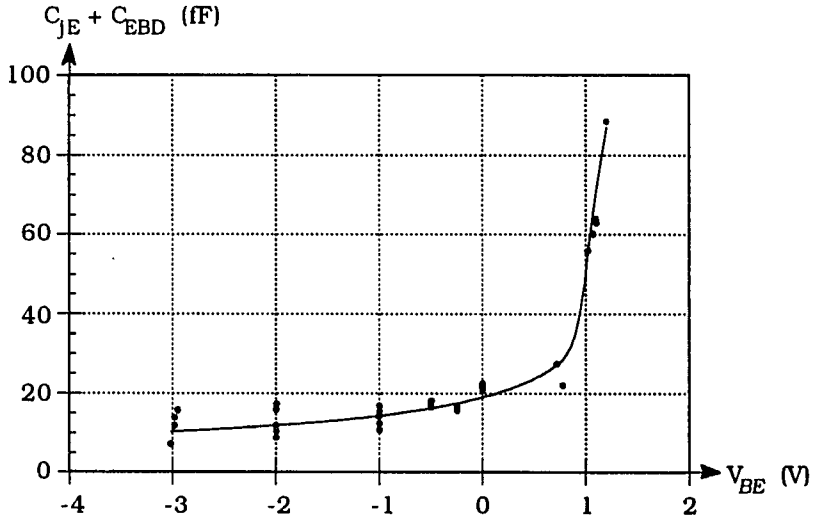

Figure 4.14. C_{jE} and C_{EBD} as a Function of V_{BE}

function of both V_{BE} and V_{BC}. As discussed by Katoh and Kurata [59], a significant mechanism which effects the carrier velocity is associated with the initial onset of the Kirk effect. As the density of mobile carriers in the depletion region increases, the electric field intensity decreases, allowing a greater percentage of the carriers to remain in the Γ-valley of the conduction band. Accordingly, the average carrier velocity increases and τ_{CBD} decreases with increasing current density. The change in τ_{CBD} as a function of V_{BC} has been attributed to the variation in the width of the base-collector depletion region [60]. However, a second mechanism will also effect this variation. As the base-collector junction is reversed biased, the electric field intensity within the depletion region increases. This causes a greater percentage of carriers to be excited out of the Γ-valley into the L- and X-valleys resulting in a lower average carrier velocity and a larger τ_{CBD}. At high collector currents, numerical analyses indicate that the onset of the Kirk effect causes the collector region to be completely depleted out to the ohmic contact [59]. Since W_c is essentially constant under this condition, the variation in the electric field intensity within the depletion region will be the dominant mechanism effecting τ_{CBD}.

The complexity of the physical phenomenon involved in carrier transport render an analytical analysis of the base-collector transit time impractical. Rather, a quasi-static capacitor model has been developed based on measured results and the results of numerical analyses. A numerical analysis performed by Katoh and Kurata [61] indicates that τ_{CBD} varies roughly as the inverse of the square root of collector current. The measured diffusion capacitance data in this work was found to vary in a similar manner. Since g_m is approximately proportional to the collector current, Equation 4.22 indicates that the capacitance due to τ_{CBD} should vary as the square root of collector current. This suggests an exponential dependence with respect to V_{BE}. The data in Fig. 4.13 also indicates that C_{BE} varies linearly with respect to V_{BC}. Accordingly, the author proposes the empirical expression

$$C_{CBD} = C_0\left(1 - \frac{V_{BC}}{\phi}\right)e^{(qV_{BE}/nkT)} \qquad (4.26)$$

where C_0, ϕ, and n are model parameters. This expression was used to perform a curve fit on the measured diffusion capacitance which was not accounted for by τ_{EBD}. This resulted in the parameter values $1.178(10^{-21})$ F, 2.203 V, and 2.707 for C_0, ϕ, and n respectively.

The capacitance model of C_{BE}, which is given by the sum of Equations 4.11, 4.24, and 4.26, is shown as the solid curve in Fig. 4.13. The model curves show good agreement with the measured data. The data in Fig. 4.13 indicates that improved accuracy could be achieved by changing the parameter ϕ in Equation 4.26 to a function which is inversely related to the collector current. However, it is questionable whether the increased complexity is justified. It should also be noted that this HBT base-emitter capacitance model is likely to have limited application for HBTs which have p-type collectors since the carrier transport mechanisms in these devices are different from those discussed here.

Since the base-emitter diffusion capacitance cannot be modelled by the standard SPICE model, the value of T_F was set to zero, and a different circuit was developed to model this nonlinear capacitance. This circuit is based on the generalized impedance converter (GIC) [62] and is shown in Figure 4.15. Using basic circuit theory, the impedance across the terminals of this circuit can be shown to be equal to that of a capacitor whose capacitance in pF is equal to the current I_{cap}. (See Figure 4.15.) Thus, this circuit can be used to model the nonlinear diffusion capacitance if a current I_{cap} is generated which is equal to the sum of Equations 4.24 and 4.26. A current which may be used to represent the capacitance given by Equation 4.26 may be generated very easily using a transistor. The

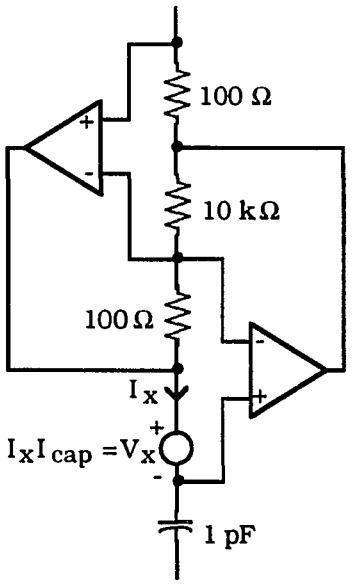

Figure 4.15. Generalized Impedance Converter which Models C_{BE}

collector current of a transistor will be identical to Equation 4.26 if the parameters of the transistor are set such that I_S is equal to C_0 in pF, N_F is set equal to n and V_A is set equal to ϕ. Specific details on how this is implemented in a SPICE file are given in the circuit file listed in Appendix C.

The circuit required to model the capacitance due to the charge stored in the base-emitter space charge region, C_{EBD}, is much more difficult to realize. Note that C_{jE} in Equation 4.24 is not a constant, but rather is also a function V_{BE}. This greatly complicates the expression. While a circuit could have been realized to exactly model this equation, to simplify the analysis, the equation was approximated by using a diode with a series ohmic contact resistance. The value of C_{EBD} as given by Equation 4.24 is plotted as the dashed curve in Figure 4.16. The diode model which was used to approximate this function is shown as the solid curve in this figure. The error between the actual and approximate curves is less than 4 fF for all bias conditions of interest. Figure 4.13 indicates that this error is very small relative to the overall base-emitter capacitance.

In order to demonstrate the accuracy of the entire HBT model developed in this section, the modelled and measured S-parameters of the HBT are plotted in Figures 4.17 through 4.21. These plots compare the modelled and measured S-parameters over a frequency range of 200 MHz to 10 GHz in all four regions of transistor operation. In

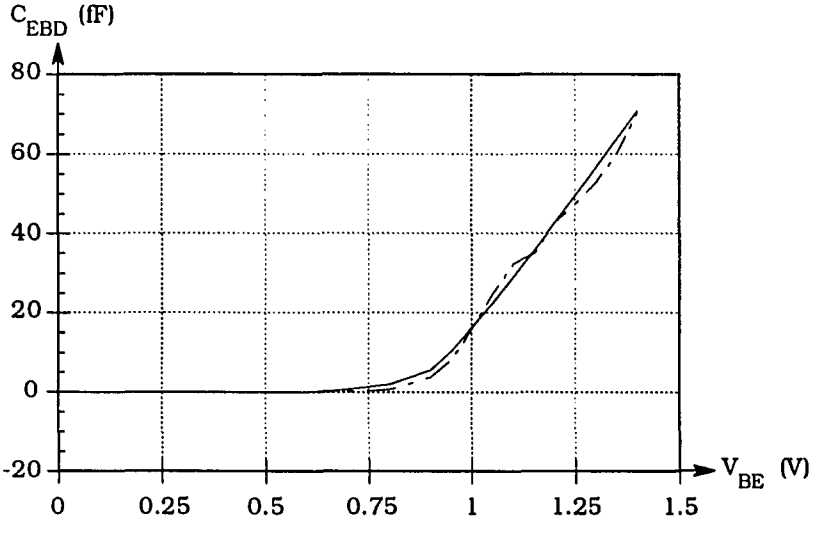

Figure 4.16. C_{EBD} as a Function of V_{BE}

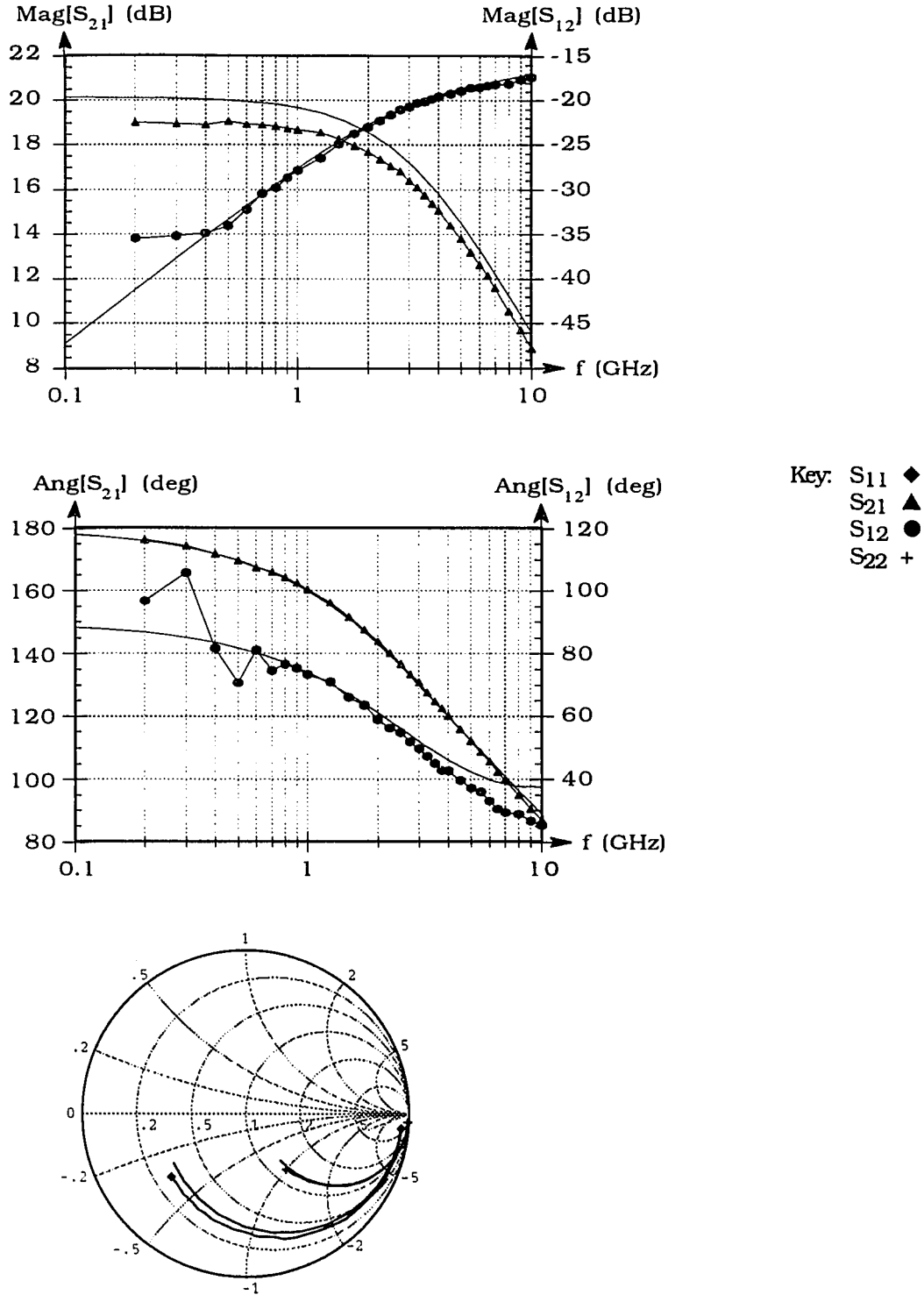

Figure 4.17. Modeled and Measured HBT S-Parameters (V_{CE}=4 V, I_C=8 mA)

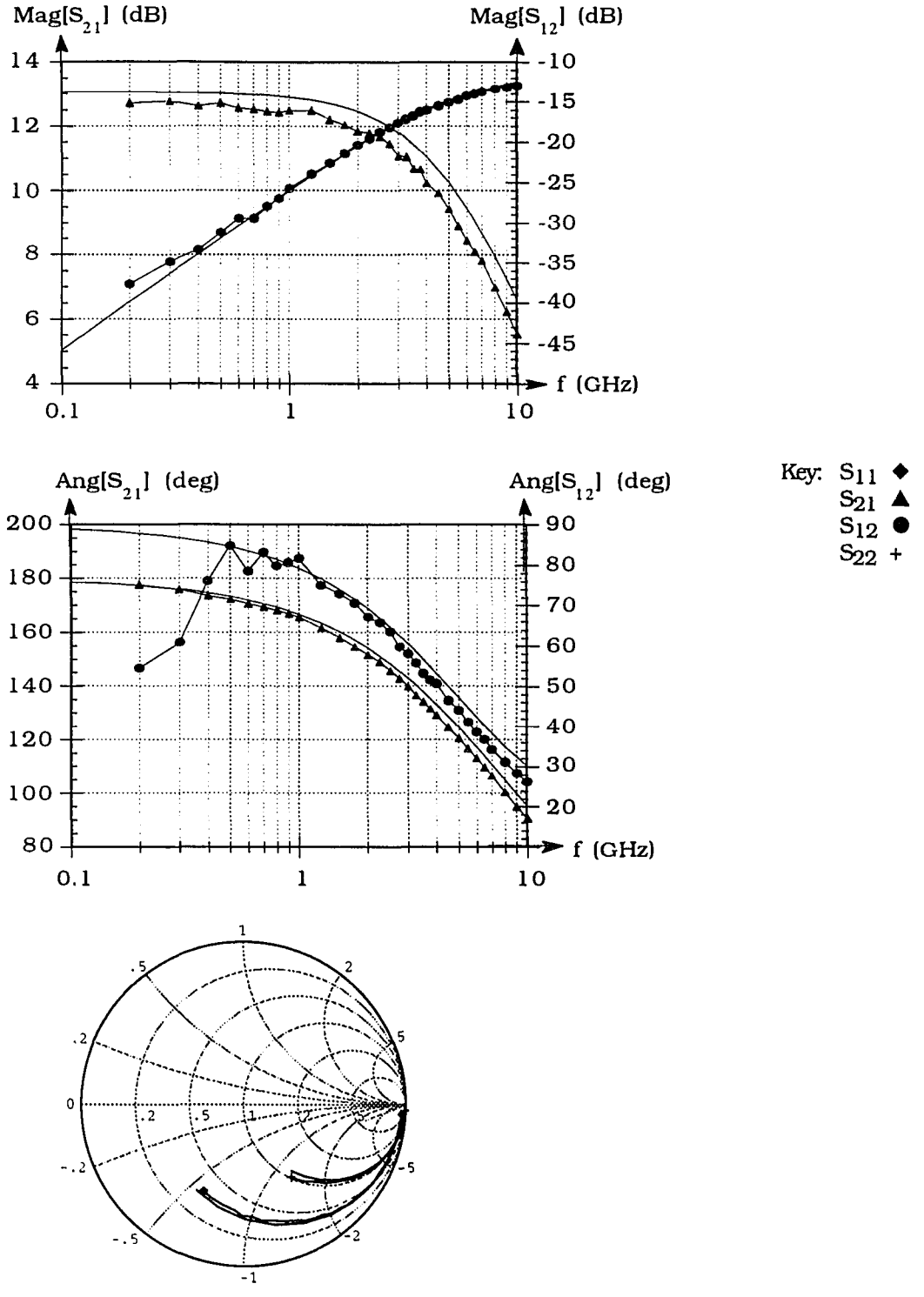

Figure 4.18. Modeled and Measured HBT S-Parameters (V_{CE}=2 V, I_C=2 mA)

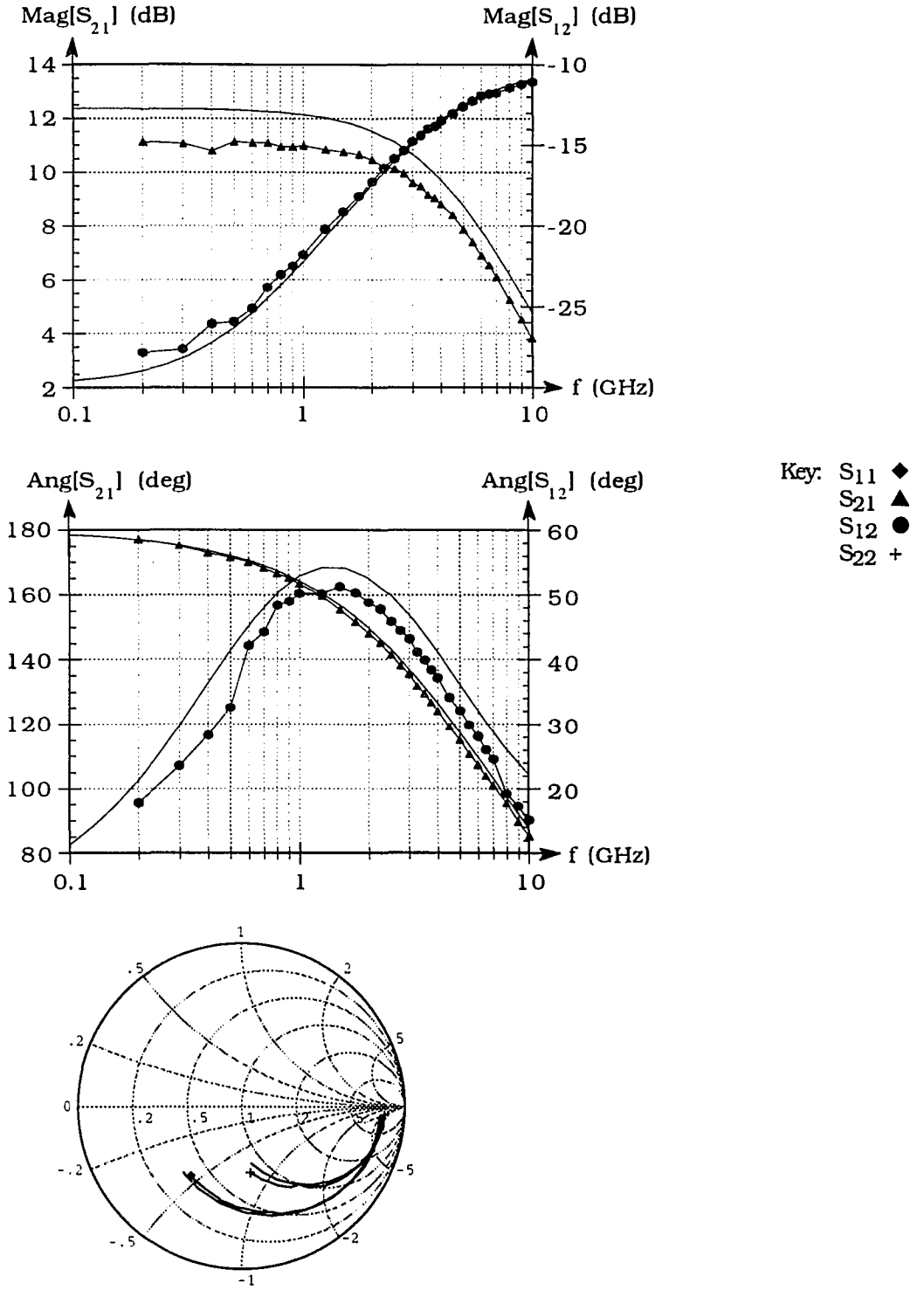

Figure 4.19. Modeled and Measured HBT S-Parameters (V_{CE}=0.6V, I_C=2.16 mA)

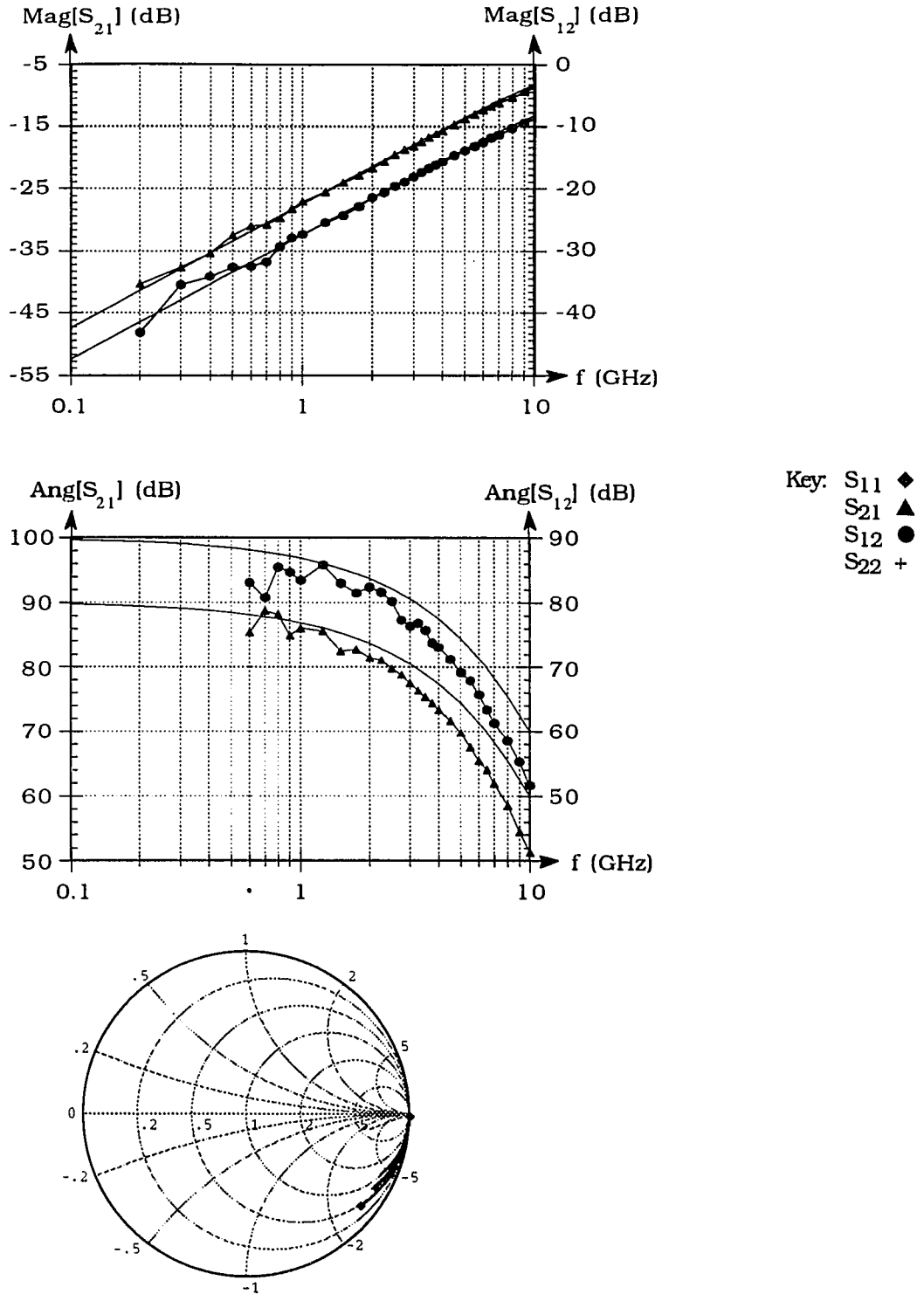

Figure 4.20. Modeled and Measured HBT S-Parameters (V_{BE}=-.5 V, V_{CE}=3 V)

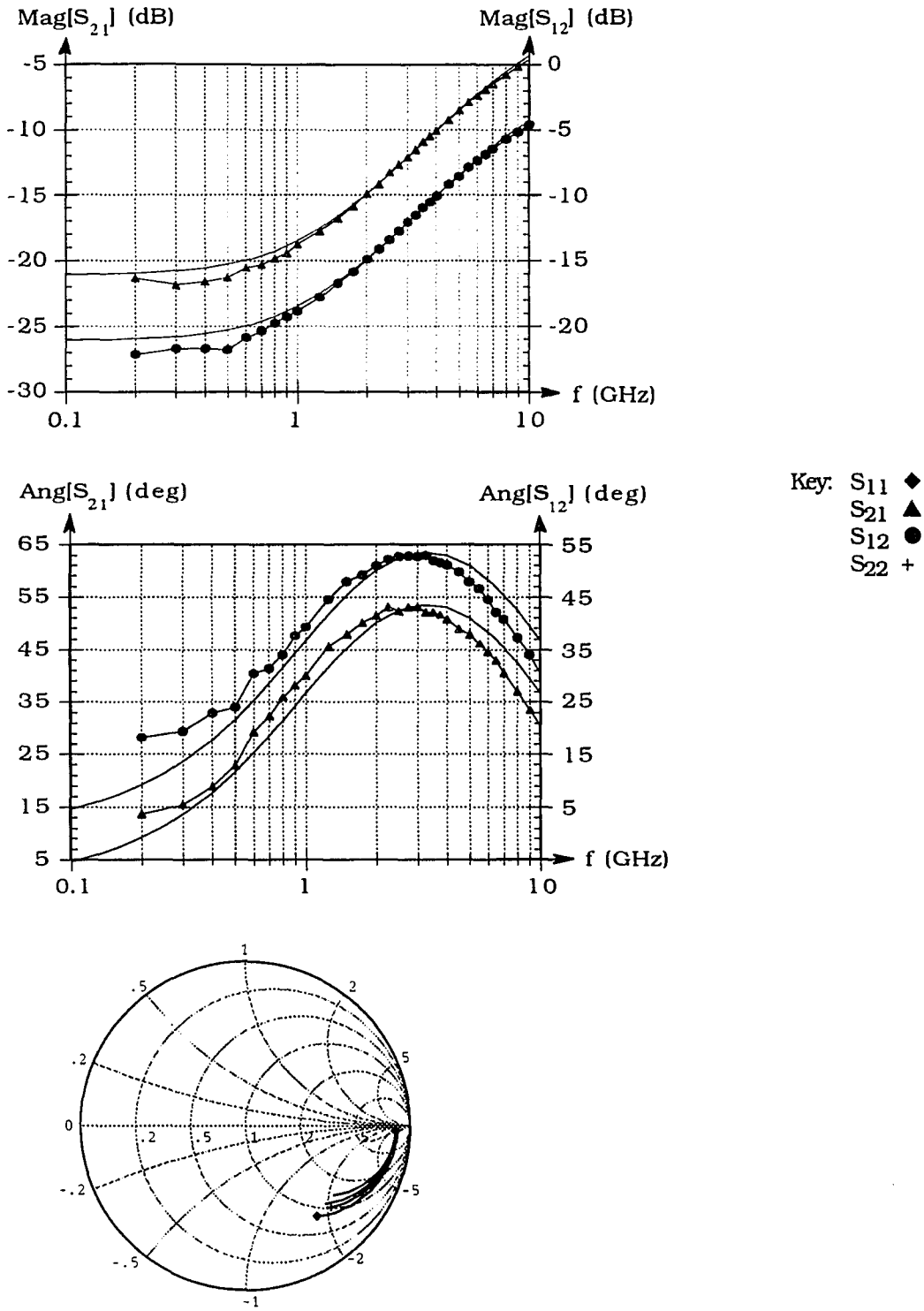

Figure 4.21. Modeled and Measured HBT S-Parameters (V_{CE}=-1 V, I_B=50 mA)

general, these plots, indicate that the HBT model is very accurate. The most significant discrepancy between the modelled and measured data is in the magnitude of S_{21} when the transistor is biased in the forward active region. The modelled value for the magnitude of S_{21} is typically about 1 dB greater than the measured value. However, the overall agreement between the measured and modelled S-parameters is quite good, especially considering the broad frequency range and wide range in bias conditions shown in the figures.

Approximately six months after the HBT model discussed in this section was completed, it was found that the HBTs had an inherent long term reliability problem. The failure mechanism which occurs in the HBT device is associated with leakage current across the base-emitter heterojunction. At some point after a long period of time, the base current of the HBT increases significantly. All of the other characteristics of the device appear to remain unaltered. The leakage across the base-emitter junction occurs even at low forward bias conditions where the junction would normally not conduct. This increase in base current significantly degrades the current gain of the HBT. While it is believed that most vendors have some ideas as to the cause of this failure mechanism, these theories are generally treated as proprietary and not available in literature.

At the time of this research, the long term reliability of the HBTs is in question. However, at present, many of the vendors of these devices feel they have the reliability issues associated with HBTs resolved. It should also be noted that essentially all of the vendors of HBT devices have had similar problems. This is demonstrated by the fact that a recent IEEE microwave symposium dedicated a rump session to the reliability of HBT devices [63].

Due to the failure of the HBT devices, new devices were obtained from the HBT vendor. The vendor indicated that these devices were similar to those modelled in this section with the only modifications being those required to eliminate the long term failure mechanism. Thus, it is likely that the only modifications to the HBT structure are associated with the base-emitter heterojunction since this is where the failure mechanism occurred. Accordingly, the Gummel-Poon parameters associated with this junction were extracted again. Gummel plots of a new HBT with V_{BC} held at zero volts are shown in Figure 4.22 along with the previously modelled Gummel plots. The previously

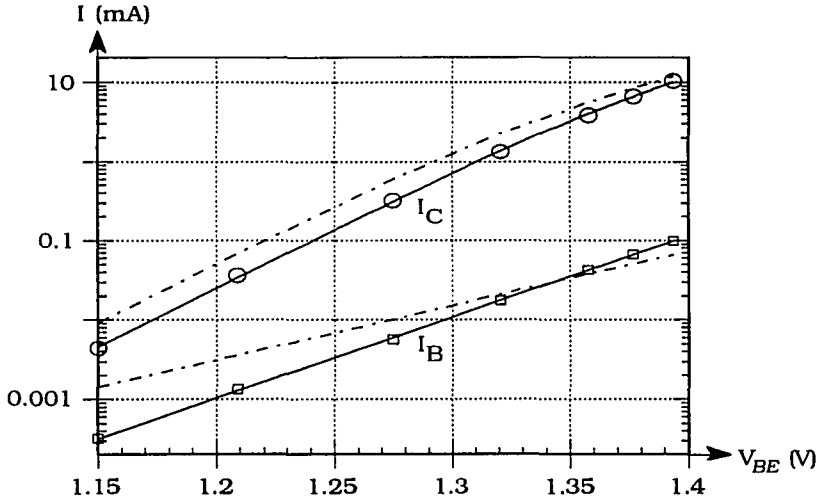

Figure 4.22. Gummel Plots of New HBT Devices

modelled Gummel plots are shown as dashed curves in this figure while the new model is given by the solid curves. The new model curves were generated by fitting Equations 4.3, 4.5, and 4.7 through 4.9 to the measured data in the same manner as discussed previously in this section. Note that the collector current shown in this figure is similar to that of the previous HBT structure. The two modelled curves have a similar slope and shape and differ in the voltage required to achieve a given current by roughly 23 mV. The base current on the other hand differs significantly between the old and new HBT designs. The new design has a steeper slope and less leakage current at low bias currents. This indicates that the alterations which were made to the HBT device structure to eliminate the failure mechanism primarily effect the base-emitter junction; especially those characteristics of the junction which effect base recombination current. The final Gummel-Poon model parameters which were extracted in this research are listed in Table 4.1.

The Gummel-Poon parameters which were extracted from Figure 4.22 were used in the HBT model. With the exception of one parameter the base-emitter diffusion capacitance model, all of the other parameters were unchanged. The base-emitter capacitance was adjusted by scaling the value of C_0 to account for the 23 mV shift the the I_C curve in Figure 4.22. By scaling the value of C_0, the new diffusion capacitance at a given collector current should be nearly equal to that obtained in the original HBT model. The

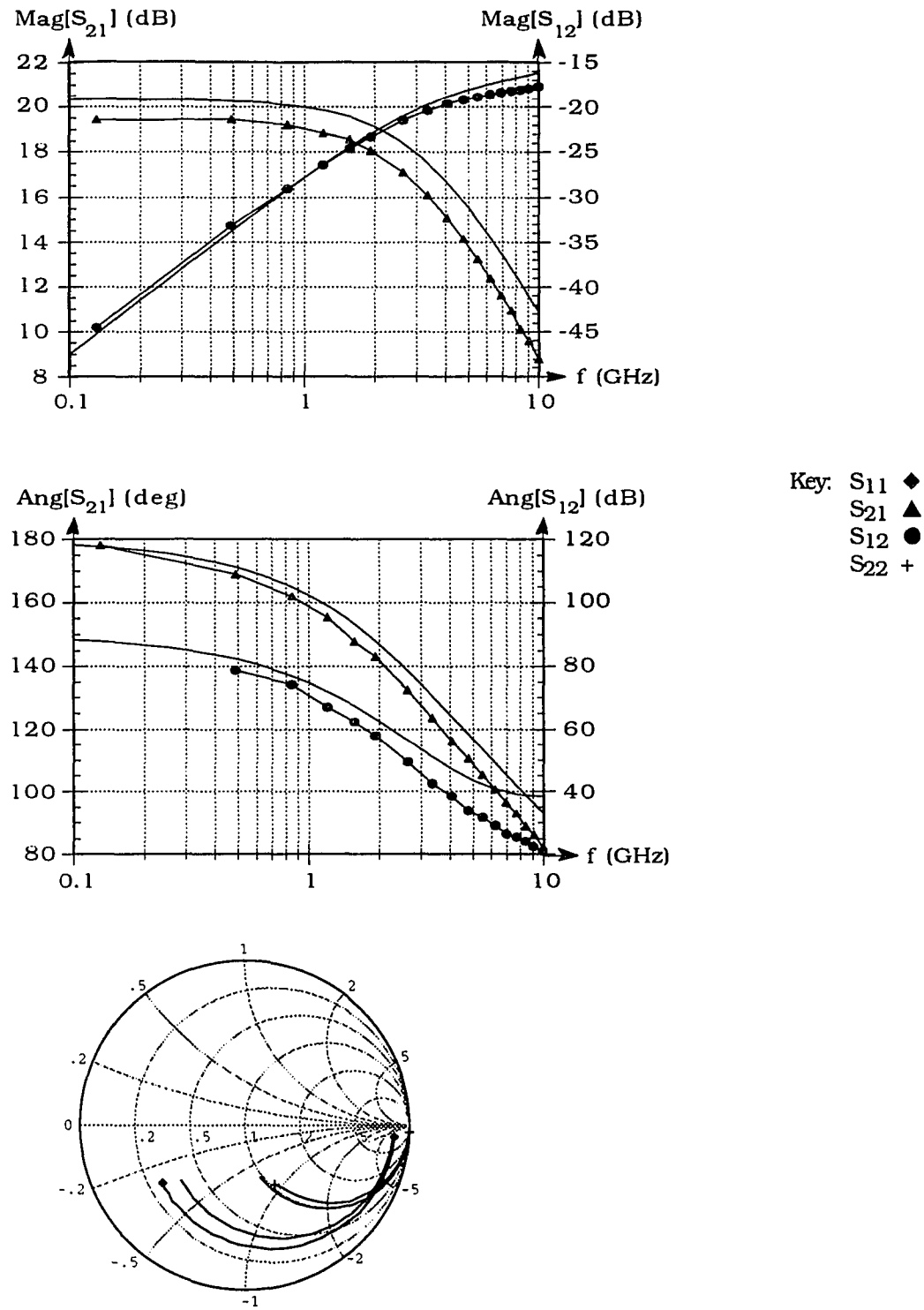

Figure 4.23. Modeled and Measured HBT S-Parameters (V_{CE}=4.0 V, I_C=8 mA)

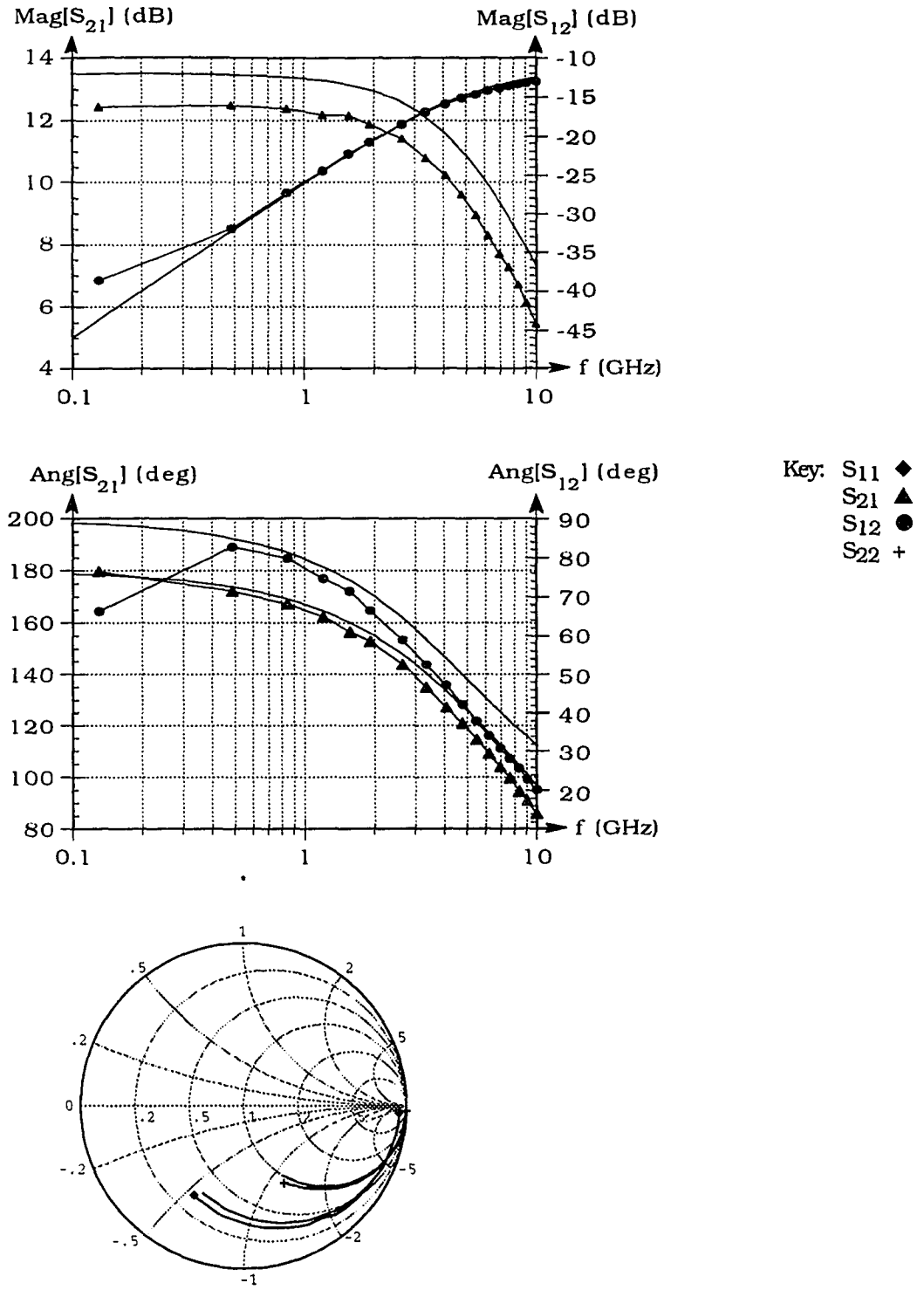

Figure 4.24. Modeled and Measured HBT S-Parameters (V_{CE}=2 V, I_C=2 mA)

new HBT model was compared to measured S-parameter data on the new device. The results are shown in Figures 4.23 and 4.24. These figures indicate that the new HBT model is about as accurate as the original HBT model.

4.2 Large Signal Oscillator Model

The oscillator analyzed in this research is shown in Figure 4.25. This topology is known as the Colpitts oscillator, and is commonly used in microwave design. It was selected as being representative of a typical microwave oscillator. In comparing the Colpitts to the Clapp and Pierce oscillators Parzen [33] noted that the Colpitts is of "... considerable popularity and of greatest difficulty to design." The Colpitts topology also provides for low cost construction of the circuit. The frequency of oscillation for this particular design is roughly 1 GHz. It should be noted, that the HBT used in this research is capable of achieving much higher frequencies of oscillation. However, the oscillator was constructed in hybrid form using bondwires for the interconnect between the components. In order to keep the parasitic effects associated with the bondwires from having a severe impact on the oscillator, the frequency of oscillation was set relatively low at 1 GHz.

The oscillator was constructed in hybrid form on a test fixture with the various components epoxied to the test fixture and bonded together. Care was taken to keep the lengths of the bondwires to a minimum. (Typically on the order of 40 mils.) The positive supply voltage was bypassed with a 39 pF and a 4.7 μF capacitor. The negative supply

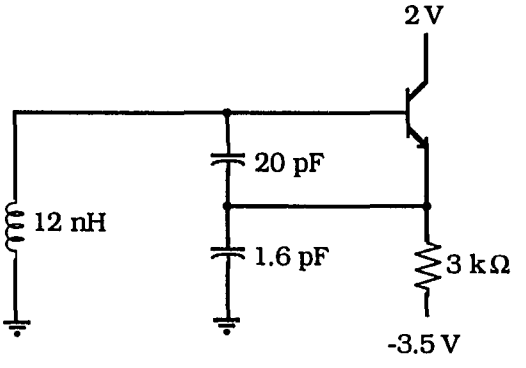

Figure 4.25. HBT Colpitts Oscillator Schematic

voltage was fed through a SMA connector. A bias tee was then used to apply the negative supply voltage, and simultaneously detect the oscillator signal.

With the completion of the large signal HBT model, the characteristics of the oscillator can be simulated with relative ease. However, the parasitic elements associated with the oscillator interconnect must be accounted for. An oscillator schematic which contains these parasitic elements is shown in Figure 4.26. The four inductors L_{BW1} through L_{BW4} model the effects of the bondwire interconnects between the components. These parameter values were extracted using the "WIRE" model in the software program LIBBRA [49]. The capacitors in Figure 4.25 were modelled as series R-L-C circuits. These equivalent circuit models were generated using information provided by the capacitor manufacturer [64]. The capacitors were selected as chip components to minimize the parasitic effects. The inductor shown in the above figure was a 3 turn air wound component. Its equivalent circuit model was generated by mounting an identical inductor on a SMA connector. (The inductor equivalent circuit is given by the components inside of the dashed box on the left side of the figure.) The reflection coefficient of the inductor was measured using a HP8753 network analyzer. The

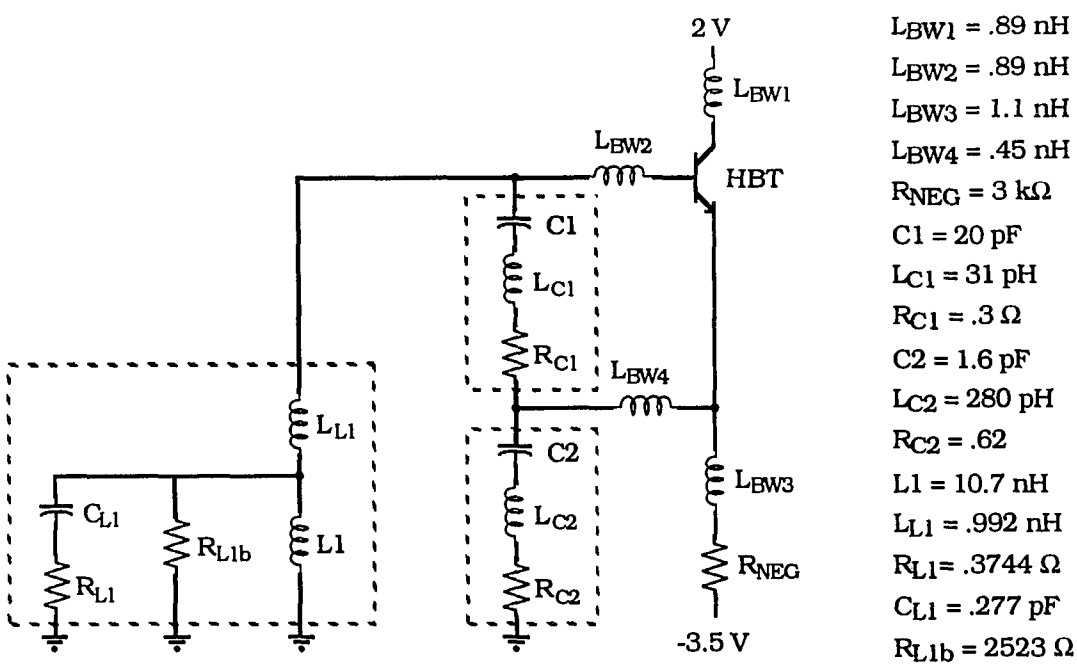

Figure 4.26. Oscillator Schematic Including Interconnect Parasitic Elements

measured data was then loaded into the software program LIBRA to generate the equivalent circuit model shown in Figure 4.26. The measured and modelled inductor data sets are shown in Figure 4.27. (There are actually two curves in this figure.) In the equivalent circuit model, inductor L_{L1} accounts for the interconnect lead and bondwire inductance, L1 accounts for the inductor itself, C_{L1} models the interwinding capacitance, and the resistors R_{L1} and R_{L1b} account for the loss associated with the inductor. A more conventional inductor model might account for the losses with a single series resistance. However, the configuration shown in Figure 4.26 allows the inductor losses to increase with frequency. Accordingly, this configuration can be used to account for phenomenon such as the skin effect.

The Colpitts oscillator topology used in this research has previously been analyzed by Parzen [33]. Extending his work to the oscillator shown in Figure 4.26 gives a loaded Q of,

$$Q_L \cong \frac{\dfrac{1}{\omega (C_1 + C_{BE})} + \dfrac{1}{\omega (C_2 + C_{CE})}}{\dfrac{(\omega L_1)^2}{R_{L1b}} + R_{C1} + R_{C2} + \dfrac{1}{R_{BE}(\omega C_1)^2} + \dfrac{1}{R_{NEG}(\omega C_2)^2}} . \qquad (4.27)$$

Applying Equation 4.27, to the oscillator analyzed in this work, yields a Q_L of approximately 17. This is a typical Q_L for oscillators which employ a lumped element tank circuit. It should be noted that Equation 4.27 was derived using small signal parameters. Thus, it is only approximate under the true large signal conditions of the

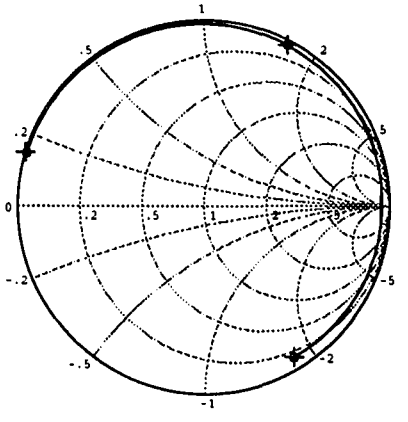

• Modelled Data
+ Measured Data

Frequency Range:
.1 GHz – 6 GHz

Figure 4.27. Modelled and Measured Inductor Refection Coefficient

oscillator.

The oscillator model shown in Figure 4.26 was analyzed in both SPICE [63] and LIBRA [49]. The circuit file listings are given in Appendix C. The SPICE file listing used the HBT model discussed in Section 4.1. However, the software program LIBRA does not contain nonlinear controlled sources, and thus is not capable of implementing the base-emitter diffusion capacitance model developed in this work. The diffusion capacitance model in LIBRA was developed using the standard Gummel-Poon diffusion capacitance model and a parallel constant capacitance. It should be noted that the value of τ_f used in this model was selected to match the bias condition of the oscillator. Thus, the LIBRA model is only accurate for HBT bias conditions near those of the oscillator. The SPICE simulation was implemented by performing a transient analysis over a period of 1 μs and a frequency of oscillation of 1.0825 GHz was obtained. By comparison, the LIBRA simulation indicated that the frequency of oscillation was 1.0824 GHz. Thus, the two simulations are in excellent agreement. This indicates that the SPICE transient analysis was carried out long enough to essentially reach a steady state condition. (As discussed in Appendix A, the only results produced by the LIBRA simulation are steady state.) The primary purpose of performing the LIBRA simulation was to verify the steady state condition of the SPICE simulation, and to demonstrate the use of harmonic balance algorithms in analyzing oscillators. Since the SPICE simulation was performed with a more accurate base-emitter diffusion capacitance model, the results of this simulation are used throughout the rest of this paper. The results of the SPICE simulation were also found to be in good agreement with the measured results. The simulated frequency of oscillation was found to be 1.0825 GHz versus a measured value of 1.0575 GHz. In addition, the simulated positive and negative supply currents were simulated to be .7439 mA and .7535 mA versus measured values of .776 mA and .784 mA respectively. These results indicate that the large signal oscillator model is quite accurate.

The voltage waveforms at the intrinsic base and emitter terminals of the HBT are shown in Figure 4.31. The voltage swing at the base and emitter terminals is roughly 3 V peak-to-peak, and very sinusoidal. This sinusoidal waveshape is very desirable as it indicates that the nonlinearities required to limit the amplitude of the oscillator are minimal. Accordingly, the amount of flicker noise which is upconverted to the oscillator sidebands is reduced. In addition, note that the base voltage does not exceed 2 V and thus

the base-collector voltage is not forward biased during any portion of the sinusoidal oscillation. This is also a favorable result. In many Colpitts oscillators, limiting occurs as a result of forward bias across the base-collector terminals. This produces a low resistance across the base-collector junction which is effectively in parallel with the resonator circuit in the oscillator. Accordingly, the Q_L of the oscillator can be severely degraded if the base-collector junction becomes forward biased. However, it is also undesirable to limit the signal swing to a very low level. As discussed in Section 2.5, the phase noise of the oscillator is inversely proportional to the available power. Accordingly, it is desirable to make the signal swing as large as possible. The 3 V signal swing obtained represents a reasonable compromise between keeping the base-collector junction reverse biased, and maximizing the signal swing.

The base-emitter voltage waveform is also plotted in Figure 4.31. This waveform is also nearly sinusoidal, and only varies by a few tenths of a volt. It is also desirable to keep this signal swing to a minimum. A small V_{BE} signal swing reduces the modulation of C_{BE} and R_{BE} and thus tends to reduce the amount of flicker noise which is upconverted. However, the amount of voltage swing across the base-emitter junction also determines the loop gain of the oscillator. If the loop gain is set too small, then no oscillations will occur. Thus, a compromise exists between the amount of oscillator loop gain and the upconversion of flicker noise.

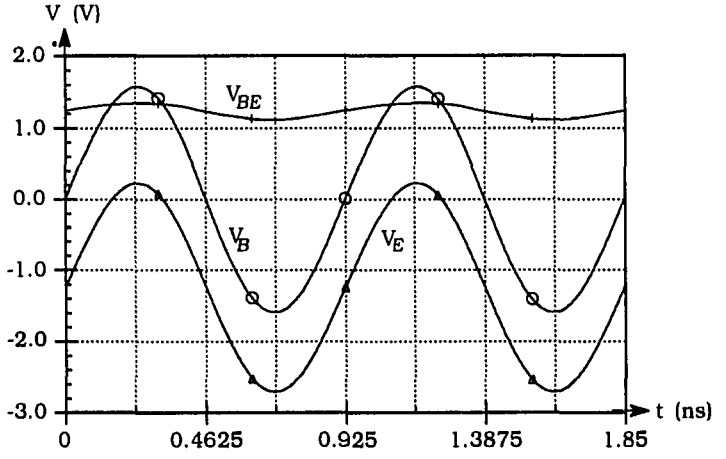

Fig 4.31. Simulated Oscillator Voltage Waveforms

The current waveforms which exist in the HBT are shown in Figure 4.32. The base current is roughly sinusoidal and 90° out of phase with the voltage waveforms. This indicates that the base current is largely a result of the current through a capacitance in the HBT. The waveforms I_E and I_C indicate that the base current is primarily associated with the base-collector capacitance. As shown in Figure 4.31, V_{BC} has a signal swing roughly an order of magnitude greater than V_{BE}. As a result, even though C_{BE} is greater than C_{BC}, the current through the base-collector capacitance is much larger. The I_E waveform appears to consist primarily of current "pulses" when V_{BE} is at its peak value. This indicates that the emitter current is primarily a result of diffusion current and does not have a large component of displacement current through C_{BE}. The collector current waveform equals the difference between I_E and I_B as required by Kirchhoff's current law.

The current waveforms in the resonator components of the oscillator are shown in Figure 4.33. Note that all of these waveforms are nearly sinusoidal which indicates that the oscillator is not operating in a heavily nonlinear manner. All of the resonator currents are much larger than the HBT emitter current. This is expected and very desirable since the ratio of the emitter current to the current in the resonator gives an indication of the loaded Q of the oscillator under large signal conditions. The current which is supplied by the HBT compensates for the power dissipated in the resonator. Thus, the energy supplied by the HBT during each cycle, at the frequency of oscillation, is equal to the energy dissipated in the resonator, and load resistor. The loaded Q of the

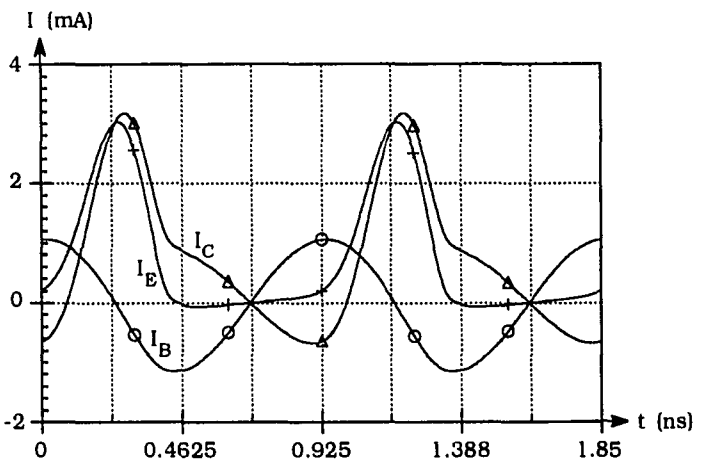

Fig 4.32. Simulated HBT Current Waveforms

5. CONVERSION NETWORKS

In order to determine how much amplitude and phase noise is present in an oscillator, it is necessary to analyze the conversion of noise between the various sidebands of the oscillator. The flicker noise sources in the oscillator, for example, will be upconverted to both of the oscillator sidebands at all of the harmonic frequencies. These sidebands may then be reconverted to other harmonics of the oscillator. The conversion of noise between the different harmonic frequencies is caused by two different mechanisms: the modulation of the nonlinear noise sources, and the mixing action which occurs in the circuit nonlinearities. The latter mechanism is considered in this section.

5.1. Large-Signal-Small-Signal Analysis

In order to determine how much noise is upconverted and downconverted between the various sidebands of an oscillator, it is necessary to derive a set of equations which govern the relationships between *incremental* changes in oscillator voltages and currents. This approach to modeling nonlinear circuits is known as a large-signal-small-signal analysis or conversion matrix theory. It was developed primarily for the purpose of analyzing microwave mixers [20, 67]. As a result, this theory has been applied primarily to MESFET circuits since these devices offer superior mixer performance. It appears that the experimental analysis of microwave oscillators based on conversion matrix theory has been reported on only a few occasions [7, 19, 21].

The basic premise of a large-signal-small-signal analysis is that a nonlinear circuit is excited by two signals: a large periodic signal and a vanishingly small signal. In the case of an oscillator, the large signal is the steady state nominal oscillation, and the small signal is the noise which perturbs the oscillation from this nominal condition. The small signal level is assumed to be low enough that any higher order products of this signal, which are generated within the oscillator nonlinearities, are negligible. For example, if a 1 V sinusoid and a 1 mV sinusoid are applied to an ideal nonlinear square law amplifier, then the output voltage is given by,

$$V_{out}(t) = [\sin(\omega_o t) + .001 \sin(\omega_m t)]^2 \quad (5.1)$$

$$Vout(t) = \sin^2(\omega_o t) + .002 \sin(\omega_o t) \sin(\omega_m t) + 10^{-6} \sin^2(\omega_m t) \quad (5.2)$$

$$Vout(t) = \frac{1 - \cos(2\omega_o t)}{2} + .001 [\cos((\omega_o - \omega_m)t) - \cos((\omega_o + \omega_m)t)] + \frac{10^{-6}}{2} [1 - \cos(2\omega_m t)]. \quad (5.3)$$

In a large-signal-small-signal analysis, the last term on the right side of Equation 5.3 would be ignored. This term is associated with the square of the small-signal sinusoid, and is considered to be negligible with respect to the amplitude of the other terms. In general, if the small-signal is several orders of magnitude lower than the large signal, then the higher order terms associated with the small signal may be ignored. In the case of oscillators, the small signal is noise which will be very small in comparison to the amplitude of oscillation. It should also be noted that this same approximation is made when a small-signal model of any nonlinear component is generated. (The hybrid-pi transistor model is an example of this.) The only difference is that in the case of large-signal-small-signal analyses, the nominal bias condition is time varying. Figure 5.1 shows the frequency components which are considered in a large-signal-small-signal analysis. From the diagram, it can be seen that no frequencies which are multiples of the small signal frequency, ω_m, are considered.

The nonlinearities of the oscillator may be modelled by first analyzing the large signal characteristics of the oscillator with no noise present. This analysis was performed in Section 4. A perturbing noise source is then injected into the oscillator model and its impact on the oscillator may be analyzed. The theory which is required to perform this analysis will now be derived.

Consider the simple case of a nonlinear resistor which is excited by a large periodic

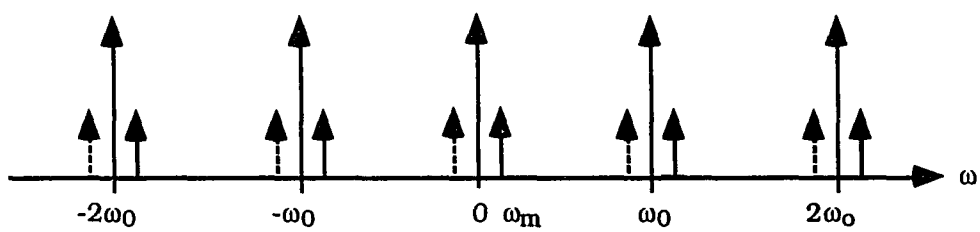

Figure 5.1. Frequency Components Considered in a Large-Signal-Small-Signal Analysis

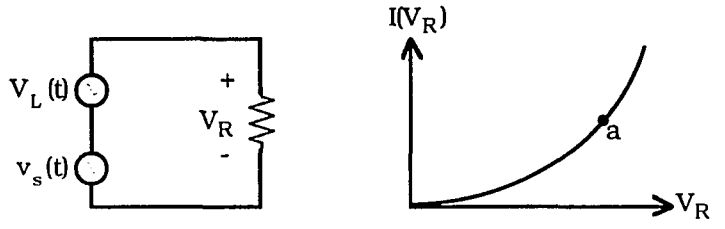

(a) Nonlinear Circuit (b) Nonlinear Resistor I-V Curve

Figure 5.2. Nonlinear Resistor Driven by a Large and a Small-Signal Voltage Source

voltage source, $V_L(t)$, and a vanishingly small voltage source, $v_s(t)$. This circuit is shown in Figure 5.2 along with the I-V characteristic of the nonlinear resistance. (This I-V characteristic is arbitrary.) Since $v_s(t)$ is very small, the voltage and current through the resistor are established by $V_L(t)$. The small signal voltage may be viewed as simply perturbing the resistor bias from this large signal condition. Consider the bias across the resistor at a given instant in time, t, which is established by the large signal voltage source. This bias condition is labelled as point a in Figure 5.2b. The small signal incremental voltage, $v_s(t)$, will perturb the bias from this point a and will create an incremental current, $i_s(t)$, given by,

$$i_s(t) = g(t)\, v_s(t). \tag{5.4}$$

where g(t), the incremental conductance of the nonlinear resistor at time t, is given by

$$g(t) = \frac{\delta I[V_R(t)]}{\delta V_R(t)}. \tag{5.5}$$

In other words, g(t) is the slope of the curve given in Figure 5.2b at point a. Note that Equations 5.4 and 5.5 are identical to those which are used to generate a small signal model of any nonlinear resistance such as a diode. The only difference is that in this case the bias condition of the component is set by a time varying large-signal voltage. Since the bias condition of the nonlinear resistor varies in a periodic manner, the incremental conductance, g(t), will also vary as a periodic function of time. Accordingly, it may be represented by a Fourier series as given by Equation 5.6.

$$g(t) = \sum_{k=-\infty}^{\infty} G_k e^{jk\omega_o t} \tag{5.6}$$

In Equation 5.6, ω_o is the radian frequency of the large signal voltage.

It is now necessary to develop a function which describes the small signal voltage source, $v_s(t)$. It is desirable to make this function as general as possible so that it may be applied to a wide variety of nonlinear circuits such as mixers or oscillators. If a small voltage is applied to an oscillator, for example, at a frequency ω_m away from any harmonic of the oscillator, then spurious signals will be generated in the oscillator at all of the sidebands as shown in Figure 5.1. Thus the small level signal will have components at any frequency which is ω_m above and below each harmonic of the oscillator. Thus, a general expression for $v_s(t)$ must contain all of the small-signal frequency components which are shown in Figure 5.1. Noting that these components are at frequencies given by $p\omega_0 \pm \omega_m$,

$$v_s(t) = \frac{1}{\sqrt{2}} \sum_{p=-\infty}^{\infty} \left[V_p e^{j(\omega_m + p\omega_o)t} + V_p^* e^{j(-\omega_m - p\omega_o)t} \right] = \sqrt{2} \sum_{p=-\infty}^{\infty} |V_p| \cos\left[(\omega_m + p\omega_o)t + e^{jV_p}\right] . \tag{5.7}$$

The $\sqrt{2}$ in the above equation is included so that V_p is an rms value. The incremental current which results from $v_s(t)$ will in general also have all of the same frequency components.

$$i_s(t) = \frac{1}{\sqrt{2}} \sum_{n=-\infty}^{\infty} \left[I_n e^{j(\omega_m + n\omega_o)t} + I_n^* e^{j(-\omega_m - n\omega_o)t} \right] = \sqrt{2} \sum_{p=-\infty}^{\infty} |I_p| \cos\left[(\omega_m + p\omega_o)t + e^{jI_p}\right] \tag{5.8}$$

Equations 5.4 and 5.6 through 5.8 may be combined to yield,

$$\sum_{n=-\infty}^{\infty} \left[I_n e^{j(\omega_m + n\omega_o)t} + I_n^* e^{j(-\omega_m - n\omega_o)t} \right] = \sum_{k=-\infty}^{\infty} G_k e^{jk\omega_o t} \sum_{p=-\infty}^{\infty} \left[V_p e^{j(\omega_m + p\omega_o)t} + V_p^* e^{j(-\omega_m - p\omega_o)t} \right] \tag{5.9}$$

The above equation must hold for each discrete frequency component. Equating the components at radian frequencies of $n\omega_0 + \omega_m$,

$$I_n e^{j(\omega_m + n\omega_0)t} = \sum_{p=-\infty}^{\infty} G_{n-p} V_p e^{j(\omega_m + n\omega_0)t} \tag{5.10a}$$

or,

$$I_n = \sum_{p=-\infty}^{\infty} G_{n-p} V_p \tag{5.10b}$$

Equating the components of Equation 5.9 at the radian frequencies of $-n\omega_0 - \omega_m$,

$$I_n^* e^{j(-\omega_m - n\omega_0)t} = \sum_{p=-\infty}^{\infty} G_{p-n} V_p^* e^{j(-\omega_m - n\omega_0)t} \tag{5.11a}$$

or,

$$I_n^* = \sum_{p=-\infty}^{\infty} G_{p-n} V_p^* \tag{5.11b}$$

Taking the complex conjugate of Equation 5.11b and noting that G_{p-n}^* equals G_{n-p}, demonstrates that Equations 5.10b and 5.11b are redundant. Equation 5.10b may be written for various values of n to yield matrix Equation 5.12. This matrix equation has been truncated at N harmonics in order to prevent the occurrence of an infinite dimension matrix. The incremental currents and voltages are assumed to be negligible for harmonics greater than N. The number of harmonics, N, which must be considered in a given analysis is dependent on the nonlinear circuit. However, the incremental currents and voltages will always be negligible at frequencies higher than some harmonic

$$\begin{bmatrix} I_{-N} \\ I_{-N+1} \\ I_{-N+2} \\ \vdots \\ I_{-1} \\ I_0 \\ I_1 \\ \vdots \\ I_{N-1} \\ I_N \end{bmatrix} = \begin{bmatrix} G_0 & G_{-1} & G_{-2} & \cdots & G_{-2N} \\ G_1 & G_0 & G_{-1} & \cdots & G_{-2N+1} \\ G_2 & G_1 & G_0 & \cdots & G_{-2N+2} \\ \vdots & \vdots & \vdots & & \vdots \\ G_{N-1} & G_{N-2} & G_{N-3} & \cdots & G_{-N-1} \\ G_N & G_{N-1} & G_{N-2} & \cdots & G_{-N} \\ G_{N+1} & G_N & G_{N-1} & \cdots & G_{-N+1} \\ \vdots & \vdots & \vdots & & \vdots \\ G_{2N-1} & G_{2N-2} & G_{2N-3} & \cdots & G_{-1} \\ G_{2N} & G_{2N-1} & G_{2N-2} & \cdots & G_0 \end{bmatrix} \begin{bmatrix} V_{-N} \\ V_{-N+1} \\ V_{-N+2} \\ \vdots \\ V_{-1} \\ V_0 \\ V_1 \\ \vdots \\ V_{N-1} \\ V_N \end{bmatrix} \tag{5.12}$$

since every practical circuit has a finite bandwidth.

The significance of Equation 5.12 should not be underestimated. It describes a *linear* relationship between the various frequency components of the *incremental* voltages and currents in the nonlinear resistor shown in Figure 5.2. However, the derivation of this matrix equation is general enough that it may be applied to any nonlinear resistance in a given circuit. The center matrix in Equation 5.12 is referred to in literature as a conversion matrix [17]. It may be used to determine the level of frequency conversion which occurs in a nonlinear circuit. For example, suppose the small voltage source in Figure 5.2 contains only a single frequency component at a frequency which is ω_m radians-per-second above the first harmonic. Then Equation 5.7 could be used to describe this voltage source which would only consist of the components V_1 and V_1^*. The value of V_1 could be substituted into Equation 5.12 to determine the small signal current components, I_{-N} .... I_N, at all of the sidebands of the large signal harmonics. The current components could then be substituted into Equation 5.8 to generate an expression for the small-signal time varying current.

A conversion matrix equation for a nonlinear capacitor may be derived in a similar manner to yield [17].

$$\begin{bmatrix} I_{-N} \\ I_{-N+1} \\ I_{-N+2} \\ \vdots \\ I_{-1} \\ I_0 \\ I_1 \\ \vdots \\ I_{N-1} \\ I_N \end{bmatrix} = \begin{bmatrix} C_0\,j\,\omega_{-N} & C_{-1}\,j\,\omega_{-N} & C_{-2}\,j\,\omega_{-N} & \cdots & C_{-2N}\,j\,\omega_{-N} \\ C_1\,j\,\omega_{-N+1} & C_0\,j\,\omega_{-N+1} & C_{-1}\,j\,\omega_{-N+1} & \cdots & C_{-2N+1}\,j\,\omega_{-N+1} \\ C_2\,j\,\omega_{-N+2} & C_1\,j\,\omega_{-N+2} & C_0\,j\,\omega_{-N+2} & \cdots & C_{-2N+2}\,j\,\omega_{-N+2} \\ \vdots & \vdots & \vdots & & \vdots \\ C_{N-1}\,j\,\omega_{-1} & C_{N-2}\,j\,\omega_{-1} & C_{N-3}\,j\,\omega_{-1} & \cdots & C_{-N-1}\,j\,\omega_{-1} \\ C_N\,j\,\omega_0 & C_{N-1}\,j\,\omega_0 & C_{N-2}\,j\,\omega_0 & \cdots & C_{-N}\,j\,\omega_0 \\ C_{N+1}\,j\,\omega_1 & C_N\,j\,\omega_1 & C_{N-1}\,j\,\omega_1 & \cdots & C_{-N+1}\,j\,\omega_1 \\ \vdots & \vdots & \vdots & & \vdots \\ C_{2N-1}\,j\,\omega_{N-1} & C_{2N-2}\,j\,\omega_{N-1} & C_{2N-3}\,j\,\omega_{N-1} & \cdots & C_{-1}\,j\,\omega_{N-1} \\ C_{2N}\,j\,\omega_N & C_{2N-1}\,j\,\omega_N & C_{2N-2}\,j\,\omega_N & \cdots & C_0\,j\,\omega_N \end{bmatrix} \begin{bmatrix} V_{-N} \\ V_{-N+1} \\ V_{-N+2} \\ \vdots \\ V_{-1} \\ V_0 \\ V_1 \\ \vdots \\ V_{N-1} \\ V_N \end{bmatrix} \tag{5.13}$$

where each frequency in the above equation is given by,

$$\omega_n = \omega_m + n\,\omega_o. \tag{5.14}$$

At this point, a word of caution about the notation which has been used is appropriate. Each of the subscripts of the frequency variable given in Equation 5.13 are in italics. This was done to avoid confusion between the frequency of oscillator, ω_o, and the frequency given by Equation 5.14 when the subscript n is equal to zero. These two frequencies are not identical. The variable ω_o refers to the fundamental frequency of the large signal, while the variable ω_0 is equal to the frequency offset of the small signal, ω_m. It should also be noted that the conventions used to describe the conversion matrices in Equations 5.12 and 5.13 are not uniform throughout literature. The convention used in this paper is believed to be the most widely accepted and is identical to that used by Held and Kerr [17]. This convention is different than that used by Maas [18, 67].

A conversion matrix may also be generated for any linear component. For example, if the resistor in Figure 5.2 were modelled as a linear device, then it would not vary as a function of time under large signal conditions. Since the resistance would not be time dependent, the conductance, g(t) in Equation 5.6 would be equal to the constant, G_0. All of the other Fourier coefficients in Equation 5.6 would be equal to zero. Thus, the conversion matrix in Equation 5.12 would be a diagonal matrix. In a similar manner, for a linear capacitor, the conversion matrix in Equation 5.13 would also be a diagonal matrix since the capacitance would not be time varying. In general, the conversion matrix of any linear device may be expressed as,

$$\begin{bmatrix} I_{-N} \\ I_{-N+1} \\ I_{-N+2} \\ \vdots \\ I_{-1} \\ I_0 \\ \\ \vdots \\ I_{N-1} \\ I_N \end{bmatrix} = \begin{bmatrix} Y(\omega_{-N}) & 0 & \cdots & 0 & \cdots & 0 \\ 0 & Y(\omega_{-N+1}) & \cdots & 0 & \cdots & 0 \\ 0 & 0 & \cdots & 0 & \cdots & 0 \\ \vdots & \vdots & & \vdots & & \vdots \\ 0 & 0 & \cdots & 0 & \cdots & 0 \\ 0 & 0 & \cdots & Y(\omega_0) & \cdots & 0 \\ 0 & 0 & \cdots & 0 & \cdots & 0 \\ \vdots & \vdots & & \vdots & & \vdots \\ 0 & 0 & \cdots & 0 & \cdots & 0 \\ 0 & 0 & \cdots & 0 & \cdots & Y(\omega_N) \end{bmatrix} \begin{bmatrix} V_{-N} \\ V_{-N+1} \\ V_{-N+2} \\ \vdots \\ V_{-1} \\ V_0 \\ V_1 \\ \vdots \\ V_{N-1} \\ V_N \end{bmatrix} \tag{5.15}$$

Thus, for a linear component, the small signal voltage and current at any harmonic sideband is related by the admittance of the component at the sideband frequency. In a similar manner, the small signal voltages and currents associated with a linear multiport network are related by the multiport parameters of the linear network at any given sideband frequency. This same result can be obtained using the concept of superposition. If a given network is linear, no frequency conversion will occur between any signals. Accordingly, superposition can be applied to describe the relationships between the small signal voltages and currents at each sideband frequency. These relationships are defined by the multiport parameters of the given linear circuit.

The above approach shows the basis for analyzing the frequency conversion of noise between the various sidebands of the oscillator. A conversion matrix analysis may be applied to an oscillator by first considering the waveforms to be perfectly periodic with no noise sidebands. This is the purpose of the large-signal oscillator analysis which is discussed in Section 4.2. This large-signal analysis establishes the amplitude of the oscillations and the time variation of all of the incremental conductances within the oscillator. A conversion matrix analysis may be applied to this oscillator by representing each component in the oscillator by an equivalent linear conversion network. This analysis is presented in Section 5.2.

5.2. Conversion Network Representation of the Oscillator

The conversion matrices discussed in Section 5.1, can be used to model the conversion of noise between the various harmonics of an oscillator. This model is generated by first simulating the large signal characteristics of the oscillator assuming that no noise is present. This simulation is used to establish the large signal waveforms within the oscillator. The large signal waveforms may then be used to establish the time variation in the incremental admittances of the nonlinear components within the oscillator model. The resulting time varying incremental admittances can then be used to establish the conversion matrix for the nonlinear element. As an example, consider to the base-emitter resistance of the HBT. This nonlinear resistance is a result of the two current sources, I_{CC}/β_f and I_{RF}, shown in Figure 4.4. As discussed in Section 4.1, the

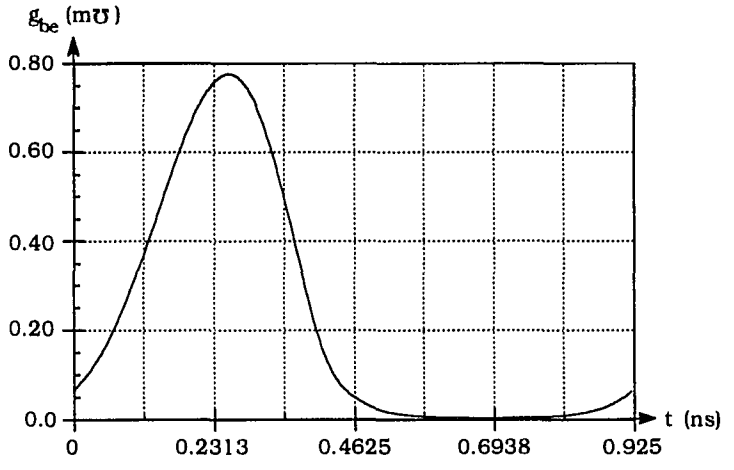

Figure 5.3. Time Variation of g_{be}

heterojunction in the HBT makes current source I_{CC}/β_f negligible in comparison to I_{RF}. Therefore, from Equation 4.5, the incremental base-emitter conductance can be expressed as,

$$g_{be} = \frac{\delta I_{RF}}{\delta V_{BE}} = \frac{q\, I_{SE}}{N_E\, k\, T}\left[e^{(q\, V_{BE}/N_E\, k\, T)}\right] \tag{5.16}$$

Using the above equation, the parameter values given in Table 4.1, and the V_{BE} waveform given in Figure 4.31, g_{be} can be plotted as a function of time as shown in Figure 5.3. The Fourier transform of the data in Figure 5.3 can then be combined with Equation 5.12 to generate the conversion matrix of g_{be}.

Using a similar approach, the Fourier series and conversion matrices of all of the nonlinear components in the oscillator can be generated. Expressions for the incremental values of all on the nonlinear components in the Gummel-Poon model have previously been reported by Antognetti and Massobria [46]. These expressions were used to generate waveforms for g_m, g_{be}, g_{bc}, g_o, $c_{bc_{int}}$, and $c_{bc_{ext}}$. The waveform for c_{be} was generated using Equations 4.11, 4.26, and the data associated with the solid curve in Figure 4.16. The Fourier coefficients associated with these waveforms are given in Table 5.1. The Fourier series associated with the data in this table is of the form given by Equation 5.6. Note that the Fourier coefficients of g_{bc} are not given in Table 5.1. As

Table 5.1. Fourier Coefficients of the Nonlinear Elements in the HBT Oscillator Model

Element	Magnitude (μ℧, fF)	Angle (°)	Element	Magnitude (μ℧, fF)	Angle (°)
g_{m_0}	22070	0.0	g_{be_0}	219.2	0.0
g_{m_1}	18130	-93.08	g_{be_1}	169.3	-92.46
g_{m_2}	10060	170.2	g_{be_2}	83.30	170.0
g_{m_3}	3603	61.91	g_{be_3}	27.05	57.34
g_{m_4}	975.4	-89.06	g_{be_4}	8.039	-92.75
g_{m_5}	609.6	106.9	g_{be_5}	4.000	109.4
g_{o_0}	1.545	0.0	c_{be_0}	124.3	0.0
g_{o_1}	1.284	-93.38	c_{be_1}	27.55	-89.39
g_{o_2}	0.7422	169.9	c_{be_2}	3.546	153.0
g_{o_3}	0.2926	63.44	c_{be_3}	1.4775	-29.62
g_{o_4}	0.08372	-72.34	c_{be_4}	0.8960	-159.8
g_{o_5}	0.03942	122.3	c_{be_5}	0.4070	51.74
$c_{bc_{int0}}$	17.61	0.0	$c_{bc_{ext0}}$	55.48	0.0
$c_{bc_{int1}}$	0.9941	-90.58	$c_{bc_{ext1}}$	3.131	-90.66
$c_{bc_{int2}}$	0.1841	173.4	$c_{bc_{ext2}}$	0.5795	173.2
$c_{bc_{int3}}$	0.04381	77.24	$c_{bc_{ext3}}$	0.1377	76.96
$c_{bc_{int4}}$	0.01184	-19.41	$c_{bc_{ext4}}$	0.03712	-19.61
$c_{bc_{int5}}$	0.003426	-127.4	$c_{bc_{ext5}}$	0.01077	-127.3

demonstrated by Figure 4.31, the base-collector junction of the HBT is reverse biased over the entire oscillation cycle. As a result, g_{bc} never exceeds 10^{-11} mhos. This small level of conductance was considered negligible, and g_{bc} was eliminated from the linearized oscillator model. (This linearized model is discussed in the later portions of this section.)

The Fourier coefficients in the above table provide some indication of the dominant nonlinearities in converting noise between the sidebands of the oscillator. For example, Equations 5.12 and 5.13 demonstrate that the amount of 1/f noise which is upconverted

to both oscillator sidebands is determined by the Fourier coefficient associated with the first harmonic. Thus, the ratio of the Fourier coefficient associated with the first harmonic to that associated with the average value gives an indication of how much 1/f noise the nonlinear element upconverts. The data in Table 5.1 indicate that the nonlinear conductances will be dominant in upconverting the 1/f noise. However, the impedances of the elements also play a role in determining how much 1/f noise they will upconvert. Since the transconductance, g_m, has the largest impact of all the conductances on the terminal impedances of the HBT, it is likely that this nonlinear element is dominant in upconverting 1/f noise in the HBT.

The conversion matrices and the data given in Table 5.1 can also be used to model the characteristics of the oscillator in a much more in-depth manner. The conversion matrices can be used to describe the linear relationships between the small signal voltages and currents at all of the oscillator sidebands. These matrices can be manipulated to analyze the characteristics of the oscillator. However, a much more insightful approach is to represent each conversion matrix as a linear circuit which has the same relationships between the voltages and currents as the conversion matrix. Such a linear circuit may be referred to as a conversion network. This approach yields a linear circuit which models the conversion of noise between all of the harmonics of the oscillator. As an example, consider the conversion matrix for a nonlinear conductance as given by Equation 5.12. If the number of harmonics, N, which are considered in the analysis is set to 2, then the equivalent conversion network is given as shown in Figure

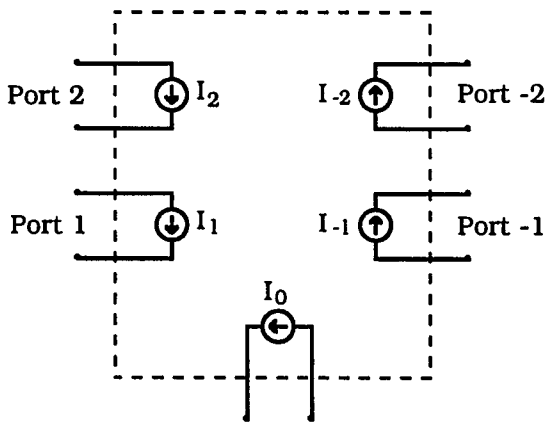

Figure 5.4. Conversion Network for a Nonlinear Conductance

5.4. Each of the current sources in this figure are defined in Equation 5.12. By using voltage controlled current sources to generate these currents, the voltages and currents produced by the conversion network satisfy this equation.

A similar technique can be used to generate conversion networks for a nonlinear transconductance and nonlinear capacitance. This may be accomplished using the software program LIBRA™. Circuit file listings which which can be used to create a conversion network for any of the nonlinear components mentioned above are given in Appendix D. These circuit file listings can be used to generate a conversion network for any nonlinear element by entering the Fourier coefficients of the element in the variable block. The resulting parameters of the conversion network are automatically stored in an output file. This output data set is essentially equivalent to the conversion matrix of the element-stored in S-parameter form. The conversion matrices given in Equations 5.12, 5.13, and 5.15 are in Y-parameter form. It is interesting to note that conversion matrices can also be expressed in any other N-port form such as Z-parameters or H-parameters [67].

A conversion network for a linear circuit can be generated in a very simple manner. As mentioned in Section 5.1, the conversion network of a linear circuit is identical to the circuit itself analyzed at each sideband frequency. This is also indicated by Equation 5.13. Thus, the conversion network of any linear circuit can be generated by simply analyzing the circuit itself.

The techniques discussed above were used to generate a conversion network model of the oscillator. A diagram of the overall conversion network of the oscillator is shown in Figure 5.5. The model accounts for the baseband frequency and two harmonics of the oscillator. This results in a total of five sideband frequencies: one for the baseband frequency, the two sidebands of the first harmonic, and the two sidebands of the second harmonic. (The tradeoffs in selecting the number of harmonic frequencies is discussed in the latter portions of this section.)

A conversion network for each of the nonlinear conductances, g_{be} and g_o, was characterized using the second circuit file listing in Appendix D. As indicated by Equation 5.12, since the conductances are nonlinear, a small signal at any sideband

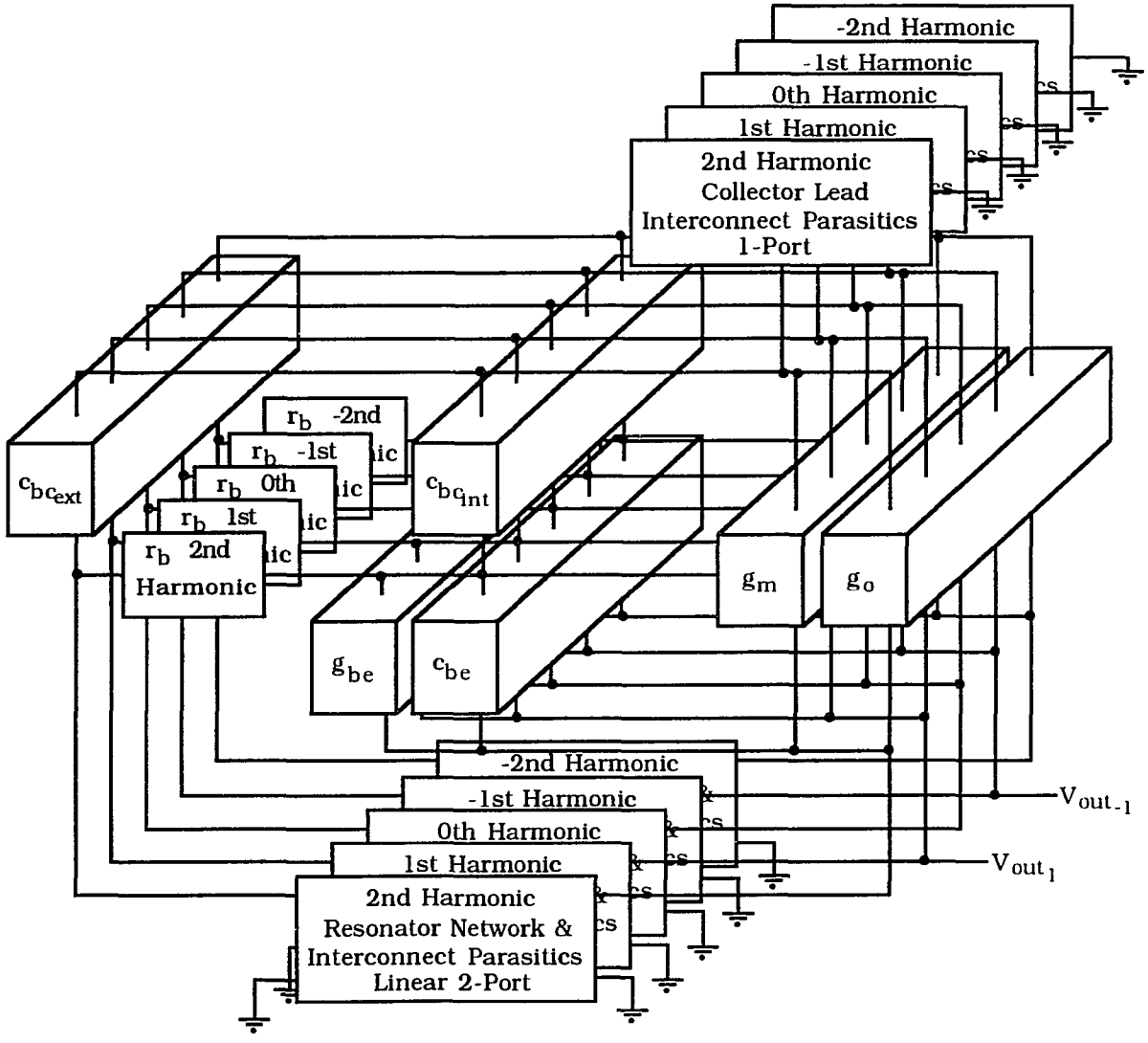

Figure 5.5. Conversion Network Representation of the HBT Oscillator

frequency will effect the small signal level at all of the other sideband frequencies. Thus, all of the sideband frequencies must be considered in the same network. Since a total of five sideband frequencies are considered in this analysis, and each nonlinear conductance has two terminals associated with it, a 10-port network is required to describe each nonlinear conductance as shown in Figure 5.5.

The conversion network for the nonlinear transconductance was characterized using the third circuit file listing in Appendix D. This nonlinear device requires a 15-port network to describe it. Again in this case, since the transconductance is a nonlinear device, the small signal currents and voltages at all five sideband frequencies interact. The transconductance has three terminals associated with it. The intrinsic base and emitter terminals are the controlling nodes, and the collector and emitter terminals are the nodes which the current flows across. The three terminals multiplied by the five harmonic frequencies results in a 15-port conversion network as shown in Figure 5.5.

The conversion networks for the nonlinear capacitors are somewhat similar to the nonlinear resistors. The nonlinear capacitors are two terminal elements which must be analyzed at five sideband frequencies. Thus, the conversions networks are 10-port circuits as shown in Figure 5.5. The circuit file which was used to characterize the nonlinear capacitors is given in the fourth listing in Appendix D.

All of the other elements in the oscillator model are linear components. These include the elements associated with the resonator circuitry shown in Figure 4.26, and the parasitic HBT interconnect elements shown in Figure 4.4. Since all of these components are linear, no frequency conversion will occur between the oscillator sidebands. As a result, the linear elements may be analyzed in a much more efficient manner. Note from Figure 5.5, that each individual nonlinear element requires a large multiport network to characterize it. However, the linear elements can all be analyzed as a network instead of as individual elements. In addition, since no frequency conversion occurs in the linear elements, these devices can be modelled by a set of networks with much smaller dimensions. (Typically one or two port networks.) This is shown by the set of networks at the top and bottom of Figure 5.5, and the base resistors, r_b, shown on the left side of Figure 5.5. Each of these linear circuits is modelled by a set of five networks– one for each sideband frequency.

Consider the set of networks shown on the bottom of Figure 5.5. This set of 2-port networks models all of the linear components shown in Figure 4.26, with the exception of L_{BW1}. In addition, some of the interconnect parasitics shown in Figure 4.4 are included in the 2-port network. These interconnect parasitics include the 20.2 fF capacitor, the 47.4 pH inductor, the 3.8 fF capacitor, the emitter resistance, and the 70.3 pH inductor. The first of these networks, shown in front in Figure 5.5, represents the characteristics of the 2-port at the upper sideband of the second harmonic. The second 2-port network represents the characteristics of the network at the upper sideband of the first harmonic. The last 2-port network represents the characteristics of the 2-port network at the frequency $\omega_m - 2\,\omega_o$ which also corresponds to the lower sideband of the second harmonic.

In a similar manner, the characteristics of the 1-port networks shown at the top of Figure 5.5 can be characterized. This 1-port linear network consists of L_{BW1} shown in Figure 4.26, the 22.6 fF capacitor shown in Figure 4.4, and the 41.2 pH inductor shown in Figure 4.4. Note that the positive and negative supply voltages which are connected to the 1-port and 2-port networks are shown as ac grounds in the conversion matrix model. The fifth and sixth LIBRA circuit file listings given in Appendix D were used to model the linear network at the baseband frequency, ω_m, and at the first harmonic. These files store the characteristics of both the 1-port and 2-port networks. Note that the 1.5 fF and 5 fF capacitors in Figure 4.4 were not included in the conversion matrix model. These capacitors were considered to be of small enough value to have a negligible effect of the conversion matrix model. The only remaining linear component is the base resistance, r_b. This element is not frequency dependent, and accordingly it was simply inserted as a resistor in the oscillator conversion network model.

Each of the multiport networks described above was analyzed in LIBRA and stored in a separate data file. Each block in Figure 5.5 represents a separate data file. All of these data files were then loaded into a main circuit file to generate an overall conversion network of the entire oscillator. The LIBRA circuit file which is a conversion network representation of the entire oscillator, is the first circuit file listed in Appendix D. Using this circuit file, the conversion of noise within the oscillator to the sidebands at the oscillator output can be modelled. For example, consider the thermal noise at the upper sideband of the second harmonic associated with the base resistance r_b. As discussed in

Section 2.2, this noise may be modelled by a current source in parallel with r_b. The conversion of this noise to the output can be determined by placing a current source in parallel with r_b at the second harmonic frequency and measuring the voltages which are produced at the upper and lower sidebands of the oscillator, V_{out-1} and V_{out1}. (See Figure 5.5.) Since the output is a voltage and the input noise source is modelled as a current, the conversion of the noise source to the output can be characterized by a transimpedance. This transimpedance is used in Section 7 to analyze the amplitude and phase noise characteristics of the oscillator which result from each noise source.

A typical oscillator transimpedance plot is shown in Figure 5.6. The lower curve in this figure shows the magnitude of the transimpedance of a current source from the collector to the emitter at the upper sideband of the first harmonic, to the upper sideband of the output voltage. Note that the transimpedance tends to be roughly inversely proportional to frequency for sideband frequencies greater than 1 MHz. For lower sideband frequencies, the transimpedance tends to have a flat response. Theoretically, the transimpedance should be roughly inversely proportional to offset frequency for all sideband frequencies close to the carrier. The flat response in the transimpedance is a result of a small error in the open loop response of the conversion network model of the oscillator. This can be seen from Equation 2.22. If a small error, ε, is introduced into the open loop response of the oscillator, then Equation 2.22 becomes (Any small error introduced into the numerator of the term on the right side of this equation will have an insignificant effect on the transfer function.),

$$\frac{V_{out}(\omega)}{e_n} = \frac{G(\omega)}{1 - G(\omega)\,\beta(\omega) + \varepsilon}. \tag{5.17}$$

As the frequency of the sidebands approaches the frequency of oscillator, the open loop transfer function, $G(\omega)\,\beta(\omega)$, will approach one. Therefore, the error term, ε, will tend to dominate the denominator on the right side of Equation 5.17 as the offset frequency approaches zero. This causes the flat response in Figure 5.6 at low offset frequencies.

The error in the open loop response of the oscillator is a result of two factors: numerical round off error, and the truncation of the conversion matrices which were used to generate the conversion network model of the oscillator. The error associated with the truncation of the conversion matrices will be considered first.

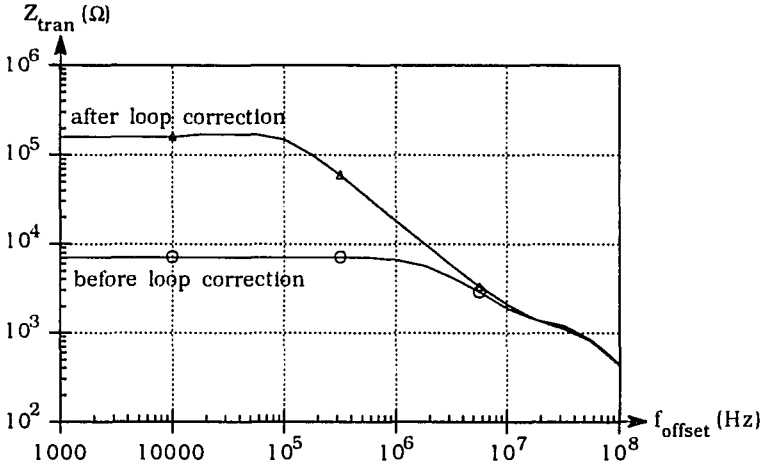

Figure 5.6. Oscillator Transimpedance Plot

As shown in Figure 5.5, the conversion network model of the oscillator considers frequencies up through the second harmonic of the oscillator. In reality, every harmonic of the oscillator will have some impact on the frequency conversion of noise. For example, some very small amount of 1/f noise will be upconverted to the tenth harmonic of the oscillator and this noise can in turn be reconverted down to the first harmonic of the oscillator. In order to account for these interaction effects, the higher order harmonics of ω_o would have to be considered in the conversion matrix model. However, as the number of harmonics which are considered in the model is increased, the size of the conversion network model increases significantly. If N harmonics of the oscillator are considered, then the number of sideband frequencies which must be included in the model is 2N+1. This is also the number of unique frequencies which the linear components must be modelled at. For example, the number of harmonics considered in the oscillator conversion network model was two and accordingly five sideband frequencies had to be analyzed for the linear components as shown in Figure 5.5. If three harmonics were considered then the number of sidebands frequencies would increase to seven, or by 40%. The situation is even more severe for the nonlinear components. The conversion matrices given in Equations 5.12 and 5.13 have dimensions of 2N+1 by 2N+1. As a result the size of a model which is required to characterize a nonlinear component is proportional to $(2N+1)^2$. If the number of harmonics which are considered in the analysis was increased from two to three, the size of the models for the nonlinear components

would nearly double. Thus, the selection of the number of harmonics represents a tradeoff between model accuracy and complexity.

The error associated with the truncation of the conversion networks may be compensated for by enforcing a condition of oscillation on the overall conversion network model. One such condition of oscillation which applies to the 2-port S-parameters of an open loop oscillator is given by Bahl [68] as

$$(S_{21} - 1)(S_{12} - 1) - S_{11} S_{22} = 0 . \qquad (5.18)$$

This condition of oscillation was derived on an oscillator model similar to that shown in Figure 2.3. The oscillator loop is broken at either the input or output of the amplifier, and the S-parameters of the resulting 2-port network must satisfy Equation 5.18 in order for the conditions of oscillation to be met. Equation 5.18 is essentially the same as the Barkhausen criteria for oscillation. However, the derivation of Equation 5.18 accounts for any impedance mismatches between the oscillator and the feedback circuit. The only assumption which is used in the derivation of Equation 5.18 is that the oscillator circuitry is modelled as being linear. In most oscillator analyses, this assumption is an approximation. However, in the linearized conversion network model, this assumption is satisfied. Thus, by enforcing Equation 5.18 on the oscillator conversion network, the error associated with the truncation of the conversion networks may be compensated for. The oscillator loop was broken at the first harmonic between the linear resonator network and the intrinsic base and the S-parameters of the resulting 2-port network were simulated in LIBRA. These S-parameters were entered into the left side of Equation 5.18 and the magnitude of the resulting error was 0.016. A series impedance was then entered into the oscillator loop at the positive and negative first harmonics. The impedance at the negative first harmonic was set to the complex conjugate of the impedance at the positive first harmonic as indicated by Equation 5.15. This series impedance was adjusted to enforce Equation 5.18. The magnitude of the error which was ultimately achieved was 0.00077. The transimpedance response which was obtained after this error correction was made is shown as the upper curve in Figure 5.6. Note that this curve is improved however, it still has a flat response for offset frequencies below 100 kHz. This flat response is a result of numerical round off error in LIBRA which is discussed on the following page. It is significant to note that the error given by Equation 5.18 can be reduced further. However, it results in a significant peaking of the upper curve in Figure

5.6 at frequencies near 30 kHz. This peaking is also a result of the numerical round off error. Due to this error, the conversion network model cannot accurately be used for frequencies below 100 kHz. However, the spectrum of the oscillator for offset frequencies below 100 kHz can be extrapolated from the higher offset frequency data. The transimpedance response of each noise source was extrapolated for offset frequencies below 100 kHz.

The numerical round off associated with the conversion networks can be observed in Table 5.2. This table gives the 2-port S-parameters of the linear resonator network for various offset frequencies at the upper sideband of the first harmonic. This is the second 2-port network shown at the bottom of Figure 5.5. The data in this table are identical to that listed in the data file which was called into the main oscillator conversion network file. Note that the data file typically only stores numbers to five of six significant figures. As a result, the data set in this table does not change significantly for offset frequencies below 100 kHz. This was typical off all of the data files which were called by the oscillator

Table 5.2. S-Parameters of the Oscillator Resonator Circuit

f_{offset} (Hz)	|S11|	/S11 (deg)	|S21|	/S21 (deg)	|S12|	/S12 (deg)	|S22|	/S22 (deg)
1.0000	0.98265	179.241	0.02007	36.3791	0.02007	36.3791	0.98501	179.364
3.1623	0.98265	179.241	0.02007	36.3791	0.02007	36.3791	0.98501	179.364
10.000	0.98265	179.241	0.02007	36.3791	0.02007	36.3791	0.98501	179.364
31.623	0.98265	179.241	0.02007	36.3791	0.02007	36.3791	0.98501	179.364
100.00	0.98265	179.241	0.02007	36.379	0.02007	36.379	0.98501	179.364
316.23	0.98265	179.241	0.02007	36.3788	0.02007	36.3788	0.98501	179.364
1000.0	0.98265	179.241	0.02007	36.378	0.02007	36.378	0.98501	179.364
3162.3	0.98265	179.241	0.02007	36.3755	0.02007	36.3755	0.98501	179.364
10000.	0.98264	179.241	0.02007	36.3675	0.02007	36.3675	0.985	179.364
31623	0.98263	179.242	0.02008	36.3423	0.02008	36.3423	0.98499	179.364
100000	0.98259	179.242	0.0201	36.2626	0.0201	36.2626	0.98496	179.365
316230	0.98248	179.244	0.02016	36.0095	0.02016	36.0095	0.98487	179.366
1000000	0.98212	179.251	0.02036	35.1989	0.02036	35.1989	0.98456	179.372
3200000	0.98097	179.278	0.021	32.5313	0.021	32.5313	0.98357	179.396
10000000	0.97731	179.423	0.02288	23.049	0.02288	23.049	0.98045	179.52

conversion network circuit file. Since the data do not vary for offset frequencies below 100 kHz, obviously the transimpedances will not vary for frequencies below 100 kHz. This is a limitation of LIBRA which can be resolved by storing the data with more significant figures of accuracy.

6. BIAS DEPENDENT HBT NOISE MODELS

In the previous two sections, a process was described which may be used to model the nonlinear characteristics of HBT oscillators. In this section, the characteristics of the noise sources within HBT oscillators are discussed. The results of the analyses presented in Sections 4, 5, and this section may be combined to describe the overall noise characteristics of HBT oscillators. This is presented in Section 7.

6.1 HBT Bias Dependent High Frequency Noise Model

Relatively little information has been reported regarding the high frequency noise characteristics of HBTs. Chen et al. [69] have reported on the minimum noise figure of an InP/InGaAs HBT over a range of bias currents. The minimum noise figure of AlGaAs/GaAs HBTs at a single bias condition, has also been reported by Asbeck et al. [6] and Kim et al. [70]. It appears that no comprehensive analysis of the high frequency noise characteristics of HBTs has been reported. It is found in this work that the noise model which is usually used for conventional BJTs may also be used for HBTs.

A noise model which is commonly used for BJTs is shown in Figure 6.1 [71]. This noise model is implem.. nted in the more popular circuit simulators such as SPICE, and LIBRA [46]. All of the noise sources shown in Figure 6.1 are a result of thermal noise or shot noise. The mean square values of these noise sources are given by Equations 6.1 through 6.6. The parameters used in these equations are defined in Table 4.1 and Equations 4.2 through 4.9. The current noise sources i_{tc}, i_{tb} and i_{te} are thermal noise sources associated with the parasitic contact resistances of the HBT. These noise sources correspond to separate resistances, and are thus uncorrelated. The three remaining current noise sources in Figure 6.1 are shot noise sources. The current noise source i_{sec} represents the shot noise associated with the current source I_{CT} shown in Figure 4.4. One component of I_{CT} is associated with the majority carriers in the emitter which overcome the base-emitter potential barrier, diffuse across the base region, and are swept across the base-collector potential. The carriers involved in this process travel from the base to the collector at independent random points in time, and thus I_{CT} shows full shot noise. The current noise source i_{sbe} is a result of the current sources I_{CC}/β_f and I_{RF}. These

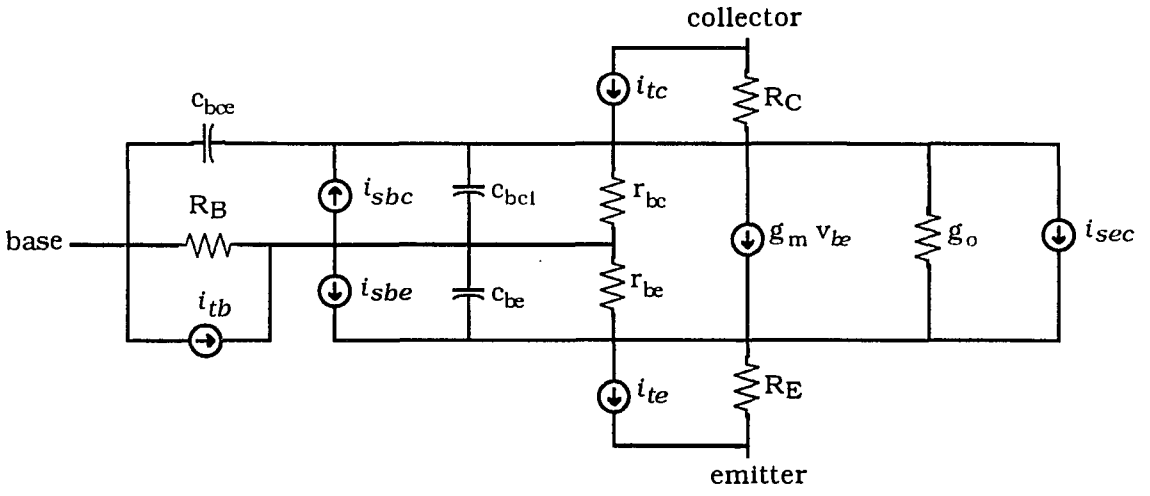

Figure 6.1. HBT High Frequency Noise Equivalent Circuit

components of current are associated with the injection of carriers from the base to the emitter and the recombination in the base-emitter depletion region. These processes effectively create current pulses at random points in time, and thus show full shot noise. The current noise source i_{sbc} is analogous to i_{sbe} except that it is associated with the base-collector junction. It should be noted that the individual processes which create all three shot noise sources are independent of each other, and thus all of the noise sources shown in Figure 6.1 are uncorrelated [71].

$$\overline{i_{te}^2} = \frac{4\,k\,T\,\Delta f}{R_E} \tag{6.1}$$

$$\overline{i_{tb}^2} = \frac{4\,k\,T\,\Delta f}{R_B} \tag{6.2}$$

$$\overline{i_{tc}^2} = \frac{4\,k\,T\,\Delta f}{R_C} \tag{6.3}$$

$$\overline{i_{sbe}^2} = 2\,q\left(\frac{I_{CC}}{\beta_f} + I_{RF}\right)\Delta f \tag{6.4}$$

$$\overline{i_{sbc}^2} = 2\,q\left(\frac{I_{EC}}{\beta_r} + I_{RR}\right)\Delta f \tag{6.5}$$

$$\overline{i_{sec}^2} = 2\,q\,I_{CT}\,\Delta f \tag{6.6}$$

The similarities between homojunction and heterojunction transistors indicate that the noise model shown in Figure 6.1 is also valid for HBTs. For an NPN HBT, the heterojunction has the effect of reducing the number of holes which are injected from the base into the emitter. However, the shot noise associated with all of the components of current which exist in a HBT are accounted for in the noise model shown in Figure 6.1. The noise model also accounts for the thermal noise associated with the ohmic contacts of the HBT. This, indicates that the noise model shown in Figure 6.1 can be used to characterize an HBT. In order to verify the use of this noise model, it was compared with noise figure measurements taken on an HBT. The device on which the noise measurements were made was fabricated on the same wafer as the HBT characterized in Section 4.

The noise figure of any linear 2-port device can be measured to determine the amount of noise which the device adds to a system. The IEEE definition of noise figure for a linear system is [72], "The ratio of (A) the total noise power per unit bandwidth (at a corresponding output frequency) delivered by the system into an output termination to (B) the portion thereof engendered at the input frequency by the input termination whose noise temperature is standard (290 °K at all frequencies)." In other words, it is the ratio of the amount of noise power per unit bandwidth at the output of a given system to that which would exist at the output if the system did not add any noise of its own. (If the system does not add any of its own noise power, then the noise power at the output would be entirely due to the thermal noise of the input termination.) It can be shown that the noise figure of any linear 2-port network is given by [66],

$$F = F_{min} + \frac{4 r_n |\Gamma_s - \Gamma_o|^2}{(1 - |\Gamma_s|^2)|1 + \Gamma_o|^2}. \tag{6.7}$$

In the above equation, Γ_s is the reflection coefficient of the source termination and F_{min}, r_n, and Γ_o are noise parameters which characterize the 2-port network. The parameter F_{min} is the minimum noise figure which can be achieved for any source impedance. Γ_o is the source reflection coefficient at which this minimum noise figure is achieved. The parameter r_n is referred to in literature as the normalized noise resistance and determines how significantly the noise figure of the linear 2-port is degraded as Γ_s is changed from the optimal value, Γ_o.

The parameters F_{min}, r_n, and Γ_o can be used to completely characterize the noise characteristics of any linear 2-port network at a given set of operating conditions. If these 2-port noise parameters are known, then this is all the information which may be obtained about the noise characteristics of a given linear circuit as long as the measurements are limited to the 2-port terminals. For a device such as a HBT, the extrinsic 2-port terminals of the device are the only terminals available for measurement. (Measurements cannot be made across the intrinsic base-emitter junction for example.) Thus, the most effective approach to verify the noise model in Figure 6.1 is to measure the HBT 2-port noise parameters at several bias conditions, and compare them with the with those of the noise model. Several systems have been developed commercially to perform 2-port noise parameter measurements. These measurement systems determine the noise parameters by first measuring the noise figure of a given device at numerous source impedances. This noise figure data set is then fit to Equation 6.7 to extract the noise parameters of the 2-port device. A great deal of work has been done in this area to improve the accuracy of the extraction technique. It should be noted that the measurement of these parameters is very susceptible to errors and to the accuracy of the curve fitting technique. A detailed discussion of these errors and techniques for reducing them is beyond the intended scope of this work. For more information regarding these errors and curve fitting techniques, the reader is referred to [73-77].

In this research, an ATN NP5 noise parameter measurement system was used to characterize the HBT. A block diagram of this system is shown in Figure 6.2. The HBT device shown in this block diagram was measured directly on chip using a coplanar waveguide probe station.

The system is calibrated by first removing the HBT and placing the coplanar waveguide probes on various termination standards throughout the calibration sequence. The two switches shown in Figure 6.2 are first set to the upward position. (The switches, network analyzer, dc power supply, and noise figure meter in this system are all computer controlled through an HP-IB bus not shown in the figure.) S-parameters associated with the cable interconnect, bias tees, switches, and electronic 2-port tuner are then measured for various coplanar waveguide probe termination impedances using the HP 8510B network analyzer. These measurements are used to calibrate out the cable interconnects, bias tees, switches, and coplanar waveguide probes and to characterize the electronic 2-

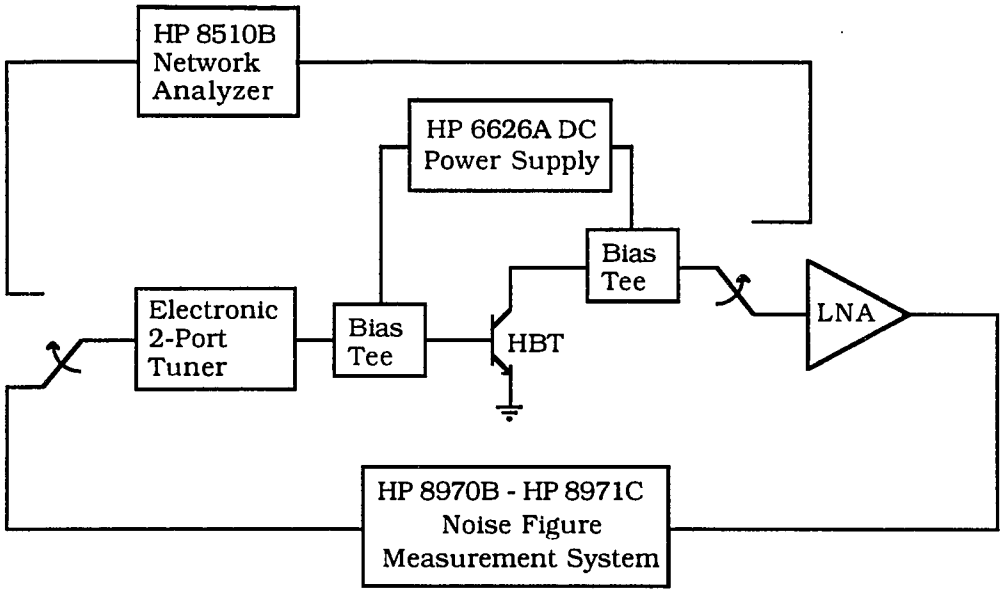

Figure 6.2. Basic Block Diagram of the ATN Noise Parameter Measurement System

port tuner. The 2-port tuner is characterized at each of its source impedance settings. The switch on the left side in the figure is then set to the lower position, and the source impedances of the hot and cold noise sources are measured by the network analyzer. This provides sufficient information to calculate the source impedance and losses of the measurement system for each setting of the electronic tuner and thus complete the calibration process. The use of the electronic tuner in this measurement system allows for much more accurate and consistent measurements. This type of tuner provides more repeatable settings than do mechanical tuners resulting in improved measurement accuracy.

With the calibration process complete, the noise figure measurements on the HBT may be performed. The coplanar waveguide probes are placed on the HBT bondpads, and bias is applied through the bias tees. At each of the electronic 2-port tuner impedance settings, S-parameter measurements and noise measurements are performed on the HBT. (The S-parameter measurements are required for the technique used by ATN [73].) These measurements are then fit automatically to determine the 2-port noise parameters of the HBT. This process was repeated over a series of HBT bias conditions to characterize the

device. This entire measurement and fitting process is performed automatically by the computer controlled system.

In order to determine the accuracy of the model in Figure 6.1, its noise parameters were calculated using the software program NAOP [79]. A comparison of the modelled and measured 2-port noise parameters over a wide range of bias conditions is given in Tables 6.1 through 6.4. These tables indicate that the HBT noise model is reasonably accurate. However, it is somewhat difficult to estimate the nominal error in noise figure based upon these data. To display the data in Tables 6.1 through 6.4 in a more insightful manner, Figures 6.3 through 6.6 were generated. As indicated by Equation 6.7, the noise figure of a linear network is a function of the source admittance. If the noise figure, F, in Equation 6.7 is set to a constant value, F_i, then only a locus of source reflection coefficients will satisfy the resulting equation. If this locus of reflection coefficients is plotted on a Smith Chart, then it will form a circle commonly known as a noise figure circle [78]. Measured and modelled noise figure circles for the HBT at various bias conditions are shown in Figures 6.3 through 6.7. The measured data in each these figures are shown as the solid curve, while the modelled data are given by the dashed curve.

In order to evaluate the accuracy of the noise parameter measurements, the noise parameters of two different HBTs were measured at the same bias condition. Both of these HBTs were fabricated on the same wafer. However, the measurements were performed on two separate occasions with two different calibration sequences of the measurement system. The resulting 2-port noise parameters and noise figure circles are given in Table 6.5 and Figure 6.7. The agreement between these two measurements gives an indication of the accuracy of the noise measurements. (The noise measurements were performed on a HBT off of the same wafer as the HBT used to develop the equivalent circuit model.)

In general, the agreement between the measured and modelled data is quite good. The best accuracy is achieved at relatively low frequencies near 1 GHz and tends to degrade slightly at higher frequencies. The data in Tables 6.1 through 6.4 show that the measured and modelled noise parameters tend to follow the same trends and are in reasonable agreement. The data in Figures 6.3 through 6.6 indicate that the measured and modelled noise figure data typically differ by about .5 dB. In some cases, it appears that the model data may be more accurate than the measured data. For example, in Tables 6.1

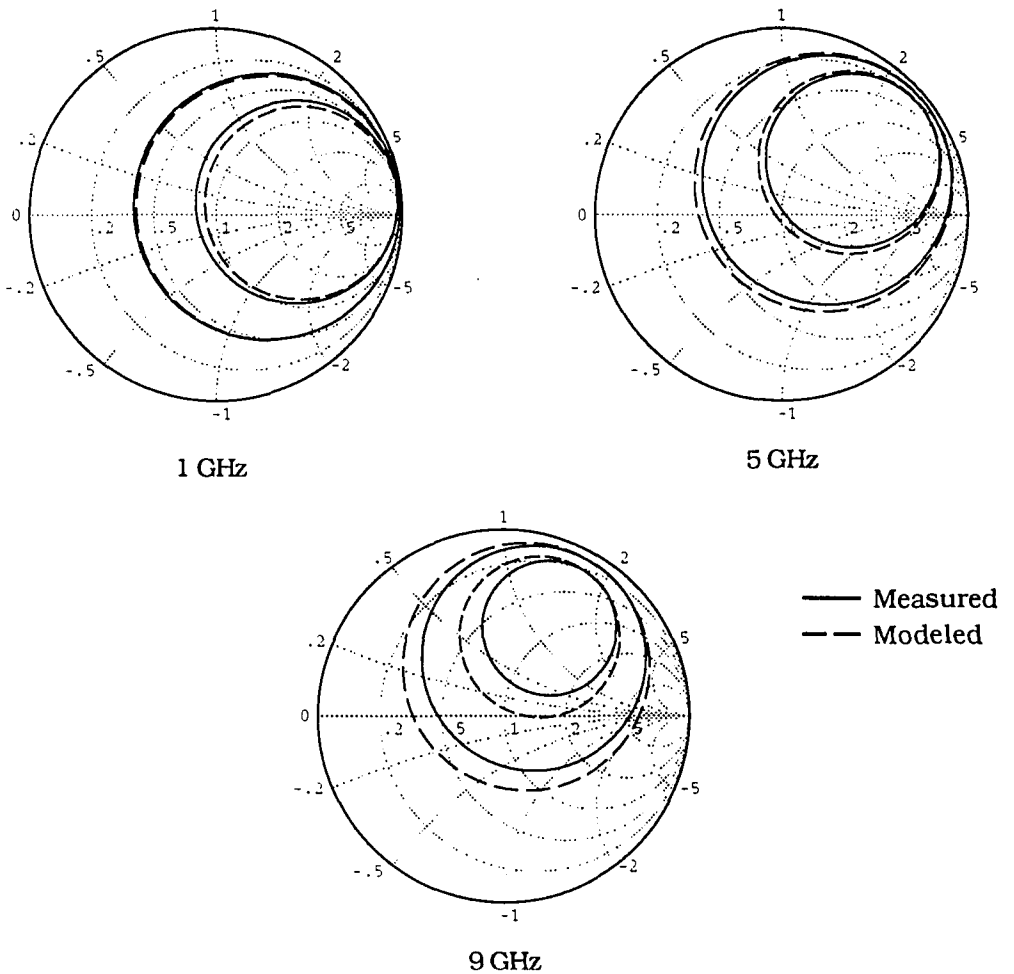

Figure 6.3. HBT 3 and 5 dB Noise Figure Circles (V_{CE}=.9V, I_C=.651mA)

Table 6.1. Measured and Modelled HBT 2-Port Noise Parameters (V_{CE}=.9V, I_C=.651mA)

Freq (GHz)	F_{min} meas (dB)	F_{min} model (dB)	r_n meas	r_n model	$\lvert\Gamma_o\rvert$ meas	$\lvert\Gamma_o\rvert$ model	meas (deg)	model (deg)
1	.34	.84	0.882	0.861	0.81	0.798	8.9	7.69
3	.95	.99	1.063	0.840	0.77	0.766	21.4	22.7
5	1.18	1.21	0.915	0.802	0.72	0.720	37.3	37.5
7	1.49	1.46	0.932	0.749	0.72	0.674	51.2	51.7
9	1.87	1.71	0.925	0.687	0.67	0.636	62.3	65.3

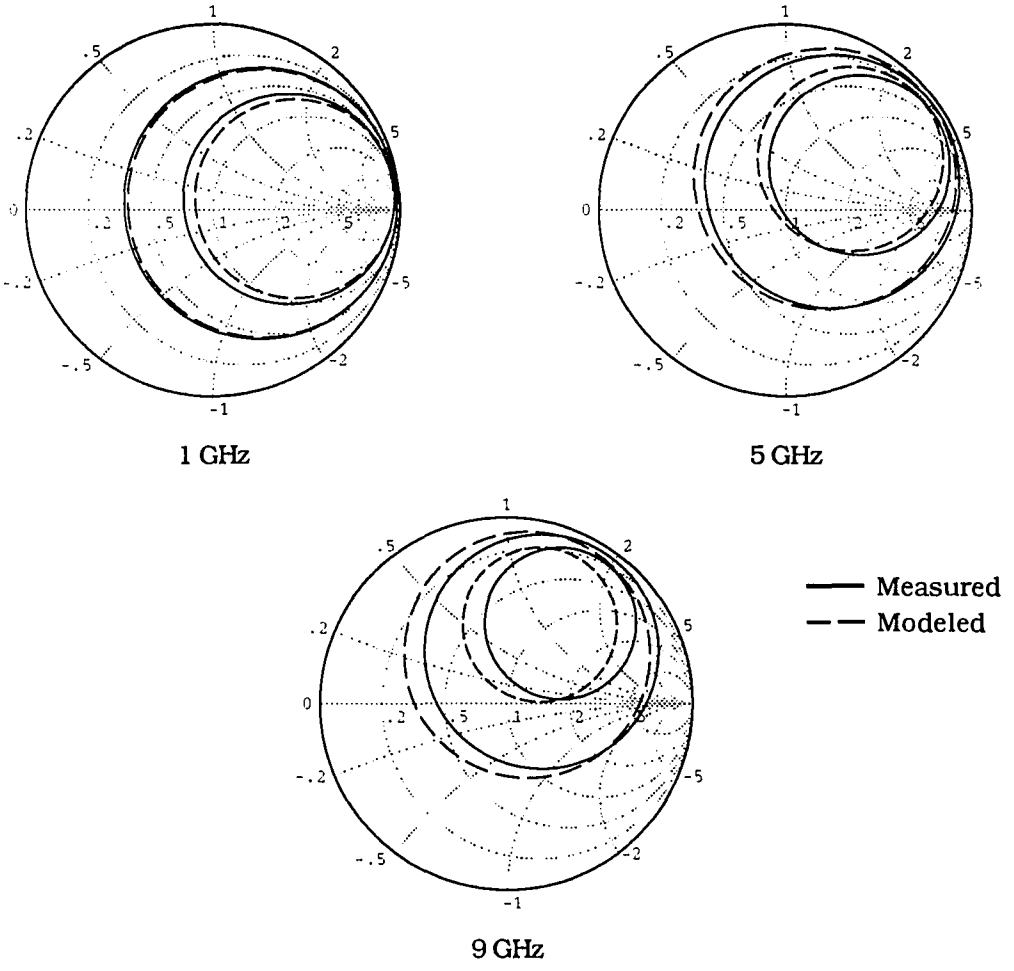

Figure 6.4. HBT 3 and 5 dB Noise Figure Circles (V_{CE}=5 V, Ic=.71 mA)

Table 6.2. Measured and Modelled HBT 2-Port Noise Parameters (V_{CE}=5 V, Ic=.71 mA)

Freq (GHz)	F_{min} meas (dB)	F_{min} model (dB)	r_n meas	r_n model	$\lvert\Gamma_o\rvert$ meas	$\lvert\Gamma_o\rvert$ model	meas (deg)	model (deg)
1	.33	.84	0.818	0.800	0.77	0.785	8.1	7.7
3	.98	1.01	1.004	0.785	0.72	0.747	17.8	23.0
5	1.09	1.28	0.898	0.756	0.72	0.693	31.2	38.0
7	1.08	1.58	0.999	0.716	0.73	0.643	42.1	52.9
9	1.55	1.88	0.912	0.666	0.70	0.601	56.1	67.1

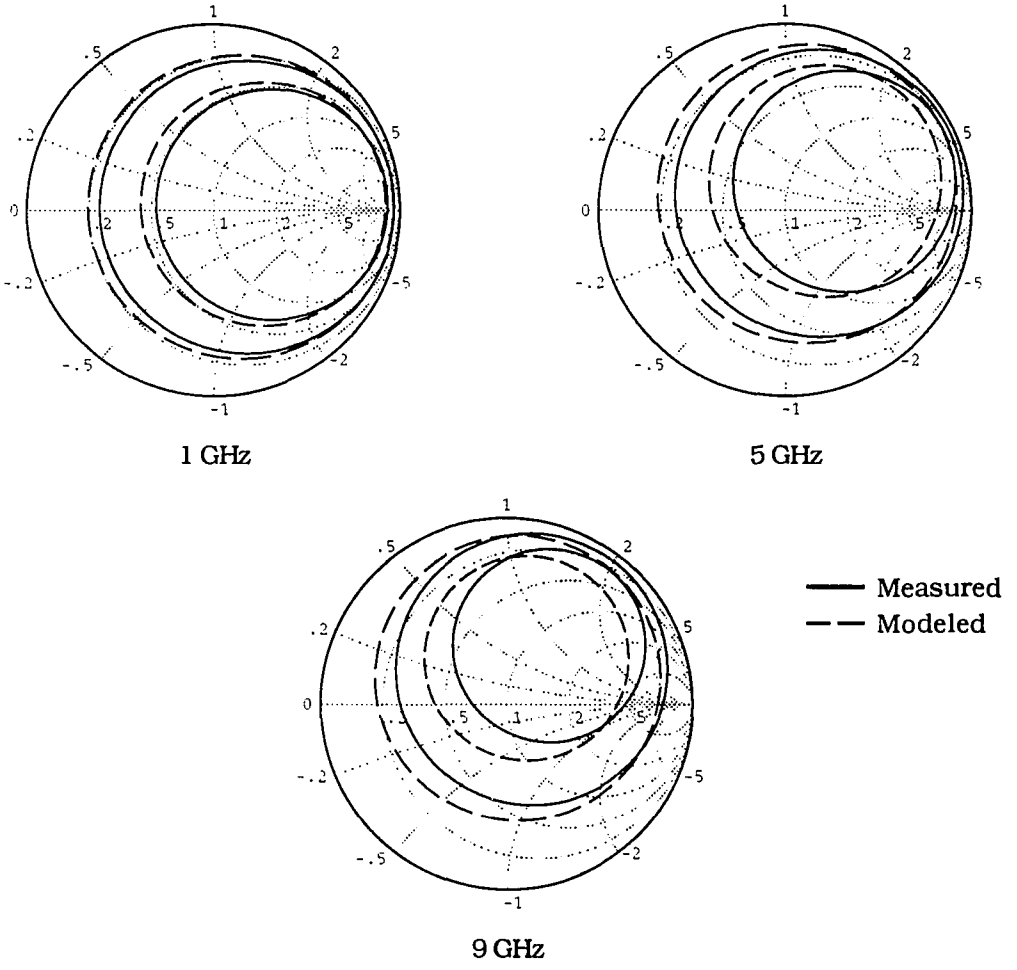

Figure 6.5. HBT 3 and 5 dB Noise Figure Circles (V_{CE}=5 V, I_C=3.3 mA)

Table 6.3. Measured and Modelled HBT 2-Port Noise Parameters (V_{CE}=5 V, I_C=3.3 mA)

Freq (GHz)	F_{min} meas (dB)	F_{min} model (dB)	r_n meas	r_n model	$\lvert\Gamma_o\rvert$ meas	$\lvert\Gamma_o\rvert$ model	meas (deg)	model (deg)
1	.97	1.07	0.526	0.418	0.60	0.542	5.5	7.2
3	1.41	1.16	0.602	0.413	0.56	0.518	12.1	21.5
5	1.00	1.31	0.559	0.403	0.66	0.480	26.2	36.2
7	1.10	1.50	0.545	0.389	0.75	0.440	43.1	51.2
9	1.49	1.72	0.559	0.371	0.60	0.407	54.1	66.5

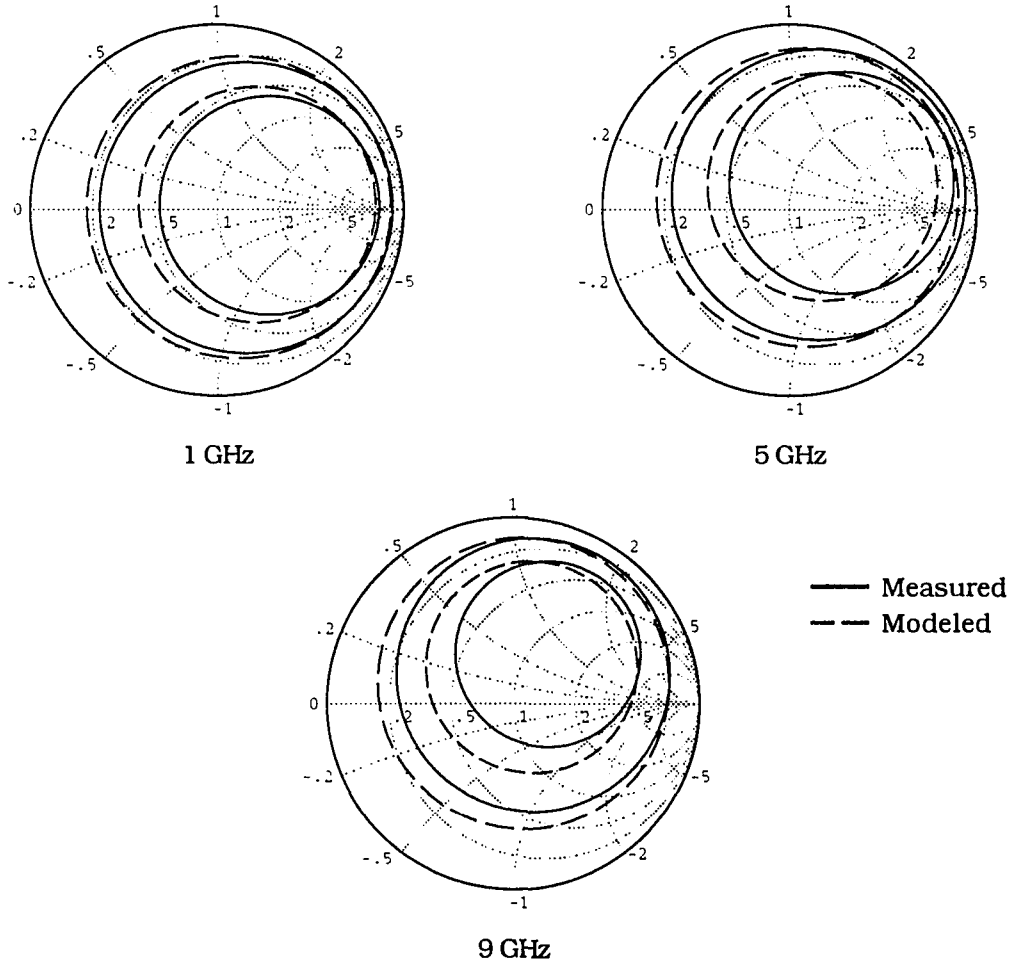

Figure 6.6. HBT 3 and 5 dB Noise Figure Circles (V_{CE}=2 V, I_C= 7.2 mA)

Table 6.4. Measured and Modelled HBT 2-Port Noise Parameters (V_{CE}=2 V, I_C= 7.2 mA)

Freq (GHz)	F_{min} meas (dB)	F_{min} model (dB)	r_n meas	r_n model	$\lvert\Gamma_o\rvert$ meas	$\lvert\Gamma_o\rvert$ model	meas (deg)	model (deg)
1	1.49	1.41	0.475	0.373	0.47	0.388	4.3	6.9
3	1.65	1.45	0.537	0.369	0.43	0.380	9.1	20.9
5	1.28	1.52	0.487	0.361	0.56	0.367	27.6	34.9
7	1.52	1.62	0.443	0.350	0.62	0.353	46.6	49.1
9	1.85	1.73	0.490	0.335	0.46	0.339	55.1	63.2

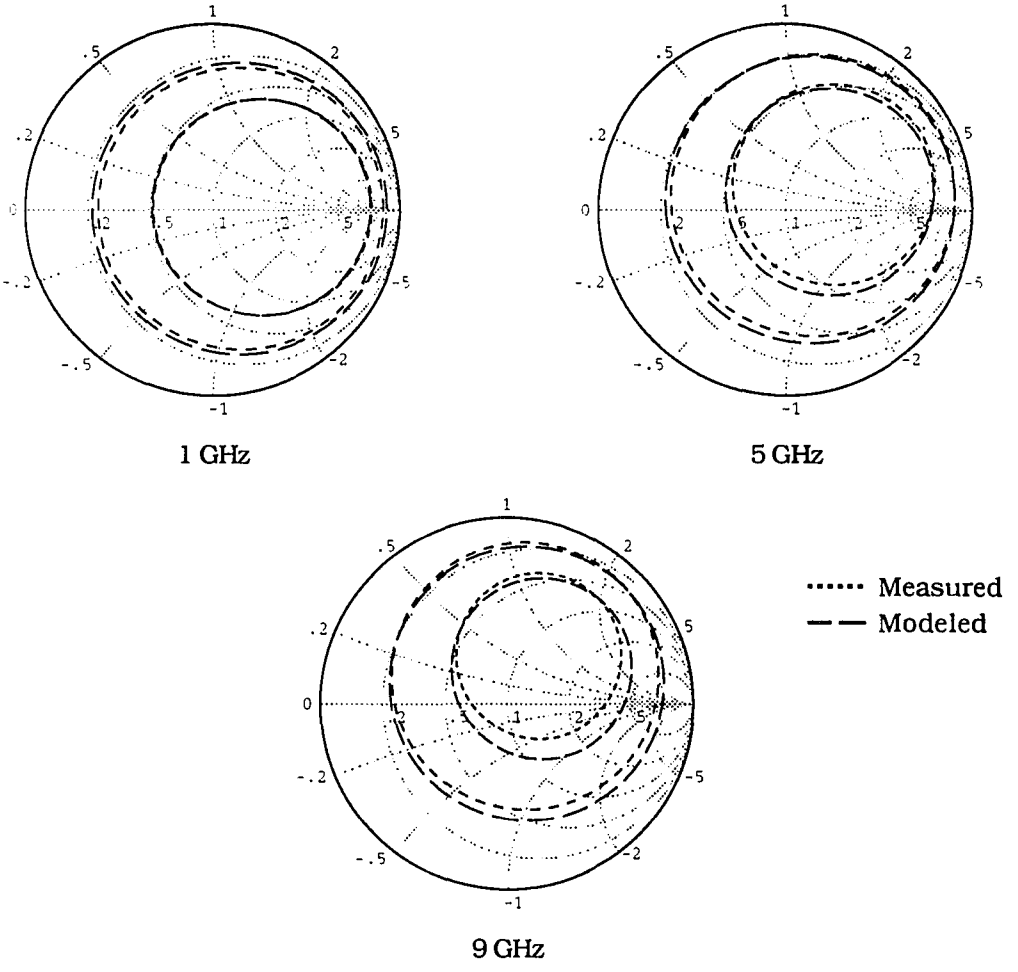

Figure 6.7. HBT 3 and 5 dB Noise Figure Circles (V_{CE} = 2.0V, I_C=10 mA, Both Measured)

Table 6.5. Measured HBT 2-Port Noise Parameters (V_{CE} = 2.0V, I_C=10 mA)

Freq (GHz)	F_{min} meas1 (dB)	F_{min} meas2 (dB)	r_n meas1	r_n meas2	$\lvert\Gamma_o\rvert$ meas1	$\lvert\Gamma_o\rvert$ meas2	meas1 (deg)	meas2 (deg)
1	1.81	1.61	0.498	0.447	0.39	0.42	2.9	3.1
3	1.96	1.79	0.544	0.467	0.38	0.48	9.9	12.2
5	1.70	1.73	0.504	0.452	0.44	0.39	28.0	22.3
7	1.88	1.76	0.460	.0488	0.50	0.35	45.5	32.6
9	2.14	2.00	0.493	0.478	0.40	0.36	56.4	45.4

and 6.2 the measured minimum noise figure appears to be unrealistically low and the measured normalized noise resistance is slightly higher than the modelled data to compensate. Generally, one would tend to expect minimum noise figures closer to the modelled values. (Some of the measured values rival the most optimal state-of-the-art HEMTs.) Note that the modelled normalized noise resistance tends to be lower than the measured values. This may be partially be a result of the HBT equivalent circuit model developed in Section 4. As shown in Figure 4.23 and 4.24, the modelled gain of the HBT is higher than the measured gain. This would have the effect of making the shot noise associated with the collector current less significant in the noise model, and thus reduce the value of r_n. However, the agreement between the modelled and measured noise data in Figures 6.3 through 6.6 is nearly as good as the agreement between two measured HBTs in Figure 6.7. This indicates that the noise model in Figure 6.1 is indeed valid for HBTs.

6.2 HBT Bias Dependent Flicker Noise Model

At frequencies close to the frequency of oscillation, the phase noise of an oscillator is often effected by low frequency flicker noise sources. The low frequency noise is upconverted to the oscillator sidebands through the circuit nonlinearities and through the modulation of these noise sources by the periodic currents which exist in the oscillator. Accordingly, a low frequency flicker noise model is required for this research in order to analyze these upconversion effects.

At present, there is a large amount of controversy regarding the physical cause of flicker noise in HBT's. As noted by Raman et al. [80]; "No unified theory exists for the low-frequency (1/f) noise behavior, even for conventional homojunction bipolar transistors (BJT's),.... The results published so far indicate that there is no clear understanding of the exact physical origin of the noise for the conventional BJT's. The situation is worse for the complex HBT's." The lack of a unified theory is also demonstrated by the fact that the flicker transistor noise model which is used in most circuit simulators such as SPICE has been developed empirically [46].

A number of BJT flicker noise models have been proposed by various authors. Kleinpenning [81, 82] and Kilmer et al. [83] have presented models based on diffusivity fluctuations in the bipolar transistor. Flicker noise in transistors has also been

attributed to trapping and recombination effects in the base-emitter depletion region or at the surface of this region [84, 85, 86]. The use of McWhorter's model which attributes flicker noise to traps in the surface oxide layer has also been proposed for bipolar transistors. However, the use of this model for bipolar transistors has been discounted by Stoisiek and Wolf [87]. A more recent analysis by van der Ziel et al. [88] assumed that the flicker noise in bipolar transistors and HBT's is due to diffusivity fluctuations, recombination at the base surface, and recombination in the base-emitter depletion region.

Theories relating to the cause of flicker noise in HBT's are much less mature. Raman et al. [80] have measured the flicker noise collector current in HBT's at room temperature and at 80 °K. They found that the power spectral density of this flicker noise current was proportional to the square of the emitter current, and proposed that the flicker noise might be due to trapping effects at the heterointerface. Jue et al. [89] also measured the flicker noise current which was present in a double heterojunction HBT. Jue et al. proposed that the flicker noise could be modelled as recombination at the heterointerface or as contact noise in the emitter. A more recent analysis by Costa and Harris [90] indicated that a portion of the flicker noise could be attributed to recombination at the extrinsic base surface.

In this research, all of the mechanisms which have been reported as being significant in HBT's are considered. These mechanisms include diffusivity fluctuations, recombination at the base surface, and recombination in the base-emitter depletion region. (This includes recombination at the heterointerface and at the depletion region surface.) All of these flicker noise mechanisms can be modelled by using the equivalent circuit shown in Figure 6.8 [88]. This equivalent circuit models the flicker noise in HBT's using three current noise sources. The current noise source i_{fbc} is connected between the base and collector nodes, and is used to model recombination effects at the surface of the base region [88]. Fogner [91] found that the surface recombination velocity in the base region fluctuates with a 1/f noise spectrum and modulates the recombination current. This noise mechanism is a partition type of noise source which modulates both the collector and base current and could be modelled as two fully correlated noise sources; one across the base-emitter junction and the other from the emitter to the collector. However, the use of the equivalent circuit shown in Figure 6.8 allows it to be modelled as a single

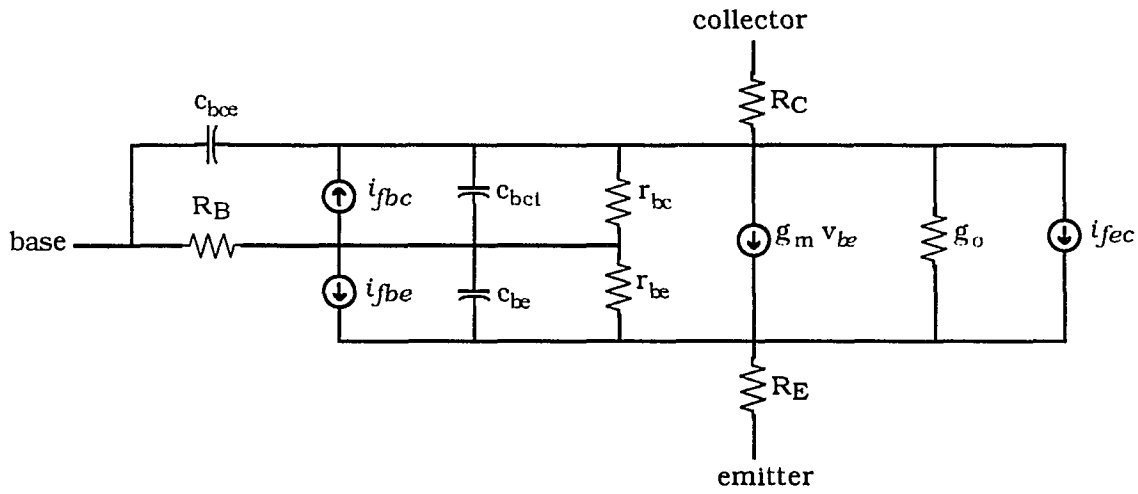

Figure 6.8. HBT flicker Noise Equivalent Circuit Model

independent noise source. Fogner [91] determined that the power spectral density of this noise source is proportional to the base recombination current squared. For the case of HBT's, the base current is nearly all recombination current since the diffusion of holes from the base into the emitter will be blocked by the heterojunction. Thus,

$$S_{i_{fbc}} = k_{bc} \frac{I_{RF}^2}{f^{\alpha}} \tag{6.8}$$

where k_{bc} is a constant which is determined by the magnitude of the noise source, α is a constant which may vary from .6 to 1.4 and is determined by the slope of the flicker noise spectrum, and I_{RF} is given by Equation 4.5.

A second flicker noise current source, i_{fbe}, models the effects of recombination within the base-emitter depletion region and at the heterointerface. The power spectral density of this noise source is also proportional to the base recombination current squared [92]. Therefore,

$$S_{i_{fbe}} = k_{be} \frac{I_{RF}^2}{f^{\alpha}} \tag{6.9}$$

where K_{be} and α are constants similar to those described above.

The final noise source shown in Figure 6.8, i_{fec}, models the effects of diffusivity fluctuations and other flicker noise mechanisms. As noted by van der Ziel [92], the power spectral density of this noise source, which is associated with diffusion fluctuations, is proportional to I_{CT}. However, measurements on some HBT devices have shown that the flicker noise which is associated with the collector-to-emitter current varies as the collector emitter squared. Relatively little work has been performed to determine the exact physical cause of this noise source. Raman [80] found that this noise source may be caused by traps at the heterointerface. However, no in depth analysis of the physical cause of this noise source in HBTs has been reported. The overall power spectral density of the noise current i_{fec} can be expressed as,

$$S_{i_{fec}} = k_{ecd}\frac{I_{CT}}{f^{\alpha}} + k_{ect}\frac{(I_{CT}+I_{RF})^2}{f^{\alpha}} \tag{6.10}$$

where k_{ecd} is a constant which determines the magnitude of the noise associated with variations in the diffusivity, k_{ect} is a constant which determines the magnitude of the noise associated with collector-to-emitter current squared, and α is a constant which determines the slope of the flicker noise spectrum.

As noted by van der Ziel [88], all of the noise mechanisms which are modelled in Figure 6.8 are a result of independent processes and accordingly, all of these noise sources are uncorrelated. For a theoretical derivation of Equations 6.9 through 6.11 the reader is referred to the cited references. It should be noted that these equations are typically derived by using many simplifying assumptions, and are often based on heuristic expressions such as the Hooge model for flicker noise. Buckingham found that [29]; "Several theories (relating to the physical cause of 1/f noise) have been proposed, the most widely discussed being surface trapping and equilibrium thermal energy exchange with the environment. Although these theories may individually account for certain specific manifestations of the phenomenon, no general theory of 1/f noise exists at present." Detailed discussions of some of the specific theories associated with physical causes of flicker noise are given in [29, 31, 93, 94].

In order to determine the relative magnitudes of the flicker noise sources i_{fbe}, i_{fbc}, and i_{fec}, measurements of the equivalent HBT collector noise current are required. The test circuit should in Figure 6.9 was developed to perform this measurement. This test

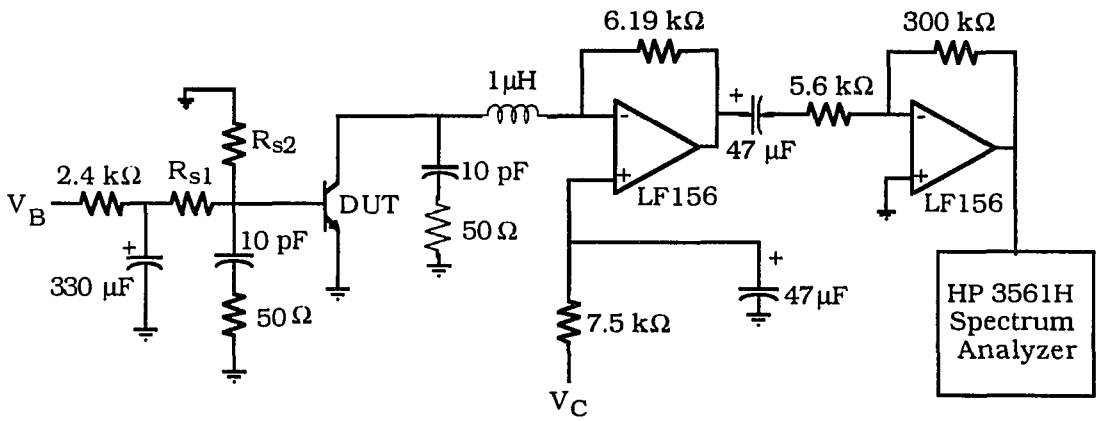

Figure 6.9. Test set up for measuring HBT flicker noise

circuit amplifies the noise current at the collector to the HBT and the amplified noise level is then measured using an HP3561H spectrum analyzer. The first of the two op amp stages in this test circuit is a transimpedance amplifier which converts a current at its input to a voltage. The second op amp stage provides additional voltage amplification such that the measured noise level is above the noise floor of the spectrum analyzer. The overall transimpedance of these two amplifier stages can be calculated to be 332 kΩ and was measured to be 345 kΩ.

Batteries were used for the supply voltages in this test circuit in order to eliminate the spurious signals which were found to be present in conventional dc power supplies. The two voltages which were used to set the HBT bias levels, V_B and V_C, were then regulated down from these power supplies using LM317T variable voltage regulators. The 7.5 kΩ and 2.4 kΩ resistors shown in Figure 6.9 were used in conjunction with the 330 μF and 47 μF capacitors to decouple any flicker noise which might be present at the output of these voltage regulators from the test circuit. The op amp supplies were connected directly to the batteries and did not require any additional noise filtering since they have a large amount of inherent supply rejection. The op amps themselves were also selected to have low flicker noise levels so that they would not mask out the HBT flicker noise current. The noise floor of the measurement system was measured to be more than 25 dB below the lowest HBT noise current measurement.

In order to prevent the HBT from oscillating at microwave frequencies during the measurements, both the base and collector terminals must be properly terminated at high frequencies. The 10 pF capacitors, 50 Ω resistors, and 1 μH inductor were included in the circuit for this purpose. These components have a negligible effect on the test circuit characteristics at frequencies below 1 MHz.

The dc bias conditions within the HBT are set by the voltages V_C and V_B. HBT collector voltage is forced to be equal to V_C by the virtual short between the input terminals of the first op amp. The HBT collector current is then provided by the first op amp through the 6.19 kΩ resistor. This collector current is set by adjusting the base bias voltage V_B.

By measuring the signal level at the spectrum analyzer and knowing the transimpedance of the amplifier, the equivalent HBT collector noise current can be determined. This equivalent output noise current was measured under various bias conditions and with several source resistances. The source resistance at the base of the HBT, is determined by resistors R_{S1} and R_{S2}. Figure 6.10 shows the measured collector noise current spectrum which was obtained for various emitter-collector voltages. The collector current was held at 2.15 mA and the source resistance was maintained at 1882 Ω for all of the measurements shown in this figure. The data in this figure indicate that the

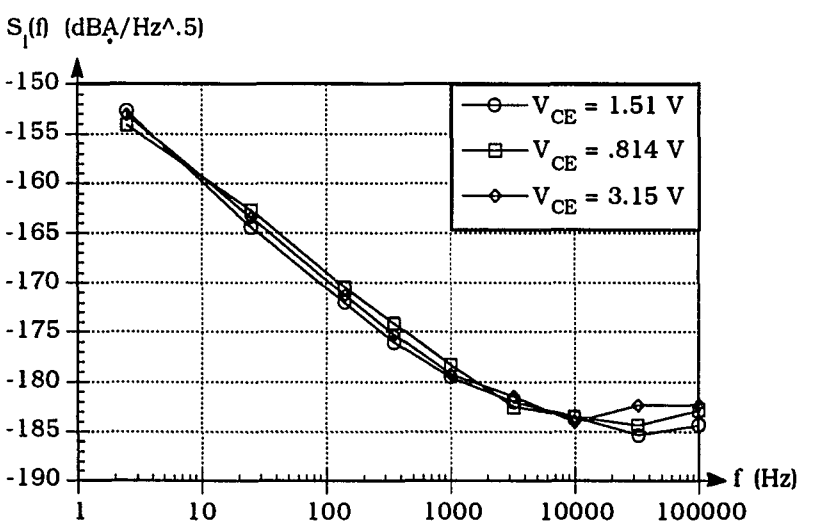

Figure 6.10. Flicker Noise Power Spectral Densities for Various Values of V_{CE}

flicker noise which is present in the HBT is not significantly dependent on the base-collector voltage. This is in agreement with HBT flicker noise measurements reported by Costa and Harris [90] and Raman et al. [80]. The data in Figure 6.10 indicate that the mechanisms which cause flicker noise in HBT's are not associated with the base-collector junction.

The measured HBT collector noise current power spectral density is plotted as a function of collector current in Figure 6.11. These measurements were taken with a source resistance of 1882 Ω and a emitter-collector voltage of 1.51 V. The data indicate that the flicker noise power which is present is approximately proportional to the square of the collector current through the device. This is also in agreement with the experimental results which have been reported elsewhere [80, 88, 89]. This indicates that the flicker noise which is associated with diffusivity fluctuations in the HBT is relatively small and thus the first term on the right side of Equation 6.10 may be neglected.

To determine the significance of the other noise mechanisms in the HBT, the collector noise current was measured at various bias currents and source resistances. The results of these measurements are shown in Figure 6.12. The emitter-collector voltage was held at 1.5 V for all of the measurements shown in this figure. The plots show a characteristic flicker noise slope for frequencies less than about 1 kHz. At frequencies

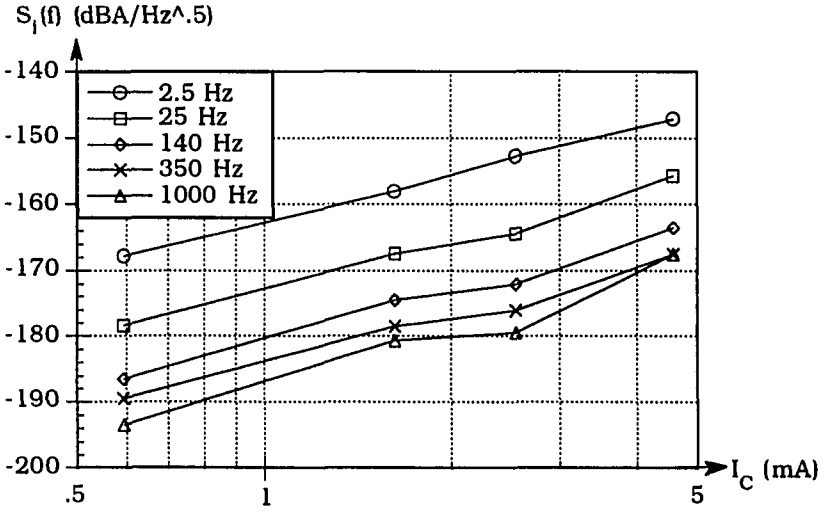

Figure 6.11. Flicker Noise Power Spectral Densities as a Function of Collector Current

above about 10 kHz, the noise spectrum is nearly flat which indicates that it is dominated by white noise sources such as thermal noise or shot noise. These white noise sources are discussed in Sections 2.4, 2.5, and 6.1 of this paper. Note that the slope of these curves at low frequencies corresponds to the values of α in Equations 6.8 through 6.10. Thus to determine the value of α, the average slope of the curves between 2.5 Hz and 1 kHz was calculated. This slope was found to be 10.07 decibels per decade. Thus, α was approximated as being equal to 1.

In order to determine the values of K_{be}, K_{bc}, and K_{ect}, and complete the flicker noise model, the data in Figure 6.12 were curve fit. To accomplish this, the HBT circuit model which was discussed in Section 4.1 of this paper was used to determine the current gains from the location of the noise sources shown in Figure 6.8 to the collector terminal. These current gains are defined as G_{be}, G_{bc}, and G_{ec}. Since the noise sources shown in Figure 6.8 are uncorrelated, the power spectral density of the current noise at the collector output, $S_i(f)$, is given by the sum of the power spectral densities due to each of the individual noise sources. In other words,

$$S_i = G_{be}^2 S_{i_{fbe}} + G_{bc}^2 S_{i_{fbc}} + G_{ec}^2 S_{i_{fec}} . \tag{6.11}$$

Combining Equations 6.8 through 6.11, and noting that α equals 1,

$$S_i = G_{be}^2 k_{be} \frac{I_{RF}^2}{f} + G_{bc}^2 k_{bc} \frac{I_{RF}^2}{f} + G_{ec}^2 k_{ect} \frac{(I_{CT} + I_{RF})^2}{f} . \tag{6.12}$$

Once the current gains G_{be}, G_{bc}, and G_{ec} are calculated at each bias condition for the source resistances shown in Figure 6.12, the data in this figure can be curve fit. However, if the device is biased in the normal active region then, the values of G_{be} and G_{bc} will be approximately equal. Accordingly, it is very difficult to distinguish between the values of k_{be} and k_{bc}. The experimental results given by Costa and Harris [90] and the preliminary results discussed by van der Ziel [88] both indicate that the noise due to recombination in the base region will dominate over the noise which is due to recombination at the base-emitter depletion region near the heterointerface. Costa and Harris were able to demonstrate this experimentally by using an AlGaAs surface passivation ledge to reduce the base surface recombination velocity. This is a strong indication that the first term on the right side of Equation 6.12 will be negligible in comparison to the second term and

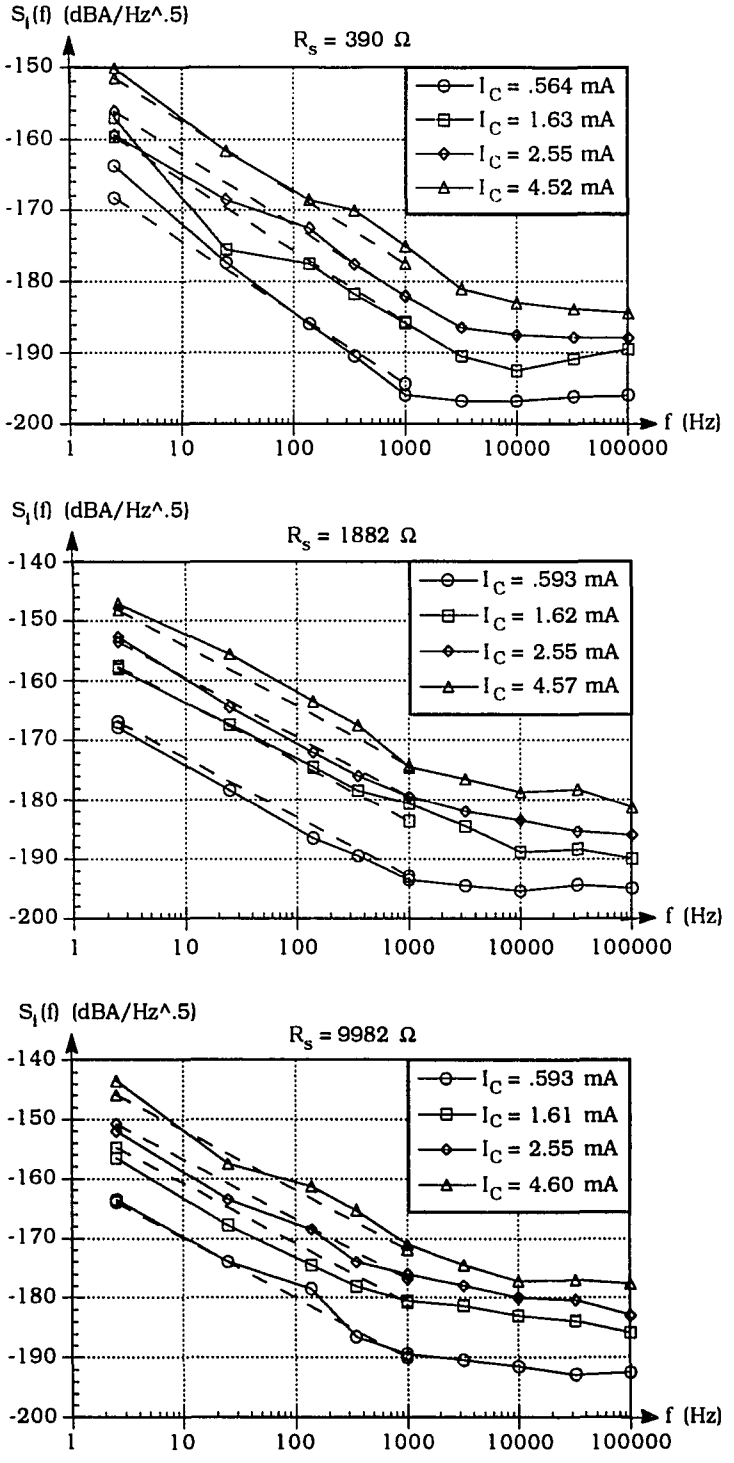

Figure 6.12. Measured and Modelled HBT Flicker Noise Power Spectral Densities

thus the first term was ignored in the curve fit. The values of K_{bc} and k_{ect} were then determined by curve fitting the data in Figure 6.12. The modelled curves, which were produced from this curve fit, are given by the dashed lines in this figure. The rms error associated with this curve fit was 1.85 dB. The resulting expressions for the power spectral densities of the noise sources are given by Equations 6.13 through 6.15. It is significant to note that when the noise due to i_{fbc} is eliminated from the model, the rms error is increased by only 1.4 dB. However, when the noise due to i_{fec} is eliminated, the rms error is increased by 5.9 dB. This indicates that the i_{fec} is dominant. Equations 6.13 through 6.15 can be used in conjunction with Figure 6.10 to model the flicker noise characteristics of the HBT device.

$$S_{i_{fbc}} = 1.82 \times 10^{-10} \frac{I_{RF}^2}{f} \tag{6.13}$$

$$S_{i_{fec}} = 1.24 \times 10^{-10} \frac{(I_{CT} + I_{RF})^2}{f} \tag{6.14}$$

$$S_{i_{feb}} \equiv 0 \, . \tag{6.15}$$

7. OSCILLATOR NOISE SOURCE MODULATION AND NOISE SPECTRUMS

With the information developed in Sections 4 through 6, it is possible to model the noise spectrum of the oscillator. However, the effects of frequency conversion due to the modulation of noise sources must first be considered. These effects are analyzed in Section 7.1. This work represents the first time that these modulations effects have been considered in microwave oscillators. The noise spectrums of the oscillator are then calculated and discussed in the remaining portions of Section 7.

7.1. Modulation of Noise Sources

The noise models developed in Section 6 indicate that the significant noise sources which are present in a HBT are thermal noise, shot noise, and flicker noise. As indicated by Equation 2.9, the thermal noise sources which are present in an oscillator are not bias dependent. As a result, these components can only be modulated through temperature variations in the components of the oscillator. Since the thermal time constant of the HBT substrate was found in Section 4 to be approximately 1 μsec, which corresponds to a frequency much less than the frequency of oscillation of most oscillators, the thermal noise sources will normally not be modulated. Even for low frequency oscillators where the temperature of the components can vary as a periodic function of time, the level of these variations is normally small in comparison to the absolute temperature of the components, and thus the modulation effects associated with the thermal noise sources will be minor. However, as indicated by Equations 6.4 through 6.6 and Equation 6.12, the shot and flicker noise sources in HBTs will be modulated as a periodic function of time. The modulation of these noise sources is analyzed in this section.

7.1.1. Modulation of shot noise sources

The shot noise sources which are present in a given oscillator will all be modulated by the periodic variations in the oscillator currents. The modulation of shot noise in periodically driven diodes has previously been analyzed by Dragone [22]. The results developed in Dragone's analysis have been used by Held and Kerr to analyze shot noise modulation effects in diode mixers [17]. It is believed that this is the first time that the results presented by Dragone have been applied to a bipolar transistor of any type and the first time they have been used in an oscillator analysis. Dragone's work was reported 25

years ago, and the standard convention used in conversion matrix analyses was quite different at that point in time. The analysis presented here is an extension of the work presented by Dragone. It is cast in the notation most commonly used for conversion matrix analyses.

Consider a solid state device which is dc biased such that one or more junctions are forward biased. The power spectral density of any shot noise sources which are present is given by Equation 2.16.

$$S_i(f) = 2\,I\,q \tag{7.1}$$

Note that the power spectral density is not frequency dependent and thus represents white noise. Accordingly, any shot noise current may be expressed as a function of time as,

$$i(t) = \sqrt{S_i}\,x(t) \tag{7.2}$$

where x(t) is a white noise source with unit spectral density. Equation 7.2 simply states that a shot noise source is white noise whose rms amplitude is equal to the square root of the power spectral density of the noise source. This follows directly from the definition of power spectral density. Also note that the frequency dependence of $S_i(f)$ has been dropped since in the case of shot noise, the power spectral density is independent of frequency.

Now consider the dynamic case where the bias condition of the solid state device varies as a periodic function of time. As discussed in Section 2.3, shot noise is generated by the transition of carriers across a potential barrier at independent points in time. If the frequencies of interest in the shot noise source correspond to periods which are much less than the transit time of a carrier across the barrier, then the statistical properties of the noise source will vary essentially as an instantaneous function of bias. If the frequencies of interest correspond to periods which are near the transit time, then the carriers which are in transit across the junction at any instant in time will be functions of the bias conditions during previous points in time. It is assumed in this analysis that the statistical properties of each shot noise source varies as an instantaneous function of time. For the case of the HBT modelled in Section 4, the *intrinsic* transit time is typically about 100 GHz. Thus, this assumption should be valid for frequencies below roughly 20

GHz. Under this assumption, the instantaneous power spectral density of the shot noise can be expressed as,

$$S_i(t) = 2\, I(t)\, q. \tag{7.3}$$

If a function h(t) is defined as the square root of the power spectral density of the shot noise current,

$$h(t) = \sqrt{S_i(t)} = \sqrt{2\, I(t)\, q}\,, \tag{7.4}$$

then combining Equations 7.2 and 7.4, the instantaneous shot noise current is given by,

$$i(t) = h(t)\, x(t). \tag{7.5}$$

Note in the above equation that x(t) is still a white noise source with unit spectral density whose statistical properties are not functions of time. In Equations 7.3 and 7.4, the functions I(t) and thus $S_I(t)$ and h(t) are deterministic functions which vary in a periodic manner. Thus, they can be expressed as Fourier series.

$$I(t) = \sum_{k=-\infty}^{\infty} I_k e^{jk\omega_b t} \tag{7.6}$$

$$h(t) = \sum_{k=-\infty}^{\infty} H_k e^{jk\omega_b t} \tag{7.7}$$

$$S_I(t) = \sum_{k=-\infty}^{\infty} S_k e^{jk\omega_b t} \tag{7.8}$$

From Equations 7.4, 7.7, and 7.8 S_k and H_k can be found to be related by,

$$S_k = \sum_{n=-\infty}^{\infty} H_n H_{k-n} \tag{7.9}$$

At this point, it is desirable to express the white noise source, x(t), in terms of its spot noise. As discussed by Rice [95], any noise source can be described as a continuous spectrum of sinusoidal signals. This follows directly from the concept of spectral density.

Any noise source can be thought of as the summation of an infinite number of sinusoids with random phase angles and average rms amplitudes equal to the square root of the spectral density function. As noted by Rice, a noise source can be expressed as,

$$x(t) = \lim_{\Delta f \to 0} \sum_{n=0}^{\infty} \sqrt{2\, S_x(f_n)\, \Delta f}\, \cos(2\pi f_n t + \phi_n)\,. \tag{7.10}$$

where

$$f_n = n\, \Delta f \tag{7.11}$$

In Equation 7.10, ϕ_n is a random phase angle which is uniformly distributed between $\pm\pi$. The function $S_x(f_n)$ is the power spectral density of x(t) and is equal to unity. It has units of 1/Hz. In other words, the function $S_x(f_n)$ determines the strength of the white noise source at a given frequency. The 2 under the radical in Equation 7.10 accounts for the fact that the square root of $S_x(f_n)$ is an rms value, while the entire function under the radical is the peak value of the cosine function. At this point, it is useful to consider the spot noise of x(t). Spot noise refers to a single frequency spectral component of a noise source. Thus the spot noise of x(t) in Equation 7.10 at 10 Hz is $\sqrt{2\, S_x(10)\, \Delta f}\, \cos(20\, \pi\, t + \phi)$. A spectrum of x(t) can be constructed from its spot noise by sweeping the spot noise over a span of frequencies. Accordingly, to simplify the analysis, only the spot noise of x(t) will be considered at radian frequencies of $n\, \omega_o \pm \omega_m$. The spectrum of noise which is due to x(t) can be obtained by varying ω_m across a span of frequencies. Accordingly, x(t) in Equation 7.10 is redefined as,

$$x(t) = \sum_{n=-\infty}^{\infty} \sqrt{2\, \Delta f}\, \cos[(\omega_m + n\, \omega_o)t + \alpha_n]\,. \tag{7.12}$$

In the above equation, advantage has been taken of the fact that $\cos(-\alpha)$ is equal to $\cos(\alpha)$ to represent x(t) in a more compact form. In addition, α_n is a random phase angle uniformly distributed between $\pm\pi$.

In a similar manner, the spot noise associated with the shot noise source, $i(t)$, can be described in the same form as Equation 7.12.

$$i(t) = \sum_{r=-\infty}^{\infty} \sqrt{2\, S_i(\omega_m + r\, \omega_o)\, \Delta f}\, \cos[(\omega_m + r\, \omega_o)t + \theta_r]\,. \tag{7.13}$$

Equation 7.13 can also be expressed as

$$i(t) = = \frac{1}{\sqrt{2}} \sum_{r=-\infty}^{\infty} \{I_{S_r} e^{j (r \omega_o + \omega_m) t} + I_{S_r}^{*} e^{j (-r \omega_o - \omega_m) t}\} \tag{7.14}$$

where

$$I_{S_r} = \sqrt{S_i(\omega_m + r \omega_o) \Delta f}\, e^{j \theta_r} \tag{7.15}$$

Expressing the spot noise of $i(t)$ in the form of Equation 7.14 has the advantage that it is directly compatible with the conversion matrix analysis in Section 5. In comparing Equation 7.14 with 5.8, it can be seen that the equations are essentially identical. In the form given by Equation 7.14, I_{S_r} is a phasor which has an rms amplitude equal to the rms amplitude of the spot noise source $i(t)$. Thus, I_{S_r} has units of amperes and is equal to the rms amplitude of the modulated shot noise source at each sideband frequency. The phase angle associated with I_{S_r} is randomly distributed between $\pm\pi$.

Combining Equations 7.5, 7.7, and 7.12,

$$i(t) = \sum_{k=-\infty}^{\infty} H_k e^{j k \omega_o t} \sum_{n=-\infty}^{\infty} \sqrt{2 \Delta f} \cos[(n \omega_o + \omega_m) t + \alpha_n] \tag{7.16}$$

$$i(t) = \sum_{k=-\infty}^{\infty} \sum_{n=-\infty}^{\infty} \sqrt{\frac{\Delta f}{2}}\, H_k \left\{ e^{j[(k+n) \omega_o t + \omega_m t + \alpha_n]} + e^{j[(k-n) \omega_o t - \omega_m t - \alpha_n]} \right\} \tag{7.17}$$

$$i(t) = \sum_{n=-\infty}^{\infty} \sum_{r=-\infty}^{\infty} \sqrt{\frac{\Delta f}{2}} \left\{ H_{r-n} e^{j[r \omega_o t + \omega_m t + \alpha_n]} + H_{n-r} e^{j[-r \omega_o t - \omega_m t - \alpha_n]} \right\} \tag{7.18}$$

Comparing Equations 7.14 and 7.18,

$$I_{S_r} = \sqrt{\Delta f} \sum_{n=-\infty}^{\infty} H_{r-n} e^{j \alpha_n}. \tag{7.19}$$

In order to determine the amount of correlation which exists between the noise currents at the different sideband frequencies it is useful to calculate the expectation value given by Equation 7.20. Using Equation 7.19,

$$\left\langle I_{S_n} I^*_{S_m} \right\rangle = \left\langle \Delta f \sum_{r=-\infty}^{\infty} H_{n-r} e^{j\alpha_r} \sum_{k=-\infty}^{\infty} H^*_{m-k} e^{-j\alpha_k} \right\rangle \tag{7.20}$$

The <> brackets in the above equation indicate that expectation value or ensemble average is being taken. Since α_r and α_k in Equation 7.20 are random phase angles uniformly distributed between $\pm\pi$,

$$\left\langle e^{j\alpha_r} e^{-j\alpha_k} \right\rangle = \begin{cases} 1 & r=k \\ 0 & r\neq k \end{cases}. \tag{7.21}$$

Combining Equations 7.20 and 7.21 and noting from the properties of Fourier series that H^*_n is equal to H_{-n},

$$\frac{\left\langle I_{S_n} I^*_{S_m} \right\rangle}{\Delta f} = \sum_{r=-\infty}^{\infty} H_{n-r} H^*_{m-r} = \sum_{r=-\infty}^{\infty} H_{n-r} H_{r-m} \tag{7.22}$$

Combining Equations 7.9 and 7.22,

$$\frac{\left\langle I_{S_n} I^*_{S_m} \right\rangle}{\Delta f} = S_{n-m} \tag{7.23}$$

However, from Equations 7.3, 7.6, and 7.8,

$$S_k = 2\,q\,I_k \tag{7.24}$$

Thus,

$$\frac{\left\langle I_{S_n} I^*_{S_m} \right\rangle}{\Delta f} = 2\,q\,I_{n-m} \tag{7.25}$$

where, as defined by Equation 7.6, I_{n-m} is a Fourier coefficient of the current which generates the shot noise. Equation 7.25 is a very significant equation. It can be used to determine the amount of correlation which exists between the sidebands of a periodically modulated shot noise source. As indicated by the equation, the more significantly the current is varied, the greater the correlation between the noise at the various sideband frequencies. This indicates that as the current varies more significantly, more noise is frequency converted between the sidebands due to noise source modulation.

7.1.2. Modulation of flicker noise sources

The flicker noise sources which are present within an oscillator will also be modulated by the periodic variations in the oscillator currents. The modulation of flicker noise in periodically driven circuits has not previously been analyzed. To the author's knowledge, the analysis presented here is the first such analysis of flicker noise source modulation. This phenomenon has a very significant impact on the noise characteristics of oscillators, since the upconversion of flicker noise to the sideband frequencies can be a dominant effect in many oscillators.

Consider an electrical component which is dc biased and generates flicker noise. For convenience, it is assumed in this derivation that this flicker noise may be modelled as a current source in parallel with the component. However, this analysis is equally valid for flicker noise voltage sources. (A flicker noise current source was chosen simply because this type of source is used in the HBT flicker noise model given in Figure 6.8.) The power spectral density of this flicker noise current source is given by Equation 2.17.

$$S_i(f) = C \frac{I^m}{f^n} \tag{7.26}$$

where C is a constant, I is the current flowing through the device, f is the frequency, m is a constant which is usually very close to 2, and n is a constant which can range from .6 to 1.5. Equation 7.26 is a generalized form of the well known Hooge equation [96] which is commonly sighted in the analysis of 1/f noise. (The Hooge equation is similar to Equation 7.26 except that m is set equal to 2 and n is set equal to 1.)

A flicker noise current source, $i(t)$, may be expressed as a function of time in a manner analogous to Equation 7.2.

$$i(t) = \sqrt{S_i(f)\, f^n}\, x(t) \tag{7.27}$$

where x(t) is a bias independent flicker noise source with unity spectral density at 1 Hz and has units of 1/Hz. Equation 7.27 follows directly from the definition of power spectral density. It simply states that $i(t)$ is a flicker noise source whose rms amplitude at any frequency is equal to the square root of its power spectral density at the same frequency.

To express the power spectral density of a flicker noise current source as a function of time, it is necessary to understand how its statistical properties vary as a function of time. As discussed in Section 2.4, flicker noise is widely believed to be a result of the modulation of current through a device. In Section 2.4, an example was given of a resistor which is biased by a constant current source. In this case, it was found that resistance fluctuations modulate the current through the resistor resulting in flicker voltage fluctuations across the resistor. The spectral density of the voltage fluctuations was found to be related to the spectral density of the resistance fluctuations through the expression

$$S_V(f) = I^2 S_r(f). \tag{7.28}$$

In any given device, flicker noise is believed to be a result of the modulation of the current through the device by some mechanism. For example, as discussed by Fogner [91] the flicker noise current source, i_{fbc} in Figure 6.8, is a result of fluctuations in the base surface recombination velocity [91]. These fluctuations were found to modulate the base recombination current resulting in a flicker noise current source. As another example, Hsu [97] found that flicker noise in Schottky barrier diodes was the result of "the modulation of the barrier height, ϕ_B." This modulation in the barrier height in turn modulates the current through the device. In FETs, flicker noise has been attributed to the modulation of the device channel by the trapping and detrapping of carriers in the depletion region and device substrate [71]. Figure 7.1 may be used to analyze flicker noise in a given device. Flicker noise current is generated by the modulation of the current through the device by some physical mechanism. This may be expressed as,

$$I + i(t) = I\,[1 + m(t)] \tag{7.29}$$

where m(t) represents the mechanism which generates flicker noise. Since the time varying components of the above equation must be equal,

$$i(t) = I\,m(t) \tag{7.30}$$

Equation 7.30 requires that the spectral densities of the flicker noise current and the modulation mechanism must be related by,

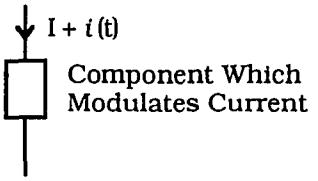

Figure 7.1. Generation of Flicker Noise Through the Modulation of Bias Current

$$S_i(f) = I^2 S_m(f). \tag{7.31}$$

Since the flicker noise current source has a 1/f noise spectrum, the fluctuations in the modulation mechanism must also have a spectrum which is inversely proportional to frequency. In addition, by comparing Equations 7.26 and 7.31, it can be seen that since m is nearly equal to 2 in Equation 7.26, the fluctuations in the modulation mechanism, m(t), must be nearly independent of bias current. Thus, Equations 7.26, 7.30, and 7.31 indicate that *the flicker noise current through a component is a result of the modulation of the bias current by a physical mechanism in the component. In addition, the physical mechanism which creates the fluctuation in the bias current is essentially independent of bias.*

Many others also view flicker noise as the modulation of current by device fluctuations [29-32, 71, 93]. As noted by Hooge, "One of the few statements about 1/f noise that has not raised controversy is that 1/f noise is a fluctuation in the conductivity. A current through the sample does not generate the noise, by turbulence or so, but only serves to measure it." There is also significant experimental evidence to support this physical view of flicker noise. Voss and Clark [32] measured the thermal noise across a resistor for a long period of time. It was found that the square of the thermal noise varied with a 1/f noise spectrum even with no bias current applied. A similar observation has been made by Beck and Spruit [98]. As indicated by Equation 2.9, this type of spectrum could only be a result of conductance variations. Additional experimental evidence that 1/f noise is due to conductance variations has been provided by Jones and Francis [99]. They applied an ac signal to a resistor which exhibited flicker noise. By measuring the correlation between the upconverted noise, and the flicker noise, they determined that the flicker noise upconversion was due to fluctuations in the conductance. Note that these analyses and the derivation given on the previous page do not make any restrictions on what physical mechanism causes the fluctuations in conductivity. They only

demonstrate that flicker noise current and voltage sources are due to the modulation of the bias condition within components. However, this provides sufficient information to analyze the modulation of flicker noise sources.

An expression may now be developed which expresses flicker noise current as a function of time. As mentioned previously, the value of m in Equation 2.26 is nearly equal to 2. Any deviation from this value is usually believed to be a result of temperature effects [29]. As the bias which is applied to a device is varied, the temperature of the device also varies. If these temperature variations affect the physical mechanisms which modulate the bias current in Equation 7.29, then exponent of the current dependence in Equation 7.31 will not be measured as being exactly equal to 2. For a periodically varying current, where the period of the frequency is much shorter than the thermal time constant, the temperature of the component will not change over a cycle. Thus, under this condition, m in Equation 7.26 will be equal to 2. If m is taken to be equal to 2, then from Equations 7.26 and 7.31, the spectral density of the mechanism which modulates the bias current, $S_m(f)$, is given by,

$$S_m(f) = \frac{C}{f^n} \tag{7.32}$$

From Equations 7.31 and 7.32,

$$S_i(f, t) = I(t)^2 S_m(f) = C \frac{I(t)^2}{f^n} \tag{7.33}$$

The transition from a dc steady state case to a dynamic condition in Equation 7.33 can be made since $S_m(f)$ is not a function of the applied bias condition and accordingly $S_m(f)$ does not vary with time. This is indicated by Equation 7.32. Thus, $S_i(f, t)$ varies as an instantaneous function of I(t). It is convenient to define a function h(t) as,

$$h(t) = \sqrt{S_i(f, t)\, f^n} = \sqrt{C}\, I(t). \tag{7.34}$$

Combining Equations 7.27 and 7.34, the instantaneous flicker noise current is given by,

$$i(t) = h(t)\, x(t) \tag{7.35}$$

Note in the above equation that x(t) is still a bias independent flicker noise source with unit spectral density at 1 Hz whose statistical properties are not time dependent. In Equation 3.34, the functions I(t) and thus h(t) are deterministic functions which vary in a periodic manner. Thus, they can be expressed as Fourier series.

$$I(t) = \sum_{k=-\infty}^{\infty} I_k e^{jk\omega_0 t} \tag{7.36}$$

$$h(t) = \sum_{k=-\infty}^{\infty} H_k e^{jk\omega_0 t} \tag{7.37}$$

In a manner similar to that discussed for shot noise, x(t) can be described in terms of its spot noise. As discussed by Rice [95], the full spectrum of x(t) can be expressed as,

$$x(t) = \lim_{\Delta f \to 0} \sum_{n=0}^{\infty} \sqrt{2\, S_x(f_n)\, \Delta f}\, \cos(2\pi f_n t + \phi_n). \tag{7.38}$$

where

$$f_n = n\, \Delta f \tag{7.39}$$

Again in the above equation, ϕ_n is a random phase angle which is uniformly distributed between $\pm\pi$. The function $S_x(f_n)$ is the power spectral density of x(t) and is equal to 1/f. It has units of 1/Hz. To simplify the analysis, only the spot noise of x(t) will be considered at a baseband radian frequency of ω_m. The noise which is due to the entire spectrum of x(t) can be obtained by sweeping this spot noise source across a span of frequencies. Note that only the baseband frequency of x(t) is considered in this case. This is in contrast to the shot noise source in Equation 7.12 where the spot noise at all of the sideband frequencies were considered. Recall that x(t) is a bias independent flicker noise source. Since it is a flicker noise source, it will only produce a significant amount of noise at baseband frequencies. (The flicker noise at higher frequencies will be much lower than the shot and thermal noise present.) Thus only the baseband frequency component of x(t) must be considered. Accordingly, x(t) in Equation 7.38 is redefined as,

$$x(t) = \sqrt{\frac{2\, \Delta f}{f_m}}\, \cos[\omega_m t + \alpha]. \tag{7.40}$$

In Equation 7.40, α is a random phase angle uniformly distributed between $\pm\pi$.

The spot noise associated with the modulated flicker noise source, $i(t)$, can be described by Equation 7.41. Note that in this equation $i(t)$ contains frequency components at all of the sideband frequencies. Since it is a periodically modulated flicker noise source, the flicker noise is upconverted to all of the sideband frequencies. Thus, Equation 7.41 accounts for the flicker noise at all of these frequencies.

$$i(t) = \sum_{n=-\infty}^{\infty} \sqrt{2\, S_i(f_n)\, \Delta f}\ \cos[(\omega_m + n\,\omega_o)t + \theta_n] \,. \tag{7.41}$$

Equation 7.41 can also be expressed in the form

$$i(t) = \frac{1}{\sqrt{2}} \sum_{r=-\infty}^{\infty} \left(I_{f_r} e^{j(r\omega_o + \omega_m)t} + I_{f_r}^{*} e^{j(-r\omega_o - \omega_m)t} \right) \tag{7.42}$$

where

$$I_{f_r} = \sqrt{S_i(f_n)\, \Delta f}\ e^{j\theta_r} \tag{7.43}$$

Just as in the case of shot noise modulation, expressing the spot noise of $i(t)$ in the form of Equation 7.42 has the advantage that it is directly compatible with the conversion matrix analysis in Section 4. The physical significance of I_{f_r} should not be over looked. This phasor represents the rms amplitude of the modulated flicker noise source. Thus, I_{f_1} is the rms amplitude of the modulated spot flicker noise source at the upper sideband of the first harmonic.

Combining Equations 7.35, 7.37, and 7.40,

$$i(t) = \sum_{k=-\infty}^{\infty} H_k e^{jk\omega_o t} \sqrt{\frac{2\,\Delta f}{f_m}} \cos[\omega_m t + \alpha] \tag{7.44}$$

$$i(t) = \sum_{k=-\infty}^{\infty} \sqrt{\frac{\Delta f}{2\, f_m}}\, H_k \left\{ e^{j[k\omega_o t + \omega_m t + \alpha]} + e^{j[k\omega_o t - \omega_m t - \alpha]} \right\} \tag{7.45}$$

$$i(t) = \sum_{r=-\infty}^{\infty} \sqrt{\frac{\Delta f}{2\, f_m}} \left\{ H_r e^{j[r\omega_o t + \omega_m t + \alpha]} + H_{-r} e^{j[-r\omega_o t - \omega_m t - \alpha]} \right\} \tag{7.46}$$

Comparing Equations 7.42 and 7.46

$$I_{f_r} = \sqrt{\frac{\Delta f}{f_m}}\, H_r\, e^{J\alpha} \tag{7.47}$$

In order to determine the amount of correlation between the noise currents at the different sideband frequencies, it is useful to calculate the expectation value given below. From Equation 7.47,

$$\left\langle I_{f_n} I^*_{f_k} \right\rangle = \left\langle \frac{\Delta f}{f_m} H_n e^{J\alpha} H^*_k e^{-J\alpha} \right\rangle = \frac{\Delta f}{f_m} H_n H^*_k \tag{7.48}$$

Recalling from the properties of Fourier series that H^*_n is equal to H_{-n}, and from Equation 7.34,

$$\frac{\left\langle I_{f_n} I^*_{f_k} \right\rangle}{\Delta f} = \frac{H_n H_k}{f_m} = \frac{C}{f_m} I_n I_k \tag{7.49}$$

Equation 7.49 is analogous to Equation 7.25. The above equation can be used to determine the amount of correlation which exists between the sideband frequencies of a periodically modulated flicker noise source. It indicates that as the Fourier coefficients of the periodically varying bias current increase, more flicker noise is upconverted to the sidebands due to noise source modulation.

7.2. Conversion of Modulated Noise Sources to the Oscillator Output

In the previous section, equations were derived which indicate how much noise exists at each of the oscillator sidebands and the correlation between the noise at these different sideband frequencies due to noise source modulation. With this information, and the results of the conversion matrix analysis presented in Section 5, it is now possible to calculate how much noise exists at each of the output sidebands of the oscillator. In order to clarify the procedure presented in this section, the analysis of the shot noise source i_{sec} shown in Figure 6.1 is discussed in detail. The calculations required to analyze the other noise sources within the oscillator are also given.

In order to model AM and PM noise spectrums of the oscillator, it is necessary to determine how much noise exists at the oscillator output sidebands, and to determine the

correlation between the noise at these sidebands. To summarize the work which has been discussed to this point, the large signal characteristics of the HBT and oscillator were modelled in Section 4. Based on the large signal HBT and oscillator models, a conversion network model was generated which characterizes the relationships between incrementally small voltages and currents within the oscillator. In other words, the conversion network model can be used to analyze how a small signal voltage or current which is injected into the oscillator will be converted to other frequencies within the oscillator due to circuit nonlinearities. This conversion network model is discussed in Section 5. In Section 6, the noise characteristics of the HBT are modelled. These noise characteristics are required to determine magnitude and location of each noise source within the HBT device. The theory required to account for the periodic modulation of these noise sources is presented in Section 7.1. This theory will now be combined with the results of Sections 4 through 6 to determine the AM and PM noise spectrums of the oscillator.

Consider the shot noise source i_{sec} in Figure 6.1. This shot noise will be converted to all of the sideband frequencies of the oscillator due to both the circuit nonlinearities and noise source modulation. Due to noise source modulation alone, the noise at all of the sideband frequencies of the oscillator will be partially correlated. From Equation 7.25, the correlation between the sideband frequencies is given by,

$$\frac{\langle I_{S_n} I^*_{S_m} \rangle}{\Delta f} = 2\, q\, I_{n-m} \tag{7.50}$$

where I_{n-m} is a Fourier coefficient of the periodically varying current which creates the shot noise. I_{S_n} is defined by Equations 7.14 and 7.15. It is a phasor whose magnitude is equal to the rms value of the spot noise of the shot noise source at the frequency $n\,\omega_o + \omega_m$. A spectrum of the noise at any sideband may be determined by sweeping this spot noise source through a span of frequencies. As indicated by Equation 6.6, the current associated with the shot noise source, i_{sec}, is I_{CT}. Using Equations 4.2 through 4.4 and the results of the large signal simulation results in Section 4, I_{CT} may be calculated and plotted as shown in Figure 7.2. The Fourier coefficients associated with the waveform in Figure 7.2 are given in Table 7.1. These Fourier coefficients can be used in conjunction with Equation 7.50 to determine the power spectral density and the correlation properties

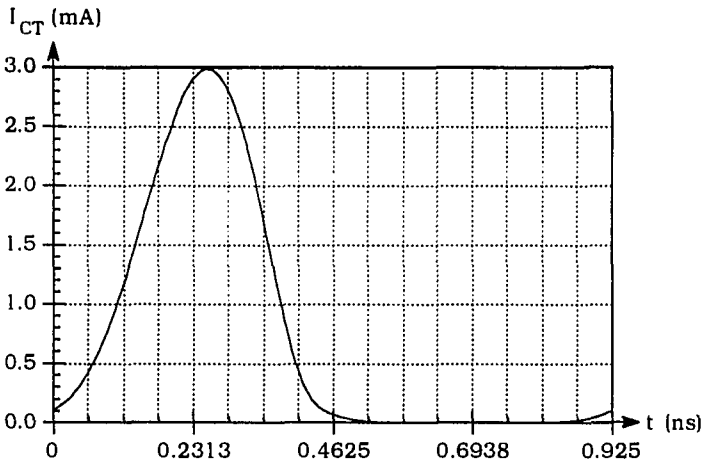

Figure 7.2. I_{CT} as a Function of Time.

of the noise at the oscillator sidebands. For example, using Equation 7.50 and the data in Table 7.1, the power spectral density of the shot noise source at each sideband frequency is given by,

$$S_I(f) = \frac{\langle I_{s_n} I^*_{s_n} \rangle}{\Delta f} = 2\,q\,I_0 = 2.38 \times 10^{-22}\ (A^2/Hz). \tag{7.51}$$

Note that the power spectral density of the periodically modulated shot noise source is identical to that of an unmodulated shot noise source and is not a function of frequency. However, the noise at the various sidebands is partially correlated as indicated by Equation 7.50. This is not the case with an unmodulated shot noise where the noise at every frequency is uncorrelated with the noise at every other frequency. Equation 7.50 also indicates how much noise a given shot noise source injects into a periodically driven circuit at each sideband frequency. However, in the case of the oscillator, it is desirable to determine how much noise voltage a given source creates at the oscillator output. This can be accomplished through the use of the conversion network model generated in Section 5. To determine how much the noise voltage is generated at the oscillator output from i_{sec}, five separate current sources must be placed in the conversion network shown in Figure 5.5. For example, to determine the amount of noise voltage which is created at the oscillator output from the shot noise at the upper sideband of the second harmonic, a current source is be placed in parallel with g_o at the two terminals which are the farthest forward in Figure 5.5. The transimpedances from

Table 7.1. Fourier Coefficients of Significant Noise Source Modulation Currents

Fourier Coef. of I_{CT}	Magnitude (mA)	Angle (°)	Fourier Coef. of I_{RF}	Magnitude (μA)	Angle (°)
I_0	0.7426	0	I_0	9.322	0
I_1	0.6173	-93.38	I_1	7.201	-92.46
I_2	0.3565	169.86	I_2	3.542	170.00
I_3	0.1404	63.40	I_3	1.150	57.34
I_4	0.04017	-72.53	I_4	0.3418	-92.78

this current source to the voltages at the outputs, V_{out-1} and V_{out1}, are then calculated. (See Figure 5.5.) These transimpedances are then multiplied by the rms value of the shot noise current at the upper-sideband of the second harmonic to determine the amount of output noise voltage which is generated at the upper and lower sidebands of the first harmonic. This process is repeated for each of the sideband frequencies. Thus, to determine how much noise voltage is generated at the output due to the shot noise at the baseband frequency, a current source would be placed in parallel with g_o at the pair of terminals which are the third from the front in Figure 5.5. Throughout the rest of this paper, the transimpedances from the upper sideband of harmonic n (i.e. at a frequency of n $\omega_o + \omega_m$) to the oscillator outputs are defined by $Z_{1,n}$ and $Z_{-1,n}$. Thus, the conversion impedance from the -2nd harmonic to the upper-sideband of the fundamental frequency at the oscillator output is defined as $Z_{1,-2}$. (The -2nd harmonic corresponds to the lower sideband of the second harmonic.) A typical transimpedance plot is shown in Figure 5.6. Since the voltages at the oscillator output, V_{out-1} and V_{out1}, are due to the sum of the shot noise currents at each of the sideband frequencies, they can be expressed as,

$$V_{out_1} = \sum_{n=-2}^{2} I_{S_n} Z_{1,n} \tag{7.52}$$

$$V_{out_{-1}} = \sum_{n=-2}^{2} I_{S_n} Z_{-1,n} \tag{7.53}$$

The limits from -2 to 2 are used in Equations 7.52 and 7.53 since the only 2 harmonics of the oscillator are considered in this analysis. In general, these limits would be equal to the number of harmonics considered in a given oscillator analysis.

Equations 7.52 and 7.53 may be used to calculate the amount of spot noise voltage which is present at the oscillator output as well as the AM and PM noise spectrums. As derived in Appendix E, the AM and PM noise spectrums are given by,

$$SSB_{PM} = \frac{\langle V_{out1} V_{out1}^* \rangle + \langle V_{out-1} V_{out-1}^* \rangle - 2\,Re\{\langle V_{out1} V_{out-1}^* \rangle \angle -2\phi_o\}}{4|V_x|^2} \tag{7.54}$$

$$SSB_{AM} = \frac{\langle V_{out1} V_{out1}^* \rangle + \langle V_{out-1} V_{out-1}^* \rangle + 2\,Re\{\langle V_{out1} V_{out-1}^* \rangle \angle -2\phi_o\}}{4|V_x|^2} \tag{7.55}$$

where the large signal voltage at the output of the oscillator at the first harmonic is given by,

$$V_{out}(t) = \sqrt{2}\, V_x \cos(\omega_o t + \phi_o). \tag{7.56}$$

In order to apply Equations 7.54 and 7.55, it is necessary to calculate several expectation values. From Equations 7.52 and 7.53,

$$\langle V_{out_1} V_{out_1}^* \rangle = \left\langle \sum_{m=-2}^{2} \sum_{n=-2}^{2} Z_{1,n} Z_{1,m}^* I_{S_n} I_{S_m}^* \right\rangle = \sum_{m=-2}^{2} \sum_{n=-2}^{2} Z_{1,n} Z_{1,m}^* \langle I_{S_n} I_{S_m}^* \rangle \tag{7.57}$$

$$\langle V_{out_{-1}} V_{out_{-1}}^* \rangle = \left\langle \sum_{m=-2}^{2} \sum_{n=-2}^{2} Z_{-1,n} Z_{-1,m}^* I_{S_n} I_{S_m}^* \right\rangle = \sum_{m=-2}^{2} \sum_{n=-2}^{2} Z_{-1,n} Z_{-1,m}^* \langle I_{S_n} I_{S_m}^* \rangle \tag{7.58}$$

$$\langle V_{out_1} V_{out_{-1}}^* \rangle = \left\langle \sum_{m=-2}^{2} \sum_{n=-2}^{2} Z_{1,n} Z_{-1,m}^* I_{S_n} I_{S_m}^* \right\rangle = \sum_{m=-2}^{2} \sum_{n=-2}^{2} Z_{1,n} Z_{-1,m}^* \langle I_{S_n} I_{S_m}^* \rangle \tag{7.59}$$

Combining Equation 7.50 with 7.57 through 7.59, the above expectation values for a shot noise source are given by,

$$\langle V_{out_1} V_{out_1}^* \rangle = 2\,q\,\Delta f \sum_{m=-2}^{2} \sum_{n=-2}^{2} Z_{1,n} Z_{1,m}^* I_{n-m} \qquad \text{(shot noise)} \tag{7.60}$$

$$\langle V_{out_{-1}} V_{out_{-1}}^* \rangle = 2\,q\,\Delta f \sum_{m=-2}^{2} \sum_{n=-2}^{2} Z_{-1,n} Z_{-1,m}^* I_{n-m} \qquad \text{(shot noise)} \tag{7.61}$$

$$\langle V_{out_l} V^*_{out_{-l}} \rangle = 2\,q\,\Delta f \sum_{m=-2}^{2} \sum_{n=-2}^{2} Z_{l,n} Z^*_{-l,m} I_{n-m} \qquad \text{(shot noise)} \qquad (7.62)$$

In a similar manner, Equation 7.49 may be combined with expressions analogous to Equations 7.57 through 7.59 to determine the same expectation values for flicker noise sources.

$$\langle V_{out_l} V^*_{out_l} \rangle = \frac{C}{f_m} \Delta f \sum_{m=-2}^{2} \sum_{n=-2}^{2} Z_{l,n} Z^*_{l,m} I_n I_{-m} \qquad \text{(flicker noise)} \qquad (7.63)$$

$$\langle V_{out_{-l}} V^*_{out_{-l}} \rangle = \frac{C}{f_m} \Delta f \sum_{m=-2}^{2} \sum_{n=-2}^{2} Z_{-l,n} Z^*_{-l,m} I_n I_{-m} \qquad \text{(flicker noise)} \qquad (7.64)$$

$$\langle V_{out_l} V^*_{out_{-l}} \rangle = \frac{C}{f_m} \Delta f \sum_{m=-2}^{2} \sum_{n=-2}^{2} Z_{l,n} Z^*_{-l,m} I_n I_{-m} \qquad \text{(flicker noise)} \qquad (7.65)$$

where C is the constant which determines the magnitude of the flicker noise source, and is defined by Equation 7.26. Equations 7.60 through 7.65 were used to determine the noise spectrums of the oscillator which result from each of the individual shot and flicker noise sources present in the oscillator. These spectrums are shown in Figures 7.3 through 7.6.

The remaining noise sources within the oscillator are all due to thermal noise sources. The thermal noise sources may be handled in a somewhat more simplified manner since they are not modulated. Consider first the thermal noise associated with the base contact resistance, R_B, and the 1-port networks in Figure 5.5 which contain the collector contact resistance, R_C. As discussed in Section 2.2, the thermal noise associated with these circuits may be represented by a current source in parallel with each of the networks. Thus the noise voltage which these current sources create at the oscillator output can be calculated using Equations 7.57 through 7.59. However, the thermal noise sources are unmodulated and thus the spot noise at each sideband frequency is uncorrelated with the spot noise at every other sideband frequency. As a result,

$$\langle I_n I^*_m \rangle = 0 \qquad (m \neq n) \qquad (7.66)$$

Combining Equations 7.57 through 7.59 with Equation 7.66,

$$\langle V_{out_1} V_{out_1}^* \rangle = \sum_{n=-2}^{2} Z_{1,n} Z_{1,n}^* \langle I_n I_n^* \rangle \tag{7.67}$$

$$\langle V_{out_{-1}} V_{out_{-1}}^* \rangle = \sum_{n=-2}^{2} Z_{-1,n} Z_{-1,n}^* \langle I_n I_n^* \rangle \tag{7.68}$$

$$\langle V_{out_1} V_{out_{-1}}^* \rangle = \sum_{n=-2}^{2} Z_{1,n} Z_{-1,n}^* \langle I_n I_n^* \rangle \tag{7.69}$$

However, from Equation 2.10,

$$\langle I_n I_n^* \rangle = 4\, k\, T\, \Delta f\, Re[Y_{11_n}] \tag{7.70}$$

where Y_{11_n} is the admittance of the 1 port network at the spot noise frequency of the nth harmonic. Combining Equations 7.67 through 7.70,

$$\langle V_{out_1} V_{out_1}^* \rangle = 4\, k\, T\, \Delta f \sum_{n=-2}^{2} Z_{1,n} Z_{1,n}^* Re[Y_{11_n}] \tag{7.71}$$

$$\langle V_{out_{-1}} V_{out_{-1}}^* \rangle = 4\, k\, T\, \Delta f \sum_{n=-2}^{2} Z_{-1,n} Z_{-1,n}^* Re[Y_{11_n}] \tag{7.72}$$

$$\langle V_{out_1} V_{out_{-1}}^* \rangle = 4\, k\, T\, \Delta f \sum_{n=-2}^{2} Z_{1,n} Z_{-1,n}^* Re[Y_{11_n}] \tag{7.73}$$

Equations 7.71 through 7.73 were used in conjunction with Equations 7.54 and 7.55 to calculate the noise spectrums due to the thermal noise associated with R_B and R_C. The resulting spectrums are shown in Figures 7.7 and 7.8.

The remaining noise sources in the oscillator are the thermal noise sources associated with the resonator circuit in Figure 4.26 and the thermal noise associated with R_E. These are the noise sources associated with the linear 2-port networks in Figure 5.5. Again, since the thermal noise sources are not modulated, the noise voltages at the different sideband frequencies are uncorrelated. As discussed in Section 2.2, all of the thermal noise sources within the linear resonator circuit may be modelled by placing a current noise source in parallel each of the external ports of the network. These current

noise sources will in general be partially correlated. Defining the current noise source across the base-to-ground terminal pair as i_1 and the current noise source across the emitter-to-ground terminal pair as i_2, the noise voltage at the oscillator outputs due to these two current sources is given by,

$$V_{out_1} = \sum_{n=-2}^{2} I_n^{i_1} Z_{1,n}^{i_1} + I_n^{i_2} Z_{1,n}^{i_2} \tag{7.74}$$

and

$$V_{out_{-1}} = \sum_{n=-2}^{2} I_n^{i_1} Z_{-1,n}^{i_1} + I_n^{i_2} Z_{-1,n}^{i_2} \tag{7.75}$$

where $Z_{-1,n}^{i_1}$ is the transimpedance from the nth port of the location of current source i_1 to the lower sideband of the first harmonic at the output. $I_n^{i_1}$ is the spot noise of the current source i_1 at the nth harmonic. The other transimpedances in these equations have corresponding definitions. From the above equations, and Equation 7.66,

$$\left\langle V_{out_1} V_{out_1}^* \right\rangle = \sum_{n=-2}^{2} \left|Z_{1,n}^{i_1}\right|^2 \left\langle I_n^{i_1} I_n^{i_1 *} \right\rangle + \left|Z_{1,n}^{i_2}\right|^2 \left\langle I_n^{i_2} I_n^{i_2 *} \right\rangle + 2\,\mathrm{Re}\left\{ Z_{1,n}^{i_1} Z_{1,n}^{i_2 *} \left\langle I_n^{i_1} I_n^{i_2 *} \right\rangle \right\} \tag{7.76}$$

$$\left\langle V_{out_{-1}} V_{out_{-1}}^* \right\rangle = \sum_{n=-2}^{2} \left|Z_{-1,n}^{i_1}\right|^2 \left\langle I_n^{i_1} I_n^{i_1 *} \right\rangle + \left|Z_{-1,n}^{i_2}\right|^2 \left\langle I_n^{i_2} I_n^{i_2 *} \right\rangle + 2\,\mathrm{Re}\left\{ Z_{-1,n}^{i_1} Z_{-1,n}^{i_2 *} \left\langle I_n^{i_1} I_n^{i_2 *} \right\rangle \right\} \tag{7.77}$$

$$\left\langle V_{out_1} V_{out_{-1}}^* \right\rangle = \sum_{n=-2}^{2} Z_{1,n}^{i_1} Z_{-1,n}^{i_1 *} \left\langle I_n^{i_1} I_n^{i_1 *} \right\rangle + Z_{1,n}^{i_2} Z_{-1,n}^{i_2 *} \left\langle I_n^{i_2} I_n^{i_2 *} \right\rangle + Z_{1,n}^{i_1} Z_{-1,n}^{i_2 *} \left\langle I_n^{i_1} I_n^{i_2 *} \right\rangle + Z_{1,n}^{i_2} Z_{-1,n}^{i_1 *} \left\langle I_n^{i_2} I_n^{i_1 *} \right\rangle \tag{7.78}$$

Combining the above equations with Equation 2.10,

$$\left\langle V_{out_1} V_{out_1}^* \right\rangle = 4\,k\,T\,\Delta f \sum_{n=-2}^{2} \left|Z_{1,n}^{i_1}\right|^2 \mathrm{Re}[Y_{11}]_n + \left|Z_{1,n}^{i_2}\right|^2 \mathrm{Re}[Y_{22}]_n + 2\,\mathrm{Re}\left\{ Z_{1,n}^{i_1} Z_{1,n}^{i_2 *} \mathrm{Re}[Y_{12}]_n \right\} \tag{7.79}$$

$$\left\langle V_{out_{-1}} V_{out_{-1}}^* \right\rangle = 4\,k\,T\,\Delta f \sum_{n=-2}^{2} \left|Z_{-1,n}^{i_1}\right|^2 \mathrm{Re}[Y_{11}]_n + \left|Z_{-1,n}^{i_2}\right|^2 \mathrm{Re}[Y_{22}]_n + 2\,\mathrm{Re}\left\{ Z_{-1,n}^{i_1} Z_{-1,n}^{i_2 *} \mathrm{Re}[Y_{12}]_n \right\} \tag{7.80}$$

$$\left\langle V_{out_1} V_{out_{-1}}^* \right\rangle = \sum_{n=-2}^{2} Z_{1,n}^{i_1} Z_{-1,n}^{i_1 *} \mathrm{Re}[Y_{11}]_n + Z_{1,n}^{i_2} Z_{-1,n}^{i_2 *} \mathrm{Re}[Y_{22}]_n + Z_{1,n}^{i_1} Z_{-1,n}^{i_2 *} \mathrm{Re}[Y_{12}]_n + Z_{1,n}^{i_2} Z_{-1,n}^{i_1 *} \mathrm{Re}[Y_{21}]_n \tag{7.81}$$

Equations 7.79 through 7.81 were used in conjunction with Equations 7.54 and 7.55 to calculate the noise spectrums of the oscillator due to the thermal noise in the resonator network. The AM and PM noise spectrums which resulted from these calculations are shown in Figure 7.9.

It is also significant to note that the noise sources associated with each of the spectrum plots shown in this section are uncorrelated. Thus, the spectral densities of these noise plots may simply be added to determine the overall noise spectrums of the oscillator. These noise spectrums are shown in Figure 7.10. The noise spectrums which have been generated in this section are discussed in Section 7.3. In addition, measurements of the overall phase noise spectrum of the oscillator are presented in Section 7.3 which are in good agreement with the modelled results.

7.3. Discussion of Modelled Results

The plots in Figures 7.3 through 7.10 provide a great deal of insight into the noise characteristics of the oscillator. Note that in all of the plots the AM noise level is below the PM noise level. This is primarily a result of the mechanisms which cause limiting in the oscillator. These limiting mechanisms tend to maintain the amplitude of oscillation at the same level. Thus, the effectiveness of any noise sources which modulates the amplitude of oscillation will be reduced by these limiting mechanisms. This is analogous to the operation of a limiter. Once a limiter is driven into a limiting mode, any increase in the drive level will only cause a slight increase in the level at the limiter. It should be noted that there is no similar limiting mechanism for the PM noise spectrum. Figure 7.10 indicates that the AM noise spectrum of the overall oscillator is 10 to 15 dB below the PM noise spectrum. However, at frequencies greater than roughly 1 MHz, the AM and PM noise spectrums tend to converge to the same levels. This indicates that for offset frequencies greater than roughly 1 MHz, some noise sources are simply adding with the oscillator output and are not effected by the oscillator limiting.

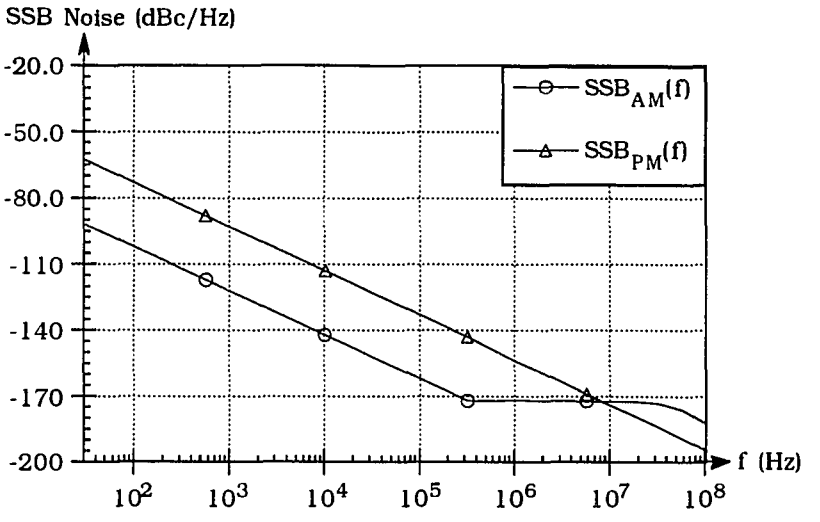

Figure 7.3. Single Sideband Spectrums Due to Base Current Shot Noise, i_{sbe}

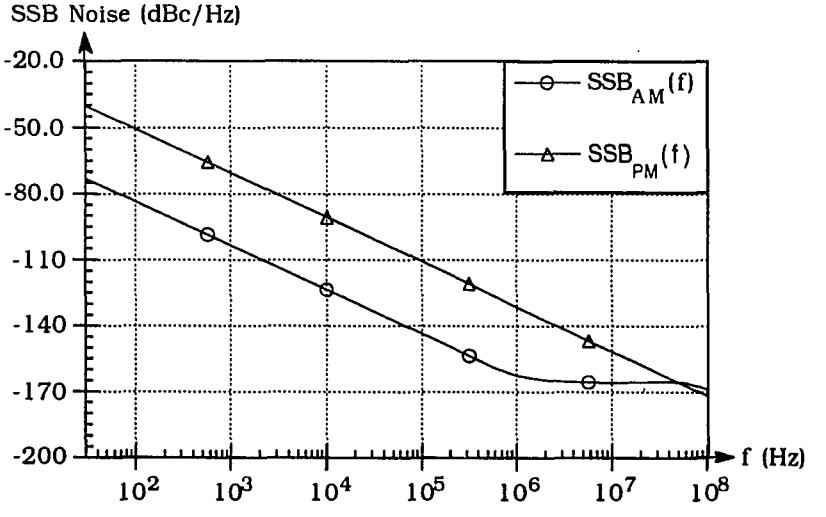

Figure 7.4. Single Sideband Spectrums Due to Collector Current Shot Noise, i_{sec}

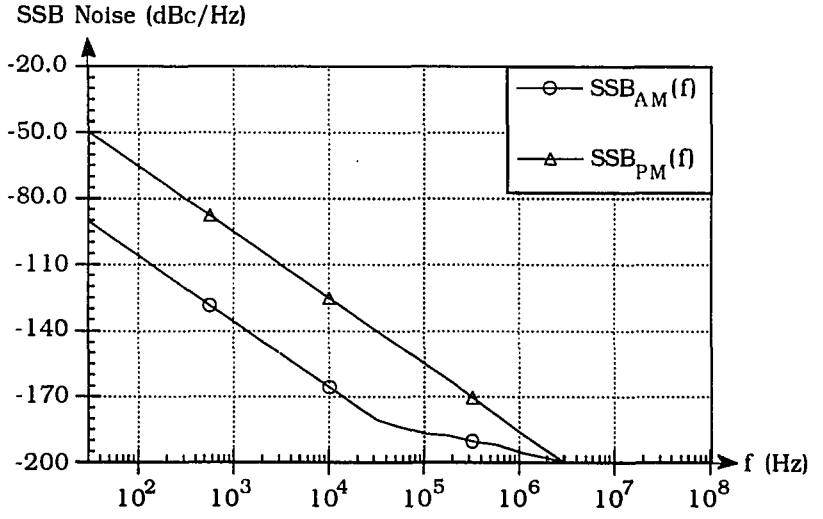

Figure 7.5. Single Sideband Spectrums Due to Base Current Flicker Noise, i_{fbc}

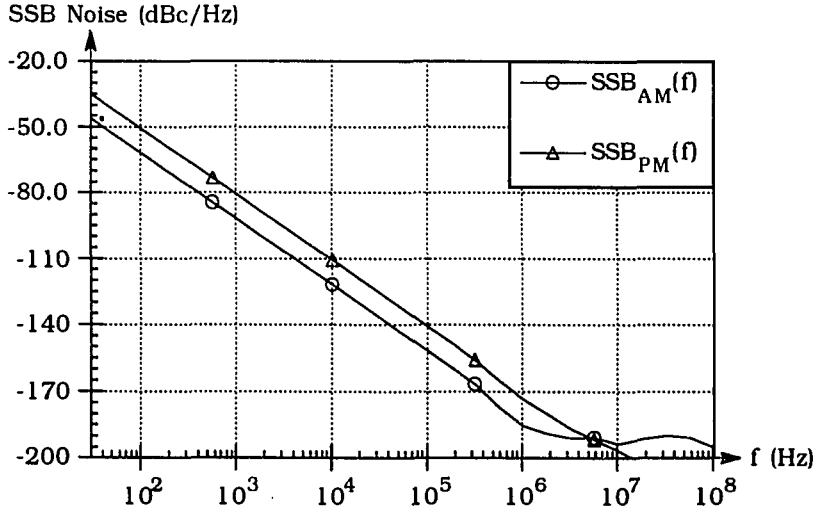

Figure 7.6. Single Sideband Spectrums Due to Collector Current Flicker Noise, i_{fec}

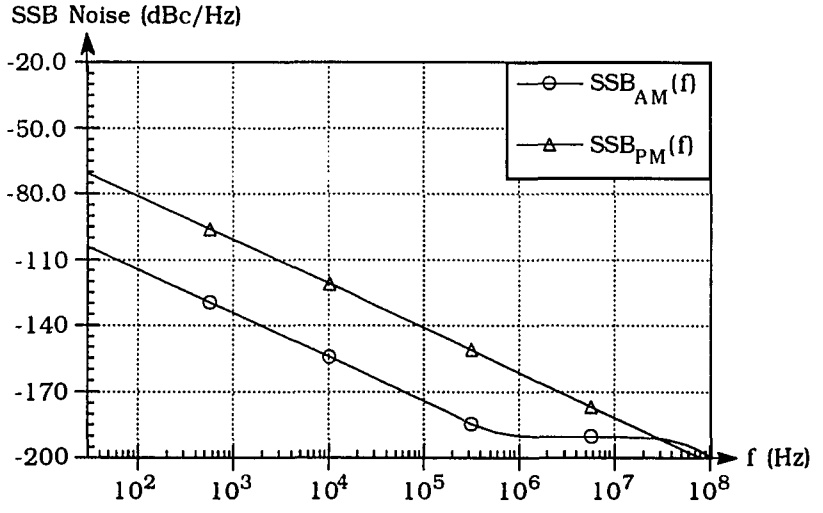

Figure 7.7. Single Sideband Spectrums Due to Thermal Noise in R_C

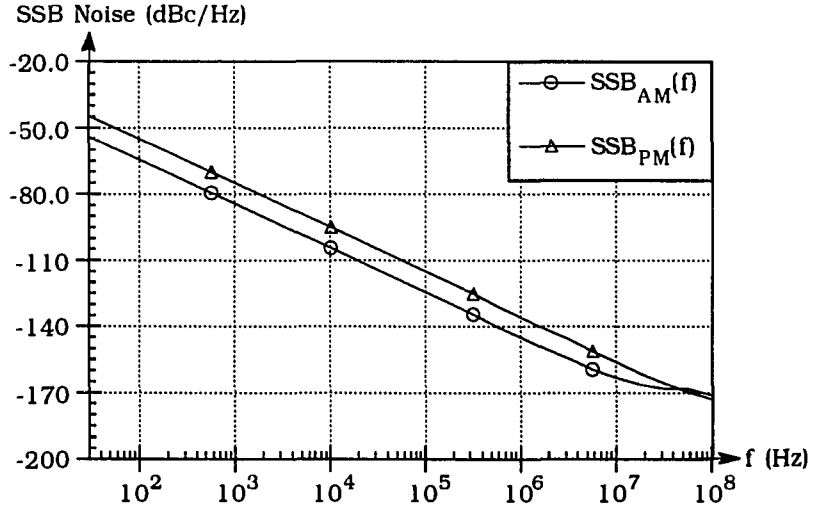

Fig 7.8. Single Sideband Spectrums Due to Thermal Noise in R_B

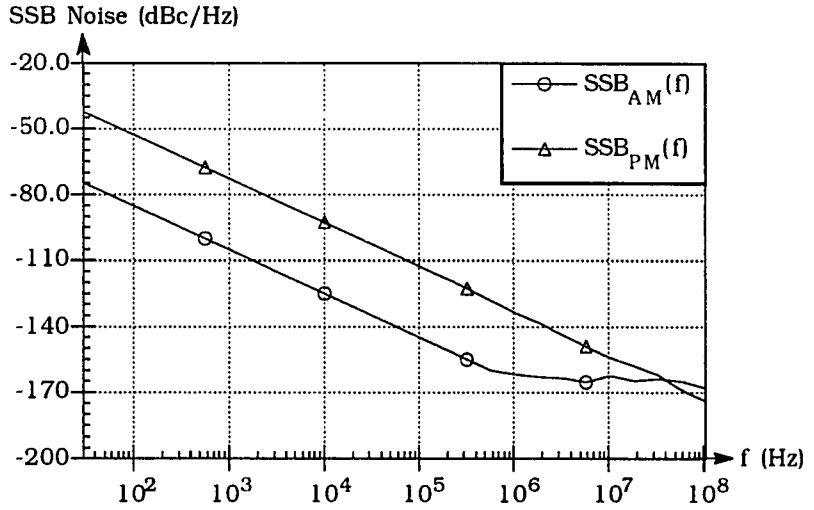

Figure 7.9. Single Sideband Spectrums Due to Thermal Noise in the Resonator Components and the HBT Contact Resistance R_E

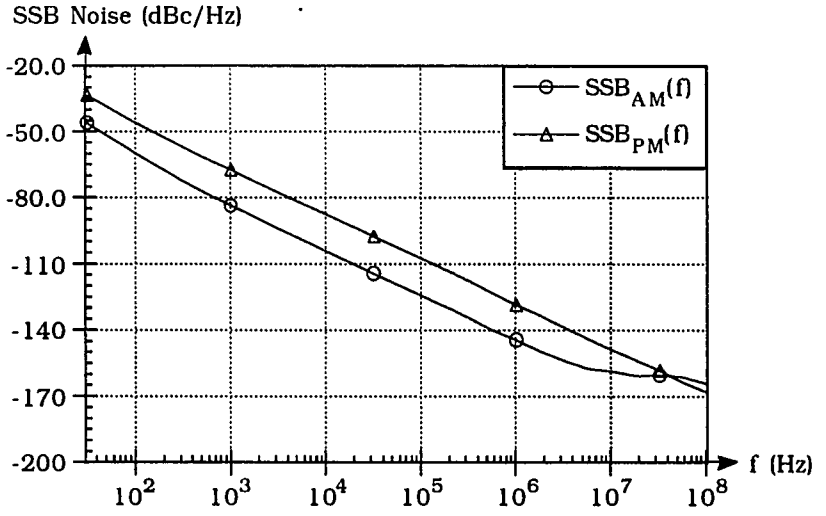

Figure 7.10. Total Single Sideband Spectrums Due to All Noise Sources

As indicated by Figures 7.7 through 7.9, the most significant thermal noise sources are associated with R_B, R_E, and the resonator circuitry. The thermal noise associated with R_C has a minimal impact on the oscillator spectrum. This is most likely a result of the fact that the collector resistance is not directly in the feedback path of the oscillator. Accordingly, the transimpedance from R_C to the oscillator output is much lower than the transimpedances associated with the other thermal noise sources. Note that the thermal noise due to R_B is nearly as significant as the thermal noise due to R_E and the resonator components combined. Thus, no individual component within the oscillator is a dominant source of thermal noise.

The noise spectrums in Figures 7.3 and 7.4 indicate that the impact of the shot noise associated with the base current is negligible in comparison with that of the collector current. This is not surprising since the base current is much less than the collector current. Thus, the only impact which the base current has on the overall noise performance of the oscillator is associated with how it degrades the loaded Q of the oscillator. If the base current were to increase, the base-emitter resistance would drop which could degrade the loaded Q of the oscillator and thus increase the overall noise spectrum. However, the added shot noise, which an increase in base current would create, would not contribute significantly to the overall noise performance of the oscillator.

In comparing Figures 7.4, 7.8, and 7.9, it can be seen that the shot noise sources and the thermal noise sources have nearly equal impact on the overall noise performance of the oscillator. Thus, the overall noise performance of the oscillator cannot be significantly improved by lowering the contribution of any one noise source. If the shot noise associated with the collector current were to be reduced by 10 dB for example, then the output phase noise spectrum would only be reduced by about 2.5 dB. The most effective method of improving the noise performance of the oscillator, is to increase the loaded Q of the oscillator. Increasing the loaded Q of the oscillator would reduce the transimpedance from each noise source to the oscillator output. Thus, increasing the loaded Q would simultaneously reduce the noise at the output of the oscillator due to each individual noise source.

In comparing the plots in Figures 7.5 and 7.6, it is obvious that the most significant source of flicker noise is associated with the collector-to-emitter flicker current source

i_{fec}. While the exact physical cause of this flicker noise source is not known, it has been speculated that this noise source is associated with traps near the base-emitter heterojunction, or at the surface of this region [80, 88]. Note that the slopes of the curves associated with the flicker noise current sources tend to follow a 30 dB-per-decade slope as compared to a 20 dB-per-decade slope for the shot and thermal noise sources. This is a result of the fact that the flicker noise sources add a 10 dB-per-decade slope. A 20 dB-per-decade slope is associated with the feedback effects of the oscillator, as discussed in Section 2.5.

The entire noise spectrums due to all of the noise sources can be observed in Figure 7.10. From this figure it can be seen that for offset frequencies above about 100 Hz the curves have a 20 dB-per-decade slope and thus represents a white FM spectrum. For offset frequencies less than roughly 100 Hz, the spectrums have a 30 dB-per-decade slope, and the spectrums are result of flicker noise. Thus, the spectrum below 100 Hz of offset frequency is referred to as flicker FM.

Some insight into the significant mechanisms in the flicker noise upconversion process can be obtained form the analysis given in this paper. From Equation 7.49 it can be seen that the ratio of the amount of flicker noise current which exists at the first harmonic to that which exists at base band frequencies is equal to the ratio of I_1 to I_0. The data in Table 7.1 indicate that for the two flicker noise sources discussed in this research, this ratio is roughly 0.8. This gives some indication of the amount of low frequency flicker noise which is upconverted to the oscillator sidebands due to noise source modulation. By comparison, an indication of the amount of flicker noise which is upconverted due to circuit nonlinearities can be determined from the conversion matrix analysis presented in Section 5. Equations 5.12 and 5.13 indicate that the ratio of flicker noise at the first harmonic to that at baseband frequencies across a given nonlinear component is equal to the ratio of the Fourier coefficients of the first harmonic to that at the dc Fourier coefficient. In other words, the ratio of the flicker noise at the first harmonic to that at the baseband frequencies due to circuit nonlinearities is equal to G_1/G_0 for Equation 5.12, and C_1/C_0 for Equation 5.13. Thus, the data in Table 5.1 indicate that the dominant nonlinear components in upconverting flicker noise are the transconductance and base-emitter resistance. The ratio of G_1 to G_0 for both of these components is also roughly 0.8. Thus, this indicates that the circuit nonlinearities and

noise source modulation mechanisms are about equally significant in upconverting flicker noise. It should be noted that the actual upconversion of flicker noise involves the interaction of noise source modulation and circuit nonlinearities and that the overall process is quite complex. However, the approach discussed above can be used to give an indication of the dominant upconversion processes.

Note that the amount of flicker noise which is upconverted to the first harmonic due to noise source modulation is determined by the Fourier coefficient I_1. Thus, the upconversion of flicker noise due to noise source modulation can be reduced by reducing the amount of collector current which exists at the fundamental frequency. This collector current is used to supply energy to the resonator circuit to compensate for the energy lost during each cycle. Accordingly, the amount of current at the first harmonic can be reduced by increasing the loaded Q of the oscillator. Thus, increasing the loaded Q of the oscillator will not only reduce the amount of flicker noise which is upconverted due to circuit nonlinearities, but it will also reduce the amount of flicker noise which is upconverted due to noise source modulation.

In order to determine the accuracy of the modelled spectrums, the phase noise spectrum of the HBT oscillator was measured. Equipment to measure the amplitude noise spectrum is not widely available since the AM noise spectrums are normally not of interest. This is a result of the fact that the phase noise levels are typically of more interest in electronic systems, and the amplitude noise spectrums can be reduced to nearly any desired level by the use of limiters. For offset frequencies below 100 kHz, the phase noise spectrum was measured using the quadrature method on a HP3048 phase noise measurement system. The basic theory behind the quadrature measurement system is described in Appendix F. For specific details on the quadrature method and how to use the HP3048 phase noise measurement system to implement this measurement the reader is referred to [100, 101]. To verify that the noise floor of the system was sufficiently low to measure the HBT oscillator, the phase noise of an HP8662 signal generator was also measured. It was found that the system noise floor or the phase noise of the signal generator was at least 20 dB below the phase noise level of the HBT oscillator for offset frequencies below 100 kHz. However, for offset frequencies greater than 100 kHz, the system noise floor was no longer low enough, so the direct spectrum method was used to measure the noise spectrum of the oscillator for offset frequencies between 100

kHz and 1 MHz. The direct spectrum measurement technique is also discussed in Appendix F. The measured phase noise spectrum is shown with the modelled spectrums in Figure 7.11. Note that the measured curve in Figure 7.11 is at roughly -21 dBc at 30 Hz of offset frequency. If the curve is plotted to lower offset frequencies, the measured single-sideband phase noise exceeds 0 dBc at roughly 7 Hz which from the definition of single-sideband phase noise is obviously not valid. The measurement of single-sideband phase noise using the quadrature system is based on the assumption that the phase noise power level must be much less than the carrier power [100]. Accordingly, the curve in Figure 7.11, and all of the noise spectrums given in this section were plotted down to 30 Hz of offset frequency.

In comparing the measured and modelled data, it can be seen that excellent agreement is obtained for offset frequencies greater than 1 kHz. the measured spectrum takes on a 20 dB-per-decade slope, and is within a few dB of the modelled phase noise level. However, for offset frequencies below 1 kHz, the error between the modelled and measured data increases to about 10 dB. This is still in reasonable agreement for a phase noise measurement. However, it does indicate that the modelled flicker noise upconversion is less than what occurs in the actual oscillator. One possible cause of this is associated with the fact that the transimpedance data discussed in Section 5 had to be extrapolated for frequencies below 100 kHz due to numerical round off error. This data set was extrapolated at a 20 db-per-decade slope, which is predicted by classical theory. If the actual slope should have been slightly higher than this (such as 22 dB per decade) then the agreement between the measured and modelled curves below 1 kHz would have been greatly improved. Since the data which were used to generate the conversion networks discussed in Section 5 were only saved to five or six significant figures (see Table 5.2) in most numerical simulators, it should be possible to eliminate this numerical round off error by increasing the numerical accuracy of this data set. However, it is uncertain whether this would provide improved agreement between the measured and modelled data in Figure 7.11. In any case, the agreement between the measured and modelled noise spectrums is generally quite good, and supports the validity of the analysis procedure discussed in this paper.

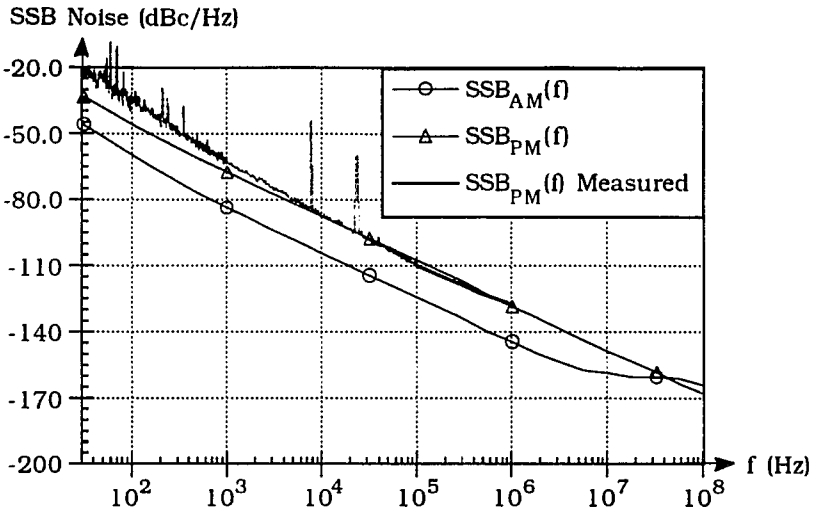

Figure 7.11. Measured and Modelled Single Sideband Noise Spectrums

8. CONCLUSIONS

8.1. Summary of Work

The goal of this work was to develop an accurate technique for analyzing the noise characteristics of HBT oscillators. The procedure presented in this paper accounts for all of the known significant physical mechanisms which effect oscillator noise performance including the effects of circuit nonlinearities and noise source modulation. Most of the previous oscillator analyses which have been completed in this area apply only to specific oscillator configurations, and often lead to conflicting results [3, 12]. It is believed that much of the reason which previous analyses lead to conflicting results is that they neglect the effects of noise source modulation. The results presented in this work indicate that noise source modulation is as significant as circuit nonlinearities in causing the frequency conversion of noise and the upconversion of flicker noise. this work represents the first time which these effects have been taken into account. In addition, the technique presented in this paper may be applied to nearly any oscillator topology.

The early portions of this paper provide a review of the relevant work which has previously been completed on oscillator noise characteristics. The work which was reviewed provides some details on the flicker noise upconversion process, and general ideas on how to reduce the impact of flicker noise on oscillator phase noise. However, these analyses require a number of simplifying assumptions which will not hold in general, and only apply to specific oscillator topologies. Various topics which are relevant to the analysis of oscillator noise characteristics were also reviewed.

In Section 3, an overall discussion of the analysis approach used in this paper was given. This discussion provides a justification for the reason why the analysis approach was chosen. In addition, the analysis approach was described in context with present state-of-the-art CAD programs. As discussed, the approach is compatible with present harmonic balance algorithms and could potentially be used to numerically optimize the noise performance of a given oscillator.

In order to determine how much noise is frequency converted between the various sidebands due to circuit nonlinearities, it is necessary to model the large signal characteristics of the oscillator. This model was generated in Section 4. A large signal HBT model was first developed based primarily on the Gummel-Poon transistor model [40]. However, it was shown in Section 4 that the base-emitter diffusion capacitance model which is normally used in conventional transistor models cannot accurately model this capacitance in HBTs. Accordingly a new base-emitter diffusion capacitance model was developed in Section 4. The large signal characteristics of the oscillator were then simulated using the large signal HBT model.

The results of the large signal oscillator model were used in Section 5 to develop a conversion matrix representation of the oscillator. This representation characterizes the relationship between the incremental changes in the voltage and current waveforms within the oscillator. Thus, the frequency conversion of noise due to circuit nonlinearities can be modelled using this representation. Conversion matrix representations have previously been used to model the mixers [8, 17]. However, it is believed that this work represents the first time that conversion matrices have been used to represent the overall characteristics of an oscillator with no simplifying assumptions. In addition, it appears that conversion matrix theory has not previously been applied to a HBT circuit.

With the nonlinearities within the oscillator characterized, it was then necessary to model the noise levels within the oscillator components. This work was presented in Section 5. The measurements presented in Section 5.1 indicate that the high frequency noise model of a conventional homojunction transistor may also be applied to an HBT. As a result, it was determined that dominant source of noise in HBTs at high frequencies are shot noise and thermal noise. At low frequencies (typically less than about 10 kHz) these shot and thermal noise sources are dominated by flicker noise sources. A HBT flicker noise model was developed in Section 5.2 which consists of two flicker noise sources-one in parallel with the base-collector junction and the other from the collector to emitter terminals. Measurements were also given in Section 6 which demonstrate that both the high frequency and low frequency HBT noise models are accurate.

Since the shot noise and flicker noise sources within the HBT are functions of bias, both of these noise sources are modulated in a periodic manner. The frequency conversion which occurs as a result of this noise source modulation was analyzed in Section 7.1. The work of Dragon [22] was extended to analyze the modulation of shot noise in HBT devices in section 7.7.1. An analysis of flicker noise source modulation has not previously been reported. This type of noise source modulation was analyzed in Section 7.1.2. The theory developed in Section 7.1 was then combined with the results of the conversion matrix analysis to analyze the calculate the noise spectrums of the oscillator due to each of the individual noise sources. The resulting noise spectrums were presented in Section 7.2. The overall noise characteristics of the HBT oscillator were discussed in Section 7.3 and compared with measured results. It was found that the measured and modelled results developed in this work are in quite good agreement.

8.2. Original Contributions

The work presented in this paper has resulted in a number of significant contributions relating to the analysis of noise in HBT oscillators. In the area of HBT modeling under large signal conditions, it has been shown that the base-emitter diffusion capacitance of HBTs cannot be accurately modeled by the expressions which are typically used for bipolar transistors. While the physical phenomenon which determine the diffusion capacitance have been analyzed based on theoretical numerical simulations [59, 60, 61], previously reported HBT large-signal circuit models [43, 44, 45] ignore these effects. In this work, a more accurate diffusion capacitance model has been generated using quasi-static modeling techniques.

Some original contributions were also made in the analysis of the high frequency HBT noise characteristics. Little information has been published regarding the high frequency noise characteristics of HBT devices. Chen et al. [69] have reported on the minimum noise figure of a InP/InGaAs HBT over a range of bias currents. The minimum noise figure, at a single bias condition, has also been reported by Asbeck et al. [6] and Kim et al. [70]. However, the overall high frequency noise characteristics of HBTs have not previously been described in detail. In this work it has been demonstrated that the high

frequency noise characteristics of HBTs can be modelled by using a popular BJT bias dependent noise model.

One of the most significant original contributions presented in this paper is in the area of noise source modulation. While some work has been done to model shot noise source modulation in diode and MESFET mixers [17, 22, 23], shot noise source modulation in bipolar transistors or HBTs has not been analyzed. In this work, Held's [17] and Dragone's [22] work on shot noise modulation in diodes was extended to the analysis of shot noise source modulation in HBTs.

More significantly, this work represents the first in-depth analysis of flicker noise modulation in any device. This is especially significant in the analysis of the noise characteristics of oscillators where the upconversion of flicker noise is often the dominant noise source. The analysis presented in this paper indicates that noise source modulation is roughly as significant as circuit nonlinearities in upconverting flicker noise. The analysis of flicker noise modulation demonstrates that odd symmetrical oscillators such as those presented by Riddle and Trew [5], and Chen et al. [14] are ineffective in eliminating the upconversion of flicker noise. Odd-symmetrical oscillators may be capable of eliminating flicker noise upconversion due to device nonlinearities, but not due to noise source modulation. It is for this reason, that the results presented by Riddle did not cause a significant reduction in flicker noise upconversion and as discussed by Hearn [15] the results of Chen et al. did not demonstrate that flicker noise upconversion is eliminated by using odd symmetrical topologies.

This research also represents the first analysis of a HBT or bipolar transistor oscillator through the use of conversion matrix techniques. A number of diode and MESFET mixer circuits have been analyzed using conversion matrix techniques. However, to the authors knowledge, conversion matrix techniques have not previously been applied to HBT or BJT devices. In addition, this research represents the first in-depth oscillator analysis which includes the effects of noise source modulation. The analysis of this phenomenon is expected to significantly improve the understanding of noise frequency conversion effects in oscillators. This research may also be applied to a wide variety of other periodically driven nonlinear circuits such as mixers, limiters, frequency multipliers, phase detectors, and digital divider chains.

Finally, this research has achieved its ultimate goal of improving the accuracy of modeling and analyzing the noise characteristics of oscillators. The approach presented in this paper allows the noise contributions of individual noise sources in an oscillator to be isolated. This information cannot be obtained from measurement, and allows the circuit designer to more effectively reduce the noise levels within an oscillator. In addition, the approach is suitable for CAD applications and could potentially be used in numerical optimization applications.

8.3. Direction of Future Work

The work presented in this paper leads to several possible areas of future development. One very significant application for this work is the development of a CAD program to implement the analysis approach presented in this paper in an automated manner. Some of the state-of-the-art CAD programs such as LIBRA™, are capable of implementing a harmonic balance algorithm with a conversion matrix analysis for the characterization of mixers. However, these CAD programs are not capable of combining a harmonic balance analysis of an oscillator with a conversion matrix analysis. In additions, these programs are not capable of analyzing the modulation of noise sources in any nonlinear periodically driven circuit. As a first step, noise source modulation, which was discussed in Section 7.1 could be accounted for in an existing CAD program. Ultimately, it would be desirable to develop a CAD program which would be capable of performing the entire procedure discussed in this paper as outlined in Section 3.

Another obvious extension of this work is in the analysis of other types of oscillators, such as MESFET oscillators, or oscillators which contain crystal resonators. While the author has previously studied the noise characteristics of MESFET oscillators [7], the modulation of noise sources within this type of oscillator has not been analyzed. Since MESFETs exhibit a very high level of flicker noise, the upconversion of flicker noise through noise source modulation in MESFET oscillators is of significant interest. In addition, oscillators containing crystal resonators are often used for frequency standards where the phase noise performance is of critical interest. Thus, the extension of this work to the analysis of crystal oscillators is also of significant interest.

The analysis of flicker noise modulation in mixers is another area of significant interest. For mixers which have low intermediate frequencies, the noise performance of the mixer can be dominated by flicker noise. While the modulation of shot noise in diode mixers has been considered [17], the analysis of flicker noise modulation has not. The work presented in Section 7.1 could potentially be extended to analyze these effects.

BIBLIOGRAPHY

[1] Rogers, R. G. Low Phase Noise Microwave Oscillator Design. Norwood, MA: Artech House, 1991.

[2] Sweet, A. A. MIC & MMIC Amplifier and Oscillator Circuit Design. Norwood, MA: Artech House, 1990.

[3] Siweris, H. J., and B. Schiek. "Analysis of Noise Upconversion in Microwave FET Oscillators." IEEE Trans. Microwave Theory and Techniques, MTT-33 (Mar. 1985): 233-242.

[4] Leeson, D. B. "A Simple Model of Feedback Oscillator Noise Spectrum." IEEE Proceedings Letters, 54 (Feb. 1966): 329-330.

[5] Riddle, A. N., and R. J. Trew. "A Novel GaAs FET Oscillator With Low Phase Noise." In 1985 IEEE NTT-S International Microwave Symposium Digest, by the Institute of Electrical and Electronic Engineers, Inc. New York, NY: Institute of Electrical and Electronic Engineers, 1985, 257-260.

[6] Asbeck, P. M., M. F. Chang, J. A. Higgins, N. H. Sheng, G. J. Sulivan, and K. Wang. "GaAlAs/GaAs Heterojunction Bipolar Transistors: Issues and Prospects for Application." IEEE Trans. Electron Devices, ED-36 (Oct. 1989): 2032-2041.

[7] Kramer, B. A. "Noise Analysis of a Monolithic GaAs Voltage Controlled Ring Oscillator." M. S. Thesis, Iowa State University, 1990.

[8] Rizzoli, V., F. Mastri, and C. Cecchetti. "Computer-Aided Noise Analysis of MESFET and HEMT Mixers." IEEE Trans. Microwave Theory and Techniques, MTT-37 (Sept. 1989): 1401-1410.

[9] Gerber, E. A., and A. Ballato. Precision Frequency Control Oscillators and Standards. Vol. 2. New York, NY: Academic Press, 1985.

[10] Scherer, D. "Today's Lesson - Learn About Low Noise Design." Microwaves. (April 1979): 116-122.

[11] Sauvage, G. "Phase Noise in Oscillators: A Mathematical Analysis of Leeson's Model." IEEE Trans. Instrumentation and Measurement, IM-26 (Dec. 1977): 408-410.

[12] Debney, B. T., and J. S. Joshi. "A Theory of Noise in GaAs FET Microwave Oscillators and Its Experimental Verification." IEEE Trans. Electron Devices, ED-30 (July 1983): 769-776.

[13] Kurokawa, K. "Some Basic Characteristics of Broadband Negative Resistance Oscillator Circuits." Bell System Technical Journal, 48 (July-Aug. 1969): 1937-1955.

[14] Chen, H. B., A. van der Ziel, and K. Amberiadis. "Oscillator with Odd-Symmetrical Characteristics Eliminates Low-Frequency Noise Sidebands." IEEE Trans. Circuits and Systems, CAS-31 (Sept. 1984): 807-809.

[15] Hearn, C. P. "Comments of 'Oscillator with Odd-Symmetrical Characteristics Eliminates Low-Frequency Noise Sidebands.' " IEEE Trans. Circuits and Systems, CAS-34 (Mar. 1987): 329-331.

[16] Takaoka, A. and K. Ura. "Noise Analysis of Nonlinear Feedback Oscillator with AM-PM Conversion Coefficient." IEEE Trans. Microwave Theory and Techniques, MTT-28 (June 1980): 654-662.

[17] Held, D. N., and A. R. Kerr. "Conversion Loss and Noise of Microwave and Millimeter-Wave Mixers: Part 1 - Theory." IEEE Trans. Microwave Theory and Techniques, MTT-26 (Feb. 1978): 49-55.

[18] Maas, S. A. Microwave Mixers. Norwood, MA: Artech House, 1986.

[19] Paillot, J. M., J. C. Nallatamby, M. Hessane, R. Quere, M. Prigent, and J. Rousset. "A General Program for Steady State, Stability, and FM Noise Analysis of Microwave Oscillators." In 1990 IEEE MTT-S International Microwave Symposium Digest, by the Institute of Electrical and Electronic Engineers, Inc. New York, NY: Institute of Electrical and Electronic Engineers, 1990, 1287-1290.

[20] Rizzoli, V., and A. Neri. "State of the Art and Present Trends in Nonlinear Microwave CAD Techniques." IEEE Trans. Microwave Theory and Techniques, MTT-36 (Feb. 1988): 343-365.

[21] Siweris, H. J., and B. Schiek. "A GaAs FET Oscillator Noise Model with a Periodically Driven Noise Source." In 16th European Microwave Conference, by Microwave Exhibitions and Publishers, Dublin, Ireland, 1986, 681-686.

[22] Dragone, C. "Analysis of Thermal Shot Noise in Pumped Resistive Diodes." Bell System Technical Journal, 47 (Nov. 1968): 1883-1902.

[23] Statz, H., H. A. Haus, and R. A. Pucel. "Noise Characteristics of Gallium Arsenide Field-Effect Transistors." IEEE Trans. Electron Devices, ED-21 (Sept. 1974): 549-562.

[24] Podell, A. F. "A Functional GaAs FET Noise Model." IEEE Trans. Electron Devices, ED-28 (May 1981): 511-517.

[25] Pettai, R. Noise in Receiving Systems. New York, NY: John Wiley & Sons, 1984.

[26] Brown, R. G. Introduction to Random Signal Analysis and Kalman Filtering. New York, NY: John Wiley & Sons, 1983.

[27] Nyquist, H. "Thermal Agitation of Electric Charge in Conductors." Physical Review, 32 (July 1928): 110-113.

[28] Hillbrand, H., and P. H. Russer. "An Efficient Method for Computer Aided Noise Analysis of Linear Amplifier Networks." IEEE Trans. Circuits and Systems, CAS-23 (April 1976): 235-238.

[29] Buckingham, M. J. Noise in Electronic Devices and Systems. New York, NY: John Wiley & Sons, 1983.

[30] van der Ziel, A. Noise. New York, NY: Prentice-Hall, 1954.

[31] van der Ziel, A. "Unified Presentation of 1/f Noise in Electronic Devices: Fundamental 1/f Noise Sources." Proceedings of the IEEE, 76 (March 1988): 233-258.

[32] Voss, R. F., and J. Clark. "Flicker (1/f) Noise: Equilibrium Temperature and Resistance Fluctuations." Physical Review, B-13 (Jan. 1976): 556-573.

[33] Parzen, B. Design of Crystal and Other Harmonic Oscillators. New York, NY: John Wiley & Sons, 1983.

[34] Phase Noise. RF & Microwave Phase Noise Measurement Seminar. Order No. 5955-8136. Hewlett Packard, Palo Also, CA 1986.

[35] Chen, Y. K., R. N. Nottenburg, Morton B. Panish, R. A. Hamm, and D. A. Humphrey. "Subpicosecond InP/InGaAs Heterostructure Bipolar Transistors." IEEE Electron Device Letters, EDL-10 (June 1989): 267-269.

[36] Asbeck, P. M. "Bipolar Transistors." In High-Speed Semiconductor Devices, ed. S. M. Sze, 335-397. New York, NY: John Wiley & Sons, 1990.

[37] Asbeck, P. M., M. F. Chang, K. C. Wang, D. L. Miller. "Heterojunction Bipolar Transistor Technology." In Introduction to Semiconductor Technology GaAs and Related Compounds, ed. C. T. Wang, 170-209. New York, NY: John Wiley & Sons, 1990.

[38] Bunting, J. M., M. J. Howes, and J. R. Richardson. "Large-Signal Time Domain Modelling of Noise in the Design of MESFET Oscillators." In 16th European Microwave Conference, by Microwave Exhibitions and Publishers, Dublin, Ireland, 1986, 201-206.

[39] Kramer, B. A., and R. J. Weber. "Base-Emitter Diffusion Capacitance in GaAlAs/GaAs HBTs." Electronics Letters, 28 (June 1992): 1106-1107.

[40] Gummel, H. K., and H. C. Poon. "An Integral Charge Control Model of Bipolar Transistors." Bell System Technical Journal, 49 (May 1968): 827-852.

[41] Lundstrum, M. S. "An Ebers-Moll Model for the Heterostructure Bipolar Transistor." Solid-State Electronics, 29 (Nov. 1986): 1173-1179.

[42] Huang, C. N., and I. M. Abdel-Moraleb. "Gummel-Poon Model for Single and Double Heterojunction Bipolar Transistors." IEE Proceedings, 138 (April 1991): 165-169.

[43] Matsuno, C. T., A. K Sharme, and K. Oki. "A Large-Signal HSPICE Model for the Heterojunction Bipolar Transistor." IEEE Trans. Microwave Theory and Techniques, MTT-37 (Sept. 1989): 1472-1475.

[44] Hafizi, M. E., C. R. Crowell, and M. E. Grupen. "The DC Characteristics of GaAs/AlGaAs Heterojunction Bipolar Transistors with Application to Device Modeling." IEEE Trans. Electron Devices, ED-37 (Oct. 1990): 2121-2129.

[45] Grossman, P. C., and A. Oki. "A Large Signal DC Model for GaAs/$Ga_{1-x}Al_xAs$ Heterojunction Bipolar Transistors." In 1991 IEEE MTT-S International Microwave Symposium Digest, by the Institute of Electrical and Electronic Engineers, Inc. New York, NY: Institute of Electrical and Electronic Engineers, 1991, 258-260.

[46] Antognetti, P., and G. Massobro. Semiconductor Device Modeling with SPICE. New York, NY: McGraw-Hill, 1988.

[47] Getrue, I. Modeling the Bipolar Transistor. Beaverton, OR: Tektronix, 1976.

[48] Adlerstein, M. G., and M. P. Zaitlin "Thermal Resistance Measurements for AlGaAs/GaAs Heterojunction Bipolar Transistors." IEEE Trans. on Electron Devices, ED-38 (June 1991): 1553-1554.

[49] LIBRA™ Version 3.0. EESOF, Westlake, CA 1991.

[50] Johnson, T. J. "Measurement, Characterization, and Modeling of High Power Class-C Medium Duty Bipolar Transistors." M.S. Thesis, Iowa State University, 1990.

[51] Park, J. S., and A. Neugroschel. " Parameter Extraction for Bipolar Transistors." IEEE Trans. on Electron Devices, ED-36 (Jan. 1989): 88-95.

[52] Sansen, W., and R. G. Meyer. "Characterization and Measurement of the Base and Emitter Resistance of Bipolar Transistors." IEEE Journal of Solid-State Circuits, SC-7 (Dec. 1972): 492-498.

[53] KaleidaGraph™ Version 2.1.2. Abelbeck Software, Mountain View, CA, 1991.

[54] Beadle, W. E., K. E. Dabrulos, and W. H. Eckton. "Design, Fabrication, and Characterization of a Germanium Microwave Transistor." IEEE Trans. Electron Devices, ED-16 (Jan. 1969): 125-138.

[55] Unwin, R. T., and K. F. Knott. "Comparison of Methods used for Determining Base Spreading Resistance." IEE Proceedings, 126 (April 1980): 53-61.

[56] D. J. Roulston. Bipolar Semiconductor Devices. New York, NY: McGraw-Hill, 1990.

[57] Neudeck, G. W., and R. F. Pierret ed. The PN Junction Diode. Reading, MA: Addison-Wesley, 1989.

[58] Sze, S. M. Physics of Semiconductor Devices. New York, NY: John Wiley & Sons, 1981.

[59] Katoh, R., and M. Kurata. "Self-Consistent Particle Simulation for (AlGa)As/GaAs HBT's Under High Bias Conditions." IEEE Trans. Electron Devices, ED-36 (Oct. 1989): 2122-2128.

[60] Horio, K., Y. Iwatsu, and H. Yanai. "Numerical Simulation of AlGaAs/GaAs Heterojunction Bipolar Transistors with Various Collector Parameters." IEEE Trans. Electron Devices, ED-36 (April 1989): 617-623.

[61] Katoh, R., and M. Kurata. "Self-Consistent Particle Simulation of Heterojunction Bipolar Transistors under High Temperature Operating Conditions." In 1989 International Electron Devices Meeting Technical Digest, by the Institute of

Electrical and Electronic Engineers, Inc. New York, NY: Institute of Electrical and Electronic Engineers, 1989, 477-480.

[62] Sedra, A., and K. Smith. Micro-Electronic Circuits. New York, NY: CBS College Publishing, 1982.

[63] "RSC: Heterojunction Bipolar Transistor Reliability." In 1992 IEEE MTT-S International Microwave Symposium Digest, by the Institute of Electrical and Electronic Engineers, Inc. New York, NY: Institute of Electrical and Electronic Engineers, 1992, 41.

[64] American Technical Ceramics Corporation. ATC UHF Microwave Capacitors. Hunington Station, NY: American Technical Ceramics, [1985].

[65] SPICE 2G.5. Department of Electrical Engineering, University of California, Berkeley, CA, 1981.

[66] Pozar, D. M. Microwave Engineering. Reading, MA: Addison-Wesley, 1990.

[67] Maas, S. A. Nonlinear Microwave Circuits. Norwood, MA: Artech House, 1988.

[68] Bahl, I., and P. Bhartia. Microwave Solid State Circuit Design. New York, NY: John Wiley & Sons, 1988.

[69] Chen, Y., R. N. Nottenburg, M. B Panish, R. A. Hamm, and D. A. Humphrey. "Microwave Noise Performance of InP/InGaAs Heterostructure Bipolar Transistors." IEEE Electron Device Letters, EDL-10 (Oct. 1989): 470-472.

[70] Kim, M. E., A. K. Oki, J. B. Camon, P. D. Chow, B. L. Nelson, D. M. Smith, J. C. Canyon, C. C. Yang, R. Dixit, and B. R. Allen. "12-40 GHz Low Harmonic Distortion and Phase Noise Performance of GaAs Heterojunction Bipolar Transistors." In 1988 IEEE GaAs IC Symposium Digest, by the Institute of Electrical and Electronic Engineers, Inc. New York, NY: Institute of Electrical and Electronic Engineers, 1988, 117-120.

[71] van der Ziel, A. Noise in Solid State Devices and Circuits. New York, NY: John Wiley & Sons, 1986.

[72] The Institute of Electrical and Electronics Engineers. IEEE Standard Dictionary of Electrical and Electronics Terms. New York, NY: The Institute of Electrical and Electronics Engineers.

[73] Adamain, V., and A Uhlir. "A Novel Procedure for Receiver Noise Characterization." IEEE Trans. Inst. and Measurement, IM-22 (June 1973): 181-182.

[74] Davidson, A., B. Leake, and E Strid. "Accuracy Improvements in Microwave Noise Parameter Measurements." IEEE Trans. Microwave Theory and Techniques, MTT-37 (Dec. 1989): 1973-1977.

[75] Pospieszalski, M. "On the Measurement of Noise Parameters of Microwave Two-Ports." IEEE Trans. Microwave Theory and Techniques, MTT-34 (April 1986): 456-458.

[76] Kuhn, N. "Curing a Subtle but Significant Cause of Noise Figure Error." Microwave Journal, 27 (June 1984): 85-98.

[77] Mitama, M., and H. Katoh. "An Improved Computational Method for Noise Parameter Measurement." IEEE Trans. Microwave Theory and Techniques, MTT-27 (June 1979): 612-615.

[78] Gonzalez, G. Microwave Transistor Amplifiers. Englewood Cliffs, NJ: Prentice-Hall, 1984.

[79] Nodal Analysis and Optimization Program. Microwave Monolithics Incorporated, Simi Valley, CA.

[80] Raman, V. K., C. R. Viswanathan, and M. E. Kim. "DC Conduction and Low-Frequency Noise Characteristics of GaAlAs/GaAs Single Heterojunction Bipolar Transistors at Room Temperature and Low Temperatures." IEEE Trans. Microwave Theory and Techniques, MTT-39 (June 1991): 1054-1058.

[81] Kleinpenning, T. "On 1/f Mobility Fluctuations in Bipolar Transistors (I): Theory." In Noise in Physical Systems and 1/f Noise - 1985: Proceedings of the 8th International Conference on 'Noise in Physical Systems' and the 4th International Conference on '1/f Noise' Held in Rome 9-13 September 1985, edited by A. D'amico and P. Mazzetti, 389-392. New York: Elsevier Science Publishing Company, 1986.

[82] Kleinpenning, T. "On 1/f Mobility Fluctuations in Bipolar Transistors (II): Experiment." In Noise in Physical Systems and 1/f Noise - 1985: Proceedings of the 8th International Conference on 'Noise in Physical Systems' and the 4th International Conference on '1/f Noise' Held in Rome 9-13 September 1985, edited by A. D'amico and P. Mazzetti, 393-396. New York: Elsevier Science Publishing Company, 1986.

[83] Kilmer, T., A. van der Ziel, and G. Bosman, "Mobility-Fluctuation 1/f Noise Identified in Silicon P^+NP Transistors." In Noise in Physical Systems and 1/f Noise: Proceedings of the 7th International Conference on 'Noise in Physical Systems' and the 3th International Conference on '1/f Noise' Held in Montpellier, France 17-20 May 1983, edited by M. Savelli, G. Lecoy and J. Nougier, 271-274. New York: Elsevier Science Publishing Company, 1983.

[84] Blasquez, G., and D. Sauvage. "f^{-1} Bulk Current Noise in Short Diodes and Bipolar Transistors." In Noise in Physical Systems and 1/f Noise: Proceedings of the 7th International Conference on 'Noise in Physical Systems' and the 3th International Conference on '1/f Noise' Held in Montpellier, France 17-20 May 1983, edited by M. Savelli, G. Lecoy and J. Nougier, 275-278. New York: Elsevier Science Publishing Company, 1983.

[85] Zhu, X., and A. van der Ziel. "The Hooge Parameters of N^+-P-N and P^+-N-P Silicon Bipolar Transistors." IEEE Trans. Electron Devices, ED-32 (March 1985): 658-661.

[86] Zhu, X., A. Pawlikiewicz, and A. van der Ziel. "1/f Noise in N^+-P-N Microwave Transistors." Solid State Electronics, 28 (May 1985): 473-477.

[87] Stoisiek, M., and D. Wolf. "Surface Influence on 1/f-Noise in Bipolar Transistors," In Noise in Physical Systems: Proceedings of the 5th International Conference on

Noise' Held in Bad Nauheim, Germany 13-16 March 1978, edited by D. Wolf, 181-186. New York: Springer-Verlag, 1978.

[88] A. van der Ziel. "Location of 1/f Noise Sources in BJT's and HBJT's - I Theory." IEEE Trans. Electron Devices, ED-33 (Sept. 1986): 1371-1375.

[89] Jue, S. C., D. J. Day, A. Margittai, and M. Svilans. "Transport and Noise in GaAs/AlGaAs Heterojunction Bipolar Transistors-Part II: Noise and Gain at Low Frequencies." IEEE Trans. Electron Devices, ED-36 (June 1989): 1020-1024.

[90] Costa, D., and J Harris. "Low-Frequency Noise Properties of N-p-n AlGaAs/GaAs Heterojunction Bipolar Transistors." IEEE Trans. Electron Devices, ED-39 (Oct. 1992): 2383-2394.

[91] Fogner, W. "A Determination of 1/f Noise Sources in Semiconductor Diodes and Transistors," In Transistors I. Princton, NJ: RCA Labs, 1956, pp. 239-295.

[92] A. van der Ziel. "Proposed Discrimination Between 1/f Noise Source in Transistors." Solid State Electronics, 25 (Feb. 1982): 141-143.

[93] F. Hooge. "Comparison of 1/f Noise Theories and Experiments." In Noise in Physical Systems and 1/f Noise - 1985: Proceedings of the 8th International Conference on 'Noise in Physical Systems' and the 4th International Conference on '1/f Noise' Held in Rome 9-13 September 1985, edited by A. D'amico and P. Mazzetti, 27-33. New York: Elsevier Science Publishing Company, 1986.

[94] M. Keshner. "1/f Noise." Proceedings of the IEEE, 76 (March 1988): 233-258.

[95] Rice, S. "Mathematical Analysis of Noise." Bell Systems Technical Journal. 24 (Jan. 1945): 46-256.

[96] Hooge, F. N. "1/f Noise if No Surface Effect." Physics Letters. 29 (April 1969):139-140.

[97] Hsu, S. T. "Low-Frequency Noise in Metal-Silicon Schottky Barrier Diodes." IEEE Trans. Electron Devices, ED-17 (Oct. 1970): 496-506.

[98] H. Beck and W. Spruit. "1/f Noise in the Variance of Johnson Noise." Journal of Applied Physics. 49 (June 1978): 3384-3385.

[99] B. Jones and J. Francis. "Direct Correlation Between 1/f and Other Noise Sources." Journal of Physics D. 8 (July 1975): 1172-1176.

[100] Hewlett Packard. Operating and Service Manual HP 3048/11740A Phase Noise Measurement System. Hewlett Packard, Spokane, Washington, 1985.

[101] Hewlett Packard. Product Note 11729C-2. Phase Noise Characterization of Microwave Oscillators - Frequency Discriminator Method. Hewlett Packard, Palo Alto, CA, 1985.

ACKNOWLEDGEMENTS

The author wishes to express his appreciation to his major professor, Dr. Robert J. Weber, for his support and guidance during this research. The commitment of time and energy by the other members of the author's graduate committee: Dr. Stanley G. Burns, Dr. David T. Stephenson, Dr. Joseph Shinar, and Dr. James L. Cornette is also greatly appreciated.

The author wishes to thank the Iowa State University Graduate College and the Department of Education Fellowship Program for their financial support during the course of this research.

The author is especially grateful to Rockwell International for the resources which it provided. The HBT devices and test fixture components which were used during this research were provided by this organization. More significantly, the test equipment which was required to complete the measurements for this research was made available by the Collins Commercial Avionics Division of Rockwell International.

Finally, the author would like to acknowledge the efforts of the following Rockwell International technical personnel who provided numerous inputs and expressed interest in this work: Mr. Don L. Landt, Dr. David E. Oliver, Mr. Wayne Edwards, Mr. Paul D. Jones, and Mr. Gary Gutierrez. The author would especially like to thank Mr. Ken E. Osborn who made several suggestions and supplied the use of his personal tools in the build of the test fixtures for this work. Mr. Gutierrez and Mr. Osborn were also responsible for the assembly of the oscillator circuit used in this research.

APPENDIX A: OVERVIEW OF HARMONIC BALANCE ALGORITHMS

A procedure which could potentially be used to optimize the noise characteristics of oscillators is discussed in Section 3. As part of this procedure a harmonic balance algorithm is required to perform a large signal simulation of the oscillator. A basic overview harmonic balance algorithms is given here.

As shown in Figure A.1, harmonic balance algorithms are implemented by separating a given circuit into linear and nonlinear sections. Interconnects are placed between these two sections to represent the topology of the circuit. Source and load ports are also connected. Initial estimates of the voltages V_1 through V_N, at the interface between the linear and nonlinear network, are made. Using these estimated voltages, the linear subcircuit is analyzed in the frequency domain and the currents I_1 through I_N which would be produced are determined. The nonlinear circuit is analyzed in the time domain using the estimated set of voltages and the currents which would be produced in the nonlinear network are calculated. The currents produced by the linear and nonlinear networks are then compared and used to produce an error function. Numerical techniques are used to iteratively converge to a set of voltages V_1 through V_N such that the currents produced by the linear and nonlinear networks are equal [13, 14].

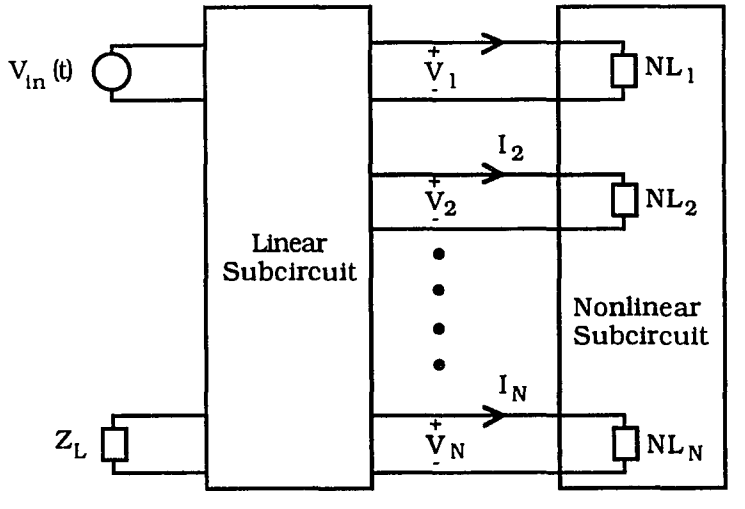

Figure A.1. Harmonic Balance Approach to Analyzing Nonlinear Circuits

The harmonic balance analysis technique results in several unique characteristics. The linear network can be represented as a multiport linear matrix; such as a Y-parameter matrix. As a result, the linear network may be analyzed once, and the multiport matrix representation can be used on subsequent iterations resulting in improved numerical efficiency. However, since the linear network is analyzed in the frequency domain, only a finite number of frequencies can be analyzed. As the number of nonharmonically related frequencies in the circuit increases, the number mixing product frequencies increases rapidly. Accordingly, in most commercially available simulators the number of nonharmonically related frequencies is limited to three or less.

For the analysis approach discussed in this research, harmonic balance algorithms have several advantages over time domain methods. Since the linear portion of the circuit is analyzed in the frequency domain, linear devices can be characterized by using S-parameters. This is extremely useful in modeling a number of linear and distributed components commonly used in oscillator circuits such as dielectric resonators or microstrip transmission lines. Equivalent circuit representations of these components are normally required in time domain simulators; most of which are only valid over a limited frequency range. A harmonic balance analysis is also compatible with the conversion matrix technique of analyzing circuits. (Conversion matrices are discussed in Section 5.) Many of the parameters which are required to generate conversion matrices are already determined in the harmonic balance algorithms. In addition, the frequency of oscillation in a harmonic balance analysis is known implicitly. If a time domain analysis is used, the frequency of oscillation must be calculated.

While harmonic balance algorithms have some significant advantages, they also have some difficulty analyzing oscillators. These algorithms were initially developed to analyze mixers and other periodically *driven* circuits. Accordingly, harmonic balance simulators are based on the assumption that the frequency of the input signal is known. In oscillators, the frequency of oscillation is not predetermined and this can cause convergence problems. As noted by Mass [130], "Because of this extra complexity, very few technical papers have addressed the harmonic-balance analysis of transistor oscillators." At present most commercially available harmonic balance simulators contain special algorithms and circuit elements which allow them to analyze oscillators. However, the analysis process in these simulators is not completely automated, is

somewhat cumbersome to use, and convergence problems are common. These problems are expected to be reduced as harmonic balance algorithms mature.

APPENDIX B: HBT SMALL SIGNAL LIBRA SIMULATION FILE

The LIBRA circuit file which was used to simulate the small signal characteristics of the HBT is listed below.

```
! DESCRIPTION: FIT A SMALL SIGNAL MODEL TO MEASURED HBT S-PARAMETERS
! PURPOSE: DISSERTATION
! AUTHOR: BRAD KRAMER

DIM
  FREQ GHZ
  RES OH
  IND PH
  CAP FF
  LNG UM
  TIME PS
  COND /OH
  ANG DEG

VAR
  CCE1#0 19.29159 11000
EQN
  CTCE1=CCE1*3.15
CKT
! gm
  VCCS  4  6  5  5 M=.05404361 A=0 R1=0 R2=0 F=0 T=0
! Rbe
  RES  4  5  R=3202.31339
! Ro
  RES  6  5  R=231575.218
! Rbc
  RES  4  6  R=8.6156E10
  CAP  4  5  C#0  235.8494 1000
  IND  1  2  L=47.4
  IND  7  8  L=41.2
  IND  9  0  L=70.3
  RES  5  9  R=3.9
  RES  6  7  R=10.8
  RES  2  3  R=3.2
  RES  3  4  R=5
  CAP  1  0  C=20.2
  CAP  2  7  C=1.5
  CAP  2  6  C^CTCE1
  CAP  3  6  C^CCE1
  CAP  6  0  C=15.3
  CAP  2  9  C=3.8
  CAP  7  9  C=5
  CAP  8  0  C=22.6
  DEF2P 1  8  HBT1

  S2PE  1  2  0 E2_2.S2P
  DEF2P 1  2  MEAS1
```

```
TERM
  ZO=100

PROC
  A=HBT1/MEAS1


OUT
  MEAS1 DB[S21]  GR1
  HBT1  DB[S21]  GR1
  MEAS1 DB[S12]  GR2
  HBT1  DB[S12]  GR2
  MEAS1 ANG[S21] GR3
  HBT1  ANG[S21] GR3
  MEAS1 ANG[S12] GR3
 HBT1  ANG[S12] GR3
  MEAS1 S11     SC2
  HBT1  S11     SC2
  MEAS1 S22     SC2
  HBT1  S22     SC2

FREQ
  SWEEP 1 8  1
  SWEEP .5 4  .5
OPT
  A  DB[S21]=0  10
  A  ANG[S21]=0
  RANGE 1  8
  A  DB[S12]=0  20
  A  ANG[S12]=0
  RANGE .15  4
  A  DB[S22]=0  100
  A  ANG[S22]=0
  A  DB[S11]=0  100
  A  ANG[S11]=0
```

APPENDIX C: OSCILLATOR LARGE SIGNAL SIMULATION FILES

The circuit file listings which were used to simulate the large signal characteristics of the oscillator are given in this appendix. The SPICE circuit file listing is given below, followed by the listing which was used to simulate the oscillator in LIBRA.

SPICE LISTING

```
HBT OSCILLATOR MODEL
*   CIRCUIT FILE TO SIMULATE A HBT OSCILLATOR
*   BRAD KRAMER
*   DISSERTATION
*   1/13/91

* POWER SUPPLIES AND BIAS RESISTOR
VPOS        1       0       PULSE(1.5 2 .2E-9 .2E-9 1E-9 9E-6 10E-6)
VNEG        4       0       DC -3.5
RNEG        3       4       3000

* FEEDBACK CAPACITANCE MODEL
C1          2       9       20E-12
LC1         16      9       .031E-9
RC1         16      8       .3

* SHUNT CAP PLUS PARASITIC COUPLING BETWEEN THE SHUNT CAP AND THE
BYPASS CAP.
C2          8       6       1.6E-12
LC2         6       15      .28E-9
RC2         15      0       .62

* INDUCTOR MODEL.
LL1         2       5       .992E-9
RL1B        5       0       2523
L1          5       0       10.7E-9
CL1         5       7       .277E-12
RL1         7       0       .3744

* BONDWIRE INDUCTANCES
LBW1        11      1       .89E-9
LBW2        12      2       .89E-9
LBW3        13      3       1.1E-9
LBW4        13      8       .45E-9

* HBT MODEL
X1 11       12      13      HBT


* HBT SUBCKT        NC      NB      NE
.SUBCKT     HBT     4       1       9

*INTERCONNECT PARASITICS
LBP         1       2       47.4E-12
```

```
LCP         4     5     41.2E-12
LEP         8     9     70.3E-12
CBP         1     0     20.2E-15
CCP         4     0     22.6E-15
CBEP        2     8     3.8E-15

* HBT MODEL
RB          2     3     8.2
RC          5     6     10.8
RE          7     8     3.9
Q1          6     3     7     QHBT
DCJC        2     6     DCBC

* EMITTER CAPACITANCE MODEL
EBE         10    0     3     7     1
EBC         11    10    6     3     1
VX1         11    12    DC 0
QC          12    10    0   QCGS
VX2         10    13    DC 0
DTE         13    0     DCTE

RGIC1       3     14    100
RGIC2       14    15    10000
RGIC3       15    16    100
VGIC1       16    17    DC 0
HGIC        17    18    POLY(3) VGIC1 VX1 VX2 0 0 0 0 0 0 1 1
CGIC        18    7     1E-12
EGIC1       16    7     3     15    1E12
EGIC2       14    7     18    15    1E12

.ENDS HBT

.MODEL QHBT NPN(IS=5.452022380E-23 BF=100000 BR=1 NF=1.09344194 NR=1
+ IKF=12.745778972E-3 VAF=480 ISE=5.826882581E-19 NE=1.57667896496
+ ISC=6.9093503746E-12 NC=1.88121031404 TF=0 CJE=19.03E-15 VJE=1.55262
+ MJE=.564668 CJC=21.46689E-15 VJC=.8740064 MJC=.1832081 XCJC=1 FC=.99)
.MODEL DCBC D(IS=0 CJO=67.622E-15 VJ=.87400639057 M=.18320810795 FC=.99)
.MODEL QCGS NPN(IS=5.041E-10 BF=1E6 BR=1E6 NF=2.707398 NR=2.739614
VAF=2.20319)
.MODEL DCTE D(IS=.7E-16 RS=6.6 N=1)

.OPTIONS TNOM=40
.OPTIONS NUMDGT=5
.TEMP 40
.TRAN .003N 1000N 996N .003N
.OPTIONS ITL5=50000
.OPTIONS ITL1=3000
.PROBE V(1) V(2) V(3) I(LL1) I(X1.RC) I(VPOS) I(VNEG) I(C2) I(C1) V(11) V(12) V(13)
+ I(X1.VX1) I(X1.RC) I(X1.RB) I(X1.RE) V(X1.8) V(X1.10) I(X1.RGIC1) IC(X1.QC) V(X1.10)
+ V(X1.12) I(X1.VX2)
.PRINT TRAN V(X1.3,X1.7) V(X1.3,X1.6) V(X1.3) V(X1.6) V(X1.7) V(X1.2) V(3) I(X1.RB)
+ I(X1.VX1) I(X1.VX2)
.END
```

LIBRA LISTING

```
! DESCRIPTION: HBT OSCILLATOR MODEL
! PURPOSE: DISSERTATION
! AUTHOR: BRAD KRAMER
! DATE: 10/27/92

DIM
   FREQ     GHZ
   RES      OH
   IND      PH
   CAP      FF
   LNG      UM
   TIME     NS
   COND     /OH
   ANG      DEG
   PWR      DBM
   VOL      V
   CUR      A

CKT
   RES_R1   3      51     R=3000
   CAP      2      9      C=20000
   IND      16     8      L=31
   RES      16     9      R=.3

   CAP      8      6      C=1600
   IND      15     0      L=280
   RES      15     6      R=.62

!  INDUCTOR MODEL
   IND      2      5      L=992
   RES      5      0      R=2523
   IND      5      0      L=10700
   CAP      5      7      C=277
   RES      7      0      R=.3744

!  BONDWIRE INDUCTANCES
   IND      11     50     L=890
   IND      12     2      L=890
   IND      13     3      L=1100
   IND      13     8      L=450

!  HBT MODEL
!  INTERCONNECT PARASITICS
   IND      12     14     L=47.4
   IND      11     15     L=41.2
   IND      30     16     L=70.3
   CAP      12     0      C=20.2
   CAP      11     0      C=22.6
   CAP      14     16     C=3.8

!  CONTACT RESISTANCES
   RES      14     17     R=8.2
```

```
   RES       15      18      R=10.8
   RES       16      19      R=3.9

!  ADD CAPACITANCE FOR THE BASE-EMITTER DIFFUSION CAPACITANCE
   CAP       17      19      C=54

!  GUMMEL-POON TRANSISTORS MODEL
   S2PA_QHBT       17      18      19      [MODEL=HBT]
   S1PA_DCBC       14      18              [MODEL=DCBC]
   OSCTEST 30      13      101     102
   DEF1P     101   VTO

MODEL
   HBT       NPN   IS=5.45202E-23 BF=100000 BR=1 NF=1.093442 NR=1 &
                   IKF=12.745779E-3 VAF=480 ISE=5.82688E-19 NE=1.576679 &
                   ISC=6.90935E-12 NC=1.88121 CJE=19.030FF VJE=1.55262 &
                   MJE=.564668 CJC=21.4669FF VJC=.87401 MJC=.18321 XCJC=1 &
                   FC=.99 TF=.79E-12
   DCBC      D     IS=0 CJO=67.622FF VJ=.87401 M=.18321 FC=.99

SOURCE
   VTO       VS_VPOS     50      0       DC=2.0
   VTO       VS_VNEG     51      0       DC=-3.5

   VTO       P_PIN       103     0       P^PWR   F^F1    R^RES_RIN
   VTO       RES_RIN     103     101     R=50
   VTO       RES_RSAMP   102     0       R=50

FREQ
   STEP      1.08
   NH=7

POWER
   STEP      7.0

OUTVAR
   VIN=VTO   VFC     101     0       H1=1
   VFB=VTO   VFC     102     0       H1=1

OUTEQN
   R=VFB/VIN

OUT
   OUTEQN    MAG[R]      GR2
   OUTEQN    ANG[R]      GR2A
   VTO       V_VOUT      30      0       GR3
   VTO       PS_PSPEC    30      0       R=RES_R1        SCN
   VTO       PS_PSPEC    30      0       R=RES_R1        GR4

GRID
   POWER     5       10      1
   GR2       0       4       1
   GR2A      -2      2       .5
   TIME      0       1       .1
```

```
    GR3         -3      1       .5
    FREQ        0       10      1
    GR4         -80     0       10

HBCNTL
    SAMPLE=2
    OSCNODE=30
    OSCVOLT=-1.1
```

APPENDIX D: LIBRA CONVERSION NETWORK CIRCUIT FILES

The LIBRA circuit files which were used to generate a conversion matrix representation of the oscillator are given in this appendix. The first circuit file which is listed is the main circuit file which represents the overall oscillator. It was used to determine the conversion impedance of a given noise source from the location of the noise source in the oscillator to the oscillator output. This main circuit file calls up numerous data files which contain the conversion matrix representation of each of the oscillator elements in S-parameter form. The circuit files which were used to generate the conversion matrix data files are then listed after the main circuit file. Only one circuit file for each type of nonlinear component is listed since these files are very similar. For example, the only file given to generate the conversion matrix for a nonlinear capacitor is that for c_{be}. However, the circuit files for the other nonlinear capacitors may easily be generated by simply changing the Fourier coefficients in the variable block.

LIBRA Circuit File Listing for the Overall Oscillator

```
! FILE NAME: HBTOSC.CKT
! DESCRIPTION: THIS CIRCUIT IS USED TO REPRESENT THE OVERALL OSCILLATOR
! AUTHOR: BRAD KRAMER

DIM
  FREQ HZ
  RES OH
  IND PH
  CAP FF
  LNG UM
  TIME PS
  COND /OH
  ANG DEG

VAR
! MEET THE OSCILLATOR CONDITON BY USING A VARIABLE IMPEDANCE
  XM#0 .10097  100
  XA#-180 59.16304 180

EQN
  MXA=-XA

CKT
  S10P_CBCE   11 13 21 23 31 33 41 43 51 53 CBCE
  S10P_CBCI   12 13 22 23 32 33 42 43 52 53 CBCI
  RES      11 12 R=8.2
  RES      21 22 R=8.2
  RES      31 32 R=8.2
```

```
  RES      41 42 R=8.2
  RES      51 52 R=8.2
  S10P_GBE   12 14 22 24 32 34 42 44 52 54 GBE
  S10P_CBE   12 14 22 24 32 34 42 44 52 54 CBE
  S15P_GM    12 14 13 22 24 23 32 34 33 42 44 43 52 54 53 GM
  S10P_GO    13 14 23 24 33 34 43 44 53 54 GO
  S1P_CTM2    13 0  CTM2B
  S1P_CTM1    23 0  CTM1B
  S1P_CT0     33 0  CT0B
  S1P_CT1     43 0  CT1B
  S1P_CT2     53 0  CT2B
  S2P_RNM2B   11 14 0  RNM2B
  S2P_RNM1B   61 24 0  RNM1B
  S2P_RN0B    31 34 0  RN0B
  S2P_RN1B    81 44 0  RN1B
  S2P_RN2B    51 54 0  RN2B

! THE FOLLOWING ELEMENTS ARE USED TO DETERMINE THE TRANSINPEADANCE
! OF A GIVEN NOISE SOURCE.
  VCCS       41 41 81 81  M^XM A^XA  R1=0 R2=0 F=0 T=0
  VCCS       21 21 61 61  M^XM A^MXA R1=0 R2=0 F=0 T=0
  CCCS       90 52 0  51  M=1  A=180 R1=0 R2=0 F=0 T=0
  CCCS       91 12 0  11  M=1  A=180 R1=0 R2=0 F=0 T=0
  DEF4P      90 44 91 24  CN

TERM
! SET Z0 TO BE ON THE ORDER OF THE COMPONENT IMPEDANCES.
  ZO=1000

OUTVAR
! X11=CN  S11
! X12=CN  S12
! X21=CN  S21
! X22=CN  S22

OUTEQN
! ERR=(X12-1)*(X21-1)-X11*X22

OUT
! OUTEQN MAG[ERR]
! CN    MAG[S11]
! CN    ANG[S11]
! CN    MAG[S12]
! CN    ANG[S12]
! CN    MAG[S21]
! CN    ANG[S21]
! CN    MAG[S22]
! CN    ANG[S22]
  CN    MAG[Z11]
  CN    ANG[Z11]
  CN    MAG[Z12]
  CN    ANG[Z12]
  CN    MAG[Z21]  GR1
  CN    ANG[Z21]
```

```
  CN   MAG[Z22]
  CN   ANG[Z22]

FREQ
  ESWEEP 1  1E8  33

OPT
! RANGE  1 1 1
! OUTEQN  MAG[ERR]=0
```

LIBRA Circuit File Listing for a Time Varying Conductance

```
! FILE NAME: CNGBE.CKT
! DESCRIPTION: GENERATES A CONVERSION NETWORK FOR A TIME VARYING
! CONDUCTANCE
! AUTHOR: BRAD KRAMER

DIM
  FREQ HZ
  RES OH
  IND PH
  CAP FF
  LNG UM
  TIME PS
  COND /OH
  ANG DEG

VAR
! ENTER THE FOURIER COEFFICIENTS OF THE TIME VARYING CONDUCTANCE BELOW.
  G0=.219187E-3
  G1=.169314E-3
  G2=.083303E-3
  G3=.0270486E-3
  G4=.00803887E-3
  A1=-92.4625
  A2=170.002
  A3=57.3441
  A4=-92.7523

EQN
  R0=1/G0
  MA1=-A1
  MA2=-A2
  MA3=-A3
  MA4=-A4

CKT
! GENERATE CURRENT THROUGH THE -2 PORT
  RES  1   11  R^R0
  VCCS 2   1   12  11  M^G1 A^MA1 R1=0 R2=0 F=0 T=0
  VCCS 3   1   13  11  M^G2 A^MA2 R1=0 R2=0 F=0 T=0
  VCCS 4   1   14  11  M^G3 A^MA3 R1=0 R2=0 F=0 T=0
  VCCS 5   1   15  11  M^G4 A^MA4 R1=0 R2=0 F=0 T=0
```

```
! GENERATE CURRENT THROUGH THE -1 PORT
  VCCS 1   2   11   12   M^G1 A^A1  R1=0 R2=0 F=0 T=0
  RES  2   12  R^R0
  VCCS 3   2   13   12   M^G1 A^MA1 R1=0 R2=0 F=0 T=0
  VCCS 4   2   14   12   M^G2 A^MA2 R1=0 R2=0 F=0 T=0
  VCCS 5   2   15   12   M^G3 A^MA3 R1=0 R2=0 F=0 T=0

! GENERATE CURRENT THROUGH THE 0 PORT
  VCCS 1   3   11   13   M^G2 A^A2  R1=0 R2=0 F=0 T=0
  VCCS 2   3   12   13   M^G1 A^A1  R1=0 R2=0 F=0 T=0
  RES  3   13  R^R0
  VCCS 4   3   14   13   M^G1 A^MA1 R1=0 R2=0 F=0 T=0
  VCCS 5   3   15   13   M^G2 A^MA2 R1=0 R2=0 F=0 T=0

! GENERATE CURRENT THROUGH THE 1 PORT
  VCCS 1   4   11   14   M^G3 A^A3  R1=0 R2=0 F=0 T=0
  VCCS 2   4   12   14   M^G2 A^A2  R1=0 R2=0 F=0 T=0
  VCCS 3   4   13   14   M^G1 A^A1  R1=0 R2=0 F=0 T=0
  RES  4   14  R^R0
  VCCS 5   4   15   14   M^G1 A^MA1 R1=0 R2=0 F=0 T=0

! GENERATE CURRENT THROUGH THE 2 PORT
  VCCS 1   5   11   15   M^G4 A^A4  R1=0 R2=0 F=0 T=0
  VCCS 2   5   12   15   M^G3 A^A3  R1=0 R2=0 F=0 T=0
  VCCS 3   5   13   15   M^G2 A^A2  R1=0 R2=0 F=0 T=0
  VCCS 4   5   14   15   M^G1 A^A1  R1=0 R2=0 F=0 T=0
  RES  5   15  R^R0

  DEF10P 1 11 2 12 3 13 4 14 5 15 CM GBE

TERM
  ZO=1000

OUT
  CM   S11
  CM   S21
  CM   S12
  CM   S31

FREQ
  ESWEEP .1 1E8 2
```

LIBRA Circuit File Listing for a Time Varying Transconductance

```
! FILE NAME: CNGM.CKT
! DESCRIPTION: GENERATE CONVERSION NETWORK FOR A TIME VARYING
! TRANSCONDUCTANCE
! AUTHOR: BRAD KRAMER

DIM
  FREQ HZ
  RES OH
```

```
  IND PH
  CAP FF
  LNG UM
  TIME PS
  COND /OH
  ANG DEG

VAR
! ENTER THE FOURIER COEFF. OF THE TIME VARYING TRANSCONDUCTANCE BELOW.
  G0=.0220662
  G1=.0181321
  G2=.0100597
  G3=.00360251
  G4=.000975367
  A1=-93.0831
  A2=170.231
  A3=61.9119
  A4=-89.0565

EQN
  MA1=-A1
  MA2=-A2
  MA3=-A3
  MA4=-A4

CKT
! GENERATE CURRENT THROUGH THE -2 PORT
  VCCS 1   101  11   11   M^G0 A=0   R1=0 R2=0 F=0 T=0
  VCCS 2   101  12   11   M^G1 A^MA1 R1=0 R2=0 F=0 T=0
  VCCS 3   101  13   11   M^G2 A^MA2 R1=0 R2=0 F=0 T=0
  VCCS 4   101  14   11   M^G3 A^MA3 R1=0 R2=0 F=0 T=0
  VCCS 5   101  15   11   M^G4 A^MA4 R1=0 R2=0 F=0 T=0

! GENERATE CURRENT THROUGH THE -1 PORT
  VCCS 1   202  11   12   M^G1 A^A1  R1=0 R2=0 F=0 T=0
  VCCS 2   202  12   12   M^G0 A=0   R1=0 R2=0 F=0 T=0
  VCCS 3   202  13   12   M^G1 A^MA1 R1=0 R2=0 F=0 T=0
  VCCS 4   202  14   12   M^G2 A^MA2 R1=0 R2=0 F=0 T=0
  VCCS 5   202  15   12   M^G3 A^MA3 R1=0 R2=0 F=0 T=0

! GENERATE CURRENT THROUGH THE 0 PORT
  VCCS 1   303  11   13   M^G2 A^A2  R1=0 R2=0 F=0 T=0
  VCCS 2   303  12   13   M^G1 A^A1  R1=0 R2=0 F=0 T=0
  VCCS 3   303  13   13   M^G0 A=0   R1=0 R2=0 F=0 T=0
  VCCS 4   303  14   13   M^G1 A^MA1 R1=0 R2=0 F=0 T=0
  VCCS 5   303  15   13   M^G2 A^MA2 R1=0 R2=0 F=0 T=0

! GENERATE CURRENT THROUGH THE 1 PORT
  VCCS 1   404  11   14   M^G3 A^A3  R1=0 R2=0 F=0 T=0
  VCCS 2   404  12   14   M^G2 A^A2  R1=0 R2=0 F=0 T=0
  VCCS 3   404  13   14   M^G1 A^A1  R1=0 R2=0 F=0 T=0
  VCCS 4   404  14   14   M^G0 A=0   R1=0 R2=0 F=0 T=0
  VCCS 5   404  15   14   M^G1 A^MA1 R1=0 R2=0 F=0 T=0
```

```
! GENERATE CURRENT THROUGH THE 2 PORT
  VCCS 1   505  11   15   M^G4 A^A4  R1=0 R2=0 F=0 T=0
  VCCS 2   505  12   15   M^G3 A^A3  R1=0 R2=0 F=0 T=0
  VCCS 3   505  13   15   M^G2 A^A2  R1=0 R2=0 F=0 T=0
  VCCS 4   505  14   15   M^G1 A^A1  R1=0 R2=0 F=0 T=0
  VCCS 5   505  15   15   M^G0 A=0   R1=0 R2=0 F=0 T=0

  DEF15P  1 11 101  2 12 202  3 13 303  4 14 404  5 15 505  CM GM

TERM
  ZO=1000

OUT
  CM   S11
  CM   S21
  CM   S12
  CM   S31

FREQ
  ESWEEP .1 1E8 2
```

LIBRA Circuit File Listing for a Time Varying Capacitance

```
! FILE NAME: CNCBE.CKT
! DESCRIPTION: GENERATE CONVERSION NETWORK FOR A TIME VARYING
! CAPACITANCE
! AUTHOR: BRAD KRAMER

DIM
  FREQ HZ
  RES OH
  IND PH
  CAP FF
  LNG UM
  TIME PS
  COND /OH
  ANG DEG

VAR
! ENTER THE FOURIER COEFF. OF THE TIME VARYING CAPACITANCE BELOW (PF).
  C0=.124329
  C1=.0275469
  C2=.00354617
  C3=.00147748
  C4=.000895998
  A1=-89.3928
  A2=152.969
  A3=-29.6182
  A4=-159.816
! SET F0 TO THE FUNDAMENTAL HARMONIC OF THE LARGE SIGNAL (THZ)
  F0=.001082477523

EQN
```

```
  MA1=-A1
  MA2=-A2
  MA3=-A3
  MA4=-A4
  W1=2*3.14159265359*F0
  W2=4*3.14159265359*F0

CKT
! GENERATE CURRENT THROUGH THE -2 PORT
  VCCS 1   101  11   111  M^C0 A=0   R1=0 R2=0 F=0 T=0
  VCCS 2   101  12   111  M^C1 A^MA1 R1=0 R2=0 F=0 T=0
  VCCS 3   101  13   111  M^C2 A^MA2 R1=0 R2=0 F=0 T=0
  VCCS 4   101  14   111  M^C3 A^MA3 R1=0 R2=0 F=0 T=0
  VCCS 5   101  15   111  M^C4 A^MA4 R1=0 R2=0 F=0 T=0
  CCCS 151  1   101  11   M^W2 A=-90 R1=0 R2=0 F=0 T=0
  IND  151      111       L=1
  VCCS 111  1   151  11   M=1  A=0   R1=0 R2=0 F=0 T=0

! GENERATE CURRENT THROUGH THE -1 PORT
  VCCS 1   102  11   112  M^C1 A^A1  R1=0 R2=0 F=0 T=0
  VCCS 2   102  12   112  M^C0 A=0   R1=0 R2=0 F=0 T=0
  VCCS 3   102  13   112  M^C1 A^MA1 R1=0 R2=0 F=0 T=0
  VCCS 4   102  14   112  M^C2 A^MA2 R1=0 R2=0 F=0 T=0
  VCCS 5   102  15   112  M^C3 A^MA3 R1=0 R2=0 F=0 T=0
  CCCS 152  2   102  12   M^W1 A=-90 R1=0 R2=0 F=0 T=0
  IND  152      112       L=1
  VCCS 112  2   152  12   M=1  A=0   R1=0 R2=0 F=0 T=0

! GENERATE CURRENT THROUGH THE 0 PORT
  VCCS 1   103  11   113  M^C2 A^A2  R1=0 R2=0 F=0 T=0
  VCCS 2   103  12   113  M^C1 A^A1  R1=0 R2=0 F=0 T=0
  VCCS 3   103  13   113  M^C0 A=0   R1=0 R2=0 F=0 T=0
  VCCS 4   103  14   113  M^C1 A^MA1 R1=0 R2=0 F=0 T=0
  VCCS 5   103  15   113  M^C2 A^MA2 R1=0 R2=0 F=0 T=0
  IND  103      113       L=1
  VCCS 113  3   103  13   M=1  A=0   R1=0 R2=0 F=0 T=0

! GENERATE CURRENT THROUGH THE 1 PORT
  VCCS 1   104  11   114  M^C3 A^A3  R1=0 R2=0 F=0 T=0
  VCCS 2   104  12   114  M^C2 A^A2  R1=0 R2=0 F=0 T=0
  VCCS 3   104  13   114  M^C1 A^A1  R1=0 R2=0 F=0 T=0
  VCCS 4   104  14   114  M^C0 A=0   R1=0 R2=0 F=0 T=0
  VCCS 5   104  15   114  M^C1 A^MA1 R1=0 R2=0 F=0 T=0
  CCCS 154  4   104  14   M^W1 A=90  R1=0 R2=0 F=0 T=0
  IND  154      114       L=1
  VCCS 114  4   154  14   M=1  A=0   R1=0 R2=0 F=0 T=0

! GENERATE CURRENT THROUGH THE 2 PORT
  VCCS 1   105  11   115  M^C4 A^A4  R1=0 R2=0 F=0 T=0
  VCCS 2   105  12   115  M^C3 A^A3  R1=0 R2=0 F=0 T=0
  VCCS 3   105  13   115  M^C2 A^A2  R1=0 R2=0 F=0 T=0
  VCCS 4   105  14   115  M^C1 A^A1  R1=0 R2=0 F=0 T=0
  VCCS 5   105  15   115  M^C0 A=0   R1=0 R2=0 F=0 T=0
  CCCS 155  5   105  15   M^W2 A=90  R1=0 R2=0 F=0 T=0
```

```
 IND   155      115      L=1
 VCCS 115  5   155  15  M=1  A=0   R1=0 R2=0 F=0 T=0

 DEF10P 1 11 2 12 3 13 4 14 5 15 CM CBE

TERM
 ZO=1000

OUT
 CM   S11
 CM   S21
 CM   S12
 CM   S31

FREQ
 ESWEEP .1 1E8 37
```

Linear Network Listings at the Baseband Sideband Frequency

```
! DESCRIPTION: GERNATE CONVERSION MATRICIES FOR THE LINEAR
! COMPONENTS AT THE BASE BAND FREQUENCY.
! AUTHOR: BRAD KRAMER

DIM
 FREQ HZ
 RES OH
 IND PH
 CAP FF
 LNG UM
 TIME NS
 COND /OH
 ANG DEG
 PWR DBM
 VOL V
 CUR A


CKT
 RES   18 0  R=3000

 CAP   10 13 C=20000
 RES   13 14 R=.3
 IND   14 15 L=31

 CAP   15 16 C=1600
 RES   16 17 R=.62
 IND   17 0  L=280

! INDUCTOR MODEL
 IND   10 11 L=992
 RES   11 0  R=2523
 IND   11 0  L=10700
 CAP   11 12 C=277
```

```
 RES  12 0  R=.3744

! BONDWIRE INDUCTANCES
 IND  9  10 L=890
 IND  19 18 L=1100
 IND  15 19 L=450

! INTERCONNECT PARASITICS
 IND  9  6  L=47.4
 IND  19 8  L=70.3
 CAP  9  0  C=20.2
 CAP  6  8  C=3.8

! EMITTER CONTACT RESISTANCE
 RES  8  7  R=3.9

 DEF2P 6  7  RN  RN0

! COLLECTOR TERMINATION IMPEDANCE
 IND  1  0  L=890
 IND  1  2  L=41.2
 CAP  1  0  C=22.6
 RES  2  3  R=10.8
 DEF1P 3    CT  CT0

TERM
 Z0=1000

FREQ
 ESWEEP .1 1E8 37

OUT
 RN   Z11
 RN   Z12
 RN   Z21
 RN   Z22
```

Linear Network Listings at the First Harmonic Sideband Frequency

```
! DESCRIPTION: GERNATER CONVERSION MATRICIES FOR THE LINEAR
! COMPONENTS AT THE FIRST HARMONIC.
! AUTHOR: BRAD KRAMER

DIM
 FREQ HZ
 RES OH
 IND PH
 CAP FF
 LNG UM
 TIME NS
 COND /OH
 ANG DEG
 PWR DBM
```

```
 VOL V
 CUR A


CKT
 RES  18 0  R=3000

 CAP  10 13 C=20000
 RES  13 14 R=.3
 IND  14 15 L=31

 CAP  15 16 C=1600
 RES  16 17 R=.62
 IND  17 0  L=280

! INDUCTOR MODEL
 IND  10 11 L=992
 RES  11 0  R=2523
 IND  11 0  L=10700
 CAP  11 12 C=277
 RES  12 0  R=.3744

! BONDWIRE INDUCTANCES
 IND  9  10 L=890
 IND  19 18 L=1100
 IND  15 19 L=450

! INTERCONNECT PARASITICS
 IND  9  6  L=47.4
 IND  19 8  L=70.3
 CAP  9  0  C=20.2
 CAP  6  8  C=3.8

! EMITTER CONTACT RESISTANCE
 RES  8  7  R=3.9

 DEF2P 6  7  RN  RN1

! COLLECTOR TERMINATION IMPEDANCE
 IND  1  0  L=890
 IND  1  2  L=41.2
 CAP  1  0  C=22.6
 RES  2  3  R=10.8
 DEF1P 3    CT  CT1

TERM
 Z0=1000

FREQ
! NOTE - FREQUENCIES MUST BE CHANGED BACK TO BASE BAND FREQUENCIES IN
! THE DATA FILES.
 STEP  1082477523.1 1082477523.18  1082477523.32  1082477523.56
 STEP  1082477524   1082477524.78  1082477526.16  1082477528.62
 STEP  1082477533   1082477540.78  1082477554.62  1082477579.23
```

```
  STEP  1082477623  1082477700.83  1082477839.23  1082478085.34
  STEP  1082478523  1082479301.28  1082480685.28  1082483146.41
  STEP  1082487523  1082495305.79  1082509145.78  1082533757.13
  STEP  1082577523  1082655350.94  1082793750.77  1083039864.33
  STEP  1083477523  1084255802.41  1085639800.66  1088100936.25
  STEP  1092477523  1100260317.10  1114100299.60  1138711655.52
  STEP  1182477523

OUT
  RN  S11
  RN  S21
  RN  S12
  RN  S22
```

APPENDIX E: EXPRESSIONS FOR AM AND PM NOISE SPECTRUMS

When discussing the output spectrum of an oscillator, it is customary to describe it in terms of it amplitude modulated (AM) and phase modulated (PM) spectrum. The AM spectrum is the part of the spectrum which effects the amplitude of a signal. For example, if a sinusiodal signal, $\cos[\omega_o t + \phi_o]$, is amplitude modulated, it can be described as,

$$f_{AM}(t) = C\,\{1 + a\cos[\omega_m t + \phi_a]\}\cos[\omega_o t + \phi_o] \tag{E.1}$$

$$f_{AM}(t) = C\cos[\omega_o t + \phi_o] + \frac{C\,a}{2}\cos[(\omega_o + \omega_m)t + \phi_o + \phi_a] + \frac{C\,a}{2}\cos[(\omega_o - \omega_m)t + \phi_o - \phi_a]. \tag{E.2}$$

In the above equation, a is referred to as the amplitude modulation index. If the same sinusiodal signal is phase modulated instead, it can be described as,

$$f_{PM}(t) = C\,\{\cos[\omega_o t + \phi_o + \beta\cos(\omega_m t + \phi_p)]\} \tag{E.3}$$

$$f_{PM}(t) = C\,\{\cos[\omega_o t + \phi_o]\cos[\beta\cos(\omega_m t + \phi_p)] - \sin[\omega_o t + \phi_o]\sin[\beta\cos(\omega_m t + \phi_p)]\} \tag{E.4}$$

In the above equation, β is referred to as the phase modulation index. If the value of β is much less than 1, then the approximations given by Equations E.5 and E.6 may be applied.

$$\cos[\beta\cos(\omega_m t + \phi_p)] \cong 1 \tag{E.5}$$

$$\sin[\beta\cos(\omega_m t + \phi_p)] \cong \beta\cos(\omega_m t + \phi_p) \tag{E.6}$$

Combining Equations E.4 through E.6, the output spectrum of a phase modulated signal may be approximated as,

$$f_{PM}(t) \cong C\,\{\cos[\omega_o t + \phi_o] - \sin[\omega_o t + \phi_o]\,\beta\cos(\omega_m t + \phi_p)\}. \tag{E.7}$$

$$f_{PM}(t) = C\cos[\omega_o t + \phi_o] + \frac{C\beta}{2}\cos[(\omega_o + \omega_m)t + \phi_o + \phi_p + \frac{\pi}{2}] - \frac{C\beta}{2}\cos[(\omega_o - \omega_m)t + \phi_o - \phi_p - \frac{\pi}{2}] \tag{E.8}$$

Equations E.2 and E.8 demonstrate that for small modulation indexes, the output spectrums of the AM and PM signals will be similar with the exception of a 180° phase

shift between the upper and lower sidebands. For example, if ϕ_o and ϕ_a are set to zero and ϕ_p is set to $-\pi/2$, then the AM and PM output spectrums which result from Equations E.2 and E.8 are shown in phasor form below. Note that the upper and lower sidebands of the phase modulated signal are 180° out of phase. If the values of ϕ_o, ϕ_a, and ϕ_p are adjusted, then nearly any phase relationship between the amplitude and phase modulated signals may be obtained. In addition, if a signal is simultaneously amplitude and phase modulated, then it is possible to get any relationship between both the amplitude and phase of the output sidebands. For example, if the modulation indexes a and β are equal, and the spectrums shown in Figure E.1 are summed, then the upper sideband of the output will double in amplitude and the lower sideband will be zero.

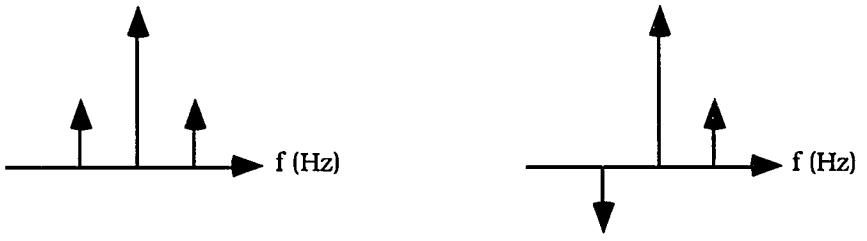

(a) AM Signal (b) PM Signal

Figure E.1. Spectral Components of an Amplitude and Phase Modulated Signal

Note that the signal in Equations E.2 and E.8 is modulated by a sinusiodal function. However, these equations can also be used to describe a signal which is modulated by noise. As discussed by Rice [115] any noise source can be described as a continuous spectrum of sinusiods. This follows directly from the concept of spectral density. Any noise source can be thought of as the summation of an infinite number of sinusiods with random phase angles and rms amplitudes equal to the spectral density function. Or as expressed by Rice, a given noise voltage source can be expressed as,

$$v(t) = \lim_{\Delta f \to 0} \sum_{n=0}^{\infty} \sqrt{2\, S_v(f_n)\, \Delta f}\, \cos(2\pi f_n\, t - \phi_n). \tag{E.9}$$

where

$$f_n = n\, \Delta f \tag{E.10}$$

In Equation E.9, ϕ_n is a random phase angle which is uniformly distributed between $\pm\pi$. The function $S_v(f_n)$ is the power spectral density of the noise voltage as a function of frequency and has units of V^2/Hz. In other words, the function $S_v(f_n)$ determines strength

of the noise source at a given frequency. The 2 under the radical in Equation E.9 accounts for the fact that the square root of $S_V(f_n)$ is an rms value, while the entire function under the radical is the peak value of the cosine function. Often in describing a noise source it is useful to consider its spot noise. The spot noise refers to a noise signal at a single frequency per unit frequency. Thus the spot noise of the signal given in Equation E.9 at 10 Hz is $\sqrt{2\ S_V(10)\ \Delta f}\cos(20\ \pi\ t + \phi)$.

Equations E.2, E.8, and the above discussion can be used to describe a signal which is simultaneously amplitude and phase modulated by a noise source. For simplicity, only the spot noise at an arbitrary modulation frequency will be analyzed. This provides all of the required information since the spot noise source can be swept through a span of frequencies to generate an entire oscillator spectrum. Thus, a signal which is simultaneously amplitude and phase modulated by a spot noise source may be expressed as,

$$f(t) = \sqrt{2}\,V_X \cos[\omega_o t + \phi_o] + \sqrt{2}\,e_a \cos[\omega_u t + \phi_a + \phi_o] + \sqrt{2}\,e_a \cos[\omega_l t + \phi_o - \phi_a] + \sqrt{2}\,e_p \cos[\omega_u t + \phi_o + \phi_p + \frac{\pi}{2}] - \sqrt{2}\,e_p \cos[\omega_l t + \phi_o - \phi_p - \frac{\pi}{2}]. \quad \text{(E.11)}$$

In the above equation, e_a and e_p are positive real random variables which are equal to $\sqrt{S_V(f)\ \Delta f}$ and have units of V . e_a represents the rms value of the spot noise voltage at the upper and lower sidebands which results from amplitude modulation. e_p represents the rms value of the spot noise voltage at the upper and lower sidebands which results from phase modulation. In other words, the noise voltage associated with e_a amplitude modulates the signal while that associated with e_p phase modulates the signal.

Note that Equation E.11 implies that the phase modulation index is much less than 1, which as indicated by Equation E.8, implies that the sideband signals are much less than 0.5 of the carrier signal. This will be satisfied in any oscillator for significant offset frequencies since the sideband noise will be much less than the carrier power. For noise extremely close to the carrier frequency, this approximation may not be valid.

Equation E.11 may be used to calculate the rms spot noise levels at the upper and lower sidebands given the levels of the AM and PM noise voltages. However, this is not

what is desired. Instead, it is desirable to express the AM and PM voltages in terms of the voltages at the upper and lower sidebands. These expressions will now be derived.

Equation E.11 demonstrates that if a signal is amplitude and phase modulated, upper and lower sidebands result. From this equation, the voltages at the upper and lower sidebands may be expressed in phasor form as,

$$e_u \angle\phi_u = e_a \angle\phi_o + \phi_a + e_p \angle\phi_o + \phi_p + \frac{\pi}{2} \tag{E.12}$$

$$e_l \angle\phi_l = e_a \angle\phi_o - \phi_a - e_p \angle\phi_o - \phi_p - \frac{\pi}{2} . \tag{E.13}$$

multiplying both sides of Equations E.12 and E.13 by $1 \angle -\phi_o$,

$$e_u \angle\phi_u - \phi_o = e_a \angle\phi_a + e_p \angle\phi_p + \frac{\pi}{2} \tag{E.14}$$

$$e_l \angle\phi_l - \phi_o = e_a \angle -\phi_a - e_p \angle -\phi_p - \frac{\pi}{2} \tag{E.15}$$

Adding and subtracting the complex conjugate of Equation E.15 from E.14, the spectral densities of the noise voltages which create AM and PM noise are given by,

$$e_a \angle\phi_a = \{e_u \angle\phi_u - \phi_o + e_l \angle\phi_o - \phi_l\}/2 \tag{E.16}$$

$$e_p \angle\phi_p = \{e_u \angle\phi_u - \phi_o - \frac{\pi}{2} - e_l \angle\phi_o - \phi_l - \frac{\pi}{2}\}/2 \tag{E.17}$$

Equations E.16 and E.17 give the AM and PM noise voltage levels as a function of the noise voltage which is present at the upper and lower sidebands. The voltages at the upper and lower sidebands can be related to the large-signal-small signal analysis which was developed in Section 5. From Equation 5.7, the amount of noise voltage which is present at the upper sideband of the first harmonic is given by,

$$v(t) = \frac{1}{\sqrt{2}} [V_n e^{j\omega_u t} + V_n^* e^{-j\omega_u t}] \tag{E.18}$$

$$v(t) = \sqrt{2} \left|V_n\right| \cos[\omega_u t + \angle V_n]. \tag{E.19}$$

Equation E.18 was obtained from the analysis in Section 5. In this analysis, the relationships between the incremental currents and voltages within nonlinear components were described. Accordingly, V_n represents the rms value of a phasor at a given oscillator sideband. In Section 7 phasors of the spot noise voltages within the oscillator are used for the phasors V_n. Thus, by definition,

$$e_u \angle \phi_u = V_1 \tag{E.20}$$

$$e_l \angle \phi_l = V_{-1}^* \tag{E.21}$$

or, taking the complex conjugate of the above equation,

$$e_l \angle -\phi_l = V_{-1} \tag{E.22}$$

In Equations E.20 through E.22 V_1 and V_{-1} are phasors of the rms values of the spot noise voltage sinusoids at the oscillator output. Combining Equations E.16, E.17, E.20, and E.22,

$$e_a \angle \phi_a = \{V_1 \angle -\phi_o + V_{-1} \angle \phi_o\}/2 \tag{E.23}$$

and,

$$e_p \angle \phi_p = \{V_1 \angle -\phi_o - \tfrac{\pi}{2} - V_{-1} \angle \phi_o - \tfrac{\pi}{2}\}/2 \tag{E.24}$$

The above expressions be used to describe the single-sideband phase noise and amplitude noise of the modulated signal. The single sideband phase noise of a signal can be defined as [34] "the ratio of the power in one phase modulated sideband (at an offset f_m away from the carrier) to the total signal power." Thus, from this definition and Equations E.11, E.23, and E.24, the single sideband phase noise at the output of the oscillator is given by,

$$SSB_{PM} = \frac{\langle e_p e_p^* \rangle}{|V_x|^2} = \frac{\left\langle |V_{out1}|^2 + |V_{out-1}|^2 - 2\,\mathrm{Re}\{V_{out1}\, V_{out-1}^* \angle -2\phi_o\} \right\rangle}{4|V_x|^2} \tag{E.25}$$

$$SSB_{PM} = \frac{\langle V_{out1}\, V_{out1}^* \rangle + \langle V_{out-1}\, V_{out-1}^* \rangle - 2\,\mathrm{Re}\{\langle V_{out1}\, V_{out-1}^* \rangle \angle -2\phi_o\}}{4|V_x|^2} \tag{E.26}$$

where V_{out1} and V_{out-1} are defined as the values of V_1 and V_{-1} at the output of the oscillator. In other words, V_{out1} and V_{out-1} are the values of the spot noise voltages at the upper and lower sidebands of the oscillator output. (See Figure 5.5.)

In a similar manner, the amplitude modulation spectrum and cross correlation spectrum between the AM and PM noise can be derived.

$$SSB_{AM} = \frac{\langle e_a e_a^* \rangle}{|V_x|^2} = \frac{\langle V_{out1} V_{out1}^* \rangle + \langle V_{out-1} V_{out-1}^* \rangle + 2\,\mathrm{Re}\{\langle V_{out1} V_{out-1}^* \rangle \angle -2\phi_o\}}{4|V_x|^2} \quad \text{(E.27)}$$

$$SSB_{AM\text{-}PM} = \frac{\langle e_a e_p^* \rangle}{|V_x|^2} = \frac{j\langle V_{out1} V_{out1}^* \rangle - j\langle V_{out-1} V_{out-1}^* \rangle + 2\,\mathrm{Im}\{\langle V_{out1} V_{out-1}^* \rangle \angle -2\phi_o\}}{4|V_x|^2} \quad \text{(E.28)}$$

In Equations E.25 through E.28, V_{out1} and V_{out-1} are phasors of the rms values of the spot noise voltage sinusoids at the oscillator output and V_x is the rms value of the carrier sinusoid at the first harmonic. Equations E.25 through E.27 are very useful in characterizing the spectrum of any signal which has been developed through the use of a conversion network analysis. The results of the analysis can be used to determine the values of V_{out1} and V_{out-1} and the cross correlation between these two variables across a given pair of nodes. In addition, V_x is simply the rms amplitude of the voltage which exists across the the same pair of nodes under large signal conditions. This amplitude can be obtained from the results of a large signal simulation such as that described in Section 4. Thus, by combining the results of a conversion matrix analysis with Equations E.25 through E.28, the spectrums of a signal within a nonlinear circuit can be determined.

APPENDIX F: QUADRATURE METHOD OF PHASE NOISE MEASUREMENT

The phase noise performance of the microwave characterized in this research was measured using both the quadrature method and the direct spectrum method. The basic theory behind the quadrature method is described in this appendix. This derivation is based on the results presented in [34] and [101]. The direct spectrum method is also briefly discussed at the end of this section. However, the main emphasis of this section is related to the quadrature method of measuring phase noise.

A block diagram of the measurement system which is used to implement the quadrature method is shown in Figure F.1. The oscillator signal which is to be characterized is fed into a splitter. One of the signals out of the splitter is fed through a long delay line into a double balanced mixer, while the other signal out of the splitter is fed directly into the double balanced mixer. If the length of the delay line is selected such that the two signals which are fed into the double balanced mixer are 90° out of phase, then the signal out of the double balanced mixer at baseband frequencies will be proportional to the phase noise of the oscillator. (This result is derived in the latter portions of this section.) Higher frequency harmonics are also produced at the output of the mixer. However, these higher order harmonics are rejected by a low pass filter. The signal out of the lowpass filter, which is proportional to the phase noise level of the oscillator is then fed into a spectrum analyzer to display the phase noise level of the oscillator.

A general expression for a phase modulated signal is given by Equation E.3. If this function is used to represent the signal out of an oscillator, then the two signals into the

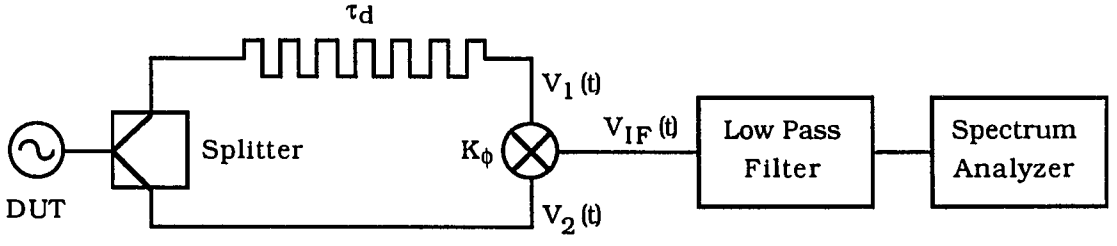

Figure F.1. Block Diagram of the Quadrature Method Measurement System

double balanced mixer in Figure F.1 are given by,

$$V_1(t) = C_1 \cos\{\omega_o (t-\tau_d) + \phi_o + \beta \cos[\omega_m (t-\tau_d) + \phi_p]\} \quad (F.1)$$

and $$V_2(t) = C_2 \cos\{\omega_o t + \phi_o + \beta \cos[\omega_m t + \phi_p]\} \quad (F.2)$$

where τ_d is the delay through the delay line. The signal out of the double balanced mixer will be proportional to the product of the voltage waveforms given above. The low frequency component of the signal out of the mixer is then be given by,

$$V_{IF}(t) = K_\phi C \cos[\omega_o \tau_d + \beta \{\cos(\omega_m t + \phi_p) - \cos(\omega_m[t-\tau_d] + \phi_p)\}] , \quad (F.3)$$

where K_ϕ is the mixer conversion gain [34]. There will also be a high frequency component produced at the output of the mixer. However, this component will be rejected by the low pass filter. If the delay line is selected to be an odd multiple of 90°, then the double balanced mixer will act as a phase detector as shown below. In this case the phase delay must be set such that,

$$\omega_o \tau_d = \frac{2n + 1}{2} \pi . \quad (F.4)$$

Combining Equations F.3 and F.4,

$$V_{IF}(t) = \pm K_\phi C \sin[\beta \{\cos(\omega_m t + \phi_p) - \cos(\omega_m[t-\tau_d] + \phi_p)\}] \quad (F.5)$$

Note, in the above equation, that β is determined by the amplitude of the phase noise out of the oscillator. In most practical oscillators, β will be very small, and thus Equation F.5 may be approximated as,

$$V_{IF}(t) \cong \pm K_\phi C \beta \{\cos(\omega_m t + \phi_p) - \cos(\omega_m[t-\tau_d] + \phi_p)\}]. \quad (F.6)$$

$$V_{IF}(t) \cong \pm 2 K_\phi C \beta \sin(\omega_m t + \phi_p - \tau_d \omega_m/2) \sin(\tau_d \omega_m/2) \quad (F.7)$$

If the length of the delay line in Figure F.1 is selected to be a reasonable length such that $\tau_d \omega_m/2$ is small, then Equation F.7 may be approximated as,

$$V_{IF}(t) \cong \pm K_\phi C \beta \tau_d \omega_m \sin(\omega_m t + \phi_p - \tau_d \omega_m/2) \quad (F.8)$$

$$V_{IF}(t) \cong \pm K_\phi C \tau_d \omega_m [\beta \cos(\omega_m t + \phi_p - (\tau_d \omega_m + \pi)/2)] \quad (F.9)$$

or,

$$V_{IF}(t) \cong \pm K_d \omega_m [\beta \cos(\omega_m t + \phi_p - (\tau_d \omega_m + \pi)/2)] \quad (F.10)$$

where the frequency discriminator constant, K_d, is given by,

$$K_d = K_\phi C \tau_d. \quad (F.11)$$

Note term inside of the square brackets in Equation F.10 is equal to the spot noise voltage associated with a single sideband spectrum of the oscillator, with an arbitrary phase shift added. (Compare this term with the second and third terms in Equation 15.8 for example.) This term is multiplied by a constant, K_d, and the modulation frequency, ω_m. Thus, the power spectral density of the signal out of the low pass filter is proportional to the power spectral density of the phase noise in a single sideband of the oscillator, multiplied by ω_m^2. This plot is known as the power spectral density of frequency fluctuations, $S_{\Delta f}(f)$ [34]. This spectrum can also be displayed as a single sideband phase noise spectrum of the oscillator by passing the signal out of the lowpass filter through an integrator. This is performed automatically by the HP 3048 phase noise measurement system. Thus, the phase noise spectrum of the oscillator can be displayed by the measurement system shown in Figure F.1.

As noted in Section 7, the phase noise of the oscillator was also measured over a frequency range of 100 kHz to 1 MHz using the direct spectrum method. This method is very straight forward and follows almost directly from the definition of single sideband phase noise. Single sideband phase noise may be defined as the ratio of noise power in one phase modulated sideband (at an offset f_m away from the carrier) to the total signal power [34]. Thus, by simply displaying the spectrum of the oscillator on a spectrum analyzer, the phase noise of the oscillator may be measured directly, if the noise power in a given sideband is assumed to be entirely due to phase noise. Figure 7.10 indicates that this is a good assumption. While the direct spectrum method is a very straight froward measurement method, it does have some limitations. The oscillator cannot drift in frequency significantly during a sweep cycle of the spectrum analyzer. As a result, the direct spectrum method is most useful for measurements with relatively large offset frequencies where the oscillator drift will be relatively small in comparison to the offset

frequency itself. Accordingly, the direct spectrum method was only used in this research for relatively high offset frequencies.

APPENDIX G: BASE-EMITTER DIFFUSION CAPACITANCE IN HBTS

The article given in this appendix was written by the author and his major professor. It is sighted as reference [39] and is reprinted with the permission of the Institute of Electrical Engineers.

BASE-EMITTER DIFFUSION CAPACITANCE IN GaAlAs/GaAs HBTs

Abstract - The voltage dependance of the base-emitter diffusion capacitance in a single heterojunction GaAlAs/GaAs HBT is discussed. It is found that conventional transistor capacitance models are not accurate for these devices. An empirical expression is given which may be used to model this diffusion capacitance.

Introduction: Heterojunction bipolar transistors (HBTs) are gaining considerable interest in a number of analog, microwave, and digital applications by virtue of their high cut off frequencies, high early voltages, and low 1/f noise levels. The use of HBTs in these applications has given rise to the need for a more accurate device model in order to minimize design and fabrication costs. In this correspondence, the voltage dependence of the base-emitter diffusion capacitance of a GaAlAs/GaAs HBT is discussed. It is found that this diffusion capacitance is a strong function of base-collector voltage and cannot accurately be characterized by conventional transistor models. However, this voltage dependence is in agreement with numerical analyses which have been performed on HBTs[1,2]. The mechanisms which determine the voltage dependance of this diffusion capacitance are discussed, and an empirical expression is given which may be used to model this diffusion capacitance.

Determination of base-emitter diffusion capacitance: A single heterojunction GaAlAs/GaAs HBT with a conventional n-type collector structure was characterized based on measured Gummel data and a series of S-parameter measurements taken at a different terminal voltages. The dc parameters of the Gummel-Poon model as implemented in SPICE[3] were extracted using techniques similar to those described by Getreu[4] and Hafizi[5] and the differential conductances in the Gummel-Poon model were calculated based on these parameter values. The resulting modeled and measured dc I-V curves are shown in Figure G.1.

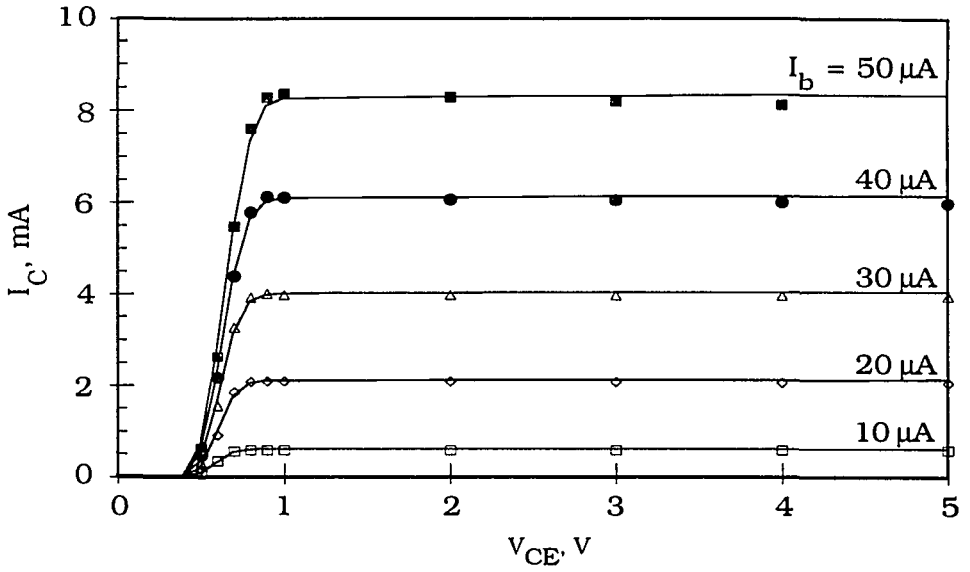

Figure G.1. Measured and Modeled HBT I-V Curves (■, ●, ▲, ◆, □ Measured Data, – Modeled Curves)

The base-emitter and base-collector capacitances were then extracted at each bias point by fitting the small signal Gummel-Poon model to the measured S-parameters using the calculated differential conductances in the model. The voltage dependence of base-collector capacitance was in good agreement with the Gummel-Poon expression for depletion capacitance. However, in the normal active region of operation, the base-emitter capacitance, C_{BE}, was found to be a strong function of both the base-emitter voltage, V_{BE}, and the base-collector voltage, V_{BC}, as shown in Figure G.2. The base-emitter depletion capacitance, was estimated by fitting C_{BE} to Equation G.1 for intrinsic base-emitter voltages of less than .7 volts. At the bias conditions shown in Figure G.2, with the HBT biased in the normal active region, the depletion capacitance was found to range from 45 to 60 fF. The remaining portion of C_{BE} was attributed to diffusion capacitance.

$$C_{je}(V_{BE}) = C_{je}(0)\left\{1-\frac{V_{BE}}{\phi_e}\right\}^m \qquad \text{(G.1)}$$

Base-emitter diffusion capacitance: Based on charge control theory, the base emitter diffusion capacitance may be expressed as[4],

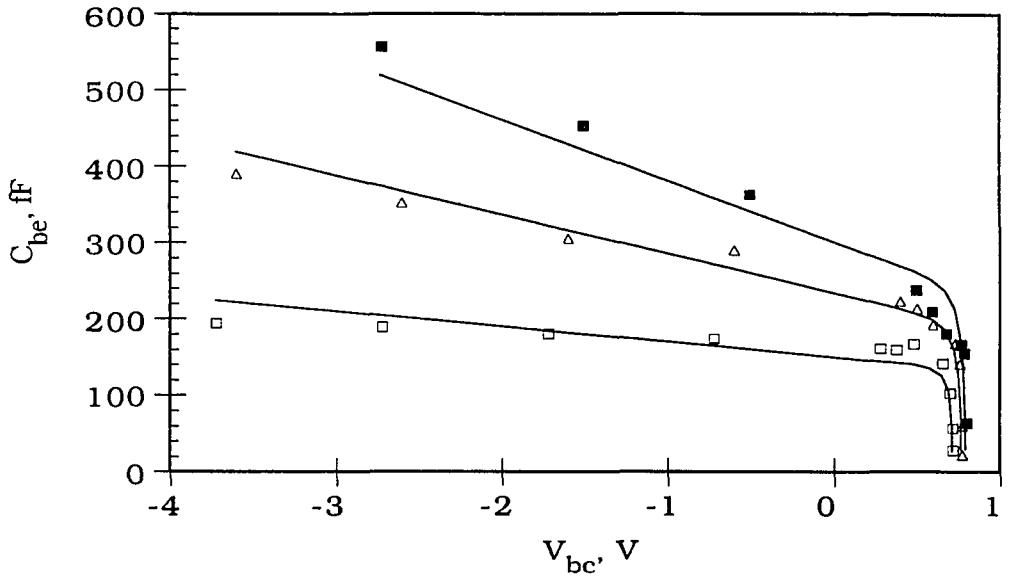

Figure G.2. Base-Emitter Capacitance for Various Bias Conditions (Symbols and Bias (Correspond to Figure G.1)

$$C_{DE} = g_m \tau_F = g_m (\tau_E + \tau_{EBD} + \tau_B + \tau_{CBD}) \quad \text{(G.2)}$$

where τ_F is the forward transit time, τ_E is the emitter delay, τ_{EBD} is the emitter-base depletion region transit time, τ_B is the base transit time, and τ_{CBD} is the base-collector depletion region transit time. In many conventional transistors, τ_B is the dominant component of τ_F. Since τ_B is nearly independent of the transistor bias, τ_F is often treated as a constant, in many transistor models. However, HBTs have very narrow base widths, and as a result, τ_B is not the dominant component and τ_F cannot be treated as a constant.

To accurately model the forward transit time in HBTs, all of the components of τ_F must be considered. The diffusion capacitance which is associated with τ_{EBD} is given by

$$C_{EBD} = g_m \tau_{EBD} = g_m C_{je} r_e \quad \text{(G.3)}$$

where r_e is the differential emitter resistance and C_{je} is the emitter-base depletion capacitance given by Equation G.1. For bias conditions in the normal active region, this diffusion capacitance, which is approximately equal to C_{je}, was found to range from 45 to

60 fF. In HBT devices, the diffusion capacitance which results from τ_E is small and may be neglected[6]. The remaining components of the forward transit time, τ_B and τ_{CBD}, are difficult to separate without detailed knowledge of the HBT device structure. However, the strong base-to-collector voltage dependence of C_{BE}, suggests that τ_{CBD} is the dominant component. This is in agreement with numerical analyses of HBTs[1,2]. For GaAlAs/GaAs HBTs, τ_B is on the order of .6 ps[6], which at a collector current of 4 mA, corresponds to a diffusion capacitance of 54 fF. Thus, the data in Figure G.2 indicates that τ_B is dominated by τ_{CBD}.

For a given carrier velocity in the base-collector depletion region, v(x), τ_{CBD} can be calculated from the expression[6]

$$\tau_{CBD} = \frac{1}{2}\int_0^{W_c} \frac{dx}{v(x)} \tag{G.4}$$

where W_C is the width of the base-collector depletion region. The carrier velocity in the base-collector depletion region is determined by several physical phenomenon and is a function of both V_{BE} and V_{BC}. As discussed by Katoh and Kurata[1], a significant mechanism which determines carrier velocity is associated with the initial onset of the Kirk effect. As the density of mobile carriers in the depletion region increases, the electric field intensity decreases, allowing a greater percentage of the carriers to remain in the Γ-valley of the conduction band. Accordingly, the average carrier velocity increases and τ_{CBD} decreases with increasing current density. The change in τ_{CBD} as a function of V_{BC} has been attributed to the variation in the width of the base-collector depletion region[2]. However, a second mechanism will also effect this variation. As the base-collector junction is reversed biased, the electric field intensity within the depletion region increases. This causes a greater percentage of carriers to be excited out of the Γ-valley into the L- and X-valleys resulting in a lower average carrier velocity and a larger τ_{CBD}. At high collector currents numerical analyses[1,2] indicate that the onset of the Kirk effect causes the collector to be completely depleted. Since W_C is nearly constant under this condition, the variation in the electric field intensity within the depletion region will be the dominant mechanism under this condition.

The complexity of the physical phenomenon involving carrier transport render an analytical analysis of the base-collector transit time impractical. Rather, a quasi-static capacitor model is proposed based on measured results and the results of numerical analyses. A numerical analysis performed by Katoh and Kurata[7] indicates that τ_{CBD} varies roughly as the inverse of the square root of collector current. The measured diffusion capacitance data in this work was found to vary in a similar manner. Since g_m is approximately proportional to the collector current, the capacitance due to τ_{CBD}, C_{CBD}, should vary as the square root of collector current. This suggests an exponential dependence with respect to V_{BE}. The data in Fig. 2 also indicates that C_{BE} varies linearly with respect to V_{BC}. Accordingly, we propose the expression

$$C_{CBD} = C_0\left(1 - \frac{V_{bc}}{\phi}\right)e^{\left(q\,V_{be}/nkT\right)} \qquad \text{(G.5)}$$

where C_0, ϕ, and n are model parameters. This expression was used to perform a curve fit on the measured diffusion capacitance which was not accounted for by τ_{EBD}. This resulted in the parameter values $1.178(10^{-21})$ F, 2.203 V, and 2.707 for C_0, ϕ, and n respectively. The capacitance model of C_{BE}, which is given by the sum of Equations G.1, G.3, and G.5, is plotted in Figure 2. The model curves show good agreement with the measured data. The data in Fig. 2 indicates that improved accuracy could be achieved by changing the parameter ϕ in Equation G.5 to a function which is inversely related to the collector current. However, it is questionable whether the increased complexity is justified. It should also be noted that this model is likely to have limited application for HBTs which have p-type collectors since the carrier transport mechanisms in these devices are different from those discussed in this work.

B. A. KRAMER
R. J. WEBER

Microelectronics Research Center
Applied Sciences Complex #1
Iowa State University
Ames, IA 50010, USA

17th March 1992

References

1 KATOH, R., and KURATA, M.: 'Self-consistent particle simulation for (AlGa)As/GaAs HBT's under high bias conditions', *IEEE Trans.*, 1989, **ED-36**, pp. 2122-2128

2 HORIO, K., IWATSU, Y., and YANAI, H.: 'Numerical simulation of AlGaAs/GaAs heterojunction bipolar transistors with various collector parameters', *IEEE Trans.*, 1989, **ED-36**, pp. 617-624

3 ANTOGNETTI, P., and MASSOBRIO, G.: 'Semiconductor device modeling with SPICE' (McGraw-Hill, New York, 1988)

4 GETREU, I.: 'Modeling the Bipolar Transistor' (Tektronix, Beaverton, OR, 1976)

5 HAFIZI, M. E., CROWELL, C. R., and GRUPEN, M. E.: 'The DC characteristics of GaAs/AlGaAs heterojunction bipolar transistors with application to device modeling', *IEEE Trans.*, 1990, **ED-37**, pp. 2121-2129

6 SZE, S. M. (Ed.): 'High-Speed Semiconductor Devices' (Wiley, New York, 1990)

7 KATOH, R., and KURATA, M.: 'Self-consistent particle simulation of heterojunction bipolar transistors under high temperature operating conditions', International Electron Devices Meeting Tech. Dig., 1989, pp. 477-480